Detailed Modeling and Sensitivity Analysis of Nonequilibrium Thermochemistry in Shock-Heated Gases

by

Timothy T. Aiken

B.S., University of Kansas, 2019

M.S., University of Colorado, 2022

A thesis submitted to the

Faculty of the Graduate School of the

University of Colorado in partial fulfillment

of the requirements for the degree of

Doctor of Philosophy

Department of Aerospace Engineering Sciences

2023

Committee Members:

Iain D. Boyd, Chair

Daniil A. Andrienko

Robyn L. Macdonald

Timothy K. Minton

Gregory B. Rieker

Aiken, Timothy T. (Ph.D., Aerospace Engineering Sciences)

Detailed Modeling and Sensitivity Analysis of Nonequilibrium Thermochemistry in Shock-Heated Gases

Thesis directed by Prof. Iain D. Boyd

During hypersonic flight, a strong bow shock is formed in front of the vehicle that compresses and heats the freestream flow, initiating complex physicochemical processes in the gas surrounding the vehicle. A key complexity of these hypersonic flows is that the timescales of internal mode excitation, chemical reactions, and flow advection are all similar, meaning that the flow is in a thermochemical nonequilibrium state. Accurate modeling of this nonequilibrium behavior is required for predictions of vehicle heating, radio communications blackout, and radiative signatures.

In this thesis, nonequilibrium internal mode excitation, dissociation, and ionization are studied using detailed modeling approaches and modern low-uncertainty experimental data. Formal sensitivity analyses are also performed to identify key uncertain model parameters that most influence the predictive accuracy of the studied thermochemistry models.

The mathematical formulation of the nonequilibrium modeling and sensitivity analysis approaches are described first, followed by a brief discussion of the implementation of these techniques into computational tools. The nonequilibrium modeling framework, which individually tracks the population in species' electronic states, requires a large number of rate parameters for the collisional and radiative processes taking place in the gas. A thorough discussion of the selected model parameters for each process is provided.

The first chemical system to be studied is oxygen. Motivated by the recent publication of low uncertainty experimental data for the vibrational relaxation and dissociation of O_2, a series of two-temperature modeling frameworks are assessed to see which is most consistent with the measured data. In performing this assessment, a technique for simulating reflected shock experiments is developed and benchmarked using unsteady computational fluid dynamic calculations. The ap-

proach accurately predicts the gas evolution at the measurement location, even in the presence of significant reflected shock deceleration. It is recommended that shock deceleration be considered when interpreting data from future experiments where the test gas undergoes significant density change. The two-temperature model assessment reveals that the widely adopted Park model is inconsistent with the measured data, while the recently developed modified Marrone and Treanor (MMT) model demonstrates promising agreement with the data.

The electronic state-resolved model is then compared with experimental measurements from dilute mixtures of O_2 in argon behind reflected shocks. Predictions of dissociation are consistent with available experimental data from 2-5% mixtures of O_2 in argon, indicating that the model can be confidently applied in conditions where dissociation is ongoing. Electron number density measurements enable the inference of several relevant rate constants, facilitating improved modeling of net ionization and a clearer understanding of the electronic excitation kinetics of oxygen. The collisional-radiative model is then assessed using measured data for three electronic states of atomic oxygen. The model successfully reproduces the multi-stage behavior observed in the measured time histories and yields new insights into the multi-stage behavior that improve upon previous interpretations. A global sensitivity analysis considering nearly 300 parameters is then conducted to identify which model parameters most sensitively influence the predicted excited state populations. Excitation of the measured states from the metastable levels and collisional excitation between the three measured states are important across all conditions. The excited state populations demonstrate complex sensitivities involving a large number of collisional and radiative processes, highlighting the importance of adopting a detailed modeling approach when interpreting excited state measurements.

Next, a similar study is performed using experimental measurements of N_2(X) and the $3s$ ^{4}P electronic state of atomic nitrogen, here referred to as N(^{4}P), in reflected shock experiments. Model predictions accurately reproduce measurements of N_2 dissociation for mixtures of 2-10% N_2 in argon, with some discrepancies observed for 20% N_2 mixtures. Net dissociation in mixtures containing 20% N_2 is significantly impacted by the dissociation of N_2(A), the first excited electronic

state of N_2, indicating that molecular electronic excitation can affect net dissociation in shock-heated nitrogen flows. The collisional-radiative model successfully predicts the three-stage behavior and induction time observed in concentration measurements of $N(^4P)$. Mechanisms for the observed behavior are discussed. As in the O_2-Ar experiments, the interpretation using the detailed model deviates from previous analyses that employed a simpler kinetic model. Excited state number density predictions are strongly influenced by the modeling of radiation self-absorption and the inclusion of the measured non-ideal pressure rise. Similar sensitivities are also found in the O_2-Ar experiments. At higher N_2 concentrations, the measured data indicate increased efficiency of atomic nitrogen electronic excitation in collisions with N as compared to collisions with N_2 and Ar. A global sensitivity analysis of the excited state predictions is then performed, identifying the processes in the kinetic model that most sensitively influence the predicted excited state time history and further clarifying the dominant mechanisms affecting the experimental observables.

Finally, plasma generation in hypersonic flows is analyzed using both two-temperature and collisional-radiative models of nonequilibrium air. Using the two-temperature model, uncertainties in electron number density predictions are assessed for flow scenarios that correspond to both strongly shocked and strongly expanded flows, and the dependencies of the calculated uncertainties on individual input parameters are quantified. Ionization levels behind 5 and 7 km/s normal shocks are found to be most sensitive to the associative ionization reactions producing O_2^+ and NO^+ in the region of peak electron number density, with nitric oxide kinetics dominating the uncertainty downstream. The higher levels of ionization behind a 9 km/s shock are found to strongly depend on the electron impact ionization of atomic nitrogen, as well as the charge exchange between N_2^+ and N. Recombining flow scenarios depend on many of the same processes that influence the shocked flows, with the notable addition of the reassociation reaction $O^+ + N_2 \leftrightarrow NO^+ + N$, which is responsible for large uncertainties in electron number density in net recombining flows. A sensitivity analysis of ionization predictions by the air collisional-radiative model is then performed, considering over 600 uncertain parameters. Associative ionization shows similar importance in the collisional-radiative model as in the two-temperature model. The dominant channels are those involving metastable

atomic species. While the excited state associative ionization channels are shown to be important, the explicit modeling of associative ionization involving excited atoms is found to only affect the post-shock electron number density profiles within a thin layer near the shock front.

Each of the studies of experimental data presented in this thesis provides value in two distinct ways. First, the measured data is used to assess the developed collisional-radiative model, yielding unique insights into the collisional-radiative kinetics relevant to shock-heated air species and argon. Second, by adopting high-fidelity flow and kinetics modeling approaches, each study reveals the importance of one or more previously unaccounted-for experimental or kinetic effects. These findings provide useful feedback to inform future experimental campaigns and the accurate interpretation of data from those campaigns.

The sensitivity analyses of ionization in air provide valuable insight into the typical magnitude of uncertainty associated with plasma formation predictions in hypersonic flows and identify the parameters that should be targeted in efforts to reduce those uncertainties.

Dedication

For my family.

Acknowledgements

I want to start by acknowledging Prof. Iain Boyd for his wise mentorship, unwavering support, and significant contributions to my development as a researcher. Professor Boyd fostered an environment that energized and encouraged me to explore my evolving interests; I count myself incredibly lucky to have had the opportunity to pursue my Ph.D. with Prof. Boyd. I wish to thank Prof. Robyn Macdonald, Dr. Daniil Andrienko, Prof. Greg Reiker, and Prof. Tim Minton for serving on my committee and for their thoughtful input to my research.

I owe an overwhelming debt of gratitude to Dr. Ross Chaudhry, who has made a profound impact on my graduate school experience, technical understanding, and perspective on research as a whole. I am thankful to Dr. Kyle Hanquist, Alex Fangman, and Dr. Michael Holloway for our productive conversations and their detailed documentation that set a strong foundation for the code development involved in this thesis. I am grateful to Dr. Jae Gang Kim for creating the first version of the solver that underpins all of the research presented here.

I would also like to acknowledge the members of NGPDL who have helped make my time at CU so enjoyable, in particular Tommy Kava, Amin Taziny, Nicholas Carter, and Pawel Sawicki. This thesis has also benefitted from productive conversations with and feedback from Jens Rataczak, Kal Monroe, Jenny Horing, Michael Sands, Sindhu Manchikanti, Marisa Petrusky, and Dr. Nicholas Campbell.

Outside of CU, the first people I would like to thank are the members of Professor Ron Hanson's research group at Stanford University. As a computational scientist, I am incredibly fortunate to have built my Ph.D. thesis around the high-quality, one-of-a-kind experimental data

that has recently been measured at Stanford. In addition to this foundational contribution to my work, Prof. Hanson and the researchers in his group, particularly Drs. Jesse Streicher, Peter Finch, Ajay Krish, and Yang Li have provided immeasurable support, feedback, and insights, without which this work would be a shadow of its current form. I have also benefitted from several productive and informative discussions with Zev Granowitz, Devin Merrell, and Dylan Drescher.

Dr. Nicolas Minesi and Dr. Mitchell Spearrin at the University of California, Los Angeles, are also gratefully acknowledged for providing experimental data that is analyzed in this thesis. In addition, Professors Marco Panesi, Hua Guo, Igor Adamovich, Klaus Bartschat, and Drs. Brett Cruden, Tom West, Nikolay Popov, and Sung Min Jo have all generously lent their time and expertise to support various aspects of this research. I am also grateful to the CU Research Computing staff, particularly RC Help, who removed countless perplexing roadblocks in my research with their timely and knowledgeable advice.

Countless people have supported me in my personal life throughout this experience as well, and it is impossible to name all of them here. I feel incredibly fortunate to be surrounded by such caring and supportive friends who have enriched my life these past four years. I would like to recognize my late father, Dave, whose keen and sincere interest was an unparalleled source of support in my first two years of graduate school. I thank my mother, Maureen, who has always encouraged my curiosity and decision to pursue a Ph.D. The love for learning that my parents instilled in me has been an invaluable asset in my schooling, research, and life. Thank you to my brother, Daniel, and my sister-in-law, Kelsey, who have consistently supported and encouraged me during my time at CU. I am grateful to my parents-in-law, Wayne and Marian, who have cheered me on during all stages of graduate school and have gone above and beyond in their support on countless occasions.

Most importantly, I would like to thank my wife, Hannah. She has supported me throughout every step of this journey, taking pride in my accomplishments, listening to my excitements and frustrations, and providing much-needed perspective during the most difficult moments. She has consistently motivated me to do my best, even when that required me to make sacrifices that

affected us both. All of this means more with her by my side.

This research was supported by funding through the U.S. Air Force Office of Scientific Research Grant FA9550-21-1-0075 and the Office of Naval Research MURI Grant N00014-22-1-2661. This work utilized the Blanca condo computing resource at the University of Colorado Boulder. Blanca is jointly funded by computing users and the University of Colorado Boulder. This work also utilized the Alpine high-performance computing resource at the University of Colorado Boulder. Alpine is jointly funded by the University of Colorado Boulder, the University of Colorado Anschutz, Colorado State University, and the National Science Foundation (award 2201538).

Contents

Chapter

Tables

Table

Figures

Figure

Chapter 1

Introduction

During hypersonic flight, a strong bow shock is formed in front of the vehicle that converts the kinetic energy of the oncoming flow into the thermal motion of the gas particles, while the energy in the internal modes (rotational, vibrational, and electronic) remains unchanged across the shock. This initiates concurrent processes of thermal and chemical relaxation whereby the translationally hot gas particles transfer their energy to internal mode excitation and endothermic chemical reactions [17]. For typical hypersonic flow conditions, this nonequilibrium state will persist within a given Lagrangian fluid element for less than a millisecond. While this timescale is brief, the convective timescale in a hypersonic flow can be similarly small – thus, a significant portion of the flow around a hypersonic vehicle has the potential to be in thermochemical nonequilibrium.

Nonequilibrium thermochemistry in the high-temperature flow surrounding hypersonic vehicles has been the subject of significant research since the 1950s [18, 17, 19]. Accurate modeling of thermal and chemical relaxation processes is required for predictions of radiative [20] and convective [21] heat flux, radio communications blackout [22], and vehicle radiative signatures [23]. Multi-temperature models are the most widely adopted approach to modeling thermochemical nonequilibrium in vehicle-scale hypersonic flows [24, 25, 26, 1]. This type of model is based on the framework of mode approximation, where separate energy conservation equations are solved to account for nonequilibrium between different energy modes of the gas. Within the mode approximation, the distribution of particle internal energies – rotational, vibrational, electronic – is assumed to follow Boltzmann statistics. However, the true energy distribution function is gener-

ally non-Boltzmann, and this distinction affects the rates of dissociation, ionization, and thermal relaxation, which, in turn, affect first-order engineering quantities of interest like heating.

State-resolved modeling provides a more accurate alternative to multi-temperature models by removing the assumption of a Boltzmann distribution and directly resolving the populations of individual internal energy levels. Significant advancements in the understanding of molecular vibrational relaxation and dissociation have been enabled by the development of vibrational and rovibrational state-resolved models that use rate coefficients determined from scattering calculations on ab initio potential energy surfaces [27]. That work has led to the development of multiple modeling frameworks for vibrational relaxation and dissociation that are based entirely on ab initio quantum chemistry data and state-resolved kinetic modeling [12, 28, 29, 30].

Because most of these models are quantum state-resolved, they are not practical for implementation in large-scale vehicle-scale CFD analyses due to their prohibitive computational cost. One exception is the modified Marrone and Treanor (MMT) model first outlined in [27] and formally proposed in [12] with subsequent elaboration in [21]. This is a two-temperature (2T) model for air that is based on statistical analyses of state-resolved simulations employing ab initio rate constants. The MMT model offers a compelling alternative to the two-temperature model of Park, which is currently the most widely adopted approach to modeling thermochemical nonequilibrium in hypersonic flows [31, 1]. While Park's model has achieved a reasonable agreement with flight test data, it has failed to reproduce the latest experimental shock tube measurements and to accurately predict shock standoff distance on blunt bodies at Mach 10-15 [32]. Work is ongoing to quantify the improvements in predictive accuracy of engineering quantities of interest by adopting the MMT model instead of the Park model [33, 34].

The wide range of next-generation vibrational relaxation and dissociation models are currently being assessed using modern low-uncertainty experimental data [35, 36, 37, 38]. However, most of the existing validation studies have focused on vibrational state-resolved models, not the 2T models of production CFD codes. The current work seeks to address that gap by presenting a parametric analysis of 2T modeling options using modern low uncertainty data from pure O_2 re-

flected shock experiments at Stanford University [5]. Special attention is paid to the MMT model, given its demonstrated potential to accurately predict the inferred time-histories of key 2T model variables [5].

In contrast to the advancements made in the modeling of vibrational excitation and dissociation, the state-resolved modeling of electronic excitation and ionization is comparatively less mature since it is far more difficult to determine the necessary rate coefficients using ab initio techniques, particularly for collisions involving two heavy particles [39]. Most existing studies of electronic excitation in hypersonic air flows are concerned with predicting radiative heating of vehicles flying in excess of 10 km/s, where dissociation and ionization are rapid, and the electron mole fraction can exceed 10% within the flowfield. Rapid dissociation and ionization mean that electronic excitation and ionization are dominated by atomic collisions with electrons throughout the vast majority of the post-shock flowfield. As a result, models that aim to predict the population of individual electronic states, so-called collisional-radiative (CR) models, often neglect or provide a very limited treatment of heavy particle-driven excitation and ionization kinetics in flows where the ionization fraction is sufficiently high.

For flight speeds in the range of 4,500 to 8,000 m/s, the formation of electrons is much slower because there is not enough freestream enthalpy to induce electron impact ionization – instead, electron formation and charged species kinetics are dominated by associative ionization (AI) and charge exchange. The rate coefficients for these processes vary widely depending on the model used [40, 41, 17]. In addition, Boyd and Josyula have recently called attention to the potential impact of atomic electronic nonequilibrium on associative ionization reactions in air, raising questions about the accuracy of current models for associative ionization under nonequilibrium conditions [40]. At flight enthalpies where associative ionization is the dominant mechanism of plasma formation, the electronic excitation of atoms and molecules is dominated by collisions between heavy particles, not electrons, introducing further uncertainty into electronic state-resolved models that are developed to study ionization at velocities below 8 km/s.

When considering the study of atomic electronic excitation in the context of associative ioniza-

tion, there are three key departures from the strongly radiating high-velocity flows discussed above. First, the states of interest are different – the low-lying states of N and O do not radiate strongly and are called the "metastable" states because of their long radiative lifetimes. Second, atom-atom and atom-molecule collisions dominate atomic electronic excitation at suborbital hypersonic speeds because electrons are scarce. It is possible to generate complete datasets for bound-bound and bound-free atomic electronic transitions under electron impact [42, 43, 44]; however, it is not possible to generate such comprehensive datasets for excitation reactions involving only heavy particles. For collisionally-induced excitation by heavy particles (HP-CIE), each individual rate coefficient requires costly and time-consuming quantum-chemical calculations of multiple potential energy surfaces and the couplings between them, followed by complex scattering calculations using those potentials [45, 46, 47, 48]. The HP-CIE cross sections calculated using the formula proposed by Drawin [49] on which several analytical rate expressions are based [50, 19, 51] have been shown to agree poorly with results of detailed quantum scattering calculations, owing to the inability of classical theory to describe the physics of near-threshold excitation reactions involving heavy particles [45].

The third key difference when studying HP-CIE and associative ionization is the lack of flight and ground tests that have published definitive measurements relevant to these processes at flow enthalpies relevant to suborbital flight. For shock velocities of 2-4 km/s, experimental ionization measurements such as those performed by Frohn and de Boer [52] have the potential to be strongly influenced by the ionization of trace impurities. Measurements by Lin, Neal, and Fyfe [16] at somewhat higher shock speeds of 4.5 to 7 km/s have investigated ionization kinetics at the conditions of interest; however, the spatial resolution limitations of their measurement technique prevent a conclusive rate validation effort for associative ionization. Other data from Niblett and Blackman over a similar velocity range yielded ionization times nearly an order of magnitude slower than those measured by Lin, Neal, and Fyfe [53], which the latter authors called into question by claiming that the "luminous front," taken to be the ionization front, was radiating driver gas from the electrical discharge [16]. In light of these uncertainties and the scarcity of experimental

ionization measurements at suborbital shock velocities, many of the widely-used ionization rate sets are based on comparisons with flight [11] or shock tube [1] data for shock velocities in excess of 7 km/s.

As a result of these model development and validation challenges, there is significant uncertainty in the accuracy of existing models that describe ionization and atomic electronic excitation at suborbital hypersonic speeds. New ab initio rate coefficients and experimental validation data are required to formulate a reliable electronic state-resolved model. However, given the large number of parameters required for such a detailed model, it is not immediately obvious which reactions should receive the considerable commitments of time and resources that are required to determine rate coefficients for a given reaction. In addition, as new experimental data becomes available, it can be difficult to discern which of the many uncertain parameters is most effectively constrained by a given measurement, particularly for a state-resolved kinetic mechanism with hundreds or thousands of individual rate and relaxation parameters.

Both of these challenges can be addressed using sensitivity analysis, a formal technique for apportioning the uncertainty in a given model prediction to different sources of uncertainty in the model input [54]. While global sensitivity analysis of a kinetic mechanism with hundreds of uncertain parameters is challenging, the literature contains several examples of such analyses [55, 56, 57]. The same techniques from those studies are applied in the present work. Sensitivity analyses enable the identification of parameters that most significantly affect the predictions of plasma formation, providing a quantitative basis for the selection of rate constants that should receive further study. In addition, sensitivity analysis of variables that can be measured experimentally provides insight into the model parameters that are most effectively constrained through comparisons with a given experimental measurement.

1.1 Scope of Dissertation

Due to the increased interest in hypersonic systems for national security, there is a renewed emphasis on the accurate quantification of plasma formation in hypersonic flows, particularly at

suborbital speeds where ionization models have not yet been conclusively validated. While several reactions are known to affect ionization predictions, there has been no comprehensive effort to quantitatively apportion the uncertainty in ionization predictions to specific chemical kinetic parameters for nonequilibrium air flows. In addition, the observations made by Boyd and Josyula motivate an increase in model fidelity to include the atomic metastable states involved in associative ionization, which dominates plasma formation at suborbital hypersonic speeds.

Motivated by these considerations, an electronic state-resolved model of an air plasma is developed in this thesis, with the specific purpose of providing higher fidelity predictions of ionization at the flow conditions typical of suborbital hypersonic flight. Several components of the developed collisional-radiative model are assessed using new experimental data, and the model predictions are assessed in detail across a wide range of conditions.

First, the coupled vibrational relaxation and dissociation of O_2 are studied using recent low-uncertainty experimental measurements by Streicher et al. [5]. A computationally efficient multi-step technique is developed and validated for the simulation of the reflected shock experiments that are analyzed throughout this thesis. Several of the available two-temperature models for vibrational relaxation and dissociation are then assessed. Conclusions from this chapter are broadly useful to the hypersonics community and also help to inform the vibrational relaxation and dissociation modeling frameworks and parameters that are adopted within the electronic state-resolved model.

Next, recent experimental measurements of electronically excited atomic oxygen [58, 59, 6, 60] and nitrogen [8, 9] are leveraged to assess and improve existing models for the collisionally induced electronic excitation of these species. The detailed collisional-radiative model also provides insight into the processes driving the observed population dynamics, helping to inform the interpretation of future atomic excited state measurements behind strong shock waves.

Grotrian diagrams of the lowest-energy electronic states of atomic oxygen and nitrogen are shown in Figure 1.1, with an orange arrow denoting the absorption transitions used to probe the measured electronic levels in the analyzed experiments. The measured states are radiatively and collisionally coupled to a large number of other electronic levels at both higher and lower energies.

Because the states are close to the continuum, they are also strongly affected by ionization processes. Due to the large number of transitions involving the measured states, it is not intuitively obvious which processes are the most important to predictions of the measured states. To address this, large-scale sensitivity analyses involving several hundred rate parameters are performed to isolate which processes most strongly influence the populations in the measured states. Sensitivity analyses yield improved insight into the kinetics under investigation and help isolate the parameters that are mostly effectively validated through model comparisons with the measured data.

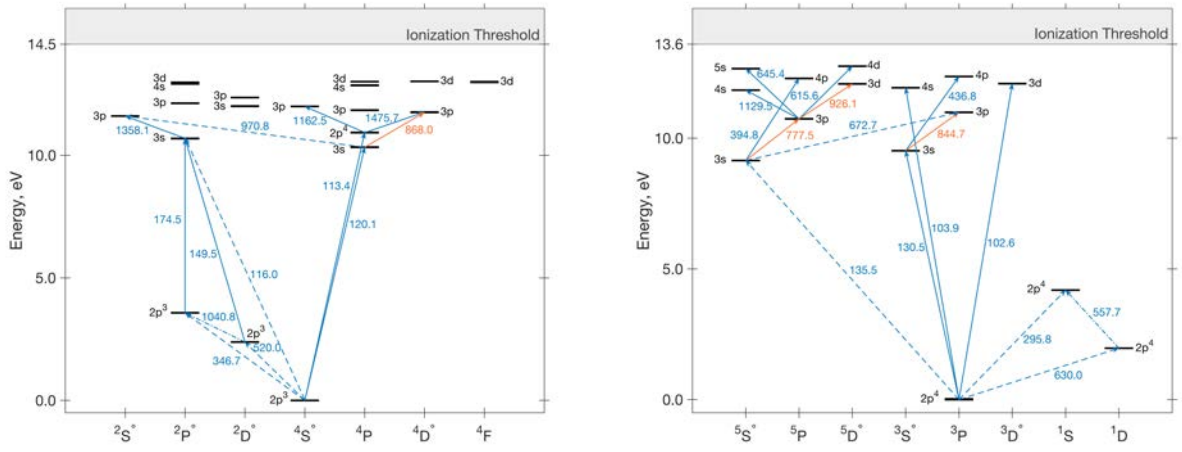

(a) N I (b) O I

Figure 1.1: Grotrian diagram of the lowest-lying electronic states of neutral atomic (a) nitrogen and (b) oxygen. Several radiative transitions are shown, with those used to perform excited state number density measurements shown in orange.

Finally, ionization kinetics in air are investigated using both two-temperature and collisional-radiative models. Sensitivity analysis and uncertainty quantification are performed to assess the accuracy of ionization predictions by two-temperature models and the parameters that most significantly contribute to the uncertainty in model predictions. Ionization kinetics in the collisional-radiative model are analyzed next, with particular attention being paid to the effects of atomic electronic nonequilibrium on the net rates of associative ionization. A large-scale sensitivity analysis is then performed to isolate the parameters in the collisional-radiative model that most affect

ionization predictions.

1.1.1 Outline

This dissertation consists of eight chapters. The first chapter discusses the context in which this work is performed, highlighting the key research gaps and questions that motivate the research being presented. In the second chapter, the mathematical formulations of the nonequilibrium thermochemical model and sensitivity analysis are developed. The software implementations of these techniques are also described. In the third chapter, the selection of rate coefficients for the collisional-radiative model is provided, and a thorough discussion of each process is given.

The main results are included in Chapters 4 - 7. The work presented in Chapter 4 focuses on the two-temperature modeling of vibrational relaxation and dissociation in pure O_2, making use of newly published measurements of vibrational temperature and O_2 number density in several shock tube experiments. Next, in Chapter 5, experiments from the same facility focusing on the electronic excitation of atomic oxygen are analyzed. Following a detailed analysis of the experiments and the observed population dynamics, a sensitivity analysis is performed to identify the collisional-radiative model parameters that most influence predictions of the measured electronic state. In Chapter 6, a similar analysis is performed for experimental measurements of electronically excited nitrogen. In Chapter 7, the ionization of air in strongly shocked and expanding flows is analyzed by means of two-temperature and collisional-radiative models. A sensitivity analysis of these models is then performed, isolating the parameters that warrant further study in future efforts to improve ionization models for shocked hypersonic flows. Finally, a summary, conclusion, and recommended next steps are provided in Chapter 8.

Chapter 2

Mathematical Formulation and Numerical Implementation

2.1 Introduction

In this Chapter, the two principal computational tools employed throughout this thesis are described in detail. A description of the chemical kinetics solver is given first, including the mathematical formulation of the collisional-radiative and multi-temperature models, the implementation of these models into a solver, and several verifications of the software implementation. Next, the developed sensitivity analysis tool is described. Mathematical principles of polynomial chaos expansion (PCE) sensitivity analysis techniques are provided, followed by a discussion of the sparse point collocation technique adopted to fit the PCE surrogate. Finally, the algorithm and its implementation are described, and a benchmarking case is presented.

2.2 Zero-Dimensional Governing Equations

The simplest flow environment considered is a zero-dimensional, adiabatic, and isochoric chemical reactor. The governing equations for this system are given by,

$$\frac{d}{dt}\begin{bmatrix}\rho_p\\ \rho h\\ \rho e_{vib}\\ \rho e_{eex}\end{bmatrix} = \begin{bmatrix}m_p\omega_p\\ -Q_{rad}\\ S_{vib}\\ S_{eex}\end{bmatrix} \tag{2.1}$$

where t is time, ρ is the bulk gas density, m_p is the mass of a particle of pseudospecies p, h is the specific enthalpy, e_{vib} is the specific vibrational energy, and e_{eex} is the specific electron-electronic

energy. Electron-electronic energy, e_{eex}, includes both the free electron translational energy and the electronic energy of species whose electronic levels are not explicitly tracked in the collisional-radiative model. The subscript p denotes a specific pseudospecies, a term that encompasses species as well as individual electronic states. The right-hand-side of Eq. (2.1) are the source terms: ω_p are the pseudospecies source terms, Q_{rad} is the rate of radiative energy emission, S_{vib} is the vibrational energy source term, and S_{eex} is the electron-electronic energy source term. An additional constraint on the governing equations is that total mass density must be conserved, i.e. $d\rho/dt = 0$.

2.3 One-Dimensional Governing Equations

A large number of shock tube experiments are analyzed in this thesis. All of these experiments are analyzed using a one-dimensional steady-state flow solver that spatially integrates a system of governing equations downstream from the shock. The jump conditions across the normal shock are calculated using the Rankine-Hugoniot relations, where vibrational, electronic, and free-electron translational energies are assumed to be frozen across the shock. The gas composition is also held constant across the shock.

The analyzed experimental data have been measured behind both incident and reflected shocks. These two systems necessitate different governing equations and modeling treatments. The treatment of incident shocks is described first in Section 2.3.1, followed by a discussion of the reflected shock modeling procedure in Section 2.3.2

2.3.1 Modeling of Incident Shock Experiments

The system of Euler equations describing the evolution of the flow downstream of an incident shock is given in Eq. (2.2), where x is the distance behind the shock. The governing equations are solved in the reference frame that moves with the shock, so the variable u is the velocity in the reference frame of the shock. The reference frame moving with the shock is inertial because incident shocks are assumed to move with constant velocity. The increment in particle time for a given spatial step dx is given by $udt = dx$. The transformation between the distance downstream

of the shock, x, and the elapsed time in the lab frame, t_{lab}, is given by $t_{lab} = \frac{x}{u_{is}}$, where u_{is} is the velocity of the incident shock.

$$\frac{d}{dx}\begin{bmatrix} \rho_p u \\ \rho u^2 + P \\ \rho u(h + \frac{1}{2}u^2) \\ \rho u e_{vib} \\ \rho u e_{eex} \end{bmatrix} = \begin{bmatrix} m_p \omega_p \\ 0 \\ -Q_{rad} \\ S_{vib} \\ S_{eex} \end{bmatrix} \tag{2.2}$$

Pressure is denoted as P in Eq. (2.2). The flow downstream of incident shocks at various flight conditions in Chapter 7 is also analyzed using Eq. (2.2).

2.3.2 Modeling of Reflected Shock Experiments

Reflected shock experiments are more complex to analyze than incident shock experiments because the shock motion is unsteady, and the gas is already in a nonequilibrium state before it passes through the reflected shock. The present work approaches these modeling challenges in the following way. First, the flow evolution downstream of the incident shock is calculated using Eq. (2.2). This provides the required information about the nonequilibrium state of the gas that is passing through the reflected shock. Second, the velocity and acceleration of the reflected shock are calculated by leveraging the stagnation boundary condition at the shock tube end wall. Results from these two calculations are then used as inputs to a third and final calculation that considers the flow evolution at the measurement location, typically located between 3 and 20 mm from the end wall.

Details of these three calculations are described in Sections 2.3.2.1 through 2.3.2.3. The present three-step modeling approach is based on that of [38], which itself is an evolution of the approach described in [37]. This thesis builds upon these previous studies in two key ways. First, in this Chapter, an improved method is presented for calculating the flow evolution at the measurement location. Second, in Chapter 4, the accuracy of the adopted three-step modeling approach is

assessed using an unsteady 1D computational fluid dynamic (CFD) simulation of a reflecting normal shock in pure O_2.

It is helpful to clarify some nomenclature before proceeding. Figure 2.1 shows a schematic space-time diagram of a reflected shock experiment. The regions of interest are each labeled with a number: Region 1 is the quiescent gas upstream of the incident shock, Region 2 is the gas behind the incident shock but upstream of the contact surface, and Region 5 is the gas behind the reflected shock. Note the curvature of the reflected shock pathline near the wall – this is a unique feature of experiments with strongly endothermic processes in Region 5. The relevant endothermic processes under consideration include vibrational excitation, dissociation, electronic excitation, and ionization.

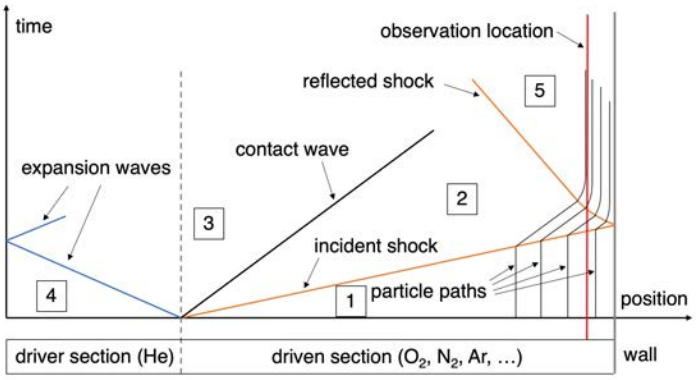

Figure 2.1: Reflected shock tube x-t diagram denoting the different regions of interest.

2.3.2.1 Incident Shock Modeling

The flowfield downstream of the incident shock is calculated as described in Section 2.3.1. Shock attenuation is negelcted by assuming a steady incident shock velocity. Boundary layer growth and its effect on the Region 2 gas is also neglected.

2.3.2.2 Reflected Shock Motion From the Wall

Reflected shocks that produce significant excitation, dissociation, or ionization in the test gas cannot be assumed to move with a constant velocity. These endothermic processes cause the stagnated gas at the wall to compress and cool, introducing a slight velocity toward the wall. As this happens, expansion waves move away from the wall and intersect with the reflected shock, weakening it as they pass through. The exact calculation of this interaction would require an unsteady flow solver. Here, an approximate solution to the reflected shock velocity is computed using the existing 1D space-marching shock tube code by specifying that the gas at the end wall remains at zero lab-frame velocity and constant pressure. The approximate method significantly reduces the computational cost required to simulate a given reflected shock experiment when compared to an unsteady CFD calculation. A computationally efficient flowfield model is critical for enabling the analysis of reflected shock experiments using computationally intensive state-resolved thermochemistry models like those adopted here [38, 37, 61].

By assuming stagnated gas at the wall, the 1D Euler equations are reformulated in the unsteady reference frame of the reflected shock. When viewed in this frame, the velocity of the stagnated wall-adjacent gas is exactly the reflected shock velocity u_{rs}. This approach was originally proposed by Appleton and is based on the assumption of constant stagnation enthalpy in the wall-adjacent gas [62]. Constant stagnation enthalpy is a reasonable approximation because the changing velocity of the reflected shock does not contribute significantly to the enthalpy balance $\left(\Delta\frac{1}{2}u_{rs}^2 \ll h\right)$. A comparison with unsteady CFD in Chapter 4 assesses whether these approximations produce a reasonable prediction for the reflected shock velocity and test gas evolution.

The system of governing equations is given in Eq. (2.3), which is derived from the work of [38, 62]. Note that the assumption $u = u_{rs}$ is only strictly valid at the wall where the no penetration boundary condition holds. From the continuity expression in Eq. (2.3), it is simple to see that changes to the gas density at the wall must be accompanied by inversely proportional changes to

the shock velocity.

$$\frac{d}{dx}\begin{bmatrix} \rho_p u_{rs} \\ \rho u_{rs}^2 + P \\ \rho u_{rs}(h + \frac{1}{2}u_{rs}^2) \\ \rho u e_{vib} \\ \rho u e_{eex} \end{bmatrix} = \begin{bmatrix} m_p \omega_p \\ S_{m,dP} \\ -Q_{rad} \\ S_{vib} \\ S_{eex} \end{bmatrix} \tag{2.3}$$

A new term is introduced into the right-hand-side of the momentum equation to ensure that the pressure at the end wall remains constant, which is expected in the limit of weak Region 2 flow gradients [63]. To specify this condition, the momentum source term, $S_{m,dP}$, must be equal to $\rho u \frac{du}{dx}$ as derived in [38]. With this relationship and the continuity equation, the conservation of momentum reduces to $\frac{dP}{dx} = 0$ as desired.

These modifications to the Euler equations allow the non-constant reflected shock velocity to be calculated using a computationally efficient space-marching simulation approach since a decelerating reflected shock arises naturally as a result of specifying the no penetration end wall boundary condition and a constant end wall pressure. Notably, however, the adopted approach neglects influences on the reflected shock velocity from flow property gradients in Region 2. The possible impact of these gradients is assessed in Chapter 4.

One additional consideration is worth mentioning. In the reflected shock experiments analyzed here, the pressure at the measurement location increases linearly throughout the test time [5]. This happens because the Region 2 gas is compressed by the growing boundary layer as it moves downstream of the incident shock. Attenuation of the incident shock also leads to higher pressures as one moves downstream from the incident shock. The reflected shock thus propagates into a region of steadily increasing pressure, leading to a positive and nonzero $\frac{dP}{dt}$ in Region 5.

Non-ideal pressure rise may be incorporated as a source term into the momentum and energy equations when calculating the reflected shock velocity [61]. This source term leads to increased gas compression, which causes additional shock deceleration when applied in the present modeling approach. This is incomplete because it treats the pressure rise as though it only occurs in Region

5 without any accounting of how the Region 2 pressure increase impacts the shock motion.

The growing boundary layer behind the incident shock may be captured by modeling the tube as a converging area duct [64], and shocks propagating into a converging duct are known to accelerate [65]. Thus, while the previously adopted $\frac{dP}{dt}$ source terms may predict shock deceleration due to Region 5 gas compression, there is a competing shock *acceleration* effect from the upstream flow changes that may be more important.

The present modeling approach is not capable of including these upstream changes when calculating the reflected shock velocity. As a result, the non-ideal pressure rise is neglected when calculating the reflected shock motion. Boundary layer effects are not expected to significantly affect the reflected shock velocity at the measurement location; however, future work should assess how the shock velocity is impacted at downstream locations.

2.3.2.3 Calculation of Measurement Location Flow Evolution

A third space-marching calculation is performed to simulate the flow evolution at the measurement location. This simulation is initialized using the nonequilibrium state of the Region 2 gas that intersects with the reflected shock at the measurement location. To do this, the particle time between the arrival of the incident and reflected shocks must be calculated for the fluid element arriving at the measurement location at the same time as the reflected shock. The particle time calculation is performed iteratively following the method presented in [38]. This method ensures that the nonequilibrium flow evolution in Region 2 and changing reflected shock velocity are included when calculating the pre-shock flow properties at the measurement location.

With a particle time in hand, the reflected shock velocity is then calculated using the sum of $u_2(t = t_p)$ from the first simulation and $u_{rs}(x = d)$ from the second, where $u_2(t)$ is the flow velocity in Region 2 at a particle time t. Both velocities for this calculation are measured in the laboratory frame. The initial condition can now be calculated using the nonequilibrium pre-shock flow properties and the reflected shock velocity measured in the Region 2 particle frame. As with the previous two calculations, the jump condition is evaluated using the Rankine-Hugoniot relations.

Notably, the shock deceleration across the distance between the wall and the measurement location weakens the reflected shock such that the flow is no longer stagnated at the measurement location.

The present approach underpredicts the measured pressure at the observation location by up to 15%. A disagreement of that magnitude cannot be explained by relaxation in Region 2 alone, which raises P_2 by a maximum of 4% for the most extreme case analyzed. The higher pressures observed experimentally are likely caused by the compression of the Region 2 gas by the growing boundary layer behind the incident shock. Analysis by Mirels shows that boundary layer growth can produce Region 2 pressure increases of the magnitude needed to explain the present discrepancy [66]. Incident shock attenuation may also play a role; however, it cannot be the sole explanation since pressure overshoots are observed even in experiments where the shock attenuation is negative.

In order to mimic this effect and to ensure agreement with the measured values of $P_{5,0}$, the upstream condition for the third marching calculation is adjusted using the isentropic relations until the desired Region 5 pressure is equal to the measured $P_{5,0}$. This has the effect of increasing the temperature in Region 5 above its nominal value by as much as 3.5%. Application of the compression to Region 2 results in a smaller rise in T_5 from its nominal value than if the compression is applied in Region 5. Compressing the Region 2 gas is motivated by the assumption that much of the observed overshoot in P_5 is caused by increases in the Region 2 pressure due to shock attenuation and boundary layer growth.

Because the flow is no longer exactly stagnated at the measurement location, u is no longer equal to u_{rs}. Thus, the flow evolution at the measurement location is evaluated using Eq. (2.4).

$$\frac{d}{dx}\begin{bmatrix} \rho_p u \\ \rho u^2 + P \\ \rho u(h + \frac{1}{2}u^2) \\ \rho u e_{vib} \\ \rho u e_{eex} \end{bmatrix} = \begin{bmatrix} m_p \omega_p \\ S_{m,dP} \\ -Q_{rad} + \rho S_{h,dP} \\ S_{vib} \\ S_{eex} \end{bmatrix} \tag{2.4}$$

Because stagnated flow is no longer assumed, $u_{rs}(x)$ is prescribed from the result of the previous calculation. The transformation between x and t_{lab} is given by Eq. (2.5).

$$t_{lab} = \int_0^x \frac{dx}{u_{rs}(x)} \tag{2.5}$$

Equation (2.4) includes additional source terms to account for the experimentally observed non-ideal pressure rise. As opposed to the second space-marching calculation described in Section 2.3.2.2, the source term in the momentum equation is constructed so that $\frac{dP}{dx} = \frac{1}{u_{rs}} \left(\frac{dP}{dt}\right)_{meas.}$ instead of $\frac{dP}{dx} = 0$. The energy equation source term accounts for the work done by the non-ideal pressure rise, modeled as $dh = vdP$ following [5]. Exact formulations of the source terms are given in Eq. (2.6) and (2.7).

$$S_{m,dP} = \frac{d}{dx}\left(\rho u^2\right) + \frac{1}{u_{rs}} \left(\frac{dP}{dt}\right)_{meas.} \tag{2.6}$$

$$S_{h,dP} = \left(\frac{dP}{dt}\right)_{meas.} \tag{2.7}$$

These source terms are necessary because the present approach cannot capture the full unsteady physics leading to a non-ideal pressure rise in Region 5. Despite this limitation, the impact on $P(t)$ is important to include in the present analysis. Matching the experimentally measured pressure allows far more meaningful conclusions to be drawn from the comparison with measured number density time histories.

2.4 Thermodynamic Properties

The collisional-radiative model applies a detailed treatment of nonequilibrium between the different energy modes of the gas. As shown in the previous Sections, separate conservation equations are solved for the vibrational and electron-electronic energies. Heavy particle translational energy and molecular rotational energy are assumed to be in equilibrium at a shared translational-rotational temperature, T_{tr}, following [17].

Within the collisional-radiative model, the specific enthalpy of the gas, h, is defined as:

$$\rho h = \sum_s h^\circ_{f,s} n_s + \sum_{s\in\mathcal{H}} \frac{5}{2} n_s k_B T_{tr} + \sum_{s\in\mathcal{M}} n_s k_B T_{tr} + \sum_{s\in\mathcal{H}_{CR}} \sum_i^{N_{ex}} \varepsilon_i n_i + n_e k_B T_{eex} + \rho e_{vib} + \rho e_{eex} \tag{2.8}$$

where $\mathcal{H}$ is the set of all heavy species, $\mathcal{H}_{CR}$ is the set of heavy species with electronic states that are modeled explicitly in the collisional-radiative model, $\mathcal{M}$ is the set of all molecular species, $h^{\circ}_{f,s}$ is the formation enthalpy of a species s, T_{eex} is the electron-electronic temperature, n is number density, i is an electronic state index, and N_{ex} are the number of electronic states for a species s. Boltzmann's constant is given as k_B. The symbol ε denotes the energy per particle for a given species ($\varepsilon_{eex,s}$ and $\varepsilon_{vib,s}$), electronic state (ε_i), vibrational state (ε_v), or rotational state (ε_J). Rotational energy is calculated using the rigid rotor approximation. The translational-rotational temperature is calculated at each timestep using Eq. (2.8) with the known total enthalpy, vibrational energy, electron-electronic energy, and pseudospecies number densities.

The pressure of the gas, P, is calculated using Dalton's law of partial pressure in Eq. (2.9).

$$P = \sum_{s\in\mathcal{H}} n_s k_B T_{tr} + n_e k_B T_{eex} \tag{2.9}$$

The electron-electronic and vibrational energies are defined as:

$$\rho e_{eex} = \sum_{s\notin\mathcal{H}_{CR}} n_s \varepsilon_{eex,s} = \frac{3}{2} n_e k_B T_{eex} + \sum_{s\in\mathcal{H}_B} n_s \left[\frac{\sum_i^{N_{ex}} Q_i \varepsilon_i}{\sum_i^{N_{ex}} Q_i}\right] \tag{2.10}$$

$$\rho e_{vib} = \sum_{s\in\mathcal{M}} n_s \varepsilon_{vib,s} = \sum_{s\in\{\mathcal{M}\cup\mathcal{H}_B\}} \left[\frac{\sum_i^{N_{ex}} g_i \exp\left(\frac{-\varepsilon_i}{k_B T_{eex}}\right) \sum_v^{N_v} Q_v \varepsilon_v}{\sum_i^{N_{ex}} Q_i}\right] + \sum_{s\in\{\mathcal{M}\cup\mathcal{H}_{CR}\}} \sum_i^{N_{ex}} n_i \left[\frac{\sum_v^{N_v} Q_v \varepsilon_v}{\sum_v^{N_v} Q_v}\right] \tag{2.11}$$

where $\mathcal{H}_B$ is the set of heavy particles where the electronic energy is assumed to follow a Boltzmann distribution at the electron-electronic temperature, and v are vibrational state indices. Note that $\mathcal{H}_{\mathcal{B}} \cup \mathcal{H}_{CR} = \mathcal{H}$ and $\mathcal{H}_B \cap \mathcal{H}_{CR} = \emptyset$.

Temperatures of the vibrational and electron-electronic modes are calculated from e_{vib} and e_{eex}, respectively. Note that in general, e_{eex} and e_{vib} are both functions of T_{eex}, T_{vib}, T_{tr}, and the pseudospecies number densities. At each integration step, the values of T_{eex} and T_{vib} are calculated iteratively using Eqs. (2.10) and (2.11) with the values of T_{vib} and T_{eex}, respectively, from the previous step.

Within an electronic state-resolved model, it is not always possible to uniquely specify the electronic state distribution using a single electronic temperature. Regardless, a species electronic

temperature, $T_{ex,s}$, is defined here as the temperature that characterizes a Boltzmann distribution of electronic states with the same total electronic energy as the true, non-Boltzmann electronic state distribution.

2.5 Partition Functions

Partition functions, Q, are calculated using Maxwell-Boltzmann statistics and the temperatures that characterize each energy mode. The partition function for a vibration level, v, is given as,

$$Q_v = \exp\left(\frac{-\varepsilon_v}{k_B T_v}\right) \sum_J^{N_J} g_J \exp\left(\frac{-\varepsilon_J}{k_B T_{tr}}\right) \tag{2.12}$$

where J are rotational state indices and N_J is the number of rotational states in a given vibrational level. The partition function for an electronic level, i, is given by Eq. (2.13) for a molecular species and Eq. (2.14) for an atomic species.

$$Q_i = g_i \exp\left(\frac{-\varepsilon_i}{k_B T_{eex}}\right) \sum_v^{N_v} Q_v \tag{2.13}$$

$$Q_i = g_i \exp\left(\frac{-\varepsilon_i}{k_B T_{eex}}\right) \tag{2.14}$$

For electrons, the translational partition function is,

$$Q_{t,e} = \left(\frac{2\pi m_e k_B T_{eex}}{h^2}\right)^{3/2} \tag{2.15}$$

where h is Planck's constant. For a heavy species s, the translational partition is

$$Q_{t,s} = \left(\frac{2\pi m_s k_B T_{tr}}{h^2}\right)^{3/2} \tag{2.16}$$

Total partition functions are equal to the product of the internal and translational partition functions. For the electron, which has two possible spin states, the internal partition function is equal to two. Thus, the total partition function for an electron is:

$$Q_e = 2Q_{t,e} \tag{2.17}$$

For a pseudospecies that corresponds to a single electronic state, i, of a species s, the total partition function is given in Eq. (2.18).

$$Q_{s(i)} = Q_{t,s} Q_i \tag{2.18}$$

The total partition function of a species s, considering all electronic state indices, is defined in Eq. (2.19).

$$Q_s = Q_{t,s} \prod_{i}^{N_{ex}} Q_i \tag{2.19}$$

Whenever a superscript h is applied to a given partition function, that means the heavy particle translational temperature, T_{tr}, is used as the temperature for all terms in the partition function. If e is the superscript, then the free-electron temperature is used for all terms in the partition function.

Atomic electronic energies and state degeneracies are taken from the NIST database [67]. Rovibrational energies of N_2(X) and O_2(X) are the same as those used in Kim and Boyd [68] and Andrienko and Boyd [69], respectively. The rovibrational energies for all other molecular electronic states are calculated using a Dunham expansion with the vibrational and rotational constants from NIST [70]. The molecular spectroscopic constants adopted in the present work are listed in Appendix A. A detailed description of how to calculate rovibrational energies and state degeneracies using a Dunham expansion may be found in Barklem and Collet [71]. The nuclear spin degeneracy of each rovibrational state is divided by the product of the nuclear spin degeneracies of the constituent atoms. This is consistent with the calculation of atomic partition functions via Eq. (2.14) where g_i is only the electronic degeneracy and does not include the nuclear spin degeneracy.

The separation of rotational and vibrational energies follows a vibration-prioritized framework in which the vibrational energy is defined using the $J = 0$ rovibrational level energies. Rotational energies are then calculated as $\epsilon_J = \epsilon_{vJ} - \epsilon_v$ where ε_{vJ} is the energy of the rovibrational level with quantum numbers v and J. Rovibrational energies are referenced with respect to the energy of their electronic level, and electronic energies are referenced with respect to the formation enthalpy of the species.

2.6 Nonequilibrium Energy Evolution Equations

2.6.1 Vibrational Energy Mode

Vibrational energy evolves through relaxation with the heavy particle and free electron translational modes and through chemical reactions.

$$\rho u \frac{de_{vib}}{dx} = S_{vib} = -S_{ev} + S_{vt} + S_{vc} \tag{2.20}$$

Electron-vibrational relaxation, S_{ev}, is modeled using the Bethe-Teller equation [72],

$$S_{ev} = \sum_{s \in \mathcal{M}} n_s \frac{\varepsilon_{vib,s} - \varepsilon^e_{vib,s}}{\tau_{ev,s}} \tag{2.21}$$

where $\mathcal{M}$ is the set of molecular species and $\tau_{ev,s}$ is the electron-vibrational relaxation time for a species s. The average vibrational energy per particle of species s is $\varepsilon_{vib,s}$, and $\varepsilon^e_{vib,s}$ is the average vibrational energy per particle of s evaluated at T_{eex}. Relaxation times, τ_{ev}, are modeled using the expressions from Laporta et al. for O_2 [73] and N_2 [74]. Relaxation in e-NO collisions is not included in the model because vibrational-electron relaxation involving NO is not expected to meaningfully impact electron energy relaxation. Nitric oxide typically comprises less than 5% of the flow and vibrational-electron relaxation is primarily driven by efficient energy exchange involving N_2 [75].

The source term for vibrational-translational relaxation, S_{vt}, is also calculated using the Bethe-Teller equation,

$$S_{vt} = \sum_{s \in \mathcal{M}} n_s \frac{\varepsilon^h_{vib,s} - \varepsilon_{vib,s}}{\tau_{vt,s}} \tag{2.22}$$

with the mixture averaged vibrational relaxation time, $\tau_{vt,s}$, calculated following Gnoffo et al. [76] with the collider-specific vibrational relaxation times given in Table 2.1.

Vibrational relaxation is strongly affected by the two-way coupling that exists between vibrational relaxation and dissociation. Several models are available to approximate the effects of this coupling, hereafter referred to as vibration-dissociation coupling, on the rates of vibrational relaxation and dissociation. The models implemented in this work are described in Section 3.3.1, and an extensive discussion of the other available models may be found in [13].

Table 2.1: Selected vibrational-translational relaxation time, τ_{vt}, expressions. Park's high-temperature correction [1] is applied whenever the relaxation time is taken from [2] or [1].

Molecule	Collider	$P\tau_{vt}$ (atm-s)	Ref.
O_2	Ar	$4.7 \times 10^{-15} \exp\left(\frac{200}{T_{tr}^{1/3}}\right) \frac{T_{tr}^{5/6}}{1-\exp\left(-\frac{2240}{T_{tr}}\right)}$	[5]
O_2	O_2	$8.4 \times 10^{-15} \exp\left(\frac{170}{T_{tr}^{1/3}}\right) \frac{T_{tr}^{5/6}}{1-\exp\left(-\frac{2240}{T_{tr}}\right)}$	[5]
O_2	O	$1.85 \times 10^{-8} \exp\left(2.08 \times 10^{-5} T_{tr}\right)$	[77][a]
O_2	N_2	$\exp\left[134\left(T_{tr}^{-1/3} - 0.0295\right) - 18.42\right]$	[2]
O_2	N	$\exp\left[72.4\left(T_{tr}^{-1/3} - 0.0150\right) - 18.42\right]$	[1]
O_2	NO	$\exp\left[136\left(T_{tr}^{-1/3} - 0.0298\right) - 18.42\right]$	[2]
N_2	Ar	$\exp\left[240\left(T_{tr}^{-1/3} - 0.0302\right) - 18.42\right]$	[2]
N_2	O_2	$\exp\left[229\left(T_{tr}^{-1/3} - 0.0295\right) - 18.42\right]$	[2]
N_2	O	$\exp\left[72.4\left(T_{tr}^{-1/3} - 0.015\right) - 18.42\right]$	[2]
N_2	N_2	$\exp\left[-82550 T_{tr}^{-1} + 17600 T_{tr}^{-2/3} - 904.9 T_{tr}^{-1/3} - 1.983\right]$	[78]
N_2	N	$\exp\left[-27300 T_{tr}^{-1} + 6667 T_{tr}^{-2/3} - 296.2 T_{tr}^{-1/3} - 14.44\right]$	[78]
N_2	NO	$\exp\left[225\left(T_{tr}^{-1/3} - 0.0293\right) - 18.42\right]$	[2]
NO	Ar	$4.6 \times 10^{-8} \exp\left(85 \times T_{tr}^{1/3}\right)$	[79]
NO	O_2, O, N	$\exp\left[49.5\left(T_{tr}^{-1/3} - 0.0420\right) - 18.42\right]$	[1]
NO	N_2	$6.2 \times 10^{-10} \exp\left(130 \times T_{tr}^{1/3}\right)$	[80]
NO	NO	$1.1 \times 10^{-9} \exp\left(70 \times T_{tr}^{1/3}\right)$	[79]

[a] The Millikan and White correlation [2] is used for temperatures below 3,000 K [81].

Vibration-dissociation coupling models are relevant to the vibrational energy conservation equation because they provide a closure for the average vibrational energy of a dissociating molecule, $\left\langle \varepsilon_{vib,s(i)} \right\rangle_d$. Because vibrationally excited molecules are significantly more likely to undergo dissociation than unexcited molecules, the average vibrational energy loss per dissociation reaction is often greater than the average vibrational energy of the species undergoing dissociation.

For non-dissociation reactions, molecular species are assumed to be created and destroyed at the average energy of that species [31]. This applies to associative ionization, charge exchange, and electronic excitation exchange reactions. The resulting expression for the vibrational energy

change due to chemical reactions, S_{vc}, is

$$S_{vc} = \sum_{s \in \mathcal{M}} \sum_{i}^{N_{ex}} \sum_{r}^{n_r} \left\langle \varepsilon_{vib,s(i)} \right\rangle_r \omega^r_{s(i)} \tag{2.23}$$

where n_r is the number of chemical reactions and r is an index for chemical reactions. The source term for a species s in electronic state i due to reaction r is $\omega^r_{s(i)}$. The average vibrational energy of the $s(i)$ molecules created or destroyed in a reaction r is $\left\langle \varepsilon_{vib,s(i)} \right\rangle_r$. Note that $\left\langle \varepsilon_{vib,s(i)} \right\rangle_r = \left\langle \varepsilon_{vib,s(i)} \right\rangle_d$ when r is a dissociation reaction. Closures for the average vibrational energy change per dissociation are discussed in Section 3.3.1.

2.6.2 Electron-Electronic Energy Mode

The electron-electronic energy evolves through relaxation with the other energy modes, chemical reactions, and radiative emission. Unlike the vibrational mode, the electron-electronic energy mode is influenced by radiative processes, electronic excitation, and ionization. Exchanges between the electron-electronic energy mode and the energy of the individually resolved electronic states is mediated by electron impact excitation (S_{e-cie}) and ionization (S_{e-cii}) source terms, while radiative losses are captured in the free-bound (S_{fbr}) and free-free (S_{ffr}) radiative emission source terms. Changes to the electron-electronic energy during chemical reactions are accounted for in the S_{ec} source term.

$$\rho u \frac{de_{eex}}{dx} = S_{eex} = S_{et} + S_{ev} + S_{e-cie} + S_{e-cii} - S_{fbr} - S_{ffr} + S_{ec} \tag{2.24}$$

The relaxation term between electron and translational-rotational energy, S_{et}, is given as,

$$S_{et} = \frac{3}{2} k_B \left(T_{tr} - T_{eex}\right) \sqrt{\frac{8 k_B T_{eex}}{\pi m_e}} \sum_{s \in \mathcal{H}} \frac{2 m_e}{m_s} n_e n_s \sigma_{e,s} \left(1 + g_{r,s}\right) \tag{2.25}$$

where $\sigma_{e,s}$ is the momentum-transfer cross-section for electron-heavy particle collisions [7], and $g_{r,s}$ is the rotational loss factor used in [82]. The values of g_{r,O_2} and g_{r,O_2^+} are set to 10, a value first used in [83] for N_2 and later used for O_2 by [84] based on the similar rotational excitation cross sections of the two species. Following [84], $g_{r,NO}$ is set to 100. Rotational loss factors are zero for the atomic species, which have no rotational energy. Momentum transfer cross-sections for Ar, O, and

N collisions with electrons are taken from the B-Spline R-Matrix (BSRM) calculations presented in [85, 86, 43]. The momentum transfer cross-sections that were calculated in both studies are in close agreement with previous experimental cross-section measurements. Equation (2.25) requires a cross-section that is a function of temperature, not collision energy, so the energy-dependent cross-sections are averaged over a Maxwellian electron energy distribution function at T_{eex} following [87] to arrive at the temperature-dependent expressions in Table 2.2. For argon, the BSRM momentum transfer cross-section is for the ground state, while for oxygen and nitrogen, the cross-sections are reported for the lowest three electronic states. The state-specific oxygen and nitrogen cross-sections are summed using the Boltzmann fraction of each state at T_{eex} to compute $\sigma_{e,O}$ and $\sigma_{e,N}$.

Table 2.2: Cross sections for electron-neutral collision cross-section used in Eq. (2.25) and the temperatures over which they have been fit.

s	$\sigma_{e,s}$ (10^{-20} m^2)	Temperature (K)	Ref.
Ar	$0.08156\left[\ln\left(T_{eex}\right)\right]^3 - 1.166\left[\ln\left(T_{eex}\right)\right]^2 + 3.678\left[\ln\left(T_{eex}\right)\right] + 4.055$	300 – 40,000 K	[85]
O_2	$2 + (6\times10^{-4})T_{eex}$	5,000 – 15,000 K	[76]
N_2	$7.5 + (5.5\times10^{-4})T_{eex} - (1\times10^{-8})T_{eex}^2$	5,000 – 15,000 K	[76]
NO	10	5,000 – 15,000 K	[76]
O	$-0.01011\left[\ln\left(T_{eex}\right)\right]^3 + 0.2431\left[\ln\left(T_{eex}\right)\right]^2 - 1.260\left[\ln\left(T_{eex}\right)\right] + 2.142$	300 – 50,000 K	[86]
N	$-2.422\left[\ln\left(T_{eex}\right)\right]^3 + 73.03\left[\ln\left(T_{eex}\right)\right]^2 - 734.0\left[\ln\left(T_{eex}\right)\right] + 2466$	1,000 – 50,000 K	[43]

Electron-ion cross-sections are treated using a Coulomb cross-section with the Debye cutoff approximation, which leads to Eq. (2.26) from [88] with the factor of 4/3 implemented by [17].

$$\sigma_{e,s} = \frac{4}{3}\frac{4.39\times10^{-10}}{T_{eex}^2}\ln\left(\frac{1.24\times10^7 T_{eex}^{1.5}}{\sqrt{n_e}}\right) \quad [\mathrm{m}^2] \tag{2.26}$$

The Debye cutoff approximation states that the Coulombic interaction potential between electrons and ions should be truncated for distances exceeding the Debye length. Goldbach et al.[89] found this approximation to be accurate within the uncertainty of their experimental conductivity measurements for Debye numbers above three. The Debye numbers encountered in the present analyses typically far exceed this value, so the Debye cutoff approximation is deemed appropriate.

Relaxation between the free electrons and the individually resolved electronic states in Eq.

(2.24) are mediated by S_{e-cie} and S_{e-cii}, which represent the electron energy change due to collisionally induced electronic excitation and ionization by electron impact. Near the shock, these terms are positive as translationally cold priming electrons, mostly generated from associative ionization and collisionally induced ionization by heavy particles (HP-CII), gain energy from excited species via superelastic collisions. Once the electron temperature increases sufficiently, the S_{e-cie} and S_{e-cii} terms become negative as the electrons become the dominant driver of excitation and ionization in the gas. This multistage behavior has been observed in radiation data from shock tube studies [15] and in measurements of excited state number densities reported in [59, 6].

Expressions for the electron-electronic energy source terms due to electron impact excitation and ionization are given below,

$$S_{e-cie} = n_e \sum_{s\in\mathcal{H}_{CR}} \sum_{i}^{N_{ex}-1} \sum_{j>i}^{N_{ex}} \varepsilon_{ij} k_{s(i,j)}^{e-cie} \left(\frac{Q_i^e}{Q_j^e} n_j - n_i \right) \tag{2.27}$$

$$\begin{aligned} S_{e-cii} = n_e \sum_{s\in\{\mathcal{H}_{CR}\setminus\mathcal{I}\}} \sum_{i}^{N_{ex}} \varepsilon_{ij^+} k_{s(i,j^+)}^{e-cii} \left[n_{j^+} n_e \frac{Q_i^e}{Q_{j^+}^e Q_e} \exp\left(\frac{I_{s(1)}}{k_B T_{eex}} \right) - n_i \right] \\ + n_e \sum_{s\in\{\mathcal{H}_B\setminus\mathcal{I}\}} \langle \varepsilon_{eex,s} \rangle_{ion} k_{s(1,j^+)}^{e-cii} \left[n_{j^+} n_e \frac{Q_s^e}{Q_{j^+} Q_e} \exp\left(\frac{I_{s(1)}}{k_B T_{eex}} \right) - n_s \right] \end{aligned} \tag{2.28}$$

where $\mathcal{H}_{CR}$ is the set of heavy species with individually resolved electronic states, $\mathcal{I}$ is the set of charged heavy species, $I_{s(1)}$ is the ionization energy of the ground electronic state of s, $\varepsilon_{ij} = \varepsilon_j - \varepsilon_i$ is the energy difference between electronic states i and j, $k_{s(i,j)}^{e-cie}$ is the rate of electron impact excitation of species s from electronic state i to state j, and $k_{s(i,j^+)}^{e-cii}$ is the rate of electron impact ionization from $s(i)$ to $s^+(j)$. In addition, Q_i, Q_e, and Q_i^e are the partition function of an electronic state i, the partition function of the free electrons, and the partition function of an electronic state i calculated at T_{eex}. For electron impact ionization for species in $\mathcal{H}_B$, the average electron-electronic energy removed during the ionization of a species s is given as $\langle \varepsilon_{eex,s} \rangle_{ion}$. Following Farbar et al. [90], it is assumed that the average electronic energy removed during electron impact ionization is equal to $0.3 I_{s(1)}$.

The electron translational energy decreases over time due to free-bound and free-free, or Bremsstrahlung, emission. The gas is assumed to be optically thin to free-free emission, and

emission due to radiative and dielectronic recombination to the ground state of argon is assumed to be completely self-absorbed due to the high concentration of ground state argon atoms. Radiation from free-bound radiative transitions to excited state argon atoms is assumed to completely escape the gas based on the low concentration of excited argon atoms [91, 7]. All free-bound emission involving recombination of an O^+ or N^+ atom is also assumed to escape the gas completely. The effective charge in Eq. (2.30), Z_{eff}, is set to 1.67 following [59, 7]. Electron-electronic energy source terms due to free-bound and free-free radiative losses are,

$$S_{e-fbr} = \sum_{s\in\{\mathcal{A}\backslash\mathcal{I}\}} \sum_{(i,j^+)\in\mathcal{T}_s^{fb}} n_e n_{j^+} k_{s(i,j^+)}^{fbr} \left(I_{s(1)} + \varepsilon_{j^+} - \varepsilon_i\right) \tag{2.29}$$

$$S_{e-ffr} = 1.42\times10^{-40} Z_{eff}^2 T_{eex}^{1/2} n_e^2 \quad [\mathrm{J/m^3{\cdot}s}] \tag{2.30}$$

where $\mathcal{A}$ is the set of atomic species and $\mathcal{T}_s^{fb}$ is the set of electronic state index pairs for free-bound recombination to form species s.

The final term in the electron-electronic energy equation is S_{ec}, the source term due to chemical reactions defined in Eq. (2.31),

$$S_{ec} = \sum_{s\in\mathcal{H}_\mathcal{B}} \omega_s \varepsilon_{eex,s} + \omega_e^{AI} \varepsilon_{eex,e} + \sum_{s\in\mathcal{M}} \sum_{i}^{N_{ex}} \omega_{s(i)}^{diss,e} \left(D_{0,s(i)} - \varepsilon_{rot,s(i)} - \varepsilon_{vib,s(i)}\right) \tag{2.31}$$

where $\mathcal{H}_B$ is the set of heavy species with electronic states that are assumed to follow a Boltzmann distribution at the electron-electronic temperature, ω_e^{AI} is the source term for electrons due to associative ionization and $\omega_{s(i)}^{diss,e}$ is the source term for $s(i)$ molecules due to electron impact dissociation. Species in $\mathcal{H}_B$ are assumed to be created or destroyed at the average electron-electronic energy of that species, $\varepsilon_{eex,s}$. For electron impact dissociation, molecules are assumed to be created or destroyed at the average rotational and vibrational energy. The average loss of electron translational energy during dissociation of a molecule $s(i)$ is thus the difference between the dissociation energy of the $s(i)$ molecule, $D_{0,s(i)}$, and the average rovibrational energy of an $s(i)$ molecule, $\varepsilon_{rot,s(i)} + \varepsilon_{vib,s(i)}$.

2.6.3 Vibrational-Electron-Electronic Energy Mode

Whenever a two-temperature model is applied, the governing equations do not include separate energy equations for e_{vib} and e_{eex}; rather, one equation is solved for a combined vibrational-electron-electronic energy, e_{vee}. The governing equation for this combined energy mode may be derived by simply summing the conservation equations for the vibrational and electron-electronic energies. The resulting conservation equation is,

$$\rho\frac{de_{vee}}{dt} = S_{vee} = S_{vt} + S_{et} + S_{e-cie} + S_{e-cii} - S_{fbr} - S_{ffr} + S_{ec} + S_{vc} \tag{2.32}$$

where all of the terms follow their formulations as described in the previous sections.

In the case of a two-temperature model without individually resolved electronic states, the governing equation becomes,

$$S_{vee,2T} = S_{vt} + S_{et} + S_{e-cii} + S_{ec} + S_{vc} \tag{2.33}$$

where the radiative loss terms have also been neglected.

2.7 Master Equation

The source term for a given pseudospecies, p, is dependent on whether p represents a species or an individual electronic state. The formulation of ω_p in these two cases is given by Eq. (2.34),

$$\omega_p = \begin{cases} \omega_s & \text{if } s \in \mathcal{P}_s \\ \omega_{s(i)} & \text{if } s(i) \in \mathcal{P}_{ex} \end{cases} \tag{2.34}$$

where $\mathcal{P}_s$ is the set of pseudospecies that includes the species in $\mathcal{H}_B$ and electrons, and $\mathcal{P}_{ex}$ is the set of pseudospecies that correspond to individual electronic states of the species in $\mathcal{H}_{CR}$.

2.7.1 Species

Source terms ω_s, for species in $\mathcal{P}_s$, are the sum of source terms due to ionization, chemical reactions, and free-bound electronic transitions.

$$\omega_s = \omega_s^{e-cii} + \omega_s^{hp-cii} + \omega_s^{chem} + \omega_s^{fbr} \tag{2.35}$$

2.7.2 Electronic States

The source terms $\omega_{s(i)}$ for pseudospecies in $\mathcal{P}_{ex}$ include the summed contributions from collisionally induced bound-bound and free-bound electronic transitions, chemical reactions, and radiative bound-bound and free-bound electronic transitions.

$$\omega_{s(i)} = \omega_{s(i)}^{e-cie} + \omega_{s(i)}^{e-cii} + \omega_{s(i)}^{hp-cie} + \omega_{s(i)}^{hp-cii} + \omega_{s(i)}^{chem} + \omega_{s(i)}^{fbr} + \omega_{s(i)}^{bbr} \tag{2.36}$$

Equilibrium constants for the collisional processes are calculated using the principle of detailed balance [71, 92]. Descriptions of the modeling of each process is given in Chapter 3 alongside a discussion of the adopted rate constants for each.

2.8 Numerical Implementation of Shock Tube Solver

2.8.1 Numerical Solution of the Governing Equations

Solution variables in the chemical kinetics solver are the translational-rotational temperature, T_{tr}, pseudospecies molalities γ_p, vibrational energy e_{vib}, and electron-electronic energy e_{eex}. The evolution of these variables is computed by integrating their spatial or temporal derivatives using an implicit Lomax method [93]. A second-order central difference scheme is used to numerically compute the Jacobian at each integration step. The evolution equations for the nonequilibrium energy modes have been described in the previous Sections. For the pseudospecies molalities, γ_p, the governing equations for ρ_p are each divided by $m_p N_A \rho$, where N_A is Avogadro's number, to obtain an equation for the evolution of the molalities.

The equation describing the evolution of T_{tr} is derived using the conservation equations for mass, x-momentum (if 1D), and total energy that are presented in Section 2.2 and 2.3. To derive the evolution equation for T_{tr} in one-dimension, the three Euler equations are reduced to two governing equations by incorporating continuity $\left(\frac{d}{dx}(\rho u) = 0\right)$ into the conservation equations for x-momentum and total energy. The remaining two equations are then rearranged into a linear system with $\frac{dT_{tr}}{dx}$ and $\frac{d(u^2/2)}{dx}$ as the independent variables. Cramer's rule is used to solve the

linear system for $\frac{dT_{tr}}{dx}$, and u is calculated after the integration step using the conservation of total enthalpy. These manipulations are applied to the three systems of Euler equations in Section 2.3.2 to obtain the formulations of $\frac{dT_{tr}}{dx}$ that are numerically integrated for each flow scenario. In the zero-dimensional case, the evolution equation of T_{tr} is directly calculated via manipulation of the 0D governing equations.

2.8.2 Code Benchmarking

Benchmarking of the developed code is of obvious importance and has been performed via several comparisons with codes that have overlapping capabilities. Comparisons with the CFD code LeMANS [24, 94] enable assessment of multitemperature kinetic models, while comparisons with PLATO [95] enable an assessment of the electronic state-resolved kinetics. All of the comparisons in this Section are performed for zero-dimensional adiabatic and isochoric chemical reactors. Because the developed code implements general multitemperature (MT) and collisional-radiative (CR) kinetics, it is referred to as MTCR throughout this Section. For several of the comparisons, the difference between predictions by two codes is quantified by root mean square error (RMSE), defined as:

$$RMSE = \sqrt{\frac{\sum_i (\gamma_i^{MTCR} - \gamma_i^{other})^2}{N}} \tag{2.37}$$

where γ_i is the variable being compared at a time point i.

2.8.2.1 Multitemperature Modeling

Comparisons with LeMANS have been performed for a variety of cases of increasing complexity to verify each component of the code. Here, only the most complex cases are shown since they encompass the effects of a large number of processes in a single benchmarking calculation.

A pure O_2 reactor with $\rho = 0.100$ kg/m^3 is analyzed first. Only two reactions, the dissociation of O_2 with O and O_2 are included, using rate coefficients and vibration-dissociation coupling from Park [1]. The vibrational relaxation of O_2 with O_2 and O is implemented using the Millikan and White correlation [2] and Park's high-temperature correction [1] for this comparison. Figure 2.2

illustrates the temperature and species number density predictions, which show excellent agreement between the two codes.

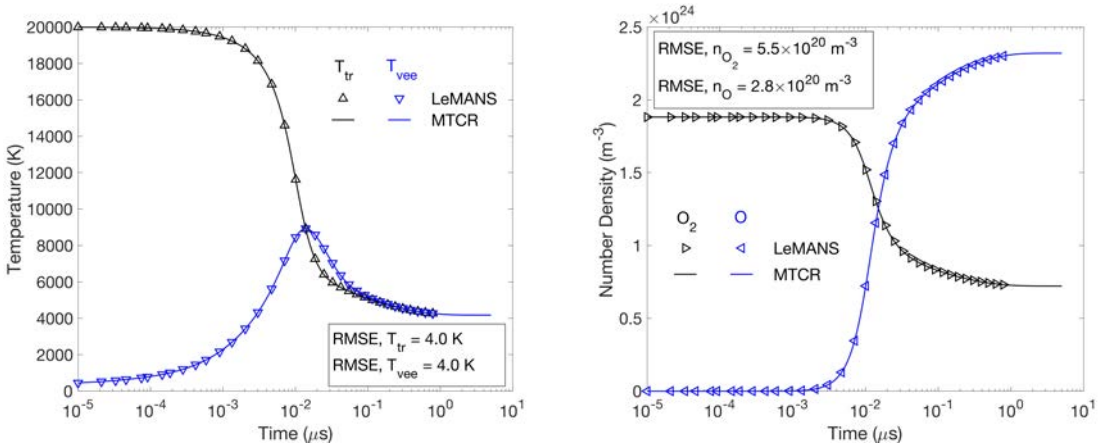

(a) (b)

Figure 2.2: Benchmarking of the Park chemical kinetics model for a 0D adiabatic reactor of 100% O_2 initialized to T_{tr}=20,000 K and T_{vib}=300 K with a density of 0.100 kg/m^3. Root mean square error between the LeMANS and MTCR predictions is given for each variable.

In Figure 2.3, the predictions of LeMANS and MTCR are compared for a zero-dimensional reactor initialized to T_{tr}=30,000 K at a pressure of 1 atm for a gas containing 95% CO_2 and 5% N_2 by volume. The chemical reaction set includes 20 species and over 150 reactions. Again, excellent agreement between the two codes is obtained. Slight discrepancies are observed at the peak value of T_{vee} in Figure 2.3a, which are due to the slightly different formulations of $\sigma_{e,s}$ in the two codes. The largest difference in the temperature values is approximately 300 K. The good agreement for this condition indicates that MTCR can be reliably used to simulate ionized nonequilibrium flows containing polyatomic species.

2.8.2.2 Electronic State-Resolved Kinetics

Because LeMANS does not have electronic state-resolved kinetics, the comparisons presented in this Section make use of PLATO [95], a library developed at the University of Illinois at Urbana Champaign. For the assessment of state-resolved kinetics, a zero-dimensional reactor of 99.9% argon

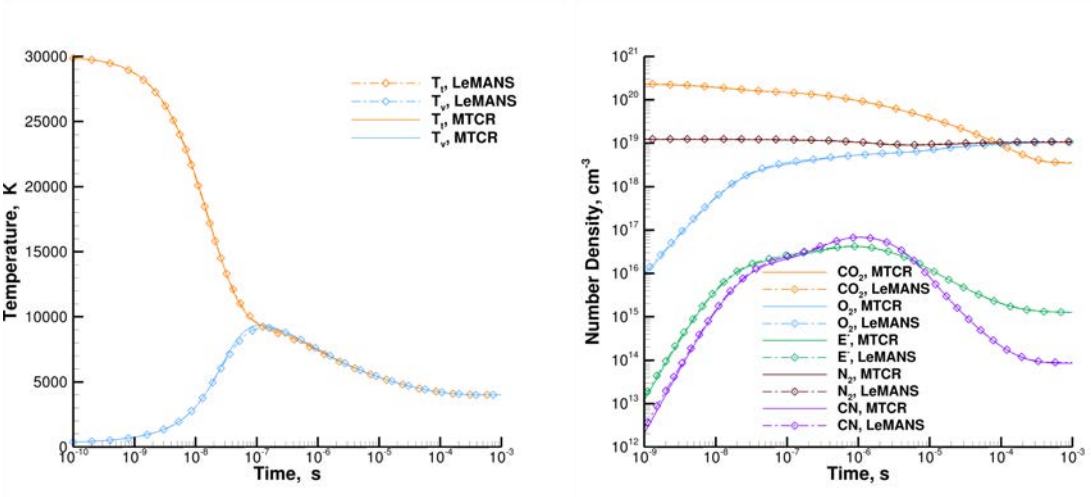

(a) (b)

Figure 2.3: Benchmarking of kinetics involving polyatomic species using a 20-species kinetic model for 95% CO_2 with 5% N_2 initialized to 30,000 K at a pressure of 1 atm.

and 0.1% electrons is initialized to 30,000 K heavy particle translational temperature and 300 K free electron temperature. Results from both codes are compared in Figure 2.4, demonstrating excellent agreement. The excitation temperature of argon, $T_{ex,Ar}$, is defined in both codes as the temperature characterizing a Boltzmann electronic state distribution with the same total energy as the true, non-Boltzmann state distribution. Slight discrepancies in the concentration of Ar^+ in Figure 2.4b are caused by numerical errors that arise during the first two timesteps.

2.8.3 Limitations

The numerical implementation of the governing equations described in Section 2.8.1 has an important limitation regarding strongly radiating flows in the one-dimensional formulation. In solving for the T_{tr}, a linear system is constructed to obtain the derivative expressions for T_{tr} and $\frac{1}{2}u^2$. However, only the T_{tr} expression is actually integrated; u is solved after the integration step using the assumption that the total enthalpy remains constant behind the incident shock.

The assumption of constant enthalpy is not valid when source terms due to non-ideal pressure rise or radiative energy loss are included. Because enthalpy is not a solution variable, its change

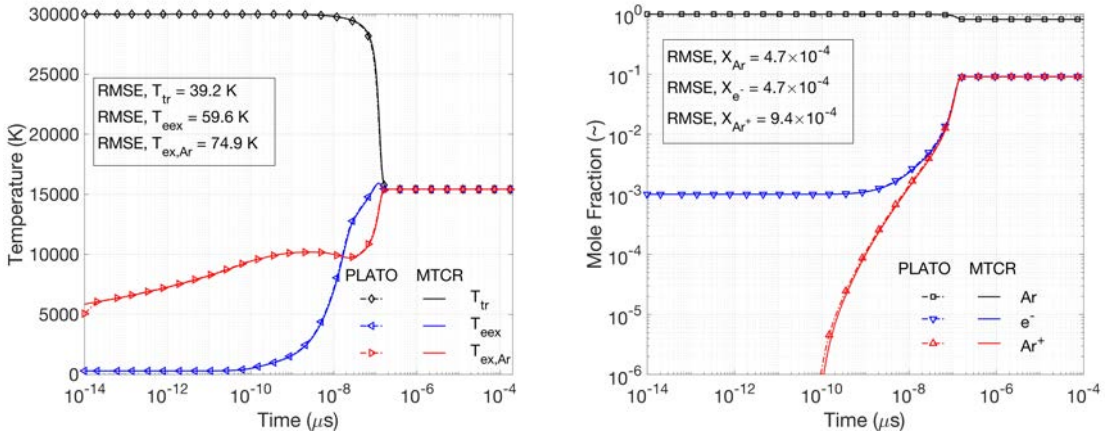

(a) (b)

Figure 2.4: Benchmarking of collisional excitation and ionization kinetics using a 31-state model of argon in a zero-dimensional adiabatic reactor initialized to 30,000 K at 100 atm in a mixture of 99.9% Ar with 0.1% e^- by volume.

is not explicitly calculated during the integration step. As a result, changes to the enthalpy must be imposed after the integration step via a first-order update. For enthalpy changes due to non-stiff terms, such as non-ideal pressure rises or mild radiative power loss, the first-order update is acceptable. However, when radiative losses are significant or change in a strongly nonlinear fashion, as is the case behind sufficiently strong shocks, the accuracy of a first-order update becomes poor. As a result, the calculation of u can return an imaginary value, stopping the execution of the code.

Solving this problem requires the inclusion of velocity as a solution variable in the 1D formulation and is a future priority in the development of the MTCR code. However, for the analyses presented in this thesis, radiative power losses are never sufficiently large to trigger the problem.

2.9 Sensitivity Analysis and Uncertainty Quantification

Sensitivity analysis and uncertainty quantification are applied throughout the present work to garner further insights into the complex nonequilibrium kinetics being investigated. In this Section, the theory and implementation of a sensitivity analysis and uncertainty quantification wrapper for MTCR are described in detail.

2.9.1 Sobol' Decomposition

The adopted variance-based sensitivity analysis techniques are based on the Sobol' decomposition of the total variance, D, which describes the variance in a given model prediction due to some prescribed variation in input parameters. The Sobol' decomposition of the variance is given as,

$$D = \sum_{i=1}^{N_\xi} D_i + \sum_{1 \le i < j \le N_\xi}^{i=N_\xi-1} D_{i,j} + \sum_{1 \le i < j < k \le N_\xi}^{i=N_\xi-2} D_{i,j,k} + ... + D_{1,2,...,N_\xi} \tag{2.38}$$

which is a sum over partial variances due to variations in N_ξ unique input parameters. First-order partial variances, D_i, account for variance that is due solely to changes in the ith parameter. Higher-order partial variances – $D_{i,j}$, $D_{i,j,k}$, etc. – capture variance contributions that result from concurrent variations in two or more parameters.

2.9.2 Sobol' Indices

Dividing the variance decomposition given in Eq. (2.38) by the total variance D, yields the Sobol' indices, which capture the fractional contributions from each of the N_ξ model parameters to the total variance of a given model prediction.

$$1 = \sum_{i=1}^{N_\xi} S_i + \sum_{1 \le i < j \le N_\xi}^{i=N_\xi-1} S_{i,j} + \sum_{1 \le i < j < k \le N_\xi}^{i=N_\xi-2} S_{i,j,k} + ... + S_{1,2,...,N_\xi} \tag{2.39}$$

The Sobol' indices are defined as,

$$S_{i_1,...,i_m} = \frac{D_{i_1,...,i_m}}{D} \tag{2.40}$$

for an mth order Sobol' index. It's also possible to define a total Sobol' index, $S_{T,i}$, which is the sum of all Sobol indices of any order that include a given parameter, i.

2.9.3 Polynomial Chaos Expansions

The adopted sensitivity analysis technique relies on the construction of a polynomial chaos expansion (PCE) surrogate model to approximate the collisional-radiative or multitemperature model predictions. The construction of a surrogate model is ideal because statistical quantities,

such as partial variances and the total variance, can be calculated analytically from the surrogate model expression, bypassing the need to obtain a statistically significant number of samples via direct evaluation of the deterministic model. Here, a "deterministic model evaluation" refers to one post-shock or zero-dimensional reactor calculation using a multitemperature or collisional-radiative model.

The polynomial chaos expansion surrogate model is given by the sum of orthogonal polynomial basis functions shown in Eq. (2.41) that approximate the mapping between uncertain parameter values and a given quantity of interest (QoI), also referred to as the response function. The PCE surrogate is defined as:

$$\hat{R} = \sum_{j=0}^{N_P} \alpha_j \Psi_j(\boldsymbol{\xi}) \tag{2.41}$$

where $\hat{R}$ is the approximated response function value, N_P is the number of polynomial basis functions, Ψ_j are the basis functions, α_j are the basis function coefficients, and $\boldsymbol{\xi}$ is the vector of uncertain parameters that have been normalized to the interval [-1,1]. In the polynomial chaos expansion framework, the relevant statistical quantities are calculated directly from the PCE basis coefficients, α_j, enabling Sobol' indices to be determined with a negligible computational cost once the surrogate has been fitted [96].

The orthonormal polynomial basis functions, Ψ_j, are generated using the three-term recurrence relationship for Legendre polynomials on the interval [-1, 1]. Normalization of uncertainty intervals for each uncertain variable, ξ_i, to the range [-1, 1] is important for enabling the Sobol' indices to be calculated directly from the basis coefficients using Eqs. (2.42), (2.43), and (2.44).

$$S_i = \sum_{\mathbf{k}\in\mathcal{A}_i} \alpha_{\mathbf{k}}^2/\hat{D}, \qquad \mathcal{A}_i = \{\mathbf{k}\in\mathcal{A} : k_i > 0, k_{j\neq i} = 0\} \tag{2.42}$$

$$S_{ij} = \sum_{\mathbf{k}\in\mathcal{A}_{ij}} \alpha_{\mathbf{k}}^2/\hat{D}, \qquad \mathcal{A}_i = \{\mathbf{k}\in\mathcal{A} : k_i, k_j > 0, k_{k\neq i,j} = 0\} \tag{2.43}$$

$$S_{T,i} = \sum_{\mathbf{k}\in\mathcal{A}_i^T} \alpha_{\mathbf{k}}^2/\hat{D}, \qquad \mathcal{A}_i^T = \{\mathbf{k}\in\mathcal{A} : k_i > 0\} \tag{2.44}$$

where $\mathcal{A}$ is the set of multi-indices $\mathbf{k} = (k_1, ..., k_{N_\xi})$, for each polynomial basis function that identifies which of the N_ξ normalized uncertain parameters, ξ_i, that each polynomial depends upon. The

subsets $\mathcal{A}_i$ and $\mathcal{A}_{ij}$ serve to isolate only the polynomial basis functions that depend on ξ_i or on ξ_i and ξ_j together, respectively. Analogous expressions can be formulated for higher-order Sobol' indices. The total Sobol' index, $S_{T,i}$ is defined in Eq. (2.44), and is defined as the sum of all Sobol indices that depend on a parameter i. Thus, the sum in Eq. (2.44) is equivalent to the sum over squared basis function weights for the polynomials with a functional dependence on ξ_i.

The approximated total variance, $\hat{D}$, is calculated using the PCE surrogate weighting coefficients as shown in Eq. (2.45).

$$\hat{D} = \sum_{\mathbf{k} \in \mathcal{A} \setminus \{\mathbf{0}\}} \alpha_{\mathbf{k}}^2 = \sum_{j=1}^{N_P} \alpha_j^2 \tag{2.45}$$

The equality of the summands in Eq. (2.45) is based on the fact that the multi-index, $\mathbf{k}$, is equal to the zero set $\{\mathbf{0}\}$ for the $j = 0$ polynomial; in other words, Ψ_0 is a constant value. The value of Ψ_0 is the mean of the approximated response function $\hat{R}$.

The number of polynomial basis functions, N_P, depends on the selected expansion order, p. A second-order ($p = 2$) expansion is used in the present study. Equation (2.46) gives the total number of expansion terms, N_t, as a function of N_ξ, the number of uncertain parameters, and p, the expansion order.

$$N_t = N_P + 1 = \frac{(N_\xi + p)!}{N_\xi!\, p!} \tag{2.46}$$

For a second-order expansion, Eq. (2.46) reduces to $N_t = \frac{(N_\xi+1)(N_\xi+2)}{2}$; i.e. the number of expansion terms grows by approximately N_ξ^2 when $p = 2$. This property affects computational cost because an unknown weighting coefficient α_i must be determined for each additional term. Increasing the number of terms in the PCE surrogate means that more deterministic model evaluations are required to fit an accurate surrogate. Due to the approximately N_ξ^p scaling for the number of unknowns in the PCE surrogate, the computational cost of sensitivity analysis can quickly become prohibitive when there are many uncertain parameters, as is the case in the present work.

2.9.4 Point Collocation with Sparse Approximation

Basis coefficients of the PCE surrogate are determined using a non-intrusive point collocation technique as in [55, 56, 57]. In this approach, the collisional-radiative model is evaluated at a set of sample points, and the sampled response function values are used to construct the linear system shown in Eq. (2.47).

$$\begin{pmatrix} R(\boldsymbol{\xi}_1) \\ R(\boldsymbol{\xi}_2) \\ \vdots \\ R(\boldsymbol{\xi}_{N_s}) \end{pmatrix} = \begin{pmatrix} \Psi_0(\boldsymbol{\xi}_1) & \Psi_1(\boldsymbol{\xi}_1) & \cdots & \Psi_{N_P}(\boldsymbol{\xi}_1) \\ \Psi_0(\boldsymbol{\xi}_2) & \Psi_1(\boldsymbol{\xi}_2) & \cdots & \Psi_{N_P}(\boldsymbol{\xi}_2) \\ \vdots & \vdots & \ddots & \vdots \\ \Psi_0(\boldsymbol{\xi}_{N_s}) & \Psi_1(\boldsymbol{\xi}_{N_s}) & \cdots & \Psi_{N_P}(\boldsymbol{\xi}_{N_s}) \end{pmatrix} \begin{pmatrix} \alpha_0 \\ \alpha_1 \\ \vdots \\ \alpha_{N_P} \end{pmatrix} \tag{2.47}$$

The matrix in Eq. (2.47), $\boldsymbol{\Psi}$, also known as the measurement matrix, contains the basis polynomials evaluated at the sampled parameter values $\boldsymbol{\xi}$, where the subscripts are sample indices. The number of samples is denoted as N_s. The response function returned by the collisional-radiative model for a given sample is denoted as $R(\boldsymbol{\xi})$.

The solution of Eq. (2.47) is fully determined when the number of samples matches the number of basis polynomials. In this study, a second-order PCE surrogate is employed to consider as many as 578 uncertain parameters, leading to an expansion consisting of up to 167,910 polynomials. Such a large number of collisional-radiative model evaluations is extremely demanding computationally, motivating the adoption of a solution technique for the case where $N_s \ll N_P$.

Equation (2.47) is underdetermined when $N_s < N_P$, so a regularization constraint is required to specify a unique solution. Following [55, 56, 57], an L_1 regularization constraint is added to Eq. (2.47), yielding Eq. (2.48), which has a unique solution when δ, the tolerance, is set to zero [55].

$$\min\|\boldsymbol{\alpha}\|_1 \text{ subject to } \|\boldsymbol{\Psi\alpha} - \boldsymbol{R}\| < \delta \tag{2.48}$$

Regularization using an L_1 constraint is a common technique in sensitivity analysis when it is not feasible to evaluate the deterministic model N_P times [97]. Minimization of the L_1 norm is chosen

because it is an effective technique for achieving solution vectors, $\boldsymbol{\alpha}$, with the minimum number of nonzero values.

2.9.5 Solution Algorithm and Implementation

While Eq. (2.48) can be solved with any number of samples, the solutions with an extremely small N_s are unlikely to accurately represent the true system behavior. To address this, Eq. (2.48) is solved with incrementally increasing values of N_s, and the changes to the Sobol' indices determined from the resulting expansion are monitored to assess the convergence of the solution.

Samples for the uncertain parameters are drawn from a joint-uniform distribution made up of N_ξ uniform marginal distributions, each one corresponding to a separate parameter. The values of each parameter are sampled over a given range that is then transformed into logarithmic space and normalized to the interval [-1,1]; this interval defines the endpoints of each marginal distribution.

A Latin hypercube of N_P samples is then generated from the resulting joint-uniform distribution. Latin hypercube sampling is preferred over Monte Carlo sampling because it provides better sample space coverage when the number of samples is low [55]. Next, orthonormal Legendre polynomials are constructed on the joint-uniform distribution.

After constructing the joint distribution, sample set, and orthonormal polynomials, the sensitivity analysis algorithm proceeds as follows:

(1) Evaluate the collisional-radiative model for a batch of $N_{s,batch}$ samples extracted from the full Latin hypercube sample set.

(2) Extract the response function values at the evaluated sample points.

(3) Solve Eq. (2.48) for the expansion coefficients of each response function PCE.

(4) Calculate Sobol' indices from the expansion coefficients using Eq. (2.44).

(5) Evaluate an additional $N_{s,batch}$ samples from the initial Latin hypercube sample set.

(6) Solve Eq. (2.48) for the expansion coefficients of each response function PCE.

(7) Evaluate convergence metrics.

(8) Repeat steps 5-7 until the maximum number of samples is reached.

A graphical depiction of the sensitivity analysis algorithm is given in Figure 2.5. The interface with MTCR treates the solver as a black-box function $\mathcal{M}(\boldsymbol{\xi})$ that returns a vector of response function variables, $\boldsymbol{R}$, which may be a function of x or t. Batches of $N_{s,batch}$ samples are run in parallel using `GNU Parallel` [98], taking advantage of the embarrassingly parallel nature of sample evaluation. Eq. (2.48) is solved using the `spgl1` Python package [99, 100].

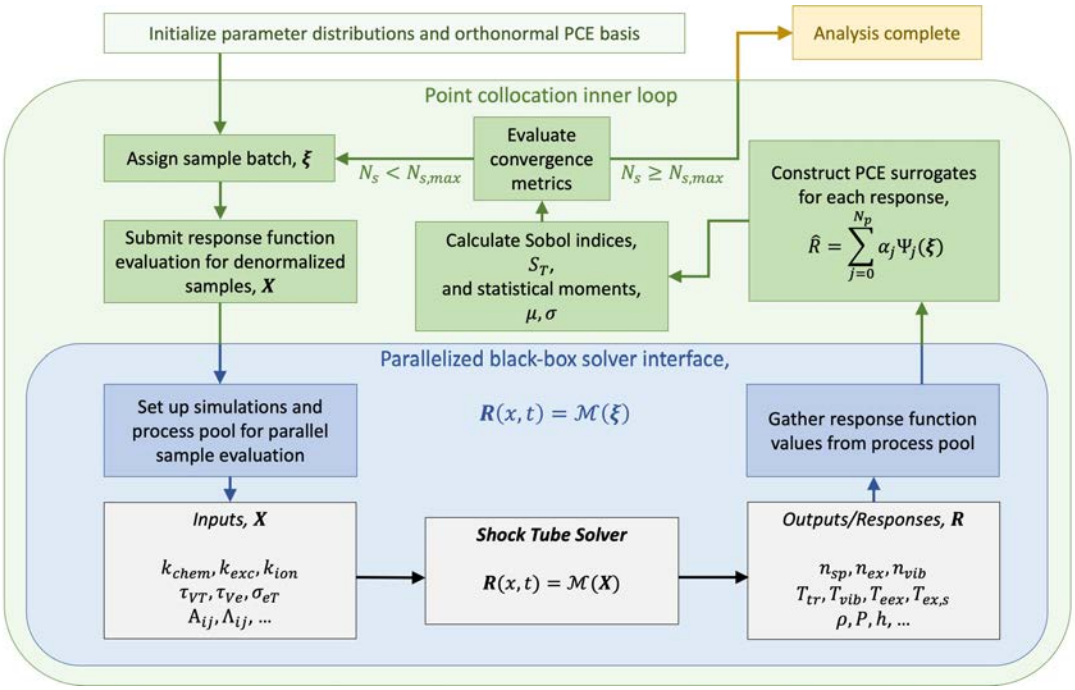

Figure 2.5: Illustration of the numerical architecture employed throughout the present work.

The Python library `chaospy` is used to manage the joint and marginal distributions, as well as the Latin hypercube parameter sampling [101]. While `chaospy` offers methods for constructing polynomial chaos expansion objects, the time complexity of these methods prohibits their use beyond approximately 3,000 polynomials. Such a limit is unacceptable for the present analyses, where over 125,000 polynomials are required for the largest analysis performed. As a result, a custom `Polynomial` class is constructed to efficiently generate and evaluate the Legendre polynomials.

Benchmarking of the custom method is performed through comparisons with `chaospy`. Figure 2.6 illustrates the time complexity for polynomial generation by the library and custom methods. The algorithms implemented in `chaospy` scale like N_ξ^5, while those in the custom `Polynomials` class scale like N_ξ^2. Deviation from N_ξ^2 scaling is observed when an expansion with 10^4 parameters is constructed, likely due to the large amount of memory that must be allocated when constructing 3×10^7 polynomials.

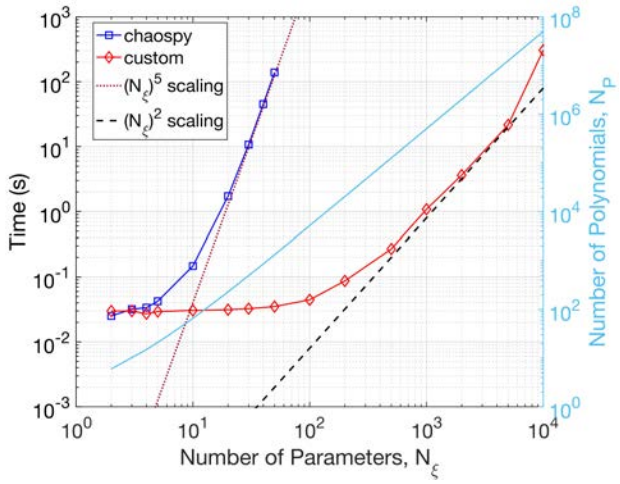

Figure 2.6: Time complexity of polynomial generation as a function of number of parameters in a second-order PCE expansion.

Evaluation of the polynomials is also highly optimized through the use of vectorized computation. As a result, the primary computational limit regarding the polynomials is the time and memory required to generate and store them. The results in Figure 2.6 indicate that the current tool is applicable up to at least 10^4 uncertain variables.

Another potential limit on the scalability of the method is `spgl1`, the solver adopted for Eq. (2.48). Because the solver is iterating to convergence for each $\boldsymbol{\alpha}$, it's impossible to report on its scaling independently of the problem being solved. To estimate the scaling, measurement matrices, $\boldsymbol{\Psi}$, and response vectors, $\boldsymbol{R}$, are initialized using Gaussian noise to provide a general sense of the solver's performance. The size of $\boldsymbol{\Psi}$ is $N_s \times N_P$, and the size of $\boldsymbol{R}$ is N_s. The value of N_s is set to 100 while N_P is set based on the N_ξ of interest with $p = 2$. In this way, a sweep over N_ξ is

performed to see how `spgl1` scales with problem size.

Figure 2.7 shows the performance results from the study. The scaling is of particular interest when the number of polynomials is much greater than the number of samples (100 in this case). Results from the study indicate that the `spgl1` solver incurs a feasible computational cost for as many as 2,000 parameters. Past this point, it may be more efficient to adopt a different solution technique like Least Angle Regression [102].

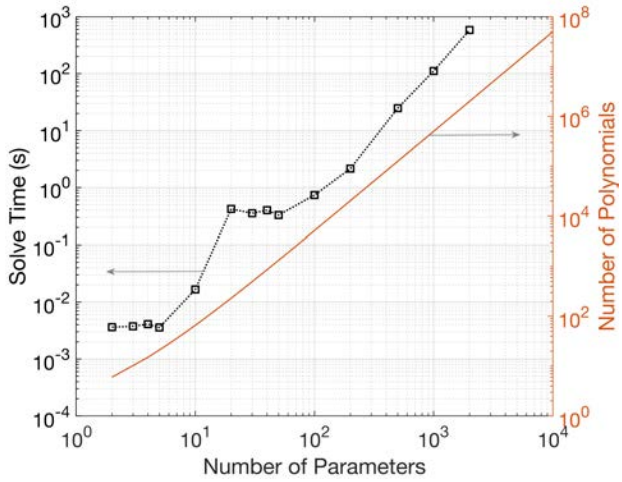

Figure 2.7: Time complexity of the `spgl1` solver for a measurement matrix with dimension $100 \times N_P$, where N_P is calculated using N_ξ and Eq. (2.46) with $p = 2$. The measurement matrix and observation vector are both constructed using Gaussian noise.

The largest systems investigated in this thesis contain over 500 uncertain variables. It is observed that the computational cost of solving Eq. (2.48) using `spgl1` is on the order of 10-20 core minutes, which is approximately 5-20x more time than in Figure 2.7. Thus, it is likely that the computational cost limits of the adopted method are set by `spgl1`. To mitigate this cost, the `spgl1` solutions for all response variables are performed in parallel using `GNU Parallel`.

2.9.5.1 Convergence Metrics

Convergence of the PCE surrogate is quantified using two metrics. The first metric tracks the maximum and average shifts in the Sobol' indices with the introduction of each new sample

batch, considering all response functions. These metrics are defined in Eqs. (2.49) and (2.50),

$$|\Delta S_T|_{\max,b} = \max\left\{\text{abs}\left(S_{T,i,b} - S_{T,i,b-1}\right)_R \mid i \in [1..N_\xi] \text{ and } R \in \mathcal{R}\right\} \tag{2.49}$$

$$|\Delta S_T|_{\text{avg},b} = \text{mean}\left\{\text{abs}\left(S_{T,i,b} - S_{T,i,b-1}\right)_R \mid i \in [1..N_\xi] \text{ and } R \in \mathcal{R}\right\} \tag{2.50}$$

where $\mathcal{R}$ is the set of all response functions, i is the parameter index, and b indicates the number of sample batches incorporated in solving Eq. (2.48) to obtain $S_{T,i,b}$.

The second metric quantifies the difference between the response function that is approximated by the PCE surrogate, $\hat{R}$, and the true response function values returned by the collisional-radiative model, R. Because the surrogate accurately predicts the response function values that inform the selection of its coefficients via Eq. (2.48), the points used to fit the surrogate model are not useful for assessing its accuracy; additional "test point" samples are needed.

To avoid evaluating the collisional-radiative model for the sole purpose of surrogate accuracy quantification, the R returned by the collisional-radiative model for the samples in the bth batch are compared with the $\hat{R}$ predicted by the surrogate model that was fitted using $b-1$ sample batches. Mathematically, this is expressed as,

$$T_{\max,b} = \max\left\{\text{abs}\left[R(\xi_s) - \hat{R}_{b-1}(\xi_s)\right] \mid s \in \mathcal{B}_b \text{ and } R \in \mathcal{R}\right\} \tag{2.51}$$

$$T_{\text{avg},b} = \text{mean}\left\{\text{abs}\left[R(\xi_s) - \hat{R}_{b-1}(\xi_s)\right] \mid s \in \mathcal{B}_b \text{ and } R \in \mathcal{R}\right\} \tag{2.52}$$

where T is the test point error, s are sample indices, $\mathcal{B}_b$ is the set of sample indices from batch b, and $\hat{R}_{b-1}$ is the surrogate model fitted using $b-1$ sample batches.

2.9.5.2 Comparison with Dakota Spectral Projection Solution

To test the performance of the developed method, total Sobol' index predictions from the in-house sensitivity analysis tool are compared with those from Dakota, a mature software developed

by Sandia National Laboratory [10]. The Dakota solution is performed using a spectral projection method, while the in-house solution is evaluated using the sparse point collocation technique described in the previous Sections.

The test case is based on a shock tube experiment reported by Streicher et al. [5] for a mixture of 20% O_2 in argon with an initial temperature of 10,310 K at a pressure of 0.13 atm. Six uncertain variables are considered, including the pre-exponential factor, A, for the dissociation of O_2 with O, O_2, and Ar, and a vibration dissociation coupling variable used within the Modified Marrone and Treanor model, denoted as a_U, for all three dissociation reactions. The pre-exponential factors are varied up and down by two orders of magnitude using log-uniform marginal distributions, while the a_U values are sampled from marginal distributions on the interval [0, 0.8].

Sobol' indices for the number density of O_2 are shown in Figure 2.8. The Sobol indices between the two codes are extremely similar, typically within 0.02 of each other. An exact agreement between the two approaches is not expected because Dakota and the in-house code apply different sampling techniques and different methods for determining the PCE basis coefficients. Understanding these differences, the agreement observed in Figure 2.8 is deemed an acceptable benchmarking of the developed code.

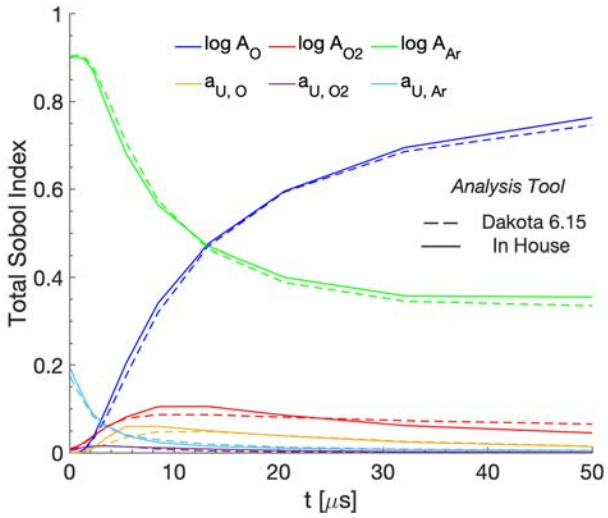

Figure 2.8: Comparison of Total Sobol' indices between the in-house sparse point collocation sensitivity analysis tool and a spectral projection solution by Dakota [10].

2.10 Summary

This chapter was devoted to providing the mathematical background and implementation details for the two primary numerical tools implemented throughout the thesis. The first numerical tool is a nonequilibrium chemical kinetics solver capable of simulating zero-dimensional or one-dimensional gas dynamics for a weakly ionized gas consisting of atomic, diatomic, and polyatomic species, as well as their ions and electrons. The code is also capable of tracking the populations of individual electronic levels. The governing equations for the various flow conditions were given in this chapter, along with the thermodynamic relations required to describe the partition of energy among the various energy manifolds in the gas. The vibrational and electron-electronic energy equations were described as well, and the necessary relaxation expressions with their necessary parameters were elaborated. Numerical implementation details were then given, followed by a discussion of the code's limitations and the presentation of several benchmarking results.

Next, the developed sensitivity analysis code was presented. The sensitivity metrics of choice, Sobol' indices, were defined first. Mathematical foundations of sparse point collocation polynomial chaos expansions were then provided, and the implementation of a framework for performing large-scale global sensitivity analyses was outlined. A thorough discussion of performance limitations was then given, followed by a discussion of benchmarking results.

Chapter 3

Collisional-Radiative Model

A large number of parameters are required when formulating the pseudospecies conservation equations in a collisional-radiative model. In this Chapter, the selection of these model parameters is discussed and motivated. Throughout the thesis, subsets of the described model are applied; however, the present discussion considers all species and processes together.

In each Section of this chapter, aside from Section 3.1, a different collisional or radiative process is discussed. For each process, a generic chemical formula is provided. The pseudospecies source terms due to each radiative process are given in their respective sections.

All collisional processes can be represented via the following formula for a reversible chemical reaction,

$$\sum_k \alpha_k [S] \leftrightharpoons \sum_k \beta_k [S] \tag{3.1}$$

where $[S]$ represents a generic pseudospecies. The symbols α_s and β_s denote the stoichiometric coefficients for each reactant and product s, respectively. It is not necessary to provide separate expressions for the source terms due to collisional processes since all follow the same template given in Eq. (3.2).

$$\omega_p^c = \sum_r^{N_r^c} \omega_{p,r}^c = \sum_r^{N_r^c} k_r^c \left(\beta_{pr} - \alpha_{pr}\right) \left[\prod_k n_k^{\alpha_{kr}} - \frac{1}{K_{eq,r}^c} \prod_k n_k^{\beta_{kr}}\right] \tag{3.2}$$

The superscript c denotes a particular type of collisional process, N_r^c is the number of reactions of that collisional process, k_r^c is the forward reaction rate coefficient for reaction r, α_{pr} is the set of reactant pseudospecies indices, β_{pr} is the set of product pseudospecies indices, and $K_{eq,r}^c$ is the equilibrium constant for reaction r.

The equilibrium constants for collisional processes may be formulated using detailed balance [92, 71]. For processes that are primarily controlled by electrons, including electron impact dissociation, electronic excitation, and ionization, the equilibrium constant is a function of T_{eex} as in Eq. (3.3).

$$K_{eq,r}(T_{eex}) = \frac{\sum_k (Q_k^e)^{\beta_{kr}}}{\sum_k (Q_k^e)^{\alpha_{kr}}} \exp\left(\frac{\sum_k \beta_{kr} h_{f,k}^\circ - \sum_k \alpha_{kr} h_{f,k}^\circ}{k_B T_{eex}}\right) \tag{3.3}$$

For processes involving only heavy particles, the equilibrium constant is instead a function of the heavy particle translational temperature, T_{tr}, as in Eq. (3.4), which is used for dissociation by heavy particle impact, electronic excitation by heavy particle impact, neutral exchange reactions, electronic excitation exchange reactions, charge exchange reactions, and reassociation reactions.

$$K_{eq,r}(T_{tr}) = \frac{\sum_k (Q_k^h)^{\beta_{kr}}}{\sum_k (Q_k^h)^{\alpha_{kr}}} \exp\left(\frac{\sum_k \beta_{kr} h_{f,k}^\circ - \sum_k \alpha_{kr} h_{f,k}^\circ}{k_B T_{tr}}\right) \tag{3.4}$$

A third class of processes, including associative ionization and heavy particle impact ionization, only involves electrons on one side of the reaction. A detailed derivation of the equilibrium constant for this class of reactions has been performed by Annaloro et al. [103], yielding the expression for K_{eq} given in Eq. (3.5).

$$K_{eq,r}(T_{tr}, T_{eex}) = \frac{\sum_k \left[(1-\delta_{ke})Q_k^h + \delta_{ke} Q_e\right]^{\beta_{kr}}}{\sum_k \left[(1-\delta_{ke})Q_k^h + \delta_{ke} Q_e\right]^{\alpha_{kr}}} \exp\left(\frac{\sum_k \beta_{kr} h_{f,k}^\circ - \sum_k \alpha_{kr} h_{f,k}^\circ}{k_B T_{tr}}\right) \tag{3.5}$$

The symbol δ_{ke} is the Kronecker delta that is equal to unity when k is an electron and zero otherwise.

3.1 Included Species and States

The considered species and their electronic states are given in Table 3.1. In the studies of air, all species and states in Table 3.1 except Ar and Ar^+ are included. For experiments performed in O_2-Ar, the nitrogen-containing species are omitted, while the oxygen-containing species are omitted in the studies of N_2-Ar mixtures. Studies of pure N_2 or O_2 are performed using a five-species mixture comprised of the diatom, its atom, the molecular and atomic ions, and free electrons.

The six electronic states of O_2 below the $O_2(X)$ dissociation limit are considered, along with the $O_2(B^3\Sigma_u^-)$ state that is involved in the Schumann-Runge system. The state grouping scheme

Table 3.1: Included species and electronic states.

Species	States	Ref.
O	${}^3P_J$, ${}^1D_2$, ${}^1S_0$, ${}^5S^\circ$, ${}^3S^\circ$, ... (40 levels)	[104]
N	${}^4S^\circ_{3/2}$, ${}^2D^\circ_J$, ${}^2P^\circ_J$, ${}^4P_J$, ... (46 levels)	[19]
Ar	${}^1S_0$, ${}^2[3/2]^\circ_2$, ${}^2[3/2]^\circ_1$, ${}^2[1/2]^\circ_0$, ${}^2[1/2]^\circ_0$, ... (31 levels)	[7]
O_2	$X^3\Sigma^-_g$, $a^1\Delta_g$, $b^1\Sigma^+_g$, $c^1\Sigma^-_u$, $A'^3\Delta_u$, $A^3\Sigma^+_u$, $B^3\Sigma^-_u$	–
N_2	$X^1\Sigma^+_g$, $A^3\Sigma^+_u$, $B^3\Pi_g$, $W^3\Delta_u$, $B'^3\Sigma^-_u$, $C^3\Pi_u$	[4]
NO	$X^2\Pi$, $a^4\Pi$, $A^2\Sigma^+$, $B^2\Pi$, $b^4\Sigma^-$	[4]
O^+	${}^4S_{3/2}$, ${}^2D^\circ$, ${}^2P^\circ$, ${}^4P$, ${}^2D$	–
N^+	${}^3P_J$, ${}^1D$, ${}^1S$, ${}^5S^\circ$, ${}^3D^\circ$	–
Ar^+	${}^3P^\circ_{3/2}$, ${}^2P^\circ_{1/2}$	[7]
O_2^+	$X^2\Pi_g$, $a^4\Pi_u$, $A^2\Pi_u$, $b'^4\Pi_g$, $b^4\Sigma^-_g$	–
N_2^+	$X^2\Sigma^+_g$, $A^2\Pi_u$, $B^2\Sigma^+_u$, $D^2\Pi_g$	[4]
NO^+	$X^1\Sigma^+$	–
e^-	–	–

for atomic oxygen was originally implemented by Bourdon et al. [104] and has also been used in [19, 105]. The adopted grouping scheme enables accurate predictions of the net ionization and recombination rates, which require the resolution of electronic states close to the ionization limit.

The state model for atomic nitrogen comes from [19] and is motivated by similar considerations as the oxygen state model. The six states of N_2 are the five given in [4], plus the $C^3\Pi_u$ state that is involved in the second positive system. The state models for N_2^+ and NO are also based on [4].

The state model from Kapper and Cambier [7] is implemented for the electronic states of atomic argon and includes the first 31 states of Ar, ungrouped, and neglects all higher excited states. Excited states of the argon atom can have one of two core configuration quantum numbers, j_c, equal to either 3/2 or 1/2. It is assumed that the argon atom in a given electronic level is ionized to the Ar^+ excited state with the same j_c following [7, 91]. Two excited states of Ar^+ must be considered to incorporate this effect.

Excited electronic states of O_2^+, NO^+, N^+, and O^+ are assumed to follow a Boltzmann

distribution at T_{eex} following [20]; i.e. $\mathcal{H}_B = \{O^+, N^+, O_2^+, NO^+\}$. Electronic state energies and degeneracies for all species are provided in Appendix A.

3.2 Dissociation by Electron Impact

Molecular dissociation by electron impact involves the breaking of a molecular bond by a colliding electron. Only diatomic molecular species are considered in this work, so the formula in Eq. (3.6) only considers a generic diatomic species, AB, in electronic state i, that dissociates to atomic fragments $A(j)$ and $B(k)$.

$$AB(i) + e^- \leftrightharpoons A(j) + B(k) + e^- \tag{3.6}$$

Rate constants for the electron impact dissociation of O_2, N_2, NO, and N_2^+ are adopted from Park [4]. The forward rate constants are evaluated at a controlling temperature that is the geometric average of T_{vib} and T_{eex}. In the two-temperature model, the rate constant is calculated using T_{vee}. The dissociated fragments are assumed to have the electronic states corresponding to the separated-atom limit for the electronic state undergoing dissociation. The separated atom limits for each of the molecular states under consideration are listed in Table 3.2. The same separated atom limits are applied when modeling dissociation via collisions with heavy particles.

Table 3.2: Separated atom limits for molecular electronic states from [3, 4].

Species	Electronic State	Separated Atom Limit
O_2	$X^3\Sigma_g^-$, $a^1\Delta_g$, $b^1\Sigma_g^+$, $c^1\Sigma_u^-$, $A'^3\Delta_u$, $A^3\Sigma_u^+$	$O(^3P) + O(^3P)$
	$B^3\Sigma_u^-$	$O(^3P) + O(^1D)$
N_2	$X^1\Sigma_g^+$, $A^3\Sigma_u^+$	$N(^4S) + N(^4S)$
	$B^3\Pi_g$, $W^3\Delta_u$, $B'^3\Sigma_u^-$, $C^3\Pi_u$	$N(^4S) + N(^2D)$
NO	$X^2\Pi$, $a^4\Pi$, $A^2\Sigma^+$	$N(^4S) + O(^3P)$
	$B^2\Pi$, $b^4\Sigma^-$	$N(^2D) + O(^3P)$
N_2^+	$X^2\Sigma_g^+$, $A^2\Pi_u$, $B^2\Sigma_u^+$, $D^2\Pi_g$	$N^+(^3P) + N(^4S)$

3.3 Dissociation by Heavy Particle Impact

Dissociation by heavy particles involves the breaking of a molecular bond in the collision of a molecule and another heavy particle. While dissociation by electron impact typically occurs via resonances with short-lived negative ionic states [106, 107], requiring a quantum mechanical treatment, dissociation in heavy particle collisions is often modeled using classical dynamics [27].

$$AB(i) + M \leftrightharpoons A(j) + B(k) + M \qquad : \; M \neq e^- \tag{3.7}$$

3.3.1 Vibration-Dissociation Coupling

In several of the analyzed conditions, the vibrational temperature remains suppressed below T_{tr} for some or all of the test time. This vibrational nonequilibrium affects the rate of dissociation, which must be modeled accurately to enable meaningful studies of electronic excitation and ionization. In addition, dissociation involves the preferential removal of high-lying vibrational states, affecting the net rate of vibrational relaxation. There are multiple ways to model the resultant two-way coupling between vibrational relaxation and dissociation. For vibration-dissociation coupling models that do not rely on an explicit resolution of the vibrational states, there are two primary quantities that must be predicted: the nonequilibrium dissociation rate constant and the average vibrational energy loss per dissociation.

The majority of hypersonic CFD codes adopt the vibration-dissociation coupling framework proposed by Park [31]. In Park's model, the nonequilibrium dissociation rate constant is calculated using a controlling temperature that is the geometric mean of T_{tr} and T_{vib}. When calculating the recombination rate constant, $k_r = k_d/K_{eq}$, the dissociation rate constant k_d is evaluated using only T_{tr} since recombination does not depend on the vibrational energy of the gas. For the average vibrational energy loss per dissociation, Park offers two options: preferential and nonpreferential. In the preferential model, the average vibrational energy loss per dissociation, $\langle \varepsilon_{vib,s(i)} \rangle_d$, is set to $0.3 \times \mathrm{D}_{0,s(i)}$ of the dissociating species, where $\mathrm{D}_{0,s(i)}$ is the dissociation energy of $s(i)$ in its ground rovibrational state. In the nonpreferential model, all vibrational states are assumed to dissociate

with equal probability, meaning that the vibrational energy loss per dissociation is just the average vibrational energy of the dissociating species at T_{vib}.

An alternative formulation is due to Marrone and Treanor, who devised a model to capture the preferential depopulation of vibrationally excited states in a dissociating gas downstream of a strong shock wave [108]. In their model, the probability of dissociation, $p_{s(i,v)}$, for a molecule in electronic state i and vibrational state v, is assumed to depend exponentially on the vibrational energy of the molecule; i.e. $p_{s(i,v)} \propto \exp\left(-\frac{D_{0,s(i)}-\varepsilon_v}{k_B U}\right)$. A free parameter, U, defines the strength of the exponential dependence on vibrational energy. The limit of $U \to \infty$ corresponds to zero dependence on vibrational energy, in which case the average vibrational energy loss per dissociation event is equal to the average vibrational energy, $\varepsilon_{vib,s(i)}$. Smaller values of U lead to an average vibrational energy loss per dissociation, $\left\langle \varepsilon_{vib,s(i)} \right\rangle_d$, that exceeds the average vibrational energy. The value of U is set to $\frac{1}{3}k_B D_{s(i)}$ in this work based on the experimental measurements of O_2 dissociation during vibrational nonequilibrium in Streicher et al. [5]. Note that a comparable study involving N_2 does not exist.

Chaudhry et al. have recently proposed a modified Marrone and Treanor (MMT) model that is based on statistical analysis of quasi-classical trajectory simulations performed on ab initio potential energy surfaces [27]. There are two forms of this model, depending on whether the so-called "variable non-Boltzmann" (VNB) correction factors are implemented [21]. When the Boltzmann version of the model (MMT-B) is used, the formulation is very similar to the original Marrone and Treanor (MT) model. The only difference is that now $1/U$ is a linear function of $1/T_{tr}$ given by $1/U = 1/U^* + a_U/T_{tr}$. In this model, a_U accounts for the broadening of the vibrational distribution function for dissociating molecules as rotational temperature increases [27].

The variable non-Boltzmann version of the model (MMT-VNB) attempts to capture the reduction of $\langle \epsilon_{vib,s(i)} \rangle_d$ and k_d that results from the depleted high energy tail of the vibrational energy distribution function at quasi-steady-state (QSS), which is a steady-state nonequilibrium condition where relaxation and dissociation are balanced. During QSS, the vibrational states closest to the dissociation limit are underpopulated with respect to a Boltzmann distribution at

T_{vib} because the dissociation of these high-energy states occurs faster than vibrational excitation can repopulate them. As a result, the QSS dissociation rate coefficient is lower than that for Boltzmann-populated vibrational states at T_{vib}. When the VNB corrections are applied to the MMT model, this reduction is approximated by subtracting $0.1 \times D_{0,s(i)}$ from $\langle \epsilon_{vib} \rangle_d$ and scaling the nonequilibrium dissociation rate constant by 0.5. The variable part of the non-Boltzmann correction ensures that the scaling on the dissociation rate constant goes to 1.0 at chemical equilibrium when the high-lying vibrational states are no longer expected to be depleted relative to a Boltzmann population [21].

3.3.2 Selected Rate Coefficients

Based on recent experimental and computational studies of O_2 dissociation [5, 13, 109], the modified Marrone and Treanor (MMT) model with variable non-Boltzmann (VNB) correction is used to model the vibration-dissociation coupling in the dissociation of ground state O_2 and N_2 using the rate coefficients and MMT model parameters from [5, 27].

The rate coefficients published by Chaudhry et al. [12] are used for the dissociation of O_2(X) in collisions with O_2 and O, and those from Kim and Boyd [110] are used for the dissociation of the ground and first two excited states of O_2 in collisions with argon. The rate coefficients from Kim and Boyd are for dissociation at QSS, while those from Chaudhry et al. are valid for a Boltzmann distribution of vibrational states. Because the MMT model assumes that the inputted dissociation rate constant expressions are those valid for a Boltzmann vibrational-state distribution, the Kim and Boyd [110] rate constants for O_2+Ar dissociation are scaled up by a factor of 2 to ensure that the desired rate constants are recovered at QSS. The MMT model constants U^* and a_U are set to 1/3 of T_d and zero, respectively, for O_2 dissociation with argon.

The rate coefficients for the dissociation of the Herzberg O_2 electronic states with argon are approximated by taking the geometric mean of the preexponential factors and the arithmetic mean of the temperature exponents for the $O_2(i$=X, a, b)+Ar dissociation rate constants. The electronic state-specific dissociation rate coefficients for O_2-Ar are given in Table 3.3.

A common approximation of excited state dissociation rate constants is to take the Arrhe-

Table 3.3: O_2-Ar dissociation rate coefficient parameters ($k_d = AT^{\eta}\exp(-T_d/T)$).

State	A (m^3/s)	η	T_d (K)
$X^3\Sigma_g^-$	4.43×10^{-14}	-0.344	60,850
$a^1\Delta_g$	2.50×10^{-14}	-0.314	49,515
$b^1\Sigma_g^+$	2.99×10^{-14}	-0.333	41,892
$c^1\Sigma_g^-$	3.21×10^{-14}	-0.330	11,884
$A'^3\Delta_u$	3.21×10^{-14}	-0.330	10,014
$A^3\Sigma_u^+$	3.21×10^{-14}	-0.330	9,021
$B^3\Sigma_u^-$	3.21×10^{-14}	-0.330	11,208

nius expression for the ground-state dissociation rate and change only the threshold to match the dissociation energy of the excited state while keeping the pre-exponential factor and temperature exponent unchanged. Using the O_2-Ar dissociation rate constants with O_2(X), O_2(a), and O_2(b), that approximation can be assessed. It is found that, over the range of 5,000 K to 15,000 K, the dissociation rate constant for O_2(a) and O_2(b) with Ar is 73-75% of what is predicted by merely changing T_d from the O_2(X) rate expression. As a result, the pre-exponential factors, A, on the MMT dissociation rate constant expressions for O_2(X) dissociation with O_2, N_2, and O are scaled by 0.75 to approximate the excited state dissociation rate constants in Table 3.4.

Table 3.4: O_2 dissociation rate coefficient parameters for collisions with O_2, N_2, and O ($k = AT^{\eta}\exp(-T_d/T)$). The dissociation temperature of each state, $T_{d,O_2(i)}$, is given in Table 3.3.

Interacting Particles	A (m^3/s)	η	T_d (K)	a_U	U^* (K)
$O_2(X^3\Sigma_g^-) + O_2$	6.1327×10^{-12}	-0.7695	60,540	0.3965	57,343
$O_2(i>1) + O_2$	4.5995×10^{-12}	-0.7695	$T_{d,O_2(i)}$	0	$T_{d,O_2(i)}/3$
$O_2(X^3\Sigma_g^-) + N_2$	3.0410×10^{-15}	-0.0223	59,380	0.3620	385,466
$O_2(i>1) + N_2$	2.2807×10^{-15}	-0.0223	$T_{d,O_2(i)}$	0	$T_{d,O_2(i)}/3$
$O_2(X^3\Sigma_g^-) + O$	1.5295×10^{-12}	-0.6541	60,552	0.3537	237,290
$O_2(i>1) + O$	1.1471×10^{-12}	-0.6541	$T_{d,O_2(i)}$	0	$T_{d,O_2(i)}/3$

For the O_2+N and O_2+NO dissociation rate constants, the MMT rate constants for dissociation with O_2+O and O_2+N_2 are used, respectively. This is based on Park's [1] assumption that atomic colliders share a similar dissociation rate constant, and the molecular species share another dissociation rate constant. The same assumption is also applied to the excited state dissociation rate coefficients of O_2.

Thermal decomposition of $N_2(X)$ has been studied for collisions with N_2 and N by Chaudhry et al. [27], and their reported rate constants and MMT fitting parameters are implemented in the present model. Experimental [14] and computational [111] studies of the dissociation of N_2 with partners N_2 and Ar have shown that the rate coefficient with argon is approximately 1/3 of the rate coefficient for N_2 + N_2 dissociation. Thus, the adopted dissociation rate for $N_2(X)$ + Ar is set to 1/3 of the dissociation rate for $N_2(X)$ + N_2. The MMT parameters for dissociation of $N_2(X)$ via N_2 collisions are also used for dissociation via impact by argon.

The dissociation of $N_2(A)$ in collisions with Ar has been studied theoretically by Shui et al. [112] with the resulting rate constant expression reported by Levin et al. [113]. The dissociation of $N_2(A)$ with argon is modeled using this rate constant, while the dissociation of $N_2(A)$ with N_2 is calculated using rate constants that are a factor of three larger than the $N_2(A)$+Ar rate constant. While Park [1] assumes that N_2 dissociation is approximately four times faster with atomic colliders than with molecular colliders, modern ab initio calculations predict that N_2 dissociation rates with N and N_2 are of similar magnitude [27]. As a result, the $N_2(A)$ + N_2 dissociation rate constant is adopted for $N_2(A)$ dissociation with all other air species. For the dissociation of excited states above $N_2(A)$, the pre-exponential factor and temperature exponent for the $N_2(A)$ dissociation rate expressions are retained, and the threshold energy is changed to match the dissociation energy of the particular excited state. Adopted dissociation rate coefficient expressions for N_2 are presented in Table 3.5. Because it is not clear whether the Shui et al. rate constants are valid for QSS or equilibrium, the unmodified Marrone and Treanor model is used to describe the vibration-dissociation coupling for the dissociation of electronically excited N_2.

The advantage of using the MMT rate constants is their electronic state specificity. In contrast to the MMT rate constants, the majority of experimentally measured dissociation rate constants are total dissociation rate constants that subsume the dissociation from all electronic states. There are two approaches to converting an experimentally measured dissociation rate constant to an electronic state-specific dissociation rate constant. The first approach assumes that the measured rate constant is measured in a condition where ground state dissociation is dominant, i.e. the measured

Table 3.5: Dissociation rate constant parameters for N_2 ($k = AT^{\eta}\exp(-\theta/T)$).

Reaction	A (m^3/s)	η	θ (K)
$N_2(X) + N_2 \rightarrow 2N(^4S) + N_2$	5.9725×10^{-12}	-0.7017	117,529
$N_2(X) + N \rightarrow 2N(^4S) + N$	1.3271×10^{-12}	-0.5625	113,957
$N_2(X) + Ar \rightarrow 2N(^4S) + Ar$	1.9908×10^{-12}	-0.7017	117,529
$N_2(A) + N_2 \rightarrow 2N(^4S) + N_2$	1.0920×10^{-7}	-1.9420	41,057
$N_2(A) + N \rightarrow 2N(^4S) + N$	1.0920×10^{-7}	-1.9420	41,057
$N_2(A) + Ar \rightarrow 2N(^4S) + Ar$	3.6400×10^{-8}	-1.9420	41,057
$N_2(i>2) + N_2 \rightarrow N(^4S) + N(^2D) + N_2$	1.0920×10^{-7}	-1.9420	$D_{N_2(i)}/k_B$
$N_2(i>2) + N \rightarrow N(^4S) + N(^2D) + N$	1.0920×10^{-7}	-1.9420	$D_{N_2(i)}/k_B$
$N_2(i>2) + Ar \rightarrow N(^4S) + N(^2D) + Ar$	3.6400×10^{-8}	-1.9420	$D_{N_2(i)}/k_B$

dissociation rate constant is exactly the ground state dissociation rate constant. The excited state dissociation rate constants are typically then estimated by simply adjusting the activation energy in the Arrhenius expression to match the dissociation energy of the excited state, as in [114]. This approach is likely to overestimate the net dissociation rate, particularly for molecules with many electronic states that correlate to the ground-state separated atom limit like CO and O_2 [115].

Another approach, proposed by Aliat et al. [116], is to assume that the dissociation rate constant is measured at a condition where all of the electronic and vibrational states are Boltzmann populated. By assuming that dissociation is equally enhanced by electronic and vibrational energies, the Marrone and Treanor preferential dissociation model can be extended to incorporate electronic energy, enabling the calculation of electronic state-resolved dissociation rates from a global rate constant. Because the vibrational and electronic states are likely underpopulated relative to a Boltzmann distribution during dissociation, this approach is likely to yield model predictions that underpredict the net dissociation rate.

Ab initio ground state dissociation rate coefficients for NO(X) have recently been determined within the MMT framework[117]; however, the resulting rate coefficient expressions have not yet been published. Streicher et al. have measured the dissociation of NO with partners Ar, NO, and N_2 behind reflected shocks [79, 80]. These rates are adopted to model the dissociation of NO(X) with the three measured partners.

The electronic quenching of NO(A) is approximately 5,000 times less efficient in collisions with Ar than with O_2 or NO [118]. Because the dissociation rate of NO with argon was determined in mixtures of 0.4-2% NO dilute in argon, it is likely that the excited electronic states of NO are not appreciably populated, meaning that the measured rate constants are representative of dissociation via NO(X) + Ar and NO(X) + NO collisions. The NO + N_2 dissociation rate constant is measured in mixtures up to 99.6% N_2 with 0.4% NO. Because NO is effectively quenched by N_2, this rate constant is likely influenced by dissociation from excited states of NO and should be revised in future studies when rate constants that better isolate NO(X) + N_2 are available.

In Park's model [1], the dissociation of NO in collisions with N and O is assumed to proceed with the same rate coefficient as dissociation with NO. The dissociation of NO with O_2 is assumed to proceed at the same rate coefficient as dissociation with N_2. These same assumptions are adopted to extend the rate coefficients from Streicher et al. to NO dissociation with N, O, and O_2.

The dissociation of NO(A) has been studied by Shui et al. [119] and, again, the resulting rate coefficient is provided by Levin et al. [113]. Because Shui et al. studied NO(A) dissociation with Ar, the rate coefficient they determined is only used to model NO(A) + Ar dissociation. The ratio of NO(X) dissociation rate constants across the various studied colliders is used to extend the NO(A) + Ar dissociation rate constant to cover the remaining reactions. The NO(A) rate constants are then used to model dissociation from all other electronically excited states of NO. The adopted Arrhenius expressions for NO dissociation are summarized in Table 3.6. Because MMT model parameters are not available for NO, the Marrone and Treanor model with $U = \frac{1}{3}k_B D_{0,NO(i)}$ is adopted to model the vibration-dissociation coupling of NO.

The dissociation rate constants for N_2^+ are taken from Park [114]. Note that unlike the other molecules considered in his review, Park was able to base his estimates of the N_2^+ dissociation rate constants on measurements that are specific to each of the considered electronic states, with the exception of the $D^2\Pi_g$ state. The dissociation rate constant in collisions with Ar is assumed to be equal to that for collisions with N_2.

Table 3.6: Dissociation rate constant parameters for NO ($k = AT^{\eta}\exp(-\theta/T)$).

Reaction	A (m^3/s)	η	θ (K)
NO(X) + M_1 → N(^{4}S) + O(^{3}P) + M_1[a]	2.32×10^{-8}	-1.500	75,210
NO(X) + M_2 → N(^{4}S) + O(^{3}P) + M_2[b]	7.14×10^{-10}	-1.500	75,210
NO(X) + Ar → N(^{4}S) + O(^{3}P) + Ar	1.20×10^{-9}	-1.500	75,210
NO($i = 2,3$) + M_1 → N(^{4}S) + O(^{3}P) + M_1	1.14×10^{-11}	-1.152	$D_{NO(i)}/k_B$
NO($i = 2,3$) + M_2 → N(^{4}S) + O(^{3}P) + M_2	3.50×10^{-13}	-1.152	$D_{NO(i)}/k_B$
NO($i = 2,3$) + Ar → N(^{4}S) + O(^{3}P) + Ar	5.86×10^{-13}	-1.152	$D_{NO(i)}/k_B$
NO($i > 3$) + M_1 → N(^{2}D) + O(^{3}P) + M_1	1.14×10^{-11}	-1.152	$D_{NO(i)}/k_B$
NO($i > 3$) + M_2 → N(^{2}D) + O(^{3}P) + M_2	3.50×10^{-13}	-1.152	$D_{NO(i)}/k_B$
NO($i > 3$) + Ar → N(^{2}D) + O(^{3}P) + Ar	5.86×10^{-13}	-1.152	$D_{NO(i)}/k_B$

[a] $M_1 = \{NO, O, N\}$
[b] $M_2 = \{N_2, O_2\}$

3.4 Electron Impact Excitation

Collisionally induced excitation via electron impact (E-CIE) is the direct electronic excitation of an atom or molecule, A, in electronic state i by an electron, proceeding as shown in Eq. (3.8). A summary of the adopted rate coefficients is provided in Table 3.7.

$$A(i) + e^- \leftrightharpoons A(j) + e^- \tag{3.8}$$

Electrons dominate the excitation kinetics when their number density and average translational energy are sufficiently high, as is the case in many hypersonic flows at velocities exceeding those of Earth orbit. As a result, electron impact excitation and ionization (E-CIE and E-CII) have been studied extensively in previous works [104, 123, 42], and several complete datasets of electron impact cross-sections exist for air species and argon [86, 85, 44, 120, 4]. Experimental cross-section measurements have been performed at a wide variety of collision energies for excitation and ionization involving select states of the species under consideration; however, the measurement uncertainties are often large, complicating the validation of computational predictions [124].

In the present model, the cross-sections calculated using B-Spline R-Matrix techniques in [85], [43] and [86] are integrated over a Maxwellian electron energy distribution, and the resulting rate coefficients are implemented. These data cover the electron impact excitation transitions involving

Table 3.7: Selected rate coefficients for electron impact excitation.

Species	i	j	Method	Ref.
O	1-10,14	2-11,14,17	RMPS[a]	[86]
	remaining		Analytical	[105]
N	1-19	2-20	RMPS	[43]
	remaining		Analytical	[105]
Ar	1-18	2-19	RMPS	[85]
O_2	1-3	2-4	Review[b]	[4]
	1-3, 6	6, 7	WTCS[c]	[120]
	remaining		Analytical	[121]
N_2	1-4	2-5	Review	[4]
	1-3	6	WTCS	[120]
	remaining		Analytical	[121]
NO	1-4	2-5	Review	[4]
Ar^+	1	2	DW[d]	[122]
N_2^+	1-3	2-4	Review	[4]

[a] RMPS = R-Matrix with Pseudostates
[b] Review = Review of experimental data
[c] WTCS = Weighted Total Cross-Section
[d] DW = Distorted Wave

the lowest 19 states of Ar, the lowest 11 states of O, and the lowest 20 states of N. Electron impact transition rates involving higher atomic levels are approximated using the fit to the Drawin [125] cross section presented by Panesi et al. [105]. The excitation rate coefficient between the two fine-structure levels of Ar^+ is calculated using the cross-sections published by Kwon and Cho [122].

The E-CIE of O_2, N_2, NO, and N_2^+ are treated using the cross-sections collected by Park [4], integrated over a Maxwellian electron energy distribution. For transitions not covered by Park's review, the rate coefficients from Teulet et al. [120] are adopted when available. Annaloro and Bultel's analytical rate expression is used for the remaining molecular E-CIE transitions [121].

3.5 Electron Impact Ionization

Collisionally induced ionization via electron impact (E-CII) is the ionization of a neutral atom or molecule by a high-energy electron. This process generally proceeds as in Eq. (3.9). An

overview of the adopted rate constants is provided in Table 3.8.

$$A(i) + e^- \leftrightharpoons A^+(j) + 2e^- \tag{3.9}$$

Table 3.8: Selected rate coefficients for electron impact ionization.

Species	i	Method	Ref.
O	1-3	Review	[19]
	remaining	Analytical	[82]
N	1-3	RMPS	[43]
	remaining	BEB[a]	[42]
Ar	1	RMPS	[85]
	2-31	DW	[126, 127]
O_2	1-3, 6-7	WTCS	[120]
	4-5	Analytical	[121]
N_2	1-3, 6	WTCS	[120]
	4-5	Analytical	[121]
NO	1, 3, 4	WTCS	[120]
	all	Analytical	[121]

[a] BEB = Binary Encounter Bethe

Electron impact ionization of the molecular species is modeled using the rate coefficient expressions from Teulet et al. [120], and the ionization of the remaining states is modeled using the analytical expression from Annaloro and Bultel [121]. Electron impact ionization rate coefficients for the ground state of argon are calculated by integrating the ionization cross-sections calculated by Zatsarinny et al. [85], while the ionization rates for the excited states are calculated using the cross-section formula and associated parameters from Deutsch et al. [127, 126]. The rate constants for the electron impact ionization of argon are given in Table 3.9.

Electron impact ionization cross-sections for the first three electronic states of N and O are taken from the B-Spline R-matrix calculations of Wang et al. [43] and Tayal and Zatsarinny [86], respectively, and are integrated to obtain rate coefficients as a function of T_{eex}. Ionization of the higher states of atomic nitrogen is modeled using the rate coefficients recently published by Ciccarino and Savin [42]. There is no equivalent dataset for the electron impact ionization of highly excited atomic oxygen, so an analytical expression is needed. Several options have been presented in the literature and are reviewed by Lemal in [128]. Here, the analytical expression from Kim

Table 3.9: Arrhenius rate parameters for the electron impact ionization of argon ($k = AT_{eex}^{\eta}\exp(-\theta/T_{eex})$).

i	j	A (m^3/s)	η	θ (K)
1	1	1.16×10^{-18}	0.928	181,720
2-3	1	7.81×10^{-16}	0.493	47,935
4-5	2	2.55×10^{-15}	0.388	47,420
6-11	1	4.84×10^{-15}	0.538	36,089
12-15	2	5.30×10^{-16}	0.751	28,984
16-21	1	1.60×10^{-13}	0.290	23,139
22-23	1	4.83×10^{-14}	0.335	19,554
24-25	1	1.60×10^{-13}	0.290	23,139
26-28	2	1.55×10^{-13}	0.299	18,540
29-30	2	1.32×10^{-13}	0.247	18,094
31	2	1.55×10^{-13}	0.299	18,540

and Boyd [82] is selected because it predicts rate coefficients of E-CII for N that are in excellent agreement with those of Ciccarino and Savin [42]. Figure 3.1 illustrates the superior predictions obtained using Kim and Boyd's expression, compared to an approximation of the Drawin rate adopted by Panesi et al. [105]. Because the ionization rate coefficients for metastable N and O are similar in magnitude, the analytical rate coefficient expression for the ionization of O is chosen based on agreement with the available data for N.

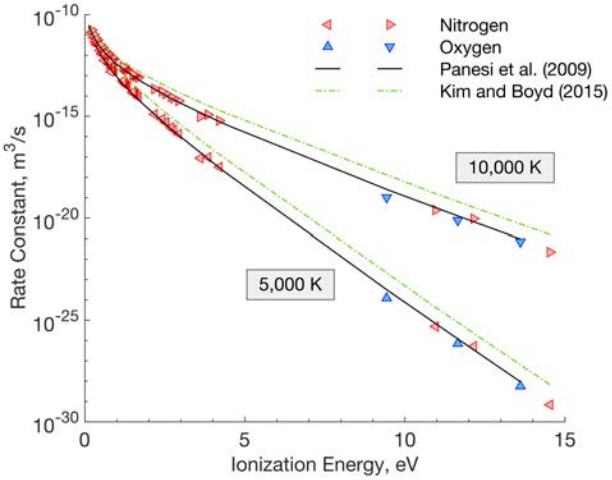

Figure 3.1: Comparison of analytical expressions for E-CII with high fidelity quantum mechanical rate coefficient calculations at T_{eex} = 5,000 K and 10,000 K. Trends shown here are consistent for $T_{eex} \in \{5{,}000 - 50{,}000\}$ K.

3.6 Heavy Particle Impact Excitation

Collisionally-induced excitation by heavy particle impact is the change of one particle's electronic state via collision with a heavy species M that does not change its electronic state or react chemically. A generic HP-CIE reaction is given in Eq. (3.10), where A can be an atom or molecule.

$$A(i) + M \leftrightharpoons A(j) + M \quad : \; M \neq e^- \tag{3.10}$$

Heavy particle impact excitation (HP-CIE) and ionization (HP-CII) have received considerably less attention than the corresponding processes involving electrons, particularly at the high temperatures relevant to hypersonic flows. Table 3.10 presents an overview of the HP-CIE rate constants and cross-sections implemented into the model and the temperature or energy range over which they were measured, calculated, or inferred.

Table 3.10: Selected rate coefficients for heavy particle impact excitation.

Species	i	j	M	Type	T (K) or ϵ (eV)	Ref.
O	1	2	O	$\sigma(\epsilon)$	2–10 eV	[48, 129]
	1	2	Ar, N_2	k_Q	195–673 K	[130]
	1	2	O_2	k_Q	195–673 K	[130, 131, 132]
	1	2	NO	k_Q	298 K	[133]
	1-2[a]	3	O	$k(T)$	—	[15, 134]
	1	3	N	k_Q[b]	298 K	[135]
	1-2	3	Ar	k_Q	298 K	[136]
	2[c]	3	O_2	k_Q	255–375 K	[131]
	1-2	3	N_2	k_Q[b]	298 K	[131, 137]
	1-2	3	NO	k_Q	298 K	[138, 131]
	4	5	Ar	$\sigma(\epsilon)$	0–8 eV	[139]
	6	7	Ar	k_Q	298 K	[140]
	6	7	O_2, N_2	k_Q	298 K	[141]
		remaining		$k(T)$	—	[15]
N	1	2	O, N[d]	k_Q	298 K	[142]
	1	2	Ar	k_Q	298 K	[143]
	1	2	N_2	$k(T)$	7,500-15,000 K	[47]
	1	2	O_2, NO[e]	—	—	[142]
	2	3	N_2	k_Q	298 K	[143]
	1	3	N_2	k_Q	298 K	[144]

	1,2	3	N	k_Q	298 K	[145]
	2	3	O	k_Q	298 K	[146, 134]
	2	3	O_2[e]	—	—	[142]
	1, 2[f]	3	NO	k_Q	298 K	[142]
	5	7	N_2, Ar	k_Q	298 K	[147]
		remaining		$k(T)$	—	[15]
Ar	1	$j \ni A_{1j} > 0$	all	$k(T)$	10,000–11,200 K	present work
	2-4	3-5	all	$k(T)$	—	[7, 91]
	$(i,j) \ni A_{ij} > 0$		all	$k(T)$	—	[49]
	10	11	Ar	k_Q	298 K	[148]
	7	8	Ar	k_Q	298 K	[148]
		remaining		$k(T)$	—	[15]
O_2	1	2	O	k_Q	700–1700 K	[149]
	1	2	O_2	k_Q	100–450 K	[150]
	1	2	N, N_2, NO	k_Q	298 K[g]	[114]
	1	2	Ar	k_Q	298 K	[151]
	1	3	O_2	k_Q	300–800 K	[152]
	1	3	Ar	k_Q	$k_Q = k_{Q,O_2(a)+Ar}$	[114, 151]
	2	3	O	k_Q	700–1,700 K	[149]
	2	3	O_2	k_Q	650–1,650 K	[153, 154]
	2	3	N, N_2, O_2, NO	k_Q	298 K[g]	[114]
	2	3	Ar	k_Q	298 K	[155, 156]
	2, 3	4	Ar	k_Q	298 K	[157, 114]
	3	4, 5, 6	O, N, N_2, O_2, NO	k_Q	298 K	[114]
	3	5, 6	Ar	k_Q	$k_Q = k_{Q,O_2(c)+Ar}$	[157, 114]
		remaining		$k(T)$	—	[15]
N_2	1	2	N	k_Q	8,000–15,000 K	[158]
	1	2	Ar	k_Q	298 K	[159]
	1	2	N_2, NO	k_Q	298 K[g]	[114]
	1[h]	2	O_2, O	$k(T)$	—	[15, 160]
	1	3	N_2	k_Q	298 K	[161]
	2	3	N, O, O_2, N_2, NO	k_Q	298 K[i]	[114]
	2	3	Ar	k_Q	298 K	[143]
	3, 4	4, 5	N, O, N_2, O_2, NO	k_Q	298 K[i]	[114]
	3	6	N, N_2, O_2	k_Q	298 K	[159]
	5	6	N_2	k_Q	298 K	[162]
		remaining		$k(T)$	—	[15]
NO	1	2	N, O, N_2, O_2, NO	k_Q	298 K	[114]
	1	3	NO	k_Q	300–2,000 K	[114]
	1	3	N, O, N_2, O_2	k_Q	298 K	[114]

	2	4	N, O, N_2, O_2	k_Q	298 K	[114]
	4	5	N, O, N_2, O_2	k_Q	298 K	[114]
			remaining	$k(T)$	—	[15]
N_2^+	1	2	N, O, N_2, O_2, NO	k_Q	298 K	[114]
	1	3	N_2	$k(T)$	8,000–15,000 K	[158]
	1	3	N, O, O_2, NO	k_Q	298 K	[114]
	2	4	N, O, N_2, O_2, NO	k_Q	298 K	[114]
			remaining	$k(T)$	—	[15]

[a] Excitation of $O(^3P \rightarrow {}^1S)$ and $O(^1D \rightarrow {}^1S)$ by $O(^3P)$ are treated using Lemal's analytical formula instead of quenching rates because $O(^1S)$ + $O(^3P)$ leads to $O(^1D)$ + $O(^1D)$ [134].

[b] Upper limit only

[c] $1 \rightarrow 3$ is neglected since the product channel for $O(^1S)$ + $O_2(X)$ leads to $O(^3P)$ + O_2(A,a,c) [131, 137].

[d] The rate of $N(^2D)$ deactivation by $O(^3P)$ is used to approximate the rate of deactivation of $N(^2D)$ by $N(^4S)$.

[e] Neglecting published removal rates because they are driven by reactive channels.

[f] In the absence of product yields, the branching ratios of $N(^2P)$ + NO $\rightarrow$ $N(^2D, {}^4S)$ + NO are assumed to be equal.

[g] Park [114] assumes a constant value of $\sigma(\epsilon)$ for optically forbidden transitions when extrapolating room temperature quenching data.

[h] N_2(A) removal by O_2 primarily leads to $2O(^3P)$ + $N_2(X)$ and removal by O primarily leads to $O(^1S)$ + $N_2(X)$ [160]. As a result, Lemal's cross-section is used for the physical quenching rate.

[i] Park [114] uses a power-law fit determined from several quenching rate measurements to extrapolate quenching rate data for optically allowed transitions.

A small number of computational studies of HP-CIE or quenching have been performed for the species considered here, most of which are concerned with comparisons to experimental quenching rate coefficients at low-temperature [163, 164, 165, 166]. One exception is the excitation of $O(^3P \rightarrow {}^1D)$ via collisions with $O(^3P)$, studied in [48] and [129] using one-dimensional quantum scattering calculations for collision energies, ϵ, from threshold to 10 eV. Another exception is the cross section calculation for $O(^3P)$ + $O(^3P)$ $\rightarrow$ $O(^1D)$ + $O(^1D)$ in [167]. More recently, Lu et al. [47] have also calculated the rate coefficient for electronic excitation of $N(^2D)$ in collisions between $N(^4S)$ and $N_2(X)$.

Experimental cross-sections of HP-CIE are also very scarce. To the author's knowledge, the only published experimental cross-sections for HP-CIE of an air species are given in [168] for

excitation between the $^5S^\circ$ and $^3S^\circ$ states of atomic oxygen under impact by O_2, N_2, Ar, and Xe. The cross-sections for excitation by collision with O_2, N_2, and Ar are integrated to obtain the rate constants that are implemented into the model. Rate constant expressions derived from the results of the aforementioned computational and experimental studies are given in Table 3.11.

Table 3.11: Arrhenius parameters for integrated theoretical and experimental cross sections ($k = AT^n \exp(-\theta/T)$).

Reaction	A (m^3/s)	n	θ (K)	Ref.
$O(^3P) + O(^3P) \rightarrow O(^3P) + O(^1D)$	1.37×10^{-19}	0.455	21,506	[129]
$O(^3P) + O(^3P) \rightarrow O(^1D) + O(^1D)$	6.10×10^{-18}	0.0158	46,044	[167]
$N(^4S) + N_2(X) \rightarrow N(^2D) + N_2(X)$	1.88×10^{-15}	-0.708	27,664	[47]
$O(^5S^\circ) + O_2(X) \rightarrow O(^3S^o) + O_2(a)$[a]	3.32×10^{-18}	0.0219	16,009	[168]
$O(^5S^\circ) + N_2(X) \rightarrow O(^3S^o) + N_2(X)$	1.31×10^{-18}	0.357	5,034	[168]
$O(^5S^\circ) + Ar(1) \rightarrow O(^3S^o) + Ar(1)$	3.12×10^{-19}	0.0448	9,412	[139]

[a] product assumed to be $O_2(a)$ based on the observed threshold energy.

Many other relevant HP-CIE transitions have been studied in the vast literature devoted to determining rate coefficients for quenching, the reverse of HP-CIE; however, the rate constants are typically measured at room temperature. If a temperature dependence is determined, it is typically only valid below 1,000 K [132]. Where available, quenching rates for the considered species are implemented into the present model. Table 3.10 provides the temperature or range of temperatures at which each rate coefficient was determined. For the rate coefficients measured at 298 K that have no published temperature dependence, the rate coefficient is extrapolated by assuming that the cross-section is constant with respect to collision energy. This yields a $\sqrt{T}$ temperature dependence in the quenching rate constant,

$$k_Q = k_{Q,298K}\sqrt{\frac{T_{tr}}{298K}} \tag{3.11}$$

where $k_{Q,298K}$ is the rate constant measured at room temperature and k_Q is the quenching rate constant adopted in the model. This extrapolation technique has also been applied in [161, 114].

Most of the implemented rate coefficients for the HP-CIE of O_2 are taken from the review by Park [114], or from quenching rate coefficients collected by Capitelli et al. [131]. However, more

recent data for the excitation of O_2(X→a) and O_2(a→b) in collisions with O(^{3}P) are taken from the recent quenching experiments in [149] that probed temperatures up to 1,700 K. Excitation occurs more rapidly using the newly determined rate coefficients, in comparison to the rate coefficients extrapolated from room temperature that are reported by Park. This is a consequence of the observed threshold behavior in the quenching reaction above 800 K. Volynets et al. did not report a definite product channel for the quenching of O_2(b), but [156] found that most quenching partners de-excite O_2(b) to form O_2(a), and not O_2(X). The quenching rate of O_2(b) measured by Volynets et al. is therefore assumed to yield O_2(a).

The HP-CIE rate coefficients for N_2 are mostly taken from the review by Park. Excitation of N_2(X→A) in collisions with N is modeled using the rate coefficient from Flagan and Appleton [158], one of the only high-temperature excitation rate coefficients that have been published. The N_2^+(X→B) excitation rate coefficient with N_2 is also adopted from Flagan and Appleton. The remainder of the N_2^+ excitation rate coefficients come from Park [114].

The electronic excitation and ionization of argon have been studied both experimentally and computationally in shock tube flows by several authors [169, 7, 170, 171]. The observed threshold energy for the ionization of argon in atom-atom collisions is approximately equal to the 11.5 eV excitation energy of the lowest energy electronic states of argon, not the ionization energy of 15.7 eV [171, 170]. As a result, previous measurements of ionization behind strong shock waves in argon have been used to infer rate constants of electronic excitation in the collision between two argon atoms.

Typically, the inference is made using the linear cross-section expression originally put forward by Drawin [49], with the fitting parameter being the cross-section slope at the threshold energy. Values for this parameter are scattered by more than an order of magnitude, as shown in Kapper and Cambier [7]. Variation between different authors is likely due to some combination of impurities [171, 169] and boundary layer effects [172], and it's worth noting that the most discordant measurements [171] have been brought closer to the other published values by modifications to the experimental equipment [173].

In the present work, measurements of electron number density in 1% mixtures of O_2 dilute in argon are used to infer a scale factor that is applied to the rate coefficients used by Kapper and Cambier [7]. Measurements in N_2-Ar were also performed in the same facility and at similar experimental conditions as these O_2-Ar experiments. Previous experimental measurements of the ionization distance behind shocks in argon with O_2 and N_2 impurities indicate that the ionization rate is not appreciably impacted by the presence of small amounts of O_2 or N_2 [169]. Thus, the Ar + Ar excitation rates inferred from the electron number density measurements in O_2-Ar mixtures are appropriate to implement into the current model for both O_2-Ar and N_2-Ar mixtures. The excitation rate constant inference from electron number density data is described in Chapter 5.

Excitation rate coefficients involving the $4s$ states of argon are modeled using the rate coefficients from Kapper and Cambier, and Drawin's formula is used for HP-CIE between pairs of radiatively coupled excited states of argon [91, 7]. For the HP-CIE between excited states of argon that are not radiatively coupled, the logarithmic cross-section suggested by Lemal et al. [15] is implemented.

Rate coefficients have only been published for electronic transitions in heavy particle collisions for the ground and metastable electronic states of the considered species. Calculating the excitation or quenching rate coefficients of higher-lying electronic states using ab initio computational techniques is often intractable due to the rapid increase of state density with energy. Experimentally, it is difficult to produce stable and long-lived populations of high-lying electronic states, many of which have very short radiative lifetimes. In the cases where removal rates have been measured, isolating product channels proves challenging due to the large number of energetically accessible removal pathways. For this reason, the majority of published removal rates for electronically excited argon are not implemented, with the exception of several from Sadeghi et al. [148] where the products are specified.

For the transitions where rate coefficient data is unavailable, several theoretical expressions are available to approximate the necessary HP-CIE rate constants [17, 19, 49, 121, 51, 50]. These models offer convenient closed-form expressions for excitation rate constants between any two states;

however, the rate coefficients predicted by the various models are spread across up to four orders of magnitude [15, 20]. For the transitions for which no data is available, the cross-section expression from Park [17], given in Eq. (3.12), is adopted with the value of $\sigma_0 = 1.21 \times 10^{-24}$ m^2 based on findings from Lemal et al. [15].

$$\sigma^{hp-cie}_{s(i,j)+M}(\epsilon) = \sigma_0 \left(\frac{\ln(\epsilon/\varepsilon_{ij})}{\epsilon/\varepsilon_{ij}} \right) \tag{3.12}$$

In Eq. (3.12), ϵ is the collision energy and $\varepsilon_{ij} = \varepsilon_j - \varepsilon_i$ is the energy difference between the i and j electronic states of the species s.

3.7 Heavy Particle Impact Ionization

Collisionally-induced excitation by heavy particle impact (HP-CII) is the process of collisional ionization without a change to the electronic state of the colliding heavy species. This process may be contrasted with Penning ionization, in which ionization also occurs during a bimolecular collision; however, the requisite energy comes from the electronic, not translational, energy of the colliding particles. Penning ionization is neglected for the present mixtures of air and argon since none of the species have metastable excited states with energies higher than the first ionization energy of any of the other considered species. A general HP-CII reaction is presented in Eq. (3.13) and the selected rate coefficients are given in Table 3.12.

$$A(i) + M \rightarrow A^+(j) + M \quad : \; M \neq e^- \tag{3.13}$$

Table 3.12: Selected rate coefficients for heavy particle impact ionization.

Species	i	M	Method	Ref.
Ar	1	Ar	Atomic beam experiment	[174]
	2-31	all	Analytical	[49]
others	all	all	Analytical[a]	[121]

[a] σ_0 is set to 1.21×10^{-24} m^2.

Experimentally measured cross-sections for ionization in the impact of two ground-state argon atoms are implemented using the experimentally measured cross-section from Haugsjaa and Amme

[174]. The resulting rate coefficient expression is given in Eq. (3.14).

$$k^{hp-cii}_{Ar(1,1)+M}(T_{tr}) = 1.311 \times 10^{-24} T_{tr}^{0.992} \exp\left(\frac{-183,690}{T_{tr}}\right) \tag{3.14}$$

Heavy particle impact ionization of the excited levels of argon is modeled using the expression from Drawin and Emard [49]. Heavy particle impact ionization of the air species is modeled using the rate coefficient expression from Annaloro and Bultel [121],

$$k^{hp-cii}_{s(i,j^+)+M} = \sqrt{\frac{8k_bT_{tr}}{\pi\mu}}\sigma_0 a_1 \left(\frac{-\varepsilon_{ij}}{k_BT_{tr}}\right)^{a_2} \exp\left(\frac{-\varepsilon_{ij}}{k_BT_{tr}}\right) \tag{3.15}$$

where $a_1 = 0.39534$, $a_2 = 0.3546$, and μ is the reduced mass of the colliding particles. The scale factor, σ_0, is set to 1.21×10^{-24} m^2 instead of Annaloro and Bultel's suggested 10^{-20} m^2 based on the findings by Lemal et al. [15] for the appropriate magnitude of HP-CIE reactions in post-shock flows.

3.8 Associative Ionization

Associative ionization involves the association of two species, A and B, to form a molecular ion AB^+ and a free electron. The inverse of associative ionization is called dissociative recombination. A generic associative ionization reaction is shown in Eq. (3.16).

$$A(i) + B(k) \leftrightharpoons AB^+(m) + e^- \tag{3.16}$$

There are a large number of associative ionization rate constants that have been applied to calculations of hypersonic flowfields [22]. These rate constants are not applied in the present CR model because they do not include information about the electronic states of the reactant atoms. Instead, the adopted rate constants for AI come from ion storage ring experiments investigating dissociative recombination (DR). Le Padellec has published expressions for channel-specific AI cross sections for the formation of NO+ and O_2^+, which are integrated to calculate the Arrhenius parameters presented in Table 3.13. Associative ionization rates coefficients for the formation of N_2^+ are calculated using the DR rate constant and product branching ratios from Peterson et al. [175]

and the principle of detailed balance. Rate coefficient expressions are also provided for the case where the atomic electronic states are in equilibrium at the rate-controlling temperature. Because these rates can be used to approximate associative ionization using a single reactive channel, they are referred to as single-channel or equilibrium rate expressions.

Table 3.13: Associative ionization rate coefficients used in the present model. Equilibrium rate coefficients are the effective single-channel rate coefficients when the atomic reactants are in equilibrium at the forward rate-controlling temperature, T.

Product Ion	Channel	A (m^3/s)	η	θ (K)	Ref.
NO^+	$N(^4S) + O(^3P)$	6.571×10^{-23}	1.0	32,142	[176, 177]
	$N(^2D) + O(^3P)$	2.500×10^{-22}	1.0	4,409	
	$N(^2P) + O(^3P)$	9.856×10^{-23}	1.0	0	
	Equilibrium	1.039×10^{-18}	0.207	34,417	
N_2^+	$N(^2D) + N(^4S)$	1.609×10^{-20}	0.637	41,392	[175]
	$N(^2P) + N(^4S)$	7.970×10^{-21}	0.637	27,556	
	$N(^2D) + N(^2D)$	9.042×10^{-21}	0.637	13,712	
	Equilibrium	1.988×10^{-14}	-0.689	72,754	
O_2^+	$O(^3P) + O(^3P)$	1.206×10^{-22}	1.0	77,164	[178, 177]
	$O(^1D) + O(^3P)$	2.292×10^{-21}	1.0	57,902	
	$O(^1D) + O(^1D)$	1.340×10^{-21}	1.0	35,043	
	Equilibrium	3.029×10^{-20}	0.680	80,684	

A notable caveat of using dissociative recombination data is that the ions are typically in the ground or first excited vibrational state, in contrast with the vibrational state distributions found in hypersonic flows. For N_2^+, the adopted DR rates have been applied in various CR models because the experimental vibrational distribution corresponded roughly to $T_{vib} \approx 6,000$ K, which is representative of a shocked hypersonic flow. Dissociative recombination rate constants for NO^+ and O_2^+ are not so fortuitous – the experimental ion populations were predominantly in the ground vibrational state. Sheehan has reviewed the DR rates for the molecular ions considered in the present model and found all of the rates to be sensitive to the vibrational excitation of the molecular ion [179]. For NO^+ and O_2^+, the DR of v=0 molecules is found to proceed approximately 3 times faster than for $v > 0$ ions. The situation is more extreme for N_2^+ at high electron temperatures, where this ratio may be as high as 10.

In Figure 3.2, the single-channel associative ionization rates are compared with those included

in several two-temperature (2T) reaction sets. The rate coefficient of AI to form N_2^+ exhibits the closest agreement with the 2T rate coefficients, potentially due to matched vibrational distributions between the DR experiment and typical hypersonic flows. The single-channel rate expressions for NO^+ and O_2^+ are within the scatter of the available 2T rate coefficients, demonstrating that the Arrhenius expressions in Table 3.13 are reasonable. The AI rate coefficients for NO^+ formation exhibit considerable scatter below 10,000 K, with predictions varying by more than an order of magnitude.

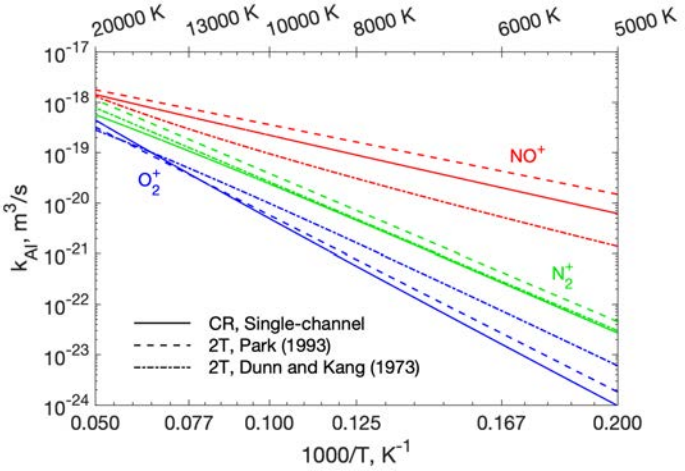

Figure 3.2: Comparison of rate coefficients for associative ionization calculated using the equilibrium expressions given in Table 3.13 and those from several two-temperature models [11, 1].

3.9 Neutral Exchange

Neutral exchange reactions involve the transfer of atoms between two molecular species. The formation enthalpy of the AC molecule on the other side of the reaction can significantly decrease the activation energy when compared with direct dissociation of AB. For this reason, neutral exchange reactions are the dominant mechanism for breaking down N_2 at orbital and sub-orbital hypersonic velocities. A generic neutral exchange reaction is given in Eq. (3.17).

$$AB(i) + C(j) \leftrightharpoons AC(k) + B(l) \tag{3.17}$$

A summary of the implemented neutral exchange rate coefficients is given in Table 3.14. The

adopted rate coefficient expressions for neutral exchange come primarily from Park [1] and Popov [133]. An improved rate coefficient for the formation of N(^{2}D) in the collision of NO(X) and O(^{3}P) is implemented from the recent publication by Lu et al. [180]. The channel involving NO(X) + O(^{1}D) is discussed by Herron [142], with experimental investigations determining that the O(^{1}D) yield from N(^{2}D) + O_2(X) is 76% at 100 K. In contrast, an ab initio study by Gonzalez et al. [181] concluded that the channel involving O(^{1}D) should contribute meaningfully to the overall N(^{2}D) + O_2(X) reactivity. The experimental result is adopted in the present model. Whenever no temperature dependence is given, a constant cross-section is assumed. A notable exception is the NO(X) + N(^{2}D) reaction, which Li et al. [182] showed to have an approximately constant rate coefficient with respect to temperature, the result of an exponentially decreasing cross-section with respect to collision energy.

Table 3.14: Neutral exchange reactions and their rate coefficient expressions ($k = AT^{\eta}\exp(-\theta/T_{tr})$).

Reaction	A (m^3/s)	η	θ (K)	Ref.
N_2(X) + O(^{3}P) → NO(X) + N(^{4}S)	9.45×10^{-12}	0.42	42,938	[183]
O_2(X) + N(^{4}S) → NO(X) + O(^{3}P)	4.14×10^{-15}	1.18	4,005	[184]
N_2(A) + O(^{3}P) → NO(X) + N(^{2}D)	2.31×10^{-18}	0.50[a]	0	[133]
N_2(C) + O(^{3}P) → NO(X) + N(^{2}D)	1.73×10^{-17}	0.50[a]	0	[133]
O_2(X) + N(^{2}D) → NO(X) + O(^{1}D)	7.30×10^{-18}	0	185	[133]
O(^{3}P) + NO(X) → O_2(X) + N(^{2}D)	8.39×10^{-17}	0	50,204	[180]
NO(X) + N(^{2}D) → N_2(X) + O(^{1}D)	3.46×10^{-18}	0[b]	0	[133, 182]
O_2(a) + N(^{4}S) → NO(X) + O(^{3}P)	5.19×10^{-21}	1.30[c]	6,797	[185]
O_2(b) + N(^{4}S) → NO(X) + O(^{3}P)	2.90×10^{-41}	6.70[c]	4,959	[185]

[a] Extrapolated from room temperature by assuming a constant cross-section with respect to collision energy.

[b] Cross-section is not assumed to be constant following the study by Li et al. [182].

[c] Rate coefficient exceeds the gas kinetic limit within the temperature range of interest, so the rate coefficient is limited to its value at 4,000 K, which is the upper limit of the range over which the constant was fitted by Pelevkin et al. [185].

3.10 Electronic Excitation Exchange

Electronic excitation exchange reactions are any collisional process in which more than one of the interacting species changes its electronic state without undergoing a chemical reaction or ionization. This definition excludes the direct excitation processes of HP-CIE and E-CIE. A general excitation exchange formula for which is given in Eq. (3.18), where A and B may be atoms or molecules. Electronic excitation exchange reaction rate coefficients are adopted from a variety of sources, and the adopted rate coefficients are listed in Table 3.15.

$$A(i) + B(k) \leftrightharpoons A(j) + B(l) \qquad : \; i \neq j, \; k \neq l \tag{3.18}$$

A constant cross-section is assumed for the reactions for which a temperature dependence has not yet been measured. The excitation exchange interactions can introduce strong couplings between excited state populations and are an important piece of the developed collisional-radiative model.

3.11 Charge Exchange and Reassociation Reactions

Charge exchange reactions involve the transfer of charge from one species to another. Reassociation reactions are those that involve simultaneous neutral exchange and charge exchange. A generic charge exchange reaction is given in Eq. (3.19), while the generic forms of a reassociation reaction involving atoms and diatoms are given in Eqs. (3.20) - (3.22).

$$A^+(i) + B(k) \leftrightharpoons A(j) + B^+(l) \tag{3.19}$$

$$AB^+(i) + C(k) \leftrightharpoons AC(j) + B^+(l) \tag{3.20}$$

$$AB^+(i) + C(k) \leftrightharpoons AC^+(j) + B(l) \tag{3.21}$$

$$AB(i) + C^+(k) \leftrightharpoons AC(j) + B^+(l) \tag{3.22}$$

The majority of charge exchange and reassociation reactions are implemented from the model of Park [1], and those reaction rate coefficients are not repeated here. Several charge exchange reac-

Table 3.15: Selected electronic excitation exchange reaction rate expressions ($k = AT^{\eta}\exp(-\theta/T_{tr})$).

Reaction	A (m^3/s)	η	θ	Ref.
$O_2(b) + O(^3P) \rightarrow O_2(X) + O(^1D)$	6.01×10^{-17}	-0.10	4,200	[131]
$O(^1S) + O_2(a) \rightarrow O(^1D) + O_2(b)$	2.08×10^{-18}	0.50	0	[137]
$O(^1S) + O_2(a) \rightarrow O(^3P) + O_2(A)$	7.51×10^{-18}	0.50	0	[137]
$O(^1D) + O_2(X) \rightarrow O(^3P) + O_2(a)$	5.79×10^{-20}	0.50	0	[131]
$O(^1D) + O_2(X) \rightarrow O(^3P) + O_2(b)$	2.60×10^{-17}	0	-67	[131]
$O(^1S) + O_2(X) \rightarrow O(^3P) + O_2(c)$	3.00×10^{-18}	0	850	[131]
$O(^1S) + O_2(X) \rightarrow O(^3P) + O_2(A)$	3.00×10^{-18}	0	850	[131]
$O(^1D) + O_2(b) \rightarrow O_2(X) + O(^1S)$	6.00×10^{-22}	0	6,731	[159]
$O(^1S) + O_2(a) \rightarrow O(^1D) + O_2(b)$	1.67×10^{-18}	0.50	0	[131]
$O_2(A) + O(^3P) \rightarrow O_2(X) + O(^1D)$	7.44×10^{-19}	0.50	0	[159]
$O_2(A) + O(^3P) \rightarrow O_2(a) + O(^1D)$	1.56×10^{-19}	0.50	0	[159]
$O_2(A) + O(^3P) \rightarrow O_2(b) + O(^1D)$	7.79×10^{-20}	0.50	0	[159]
$O_2(B) + O(^3P) \rightarrow O_2(A) + O(^1D)$	7.29×10^{-29}	2.15	20,782	[159]
$O_2(X) + N_2(A) \rightarrow O_2(b) + N_2(X)$	4.33×10^{-20}	0.50	0	[133]
$O_2(a) + O_2(a) \rightarrow O_2(b) + O_2(X)$	7.00×10^{-34}	3.80	-700	[131]
$O_2(A) + O_2(X) \rightarrow O_2(b) + O_2(b)$	1.68×10^{-20}	0.50	0	[159]
$O_2(A) + O_2(X) \rightarrow O_2(b) + O_2(X)$	1.68×10^{-20}	0.50	0	[159]
$O_2(A) + O_2(b) \rightarrow O_2(B) + O_2(X)$	5.62×10^{-23}	0.50	1,045	[159]
$Ar(4) + N_2(X) \rightarrow Ar(1) + N_2(C)$	1.67×10^{-18}	0.50	0	[186]
$Ar(2) + N_2(X) \rightarrow Ar(1) + N_2(C)$	1.67×10^{-18}	0.50	0	[186]
$N_2(A) + N_2(A) \rightarrow N_2(C) + N_2(X)$	5.54×10^{-10}	-2.64	0	[137]
$N_2(A) + N_2(A) \rightarrow N_2(B) + N_2(X)$	2.02×10^{-17}	0.50	0	[142]
$N_2(B) + N_2(A) \rightarrow N_2(X) + N_2(C)$	2.66×10^{-17}	0.50	0	[159]
$NO(X) + N_2(A) \rightarrow NO(A) + N_2(X)$	6.64×10^{-17}	0	0	[187]
$N_2(A) + N(^4S) \rightarrow N_2(X) + N(^2P)$	1.84×10^{-15}	-0.66	0	[131]
$N_2(A) + O(^3P) \rightarrow N_2(X) + O(^1S)$	1.73×10^{-12}	0.50	0	[133]
$O(^3P) + O(^3P) \rightarrow O(^1D) + O(^1D)$	6.10×10^{-18}	0.0158	46,044	[159]
$O(^1S) + O(^3P) \rightarrow O(^1D) + O(^1D)$[a]	5.00×10^{-17}	0.00	301	[131, 134, 188]

[a] Assuming that the measured $O(^1S) + O(^3P)$ removal rate is primarily due to the production of $O(^1D) + O(^1D)$ following discussions by Olson [188] and Bates [134].

tions have been implemented from other authors, particularly for charge exchange between N^+ and N_2^+, and reactions involving argon. The rate coefficient implemented for N^+ charge exchange with N_2 is taken from Phelps [189], which lies between the lower rate constant measured by Freysinger et al. [190] and the higher rate constant used by Park [1].

Table 3.16: Charge exchange reaction rate coefficients that do not come from Park [1] ($k = AT^{\eta}\exp(-\theta/T_{tr})$).

Reaction	A (m^3/s)	η	θ (K)	Ref.
$N^+ + N_2(X) \rightarrow N_2^+(X) + N(^4S)$	1.16×10^{-23}	1.47	13,130	[161, 189]
$Ar^+(1) + N_2(X) \rightarrow N_2^+(X) + Ar(1)$	2.57×10^{-17}	0.50	0	[143]
$Ar^+(1) + O(^3P) \rightarrow O^+ + Ar(1)$	6.39×10^{-18}	0.0	0	[159]
$Ar^+(1) + O_2(X) \rightarrow O_2^+ + Ar(1)$	-4.20×10^{-15}	-0.78	0	[5]

3.12 Bound-Bound Radiative Emission

Radiative transitions between two bound electronic levels of a molecule are referred to as bound-bound radiative emission. A generic bound-bound emission process is shown in Eq. (3.28), where $h\nu$ represents a photon with energy given by h, Planck's constant, and ν, the frequency of the emitted light. The species A may be an atom or molecule.

$$A(j) \rightarrow A(i) + h\nu \tag{3.23}$$

The source term due to bound-bound radiative transition for a pseudospecies in $\mathcal{P}_{ex}$ is given in Eq. (3.24),

$$\omega_{s(i)}^{bbr} = \sum_{j>i}^{N_{ex}} n_j A_{ij} \Lambda_{ij} - \sum_{j<i}^{i-1} n_i A_{ji} \Lambda_{ji} \tag{3.24}$$

where A_{ij} and Λ_{ij} are the Einstein coefficient and escape factor, respectively, for a radiative transition from an upper electronic state j to a lower state i of the species s. The transitions considered in the present model are given in Table 3.17.

Bound-bound radiative transitions for the molecular species are implemented using the vibrationally-resolved Einstein coefficients from Laux [191]. The vibrationally-resolved Einstein coefficients for the molecular systems are converted to an effective Einstein coefficient between the two electronic states, i and j, using Eq. (3.25) from Panesi et al. [192],

$$A_{ij} = \frac{\sum_{v'v''} A_{v'v''} Q_{v'}}{\sum_v Q_v} \tag{3.25}$$

where v' and v'' are vibrational state indices in the j and i electronic states, respectively, and $A_{v'v''}$

Table 3.17: Bound-bound radiative transitions considered in the CR model.

Species	Transition(s)	System	Ref.
O_2	$B^3\Sigma_u^- \rightarrow X^3\Sigma_g^-$	Schumann-Runge	[191]
N_2	$B^3\Pi_g \rightarrow A^3\Sigma_u^+$	First positive	[191]
	$C^3\Pi_u \rightarrow B^3\Pi_g$	Second positive	[191]
NO	$A^2\Sigma^+ \rightarrow X^2\Pi$	γ	[191]
	$B^2\Pi \rightarrow X^2\Pi$	β	[191]
N_2^+	$B^2\Sigma_u^+ \rightarrow X^2\Sigma_g^+$	First negative	[191]
O	119 lines	—	[67]
N	252 lines	—	[67]
Ar	102 lines	—	[67]

is the Einstein coefficient for transitions from v' to v''. The sum in the denominator is over v states in the upper, jth, electronic state.

For atomic species, all lines from the NIST database that involve the modeled states are included [67]. When the upper state for a given line is within a grouped state, the Einstein A coefficient is scaled by the ratio of the upper state electronic degeneracy to the total electronic degeneracy of its grouped state. This procedure is appropriate for the present model since all states in a given group are close in energy to one another. The resulting atomic lines are listed in Appendix B.

The escape factors for the molecular radiative transitions are all set to one, while those for the atomic lines are calculated using the analytical expression from Holstein [193, 194] for an infinite slab of thickness L_{rad} by assuming that Doppler broadening is the dominant broadening mechanism [8]. The expression for the escape factor is,

$$\Lambda_{ij} = \frac{1.875}{k_0 L_{rad} \left[\pi \log(k_0 L_{rad})\right]^{1/2}} \tag{3.26}$$

where L_{rad} is the thickness of the infinite slab, and k_0 is the absorption coefficient at the line center defined in Eq. (3.27).

$$k_0 = \frac{\lambda_{ij} n_i}{8\pi} \frac{g_j}{g_i} \frac{A_{ij}}{\sqrt{\pi}\nu_{0,s}} \tag{3.27}$$

The wavelength of the transition is λ_{ij}, the electronic degeneracies of the upper and lower states are g_j and g_i, and the number density of the lower state is n_i. The resonance frequency of a stationary

atom of species s, $\nu_{0,s}$, is defined as $\nu_{0,s} = (2k_B T_{tr}/m_s)^{1/2}$.

The three-dimensionality of radiation reabsorption introduces ambiguity in the choice of length scale L_{rad} to use for the escape factor calculation. Some authors model reabsorption in shock tube flows using the radial length scale, typically the diameter of the shock tube as in Nations et al. [58] and Finch et al. [9]. Other authors consider the axial direction to be most important, arguing that the reabsorption length scale should be representative of the length scale for mean flow gradients, roughly approximated using $L_{rad} = 1$ cm [195][1] . The effect of varying L_{rad} between these two limiting values is explored in Chapters 5 and 6.

3.13 Free-Bound Radiative Emission

Free-bound radiative emission involves the capture of an electron by an ion, followed by the neutralization of the ion. As opposed to three-body recombination, where the excess energy is carried off by the third particle, the excess energy in the two-body recombination of an ion and electron is carried off by an emitted photon. A generic free-bound emission process is shown in Eq. (3.28).

$$A^+(j) + e^- \rightarrow A(i) + e^- + h\nu \tag{3.28}$$

The pseudospecies source terms due to free-bound radiative transitions are given in Eqs. (3.29)–(3.30).

$$\omega^{fbr}_{s(i)} = n_e \times \begin{cases} \sum_{(i,j^+)\in\mathcal{T}^{fb}_s} k^{fbr}_{s(i,j^+)} n_{j^+} & \text{if } q_s = 0 \\ -\sum_{(j^0,i)\in\mathcal{T}^{fb}_s} k^{fbr}_{s(j^0,i)} n_i & \text{if } q_s = 1 \end{cases} \tag{3.29}$$

$$\omega^{fbr}_{s} = -n_e \times \begin{cases} \sum_{(i,1)\in\mathcal{T}^{fb}_N} k^{fbr}_{s(i,1)} n_{N^+} & \text{if } s \in \{N^+, O^+\} \\ \sum_{s\in\{\mathcal{H}\setminus\mathcal{I}\}} \sum_{(i,j^+)\in\mathcal{T}^{fb}_s} k^{fbr}_{s(i,j^+)} n_{j^+} & \text{if } s = e^- \end{cases} \tag{3.30}$$

where q_s is the charge of species s.

Free-bound radiative emission encompasses the two processes of radiative and dielectronic recombination, both of which result in the process shown in Eq. (3.28). Radiative recombination is

[1] B. Cruden, personal communication, August 2023

the exact process shown in Eq. (3.28), while dielectronic recombination is a two-step process that occurs via,

$$A^+(j) + e^- \rightarrow A^* \rightarrow A(i) + h\nu \tag{3.31}$$

where the electron is first non-radiatively captured to a bound-autoionizing state, A^*, that then radiatively decays to a neutral electronic level. Dielectronic recombination of N^+ and O^+ is modeled using the rate coefficients from Nussbaumer and Storey [196]. Radiative recombination of N^+ and O^+ is modeled using the rate expressions from Bourdon et al. [123, 104]. Radiative recombination of argon is modeled using the expression adopted by Vlcek [51] and later adopted by Bultel et al. [91] and Kapper and Cambier [7]. Following these same authors, the dielectronic recombination of Ar^+ is neglected. A summary of the total free-bound recombination rate coefficients is presented in Table 3.18.

Table 3.18: Free-bound radiative transition rate coefficients, the fitting variable t is defined as $t = \frac{T_{eex}}{10000}$. The first line of the N^+ and O^+ rate constants correspond to the contribution from dissociative recombination, while the second line accounts for radiative recombination.

$s^+(j)$	$s(i)$	$k^{fbr}_{s(i,j)}$ (cm^3/s)	Ref.
N^+	N	$10^{-12}\left[0.6310 + 0.1990t - 0.0197t^2\right] \times t^{-3/2} \exp\left(\frac{-0.4398}{t}\right)$	[196]
		$+ 7.64 \times 10^{-12} T_{eex}^{-0.40}$	[123]
O^+	O	$10^{-12}\left[\frac{-0.0001}{t} + 0.0001 + 0.0965t + 0.0193t^2\right] \times t^{-3/2} \exp\left(\frac{-0.4106}{t}\right)$	[196]
		$+ 2.12 \times 10^{-12} T_{eex}^{-0.29}$	[104]
$Ar^+(1)$	Ar(2)	$\exp\left[0.2426t - 35.84 + 0.3942\ln(t) + \frac{0.0152}{t} - \frac{2.549\times10^{-4}}{t^2}\right]$	[91]
$Ar^+(1)$	Ar(3)	$\exp\left[0.2420t - 36.89 + 0.3894\ln(t) + \frac{0.0158}{t} - \frac{2.661\times10^{-4}}{t^2}\right]$	[91]
$Ar^+(2)$	Ar(4)	$\exp\left[0.2427t - 37.67 + 0.3944\ln(t) + \frac{0.0151}{t} - \frac{2.546\times10^{-4}}{t^2}\right]$	[91]
$Ar^+(2)$	Ar(5)	$\exp\left[0.2420t - 35.52 + 0.3876\ln(t) + \frac{0.0161}{t} - \frac{2.701\times10^{-4}}{t^2}\right]$	[91]

Following Kapper and Cambier [7], the gas is assumed to be optically thick to emission from the free-bound recombination to form Ar(1) and optically thin to emission via radiative recombination that forms Ar(i=2,3,4,5). For this reason, the recombination rate coefficient to form

Ar(1) is not provided in Table 3.18. Emission from radiative and dielectronic recombination to form N and O is assumed to fully escape the gas.

3.14 Summary

In this chapter, the electronic state-resolved model of N_2-O_2-Ar mixtures was described in detail. A large number of collisional and radiative processes are required to accurately model the nonequilibrium excitation and ionization dynamics in a high-temperature gas mixture containing air species and argon.

Each section in this chapter was devoted to a different collisional or radiative process occurring in the gas. The modeling of coupled vibrational relaxation and dissociation was discussed first, with the Marrone and Treanor and modified Marrone and Treanor (MMT) modeling frameworks being adopted in the model. Dissociation rate coefficients for the ground and electronically excited states were then outlined for N_2, O_2, and NO, leveraging the available electronically-specific rate coefficients for each species that have been published by several authors.

Collisional excitation and ionization processes were discussed next. Electron impact excitation and ionization were modeled using integrated energy-dependent cross-sections spanning from threshold to several hundred electron volts for the majority of key electron impact processes. The remainder of electron impact excitation and ionization processes were modeled using analytical expressions. Rate coefficient or cross-section data is far more scarce for modeling excitation and ionization by heavy particle impact. The available data was collected and reviewed, and the selected rate expressions were described.

Associative ionization was modeled using rate coefficients that separately take into account the interaction of ground state and excited state atoms. Rate coefficients corresponding to an equilibrium distribution of electronically excited states were found to compare reasonably with other rate coefficients published in the literature. The adopted rate coefficient expressions for neutral exchange, electronic excitation exchange, and charge exchange were also given. Finally, the modeling of radiative emission and the self-absorption of resonance radiation was discussed.

Chapter 4

Two-Temperature Modeling of Coupled Vibrational Relaxation and Dissociation of O_2

The contents of this chapter have been included in the ***Journal of Thermophysics and Heat Transfer*** *[109]. Reproduced with the permission of the American Institute of Aeronautics and Astronautics.*

4.1 Introduction

The dissociation of O_2 is the first step toward plasma formation behind a strong shock wave in air because atomic oxygen is a key reactant in the associative ionization to form NO^+, the dominant ion at suborbital hypersonic speeds. In addition, atomic oxygen is a necessary reactant for the formation of NO via the first Zel'dovich reaction:

$$N_2 + O \leftrightharpoons NO + N \tag{4.1}$$

which offers a lower activation energy path, compared to the direct dissociation of N_2, to the formation of nitrogen atoms that are also required to form NO^+. At suborbital hypersonic speeds, the formation of atomic nitrogen is therefore dominated by Zel'dovich exchange reactions and by the dissociation of NO, which has a weaker bond than N_2.

In addition to its importance to plasma formation modeling, the dissociation of O_2 is critically important to predictions of vehicle heat flux in non-ionizing hypersonic flows. In a sensitivity analysis performed by Holloway and Boyd, the rate constants for the dissociation of O_2 in collisions

with O and N_2 were found to be the most important chemical kinetic parameters influencing heat flux to a cylindrical geometry in a Mach 5 and 7 freestream flow [197]. In their comparison of heat flux predictions by the Park and MMT models, Chaudhry and Boyd found that the greatest differences could be attributed to the recombination of O_2 with partner N_2, which is largely a function of the adopted dissociation rate constant for O_2 with N_2.

Recent low-uncertainty experimental measurements of the coupled vibrational relaxation and dissociation of O_2 by Streicher et al. [5] from the Hanson Group at Stanford University provide a valuable opportunity to assess the modeling of the nonequilibrium dissociation kinetics of O_2. The present chapter is devoted to the analysis of these experiments using several two-temperature models in order to yield conclusions that are most relevant to vehicle-scale hypersonic flows. Because the developed collisional-radiative model relies on multi-temperature modeling of dissociation, not resolving the individual vibrational or rovibrational states, the conclusions from this chapter are immediately applicable to the collisional-radiative model that is applied throughout this thesis.

In this chapter, comparisons are made with three of the pure O_2 shock tube experiments reported by Streicher et al. [5]. Nominal initial translational temperatures ($T_{5,0}$) and pressures ($P_{5,0}$) behind the reflected shock are given in Table 4.1. The value of $P_{5,0}$ was measured 5 mm from the end wall at the measurement location. It is important to note that the reflected shock velocity is not measured in these experiments – the values in Table 4.1 are calculated using the measured incident shock velocity, extrapolated to the wall, and the no penetration end wall boundary condition. The reported values of $T_{5,0}$ are calculated from ideal theory by assuming a constant reflected shock velocity with frozen composition and vibrational temperature in Region 2. Pressure is directly measured during the tests, making $P_{5,0}$ and dP/dt some of the most direct measurements from the experiments.

In these experiments, laser absorption spectroscopy (LAS) is used to infer vibrational state-specific time histories of O_2. The raw data from each experiment includes the measured intensities, pressure at the x-location where the laser beam is located, and incident shock velocity determined using five piezoelectric pressure transducers. The transmitted laser intensities are used to deter-

Table 4.1: O_2 vibrational relaxation and dissociation experiments from [5] that are analyzed in the present study.

Name	$T_{5,0}$ (K)	$P_{5,0}$ (Pa)	dP/dt (Pa/μs)
100-1	6,230	7,599	13
100-6	7,940	5,466	20
100-8	9,560	4,533	32

mine absorbances, which are then converted to quantum state-specific number densities via the Beer-Lambert law and the absorption cross-section models described in [198, 199]. Time-zero uncertainties due to shock curvature and the finite beam width are estimated to be less than 2 μs for the experiments analyzed here. A complete description of the experiments, diagnostics, post-processing techniques, and uncertainty analysis can be found in [5].

4.2 Evaluation of Three-Step Reflected Shock Modeling Approach

The first goal of the work presented in this chapter is to assess the accuracy of the space-marching approach presented in Section 2.3.2 for modeling reflected shock experiments in pure O_2. To do this, unsteady one-dimensional CFD simulations are performed using LeMANS – a mature hypersonic CFD code originally developed at the University of Michigan and now at the University of Colorado [24]. A complete description of the code can be found in Ref [200]. Simulations for the present work are carried out using a second-order accurate finite volume spatial discretization and first-order explicit forward Euler time integration.

The unsteady simulation is performed on a 5.25-meter domain with $x \in [-5, 0.25]$ m. No penetration wall boundary conditions are applied at both ends of the domain. The initial condition is chosen to form an incident shock $x = 0$ and $t = 0$ with some desired velocity. Using shock tube nomenclature, this means that Region 2 properties are assigned for $x \in [-5, 0]$ while Region 1 properties are assigned for $x \in [0, 0.25]$. The Region 2 properties are calculated using the desired shock velocity and the Rankine-Hugoniot relations for a chemically and vibrationally frozen gas. Numerical difficulties associated with the contact wave are avoided by considering only the driven

gas and initializing the simulation with the already-formed shock at $x = 0$. The length of the domain in the $x < 0$ direction is selected to ensure that the expansion wave originating from the left end wall does not interact with the reflected shock during the simulated test time.

Conditions from the 100-8 experiment are used to assess the present modeling approach. This case exhibits the strongest nonequilibrium effects and is, therefore, expected to show the most significant reflected shock deceleration. The incident shock velocity attenuates by roughly 3% due to numerical dissipation, so the initial condition is adjusted to produce a slightly stronger incident shock at $t = 0$. The adopted initial condition produces the desired 2,760 m/s incident shock velocity at the right end wall. Calculations are performed using the standard 2T model of Park [1]. For the same experiment, the LeMANS simulation takes 360 times longer to execute than the corresponding space-marching calculation.

The first model prediction assessed is the reflected shock velocity. Figure 4.1 shows reflected shock velocity profiles computed by LeMANS and by the space-marching code used in the present study. The shock is located in the CFD flowfield by finding the maximum value of the pressure gradient at each timestep. The shock velocity is then calculated using a first-order finite difference of the shock position at each timestep. The LeMANS values of u_{rs} plotted in Figure 4.1 are the moving average of five points since the raw shock velocities are scattered across only a handful of values due to the discrete nature of the grid. Shock velocity predictions are also shown from the space-marching method employed in [61, 35], where the gas is assumed to be stagnated at the measurement location. Both space-marching approaches use the same model for the reflected shock velocity between the wall and the measurement location; however, the present approach abandons the assumption of stagnated flow at the measurement location and attains much better agreement with the CFD as a result. Shock velocity is predicted within 10% of the CFD solution using the present approach, a significant improvement over the 30% errors obtained using the previous approach that assumes $u_5(x = d) = 0$.

There is a slight but persistent overprediction of the reflected shock velocity predicted by the space-marching technique when compared with the LeMANS solution. The observed overprediction

arises because Region 2 relaxation is not included when calculating shock velocity in the space-marching method, while LeMANS does include the effect. The slight suppression of the late-time reflected shock velocity caused by Region 2 relaxation is consistent with a previous analysis by Presley and Hanson [63].

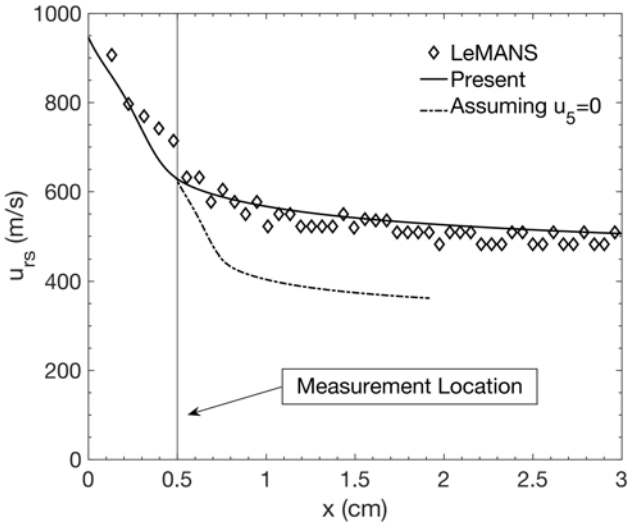

Figure 4.1: Comparison of reflected shock velocity profiles computed by unsteady CFD and space-marching codes.

Throughout the simulated 100-8 experiment, the reflected shock decelerates to approximately half its initial velocity. The lab frame shock velocity drops by 280 m/s as it travels from the wall to the measurement location, resulting in a roughly 10% reduction of the shock velocity measured in the moving reference frame of the Region 2 gas. The result is that T_{tr} at the measurement location is 1,200 K less than the value predicted without accounting for shock deceleration. This effect is important to include when modeling reflected shock experiments in non-dilute gasses.

The VT relaxation time for O_2-O_2 collisions was extracted from the experiments analyzed here using the assumption of a constant reflected shock velocity. The inferred relaxation time was found to be slower than most of the formulations available in the literature [5]. Accurately accounting for the non-constant reflected shock velocity pushes the inferred $\tau_{O_2-O_2}$ closer to the other values reported in the literature by lowering the value of T_{tr} associated with each data point.

Additionally, if T_{tr} is lower than the experimentalists predicted, the numerator of the Landau-Teller expression would be smaller, and the inferred relaxation time would appear slower as a result. While the magnitude of these effects on the inferred values of $\tau_{O_2-O_2}$ are hard to quantify, the present study can assess whether the experimental measurements are still reasonably reproduced using the inferred relaxation times and dissociation rate constants.

It is important to note that after passing the measurement location, the shock still decelerates by an additional 180 m/s. This means that gas will move into the measurement location that was processed by a weaker shock than the gas located at $x = d$ when the test time began. Using the LeMANS solution, pathlines of particles located at $x = d$ are traced back to see when they passed through the reflected shock. Owing to the low velocity of the Region 5 gas, the particles entering the measurement location are never shocked more than 4 μs after the shock passed $x = d$. This observation is in line with the arguments of Streicher et al., who reasoned using simple arguments that the timing uncertainty due to non-stagnated gas should not exceed 5 μs [5]. Tracing back particle pathlines, it is also possible to determine the difference in shock velocity and peak translational temperature experienced by the particles in the measurement location at a given time. For the case analyzed here, which is believed to experience these effects most severely, these quantities are different by -32 m/s and -98 K, respectively, by the end of the test time.

Figure 4.2 shows the evolution of the translational and vibrational temperatures at the measurement location. Excellent agreement is observed between the present space-marching method and the LeMANS solution. Relaxation appears to proceed much more quickly when the gas is assumed to be stagnated at the measurement location. This occurs because of the underpredicted shock velocity, which affects the transformation from the distance behind the shock to t_{lab}.

Peak vibrational temperature is expected to be slightly lower in LeMANS than in the space-marching code. The space-marching code initializes the gas to a slightly higher translational temperature than the particles entering the measurement location after $t = 0$ have experienced. This effect is expected to be slight, given the maximum 98 K difference in peak T_{tr}, and it is probably not observed because of incident shock attenuation in the LeMANS simulations.

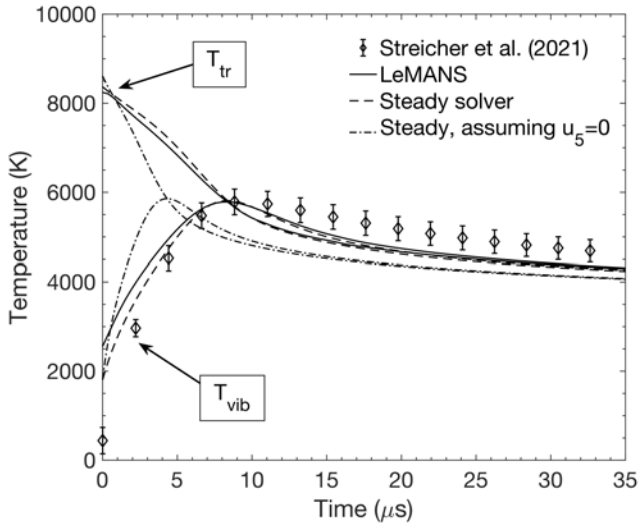

Figure 4.2: Comparison of temperature evolution at the measurement location predicted by LeMANS, the space-marching approaches, and experimental measurement for the 100-8 case ($T_{5,0} = 9,560$ K)

It is worth noting that the pressure at the measurement location predicted by the space-marching approach is slightly higher than the corresponding pressure predicted by LeMANS. The difference is 3% near time-zero and grows to 8% by the end of the test time. The different pressure predicted by LeMANS is most likely due to its ability to capture the full unsteady pressure field behind the decelerating reflected shock. Finally, both modeling approaches underpredict $P_{5,0}$ by approximately 15% relative to the measured value, indicating that the higher pressure observed in the experiment is likely a result of multidimensional and viscous effects not included in the 1D inviscid CFD calculation.

The second aim of the work presented in this chapter is to assess the available models for the vibrational relaxation and dissociation of O_2 with partners O_2 and O. The conditions of the experiments that are analyzed in the present study are given in Table 4.1. The experiments are modeled using the procedure described in Section 2.3.2. A large set of vibrational relaxation times, vibration-dissociation coupling models, and dissociation rate constants are assessed. These models are described in Sections 4.3.1, 4.3.2, and 4.3.3, respectively. The comparison of these models with experiment is then presented in Section 4.4.

4.3 Overview of Assessed Two-Temperature Modeling Choices

4.3.1 Vibrational Relaxation Times

Numerous vibrational relaxation times are available in the literature for O_2 with partners O_2 and O. The current study assesses three sets of relaxation times: the empirical formula from Millikan and White [2], the full ab initio relaxation times of Grover et al. [201, 77], and the experimentally inferred O_2-O_2 relaxation time from [5].

Most hypersonic CFD codes employ the two-parameter function for $p\tau_v$ devised by Millikan and White [2] with the fitting parameters tabulated by Park [1]. For O_2-O_2, Park's fitting parameters are calculated using Millikan and White's empirical formula. For O_2-O, Park's parameters come from fitting the experimental data published by Kiefer and Lutz for experiments covering 1,600 K to 3,300 K [202]. Millikan and White's formula with the parameters advocated by Park will be called the "modified Millikan & White (M&W)" relaxation set. Park's high-temperature correction is also applied whenever the modified M&W relaxation set is used [1].

Ab initio relaxation times for O_2 with partners O_2 and O have been determined by Grover et al [201, 77]. These relaxation times were calculated using the direct molecular simulation (DMS) method, where the only inputs are the relevant potential energy surfaces (PES). These relaxation times represent the best available modeling of O_2 relaxation using only first principles.

The third set of relaxation times was determined directly by Stanford from their experiments currently being analyzed [5]. A relaxation time expression for O_2-Ar was determined from previous dilute O_2-Ar experiments, and for O_2-O_2 from more recent non-dilute experiments. No fit for O_2-O was derived from the experimental data, owing to the low sensitivity of the measurements to this parameter. Relaxation times fitted from of Grover et al. [77] are used for O_2-O interactions whenever the Stanford relaxation times are used for O_2-O_2 interactions.

4.3.2 Vibration-Dissociation Coupling Models

There are multiple ways to model the two-way coupling between vibrational relaxation and dissociation, and a review of several leading approaches is given in Section 3.3.1. In this chapter, four different vibration-dissociation coupling models are assessed. The Park model with nonpreferential vibrational energy change per dissociation is included because it is the most widely adopted vibration-dissociation coupling model. The controlling temperature for the dissociation rate constant is set to $\sqrt{T_{tr}T_{vib}}$ whenever the Park model is used [1]. The next model being assessed is the Marrone and Treanor model. Based on the findings of Streicher et al. [5], only the value $U = \frac{1}{3}k_B D_{0,O_2(X)}$ is tested. The other two models are based on the modified Marrone and Treanor (MMT) framework, either with or without the variable non-Boltzmann correction factors. When the correction factors are neglected, the model is denoted as MMT-B. When the factors are included, the model is referred to as MMT-VNB.

4.3.3 Dissociation Rate Constants

There are also a variety of dissociation rate constants available in the literature; three different sources are used in the present study. First, there are the rate constants presented by Park [1] that are used in most hypersonic CFD codes. Next, there are the rate constants inferred from the Stanford experiments [5]. Finally, there are the rate constants that accompany the MMT model [12].

The dissociation rate constants that accompany the MMT model are only valid for the dissociation of O_2 in its ground electronic state. For O_2 dissociation with partner O, the effect of electronically excited O_2 is often approximated by scaling the reaction rate constant by a "multi-surface correction factor", η. This factor is approximated by assuming that the dissociation rate constant of electronically excited O_2 is governed by the same Arrhenius parameters as O_2(X), just with the threshold reduced by the excitation energy of that state. This approximation, combined with an assumption of Boltzmann populated electronic states with energies below the dissociation

limit, yields a value of η=16/3. This can be considered the upper bound of η. If only the low energy excited states of O_2 are assumed to be Boltzmann populated, then this factor becomes 6/3. A thorough discussion of these factors and their derivation can be found in [203]. The effect of using these correction factors, or no factor at all, is assessed.

4.4 Comparison with Experiment

The 100-8 case has the strongest nonequilibrium conditions of the pure O_2 cases. As a result, the largest number of models are evaluated for this case. Table 4.2 shows the root mean square error (RMSE) of the relative differences between simulation and experiment for the variety of 2T models that are run for this case. RMSE is calculated considering all data points after 2 μs, which is chosen based on the experimental time-zero uncertainty [5]. The RMSE for each variable is normalized by the experimentally measured value, as shown in Eq. (4.2).

$$RMSE(\phi) = \sqrt{\sum_{t=t_{min}}^{t_{end}} \left(\frac{\phi_{sim}(t) - \phi_{exp}(t)}{\phi_{exp}(t)} \right)^2} \tag{4.2}$$

These models are sorted in order of ascending RMSE for T_{vib} because this is the most relevant variable for the overall model assessment. Vibrational temperature is more sensitive to the nonequilibrium kinetics under investigation than number density, which can also be affected by total density errors arising from incorrect T_{tr}. The influence of temperature errors on the predicted n_{O_2} can be mitigated by ordering the models based on T_{vib} errors since accurate predictions of T_{tr} are expected to follow from accurate T_{vib} predictions. Note that the RMSE values for T_{vib} are artificially large due to large discrepancies at early times that arise because of the assumed 296 K initial value of T_{vib}.

Experimentally derived n_{O_2} time histories provide additional information that is valuable for distinguishing models that predict T_{vib} with similar accuracy. For the 100-8 experiment, the uncertainties on the n_{O_2} time histories are scaled up by 60% from the originally reported values based on propagating a $\pm$700 K uncertainty on $T_{tr}(t = 0)$, motivated by the lower initial T_{tr}

predicted in the present study, through the experimental data processing pipeline[1] . This scaling is included when calculating the RMSE values presented in Table 4.2. None of the models accurately predict the inferred number density of O_2 throughout the entire test time of the 100-8 experiment – the minimum RMSE of n_{O_2} is 13.55%. However, some of the models perform much better than others, enabling conclusions to still be drawn from comparisons with the n_{O_2} data. The present study relies primarily on T_{vib} time histories for the bulk of model comparisons, with n_{O_2} providing additional information when needed.

Table 4.2: Comparison of the various 2T model results for the 100-8 case.

Rate Constant Set	Coupling Model	Relaxation Set	RMSE of T_{vib} (%)	RMSE of n_{O_2} (%)
MMT	MMT-B	Stanford	5.83	14.91
Stanford	MMT-B	Stanford	6.09	15.16
Stanford	Park Nonpref.	Stanford	6.29	19.17
MMT w/ 16/3	MMT-B	Stanford	6.35	15.67
MMT w/ 16/3	MMT-VNB	Stanford	6.49	13.90
Stanford	MT	Stanford	6.68	16.27
Stanford	MMT-VNB	Stanford	7.26	13.55
MMT w/ 6/3	MMT-VNB	Stanford	9.04	13.64
MMT	MMT-VNB	Stanford	10.11	13.57
Stanford	Park Nonpref.	Grover et al.	12.00	22.60
Stanford	MT	Grover et al.	12.23	18.55
Stanford	MMT-VNB	Grover et al.	13.01	16.14
Stanford	Park Nonpref.	Modified M&W	14.21	23.22
MMT w/ 16/3	MMT-VNB	Modified M&W	14.31	18.47
MMT	MMT-VNB	Grover et al.	14.42	16.01
Stanford	MT	Modified M&W	14.42	20.46
Park	Park Pref.	Modified M&W	14.63	23.63
Stanford	MMT-VNB	Modified M&W	14.76	18.10
Park	Park Nonpref.	Modified M&W	15.31	24.81
MMT	MMT-VNB	Modified M&W	16.11	17.96

There are multiple important observations to be made from Table 4.2 about the performance of the various 2T models. Most obviously, the Stanford relaxation times outperform the two other options that are tested. This is explained by the much slower O_2-O_2 relaxation time derived from the experiments [5]. Using the Stanford O_2-O_2 relaxation time significantly improves agreement at early times. Figure 4.3a shows an example of the T_{vib} evolution predicted by the three relaxation

[1] J. Streicher, personal communication, August 2022

times. Note that the Stanford relaxation time was derived from the experiments being analyzed, so the present result is not unexpected. However, agreement using the experimentally derived model parameters is not guaranteed due to the different assumptions used in the present validation effort.

The researchers in [5] assumed that the flow remains vibrationally and chemically frozen behind the incident shock during the entire experiment. Hence, the best-fit simulations used to infer 2T model parameters from the experimental data are initialized with $T_{vib} = 296$ K. As seen in Figure 4.3a, the initial value of T_{vib} is roughly 2,000 K when Region 2 vibrational relaxation is considered. This leads to significant disagreements with the measured data at early times for all models tested. Interestingly, the experimentally inferred relaxation time still performs best, even when accounting for the higher initial T_{vib} and lower initial T_{tr} predicted by the current modeling method. Both of these changes to the initial condition weaken the vibrational relaxation source term, but the present results show that the Stanford $\tau_{O_2-O_2}$ is still consistent with the T_{vib} time histories when the initial condition is more accurately computed. Of course, there are differences between the model and experiment at $t = 0$ that persist regardless of the model. Recall that the experimental data is derived from a best-fit simulation using the measured absorbance. At early times (t$\leq 2\mu s$), the absorbance is very low, so the best-fit simulation prediction of T_{vib} is primarily a function of the chosen initial condition during that period[2] . As a result, disagreements at $t = 0$ should not be interpreted as indicative of model failure in the present context.

With the Stanford relaxation times emerging as the clear preference, the next step is to evaluate models for the nonequilibrium dissociation process. Here, the preferred models are less clear. Unlike the relaxation time, which primarily influences the early T_{vib} time history, the rate constant set and coupling model both influence the T_{vib} time history after peak T_{vib}. In this case, the n_{O_2} time histories provide further essential insights for the parametric assessment.

Figure 4.3b shows results obtained using the various vibration-dissociation coupling models alongside the Stanford rate constant and relaxation sets. The MMT-B model predicts T_{vib} at the lower edge of the experimental uncertainty, while the MMT-VNB model predicts T_{vib} just above

[2] Private communication with J. Streicher

the upper experimental uncertainties. This difference is due to the suppressed dissociation rate and vibrational energy loss when the non-Boltzmann correction factors are used.

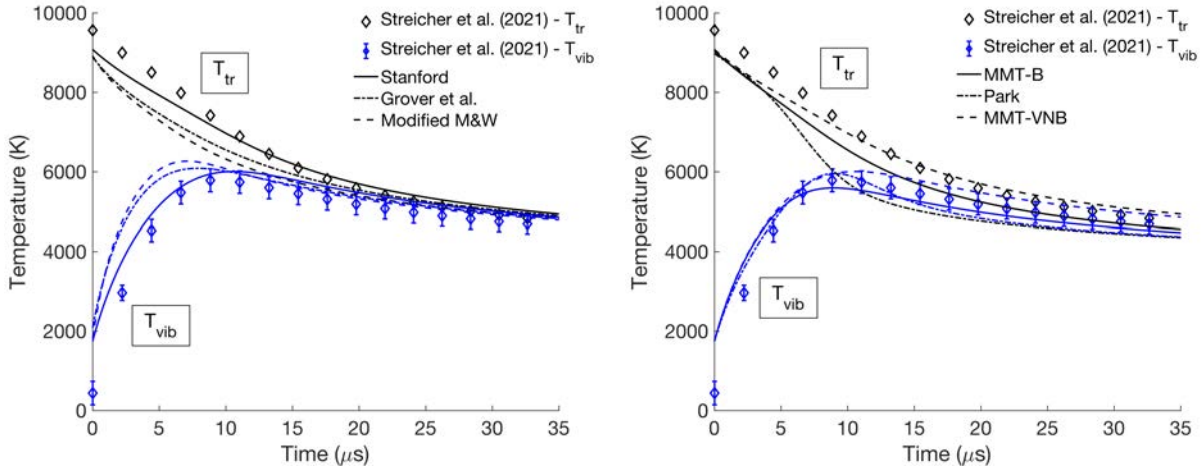

(a) (b)

Figure 4.3: (a) Comparison of predictions using different relaxation times for the 100-8 case ($T_{5,0}$=9,560 K). The Stanford rate constants with MMT-VNB coupling are used for the three simulations. (b) Comparison of nonequilibrium coupling models. Stanford rate constants and relaxation times are used for these three simulations.

The Park coupling models perform reasonably well at predicting T_{vib}; however, this comes at the expense of accurate n_{O_2} predictions. Within the results of each relaxation set, Park's coupling models yield the worst RMSE of n_{O_2} time histories. The Park rate constants also perform poorly. When the Park rate constants and coupling model are put together, neither experimentally inferred time history is accurately predicted. These results are expected based on comparison with the experimentally inferred nonequilibrium coupling factor, vibrational energy change per dissociation, and O_2-O dissociation rate constant [5].

The use of a multisurface correction factor for the MMT value of k_{d,O_2-O} improves agreement with experiment whenever the MMT-VNB coupling model is used. This is shown graphically in Figure 4.4. While the n_{O_2} RMSE increases slightly with η, the RMSE of T_{vib} decreases significantly with increasing η. These results indicate that η=16/3 is the most consistent with experiment when used alongside the MMT-VNB coupling model. In contrast, the use of η makes predictions worse

if the MMT-B coupling model is used. Thus, it is recommended to use $\eta = 16/3$ with the MMT-VNB coupling model for conditions similar to the 100-8 experiment. Notably, a similar level of agreement is also obtained via the MMT-B model if $\eta = 1$. It is unclear which combination of choices is representative of the true physics since both model combinations yield T_{vib} predictions within the experimental uncertainties for t >10 μs. Either the O_2-O dissociation rate constant is roughly 5 times stronger than the MMT rate constant suggests, or the VNB coupling model is overcorrecting for QSS reductions of $\langle \epsilon_{vib} \rangle_d$ and Z late in the test time. The true story is likely some combination of these effects.

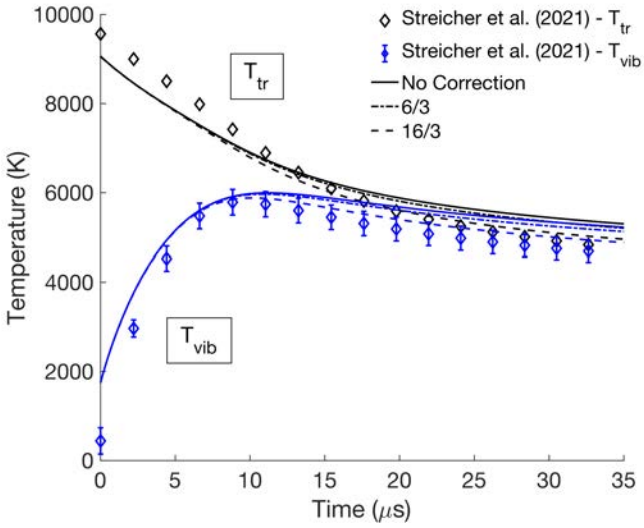

Figure 4.4: Temperature evolution predicted using various options for the multisurface correction factor on k_{d,O_2-O} for the 100-8 case ($T_{5,0}$=9,560 K).

Finally, it is worthwhile to compare the Park and MMT models directly since these are both available for use in widely used hypersonic CFD packages like LeMANS and US3D. Within those codes, the Park and MMT rate constants and coupling models are used alongside the Modified M&W relaxation set [24, 12]. Predictions from the two models for the 100-8 case are compared in Figure 4.5. For this experiment, the MMT model clearly outperforms the Park model.

Following the model assessment using the 100-8 experimental data, a reduced set of models is run for the 100-1 and 100-6 cases. The reduced set of models is listed in order of increasing

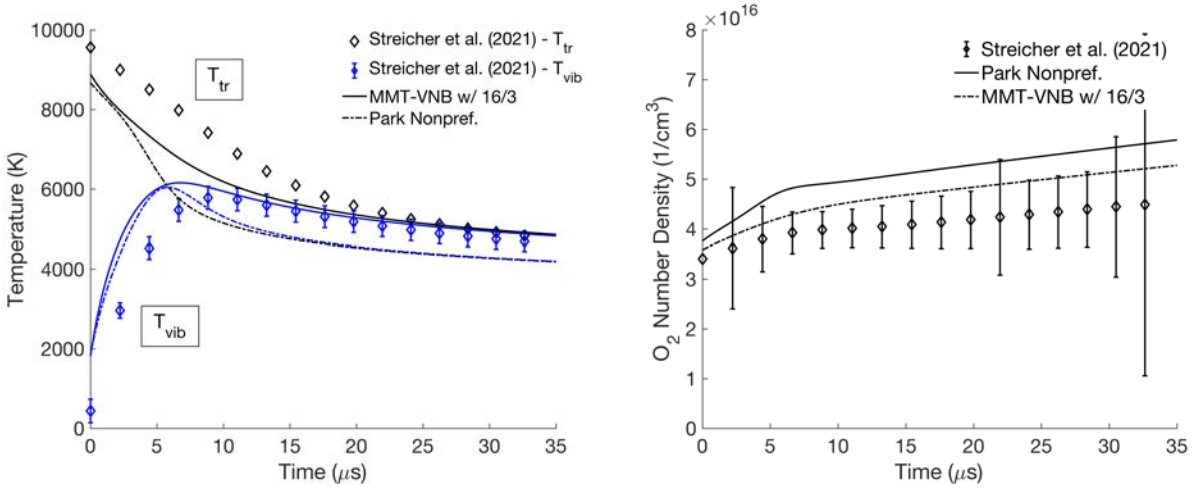

Figure 4.5: Comparison of model predictions by the nonpreferential Park model with MMT-VNB predictions for the 100-8 case ($T_{5,0}$=9,560 K). Modified M&W relaxation times are used in both the Park and MMT simulations, following the standard implementation of those models [1, 12]

T_{vib} RMSE in Table 4.3 for the 100-1 experiment. The Stanford relaxation time is still the best option for this case, producing T_{vib} predictions that are the most consistent with the measured data. For this lowest temperature experiment, the non-Boltzmann correction to the MMT model significantly increases the RMSE of T_{vib} when compared to the Boltzmann form of the model. Finally, it is important to note that the Park model performs far better for the 100-1 case than for 100-8, although it still does not match the experimental time histories within the measurement uncertainties. A comparison of Park's model with the Boltzmann and non-Boltzmann variants of MMT is shown in Figure 4.6 for both the 100-6 and 100-1 experiments.

Table 4.3: Comparison of a reduced set of 2T model results for the 100-1 case ($T_{5,0}$=6,230 K).

Rate Constant Set	Coupling Model	Relaxation Set	RMSE of T_{vib} (%)	RMSE of n_{O_2} (%)
Stanford	MMT-B	Stanford	2.93	1.34
MMT w/ 16/3	MMT-B	Stanford	4.10	1.78
Park	Park Pref.	Modified M&W	6.06	6.72
Park	Park Nonpref.	Modified M&W	6.26	7.33
Stanford	MMT-VNB	Stanford	6.38	2.53
MMT w/ 16/3	MMT-VNB	Stanford	8.83	3.23
MMT w/ 16/3	MMT-VNB	Modified M&W	9.41	3.06
MMT w/ 16/3	MMT-VNB	Grover et al.	10.15	3.13

The MMT-B model outperforms the MMT-VNB model for both the 100-1 and 100-6 cases. For all three cases, T_{vib} trends progressively higher than the experimental measurements at late times whenever the MMT-VNB coupling model is used. In contrast, the Boltzmann form of the model predicts the late-time behavior fairly well for the 100-1 and 100-6 cases. Such a pattern could be explained by a gradual weakening of the QSS depletion of k_d and $\langle \epsilon_{vib,O_2(X)} \rangle_d$ as time elapses. Currently, the non-Boltzmann correction factor for the dissociation rate constant goes to its equilibrium limit of 1.0 at chemical equilibrium. The present results indicate that the current blending may not be accurate, at least for the conditions of these shock tube experiments. It is also possible that the correction should be smaller for the weaker nonequilibrium conditions of the 100-1 and 100-6 experiments.

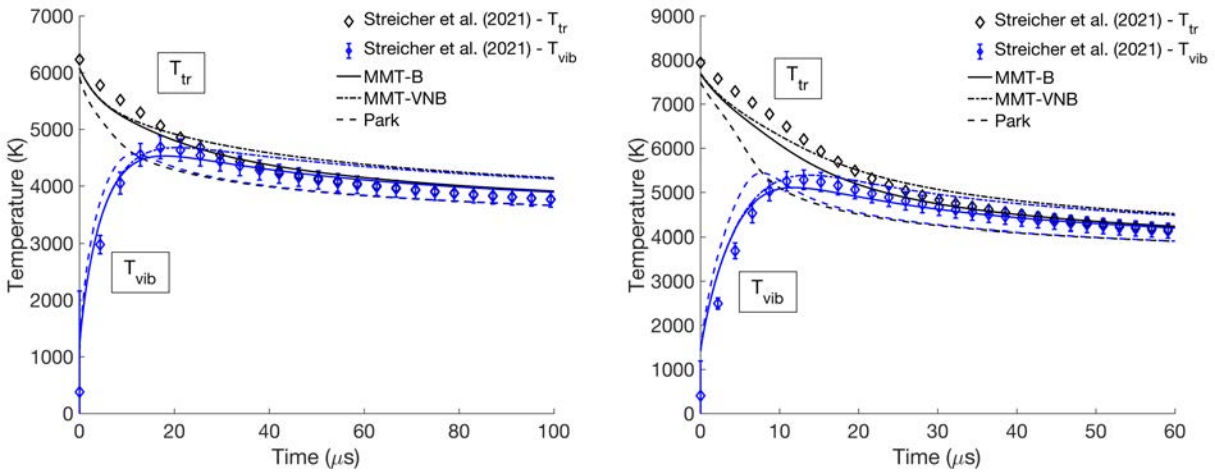

(a) 100-1 ($T_{5,0}$=6,230 K) (b) 100-6 ($T_{5,0}$=7,940 K)

Figure 4.6: Comparison of predictions by MMT-B, MMT-VNB, and Park's model. MMT is run with the 16/3 correction factor on k_{d,O_2-O} and the Stanford relaxation set. The Park model is run using the modified M&W relaxation set.

4.5 Summary

An assessment of two-temperature model parameters for the coupled vibrational relaxation and dissociation of shock-heated oxygen was presented in this chapter. The assessment is based

on recent low-uncertainty experimental measurements of O_2 vibrational temperature and number density in a series of reflected shock experiments performed at Stanford University. To enable a confident comparison of model predictions with measured experimental data, the adopted modeling approach for reflected shock experiments was first benchmarked through comparison with an unsteady computational fluid dynamic simulation. The flow modeling approach accurately predicted the flow evolution at the measurement location, even in conditions where the reflected shock was decelerating strongly. It was found that reflected shock deceleration can reduce the initial translational-rotational temperature at the measurement location by over 1,000 K from its nominal value. Thus, reflected shock deceleration should be included when interpreting future experiments where the test gas undergoes significant density change.

In general, the two-temperature modeling approach due to Park was not consistent with the measured data, particularly at high temperatures. The newly developed modified Marrone and Treanor (MMT) model was overall more consistent with the measured data. The adoption of non-Boltzmann correction factors in the MMT model improved agreement with the data at high temperatures but not at low temperatures, indicating that the accuracy of the non-Boltzmann corrections at low temperatures should be assessed further. Finally, in spite of the lower initial temperatures predicted by the adopted modeling approach, the O_2-O_2 vibrational-translational relaxation time originally inferred from the experimental data was still more consistent with the measured data than the other relaxation time expressions that were tested.

Chapter 5

Electronic State-Resolved Analysis of Weakly Ionized Oxygen Mixtures

5.1 Introduction

In this chapter, the nonequilibrium electronic excitation of atomic oxygen is studied through detailed comparisons with shock tube experimental data. The nonequilibrium electronic excitation of atomic oxygen is of particular interest since atomic radiation is a major contributor to vehicle heating during high-speed Earth entry. In addition, and as previously discussed, atomic electronic excitation is an essential precursor to the formation of free electrons behind strong shock waves in air [40].

The study presented in this chapter is motivated by recent measurements of electronically excited oxygen atoms in O_2-Ar shock tube experiments [58, 59, 6, 60] that provide a unique and valuable opportunity to study the excitation and ionization kinetics of highly-excited oxygen atoms. The experiments have previously been studied using simplified electronic state-resolved models; however, these models lacked the necessary fidelity to fully describe the system behavior. In this Chapter, the experiments are studied using the collisional-radiative model described in Chapters 2 and 3, which was developed following a comprehensive review of the rate parameters available to model each process. The developed model enables an in-depth study of the observed excitation dynamics, improving upon the current understanding of excited state oxygen kinetics and informing the interpretation of future excited state measurements.

5.2 Comparison with Experiment

5.2.1 Description of Experiments

The collisional-radiative model is assessed using a selection of the shock tube experiments presented in [58, 59, 6, 13, 60]. The conditions of the analyzed experiments are listed in Table 5.1. The Streicher, Nations, and Li experiments were all performed in the same shock tube with an inner diameter of 15.24 cm, while the Minesi data was measured in a different shock tube with a 10.32 cm inner diameter. Data from the Nations-16 experiment was measured using cavity-enhanced absorption spectroscopy (CEAS), while the Streicher-20, Li-20, Li-21, and Minesi experiments used single-pass laser absorption spectroscopy (LAS). In all experiments, the measured absorbances were used to infer quantum state-specific number density time histories. In addition, T_{tr} is inferred from the Doppler broadening of the 777 nm line in the experiments from [6, 60], and the Stark shift of the 926 nm line is used to infer electron number density in [6]. Stark broadening of the 777 nm line may also be used to infer n_e; however, uncertainty in the Stark coefficient means that n_e inferences from that line are highly uncertain [60, 204].

Table 5.1: Reflected shock experiments analyzed in the present study.

Name	$T_{5,0}$, K	$P_{5,0}$, atm	X_{O_2}, %	ΔP_5, %	Time Res., μs	Measured Time Histories	Ref.
Streicher-20-L	5,280	0.45	2	2.2	1	T_{vib}, n_{O_2}	[13]
Streicher-20-M	8,120	0.11	2	11.8	1	T_{vib}, n_{O_2}	
Streicher-20-H	10,710	0.04	5	11.1	1	T_{vib}, n_{O_2}	
Nations-16	7,250	0.61	1	$\lesssim 1$	10	$n_{O(^3S^\circ)}$, $n_{O(^5S^\circ)}$	[58]
Li-20-L1	8,124	0.35	1	< 12	20	$n_{O(^5S^\circ)}$	[59]
Li-20-L4	10,296	0.15	1	< 12	20	$n_{O(^5S^\circ)}$	
Li-20-H2	9,161	0.95	1	< 12	20	$n_{O(^5S^\circ)}$	
Li-21-1	10,153	0.49	1	$\lesssim 6$	20	n_e, $n_{O(^5P_3)}$, T_{tr}, $n_{O(^5S^\circ)}$	[6]
Li-21-2	10,623	0.44	1	$\lesssim 6$	20	n_e, $n_{O(^5P_3)}$, T_{tr}, $n_{O(^5S^\circ)}$	
Li-21-3	10,923	0.33	1	$\lesssim 6$	20	n_e, $n_{O(^5P_3)}$, T_{tr}, $n_{O(^5S^\circ)}$	
Li-21-4	11,209	0.37	1	$\lesssim 6$	20	n_e, $n_{O(^5P_3)}$, T_{tr}, $n_{O(^5S^\circ)}$	
Minesi-1920	9,525	0.32	1	19.3	0.2	T_{tr}, $n_{O(^5S^\circ)}$	[60]
Minesi-2037	12,199	0.23	1	26.1	0.2	T_{tr}, $n_{O(^5S^\circ)}$	

The experiments in Table 5.1 are a subset of the published experiments in which excited

atomic oxygen number densities have been measured. Figure 5.1 illustrates the distribution of experimental conditions within temperature and pressure space, with the experiments selected for in-depth analysis marked in red. The three experiments from [13], which are used to validate the predictions of O_2 dissociation within the model, are shown in Figure 5.1 as well.

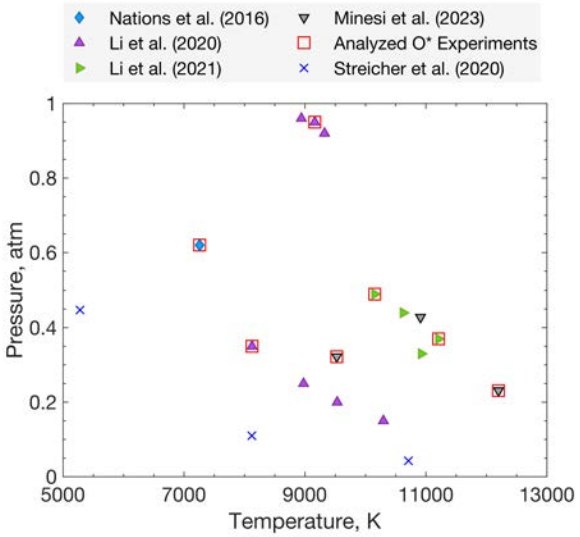

Figure 5.1: Available and selected experimental conditions for measurements of excited atomic oxygen and ground-state molecular oxygen.

The excited state measurements span a wide temperature range from 7,000 to 12,000 K at pressures from 0.15 to 0.96 atm. The selected experiments for in-depth analysis are chosen based on their location in temperature-pressure space, the type(s) of measured time histories, and the time resolution of the measurement. This last consideration, the time resolution, is a major distinguishing feature of the data published by Minesi et al. [60], in addition to the higher temperatures probed.

Values for the non-ideal pressure rise are not reported in [58, 6, 59]; those authors report low total pressure-rises ranging from 1% [58] to 6% [59, 6], accomplished through the use of a driver insert. In contrast, non-ideal pressure rises are reported in the Minesi et al. experiments and range from 0.24 to 0.40 torr/μs, corresponding to total pressure rises of 19 to 31%.

5.2.2 O_2 Dissociation

The dissociation of O_2 is an important process that significantly influences the predicted atomic oxygen excited state time histories. In several experiments, the dissociation of O_2 is nearly complete before the first laser scan is complete; however, in many cases, the excited state measurements are taken while O_2 dissociation is still ongoing. Measurements by Streicher et al. [13, 5] of the number density and vibrational temperature of $O_2(X)$ during vibrational relaxation and dissociation in mixtures of 2% to 5% O_2 in argon enable validation of the adopted O_2 dissociation model.

Predictions of O_2 dissociation by the collisional-radiative model are shown in Figure 5.2. Two-temperature model predictions are also shown as a reference, calculated using the dissociation rates and relaxation times from [13]. The collisional-radiative model achieves excellent agreement with the measured O_2 number density time-histories across the 5,200-10,700 K range of temperatures. Results in Figure 5.2 indicate that O_2 dissociation is effectively modeled in the adopted collisional-radiative model.

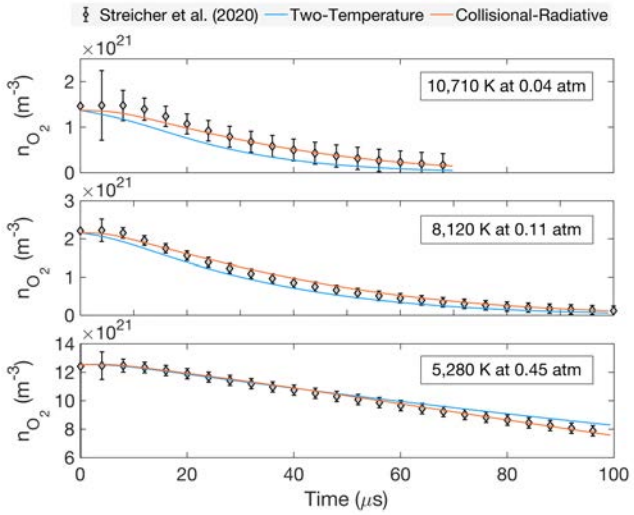

Figure 5.2: O_2 number density predictions using the present collisional-radiative model alongside predictions from a two-temperature model using parameters from [13].

5.2.3 Argon Ionization

The net ionization rate is a primary determinant of the overall system behavior. The HP-CIE reaction Ar(1) + Ar $\leftrightharpoons$ Ar(i) + Ar, where i is a level with strong radiative coupling to Ar(1), is the critical process influencing the electron number density across all analyzed experiments. To assess the validity of this assumption, the observed threshold energy of ionization is deduced by linearly fitting the rise of n_e that is measured in the four Li-21 experiments. Linear regression of the fitted dn_e/dt values from each experiment yields a threshold of 12.6 eV with a standard error of 1.6 eV and an adjusted R^2 of 0.95. The fitted slope supports argon excitation, with a threshold of 11.55 eV, as the primary rate-limiting mechanism for ionization.

A straightforward improvement of the model may thus be realized by inferring a scale factor for the rate coefficients of Ar(1$\rightarrow i$) heavy particle impact excitation using the electron number density measurements in the Li-21 experiments. A single scale factor of 55 is found to satisfactorily reproduce the measured electron number density in three of the four experiments, with the Li-21-4 experiment requiring a scale factor of 33. As a result, the excitation rate constants for the HP-CIE of Ar(1$\rightarrow i$) are increased by a factor of 55, producing the model predictions shown in Figure 5.3. Arrhenius expressions for the fitted Ar(1$\rightarrow i$) excitation rate constants are provided in Table 5.2.

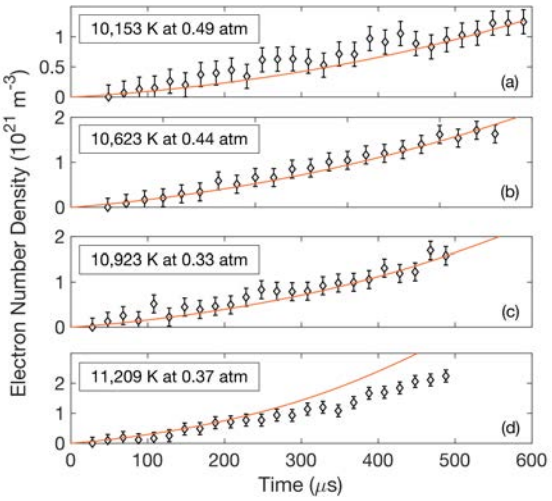

Figure 5.3: Electron number density predictions by the collisional radiative model using the inferred rate constant expressions for Ar(1) + Ar $\leftrightharpoons$ Ar(i) + Ar.

Table 5.2: Excitation rate coefficient parameters for Ar(1) + Ar $\rightarrow$ Ar(i) + Ar inferred using the measured n_e data from [6]. The rate coefficients are scaled up by a factor of 55 from those reported in [7].

i	A (m^3/s)	n	θ (K)
3	1.8359×10^{-21}	0.7639	134,170
5	6.9124×10^{-21}	0.7606	136,540
17	2.5366×10^{-23}	0.7314	160,240
23	8.5725×10^{-22}	0.7286	162,870
25	2.3876×10^{-21}	0.7278	163,600
30	4.5150×10^{-22}	0.7267	164,790
31	1.9837×10^{-21}	0.7260	165,360

In Figure 5.4, the inferred rate constant for excitation of Ar(1$\rightarrow$5) is plotted against several rate constants from the literature. The inferred argon HP-CIE rate constant is faster than the baseline rate constant, which was fitted to experimental data at temperatures above 20,000 K by Kapper and Cambier [7]. The baseline rate coefficient from [7] is the lowest available rate constant from the literature, and several other authors have inferred rate constants that range from 2.5 to 28 times larger than Kapper and Cambier's inferred value. Harwell and Jahn [171] arrived at a rate constant that is 71 times larger than the baseline rate constant but subsequently revised their value down by a factor of ten, citing "equipment modifications" [173]. Thus, the largest published rate constant is that of Wong and Bershader [205], which is 28 times larger than the baseline value taken from Kapper and Cambier and 50% smaller than the rate expression adopted in the present model.

Several effects may explain the increased rate of ionization observed in the Li-21 experiments. For one, all of the literature rate constants presented in Figure 5.4 were measured in experiments involving pure argon, while the Li-21 experiments contained 1% O_2. Notably, however, interferograms obtained by Glass and Liu [169] for argon test gasses with an O_2 impurity of 0.46% did not reveal a notable reduction of the ionization length compared to the pure argon experiments, indicating that the addition of O_2 does not appreciably impact the net ionization rate of the argon bath gas. In contrast, impurities containing hydrogen are known to strongly impact the ionization rate in pure argon experiments – Harwell and Jahn report that impurity levels of 1 part per million

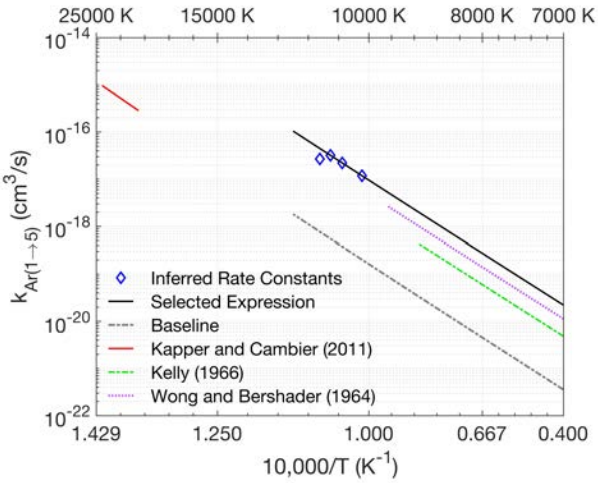

Figure 5.4: Comparison of rate constants available for the electronic excitation of Ar(1→5) in Ar + Ar collisions.

are sufficient to influence the measured ionization rate in their pure Ar experiments [171]. One part per million is an upper limit on the expected water vapor impurity in the shock tube where Li et al. performed their experiments [1] , so it is unlikely that hydrogen impurities fully explain the observed rate; however, other impurities may also be present.

Gas compression induced by non-ideal pressure rises behind the reflected shock may also increase the ionization rate of the system. In their analysis of ionization rates behind incident shocks in argon, McLaren and Hobson [172] state that the inclusion of boundary layer growth and test gas compression via Mirels theory [66] has the effect of reducing the inferred argon excitation rates from Kelly [170] and Morgan and Morrison [173] by roughly a factor of three. When a dP/dt corresponding to the maximum 6% total pressure rise reported by Li et al. is implemented, the inferred Ar(1) + Ar → Ar(i) + Ar excitation rate is decreased by 30%. None of the aforementioned effects appear to be sufficient for explaining the discrepancy from previously inferred rate constants. The observed rate constant is likely influenced by a combination of these factors; thus, the adopted rate expression for the HP-CIE of Ar($1 \rightarrow i$) should be understood as an "effective" rate expression that subsumes the effects of argon electronic excitation, impurity ionization, and Region 5 gas

[1] Y. Li, personal communication, August 2023

compression.

5.2.4 Atomic Oxygen Electronic Excitation

When analyzing the measured data for atomic oxygen excited states, rate constant inferences become considerably more complicated. The best information on individual rate constants may be derived not from measurements of an individual electronic state but from the observed relationship between multiple simultaneously measured electronic states. Two experimental datasets provide simultaneous measurements of two electronic states: the Nations-16 and Li-21 experiments. The kinetics of the Nations-16 experiment are simpler than those of the Li-21 experiments because the former was performed at a low temperature where electron-driven processes are not significant contributors to the excited state dynamics.

One key parameter that may be derived using the measured populations of two excited states is the excitation temperature, $T_{ex,s(i,j)}$, defined by the ratio of populations in levels i and j of a species s where $j > i$. The excitation temperature is calculated via Eq. (5.1). The degeneracies, g, of the ^{5}S° and ^{3}S° states are 5 and 3, respectively. When using the measured O(^{5}P$_2$) data from Li-21, the degeneracy is set to 7 since only the $J = 2$ state is measured. Otherwise, the total ^{5}P degeneracy is 15.

$$T_{ex,s(i,j)} = \left[\frac{k_B}{\varepsilon_{ij}} \ln\left(\frac{n_i/g_i}{n_j/g_j}\right)\right]^{-1} \tag{5.1}$$

The Nations-16 experiment is the only one in which the ^{3}S° state of oxygen is measured. Within the adopted model, the populations of the ^{5}S° and ^{3}S° states are controlled by a balance between collisional excitation and radiative transitions. For the ^{5}S° state, the principal radiative transitions are with the sixth excited $3p$ ^{5}P state, while the principal transitions of the ^{3}S° state involve the seventh excited $3p$ ^{3}P and ground $2p^4$ ^{3}P electronic levels. These interactions induce a coupling of the excitation temperatures $T_{ex,O(4,5)}$ and $T_{ex,O(6,7)}$, the former of which is measured in the Nations-16 experiment.

Energy-dependent cross-sections for the excitation of O(^{5}S°) to O(^{3}S°) in collisions with argon have been measured by Kiefl and Fricke [139] from threshold to 8 eV. Dagdigian et al.

and Piper have also measured the quenching rate of O($3p$ ^{3}P$\rightarrow$ $3p$ ^{5}P) in collisions with O_2 and argon, respectively, at room temperature [140, 141]. The collisional couplings between the ^{5}S° and ^{3}S° states and between the $3p$ ^{3}P and $3p$ ^{5}P states are weak when these rate coefficients are adopted. Weak collisional coupling between the quintet and triplet states is consistent with the experimentally observed suppression of the excitation temperature $T_{ex,O(4,5)}$ throughout the test time. The value of $T_{ex,O(4,5)}$ stays between 2,000 and 2,700 K throughout the entire test time, much lower than the equilibrium temperature of 7,039 K, indicating that the collisional excitation of O(^{3}S°) and O($3p^3$P) is weak compared to the radiative de-excitation of these states to form to ground-state O($2p^{43}$P).

Predictions of the collisional-radiative model are compared with the Nations-16 experimental data in Figure 5.5. A major success of the present model is its accuracy in capturing the depressed O(^{3}S°) population relative to the measured O(^{5}S°) population. Model predictions are improved significantly by scaling up the rate coefficient for the HP-CIE reaction O(^{3}P) + Ar $\rightarrow$ O(^{5}S°) + Ar by a factor of ten from the baseline value adopted from Lemal et al. [15]. Based on these results, the HP-CIE rate scaling for the O(1$\rightarrow$4) rate constant is adopted throughout the remainder of the present work.

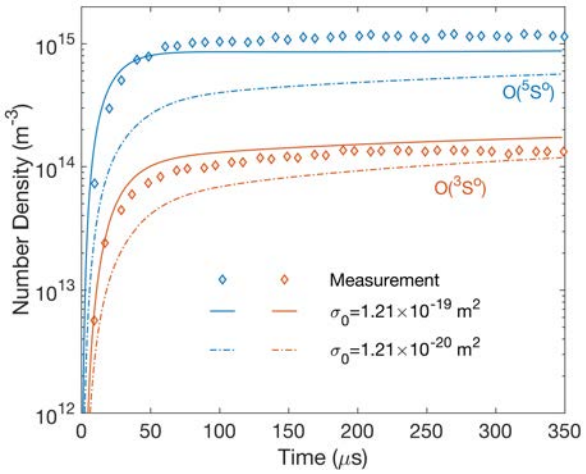

Figure 5.5: Model predictions compared with experimental data from Nations-16 using two values of the cross-section scale factor σ_0 for the HP-CIE reaction O(^{3}P) + Ar $\rightarrow$ O(^{5}S°) + Ar.

Experimental measurements in the Li-21 dataset provide information on the coupling between the fourth and sixth excited states of O. In the original analysis of this data, the excitation temperature was found to quickly equilibrate with the translational temperature, indicating that the $^5S^\circ$ and ^5P levels are strongly coupled via heavy particle collisions. In the present work, reprocessing of the experimental data yields different results for $T_{ex,O(4,6)}$, and the original author has confirmed this error in the initial analysis[2] .

The measured and predicted values of $T_{ex,O(4,6)}$ for the Li-21-1 experiment are shown in Figure 5.6 alongside the electron and heavy particle translational temperatures. Results obtained using two rate constants for the heavy particle impact excitation reaction $O(^5S^\circ) + Ar \rightarrow O(^5P) + Ar$ are shown in the Figure. The baseline rate, based on the recommended cross-section of Lemal et al. [15], yields early-time predictions of $T_{ex,O(4,6)}$ that are consistent with the measured data. In contrast, when the O(4→6) excitation cross-section is set to the hard-sphere cross-section of the oxygen atom – assuming that every collision of $O(^5S^o)$ with Ar results in an excitation to $O(^3P)$; i.e. the gas kinetic limit – the excitation temperature of O(4→6) is much higher than the experimental data suggests. The rate constant inferred by Li et al. [6] for the HP-CIE excitation of O(4→6) is within a factor of 2 of the gas kinetic limit, while the rate constant used in the present model is four orders of magnitude smaller.

In the present model, the free electron temperature relaxes to the translational temperature much faster than the model adopted by Li et al. [6] predicts. The fast relaxation is caused by rapid energy transfer between the heavy particle and electron translational modes that is mediated by $O(^1D)$, a state that is not included in the model of Li et al. First, $O(^1D)$ is formed in O + O and O + Ar collisions, quickly bringing the ^1D state to equilibrium with the heavy particle translational temperature, illustrated using the $T_{ex,O(1,2)}$ line in Figure 5.6. The large population of $O(^1D)$ then serves as an energy reservoir from which the electrons gain translational energy via superelastic scattering in the de-excitation reaction $O(^1D) + e^- \rightarrow O(^3P) + e^-$. For this reason, the free electron translational temperature, T_{eex}, follows closely behind $T_{ex,O(1,2)}$ and quickly rises

[2] Y. Li, personal communication, August 2023

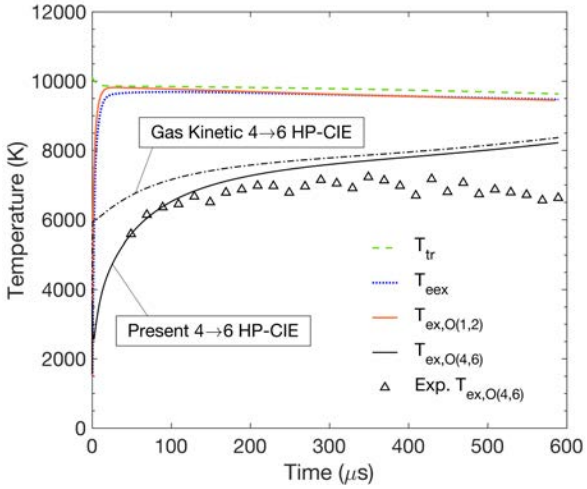

Figure 5.6: Temperature predictions for the Li-21-1 experiment, including the electronic temperature for the 4th and 6th excited states of O as calculated from the measured data and the model predictions.

to a quasi-steady state value that is approximately 400 K below T_{tr}.

Rapid relaxation of the free electron temperature is a major change to the overall system kinetics that arises from including the metastable states of oxygen and the best available rate constants for the heavy-particle impact excitation of those states. It is recommended that the metastable atomic electronic states be included in future interpretations of measured data for high-lying atomic electronic states in shock tube experiments.

By including the kinetics of the O(^{1}D) state, the present analysis arrives at a much slower rate coefficient for the HP-CIE of ^{5}S$^\circ$ to ^{5}P in collisions with argon. In Figure 5.7, rate constants used in the current study are compared to those used in Li et al.'s initial interpretation of the experimental data. The current HP-CIE rate constant is approximately four orders of magnitude lower than the rate constant used by Li et al., in large part because the strong collisional coupling of O(^{5}S$^\circ$) to O(^{5}P) is accomplished via collisions with electrons in the present model. Electron collisions are effective at coupling the two states because of the high electron translational temperature and an E-CIE rate that is approximately 400 times larger than that used by Li et al. The large discrepancy in the O(^{5}S$^\circ$→^{3}P) E-CIE rate is caused by assuming that the effective collision strengths of the

$O(^3P \rightarrow {}^5S^o)$ and $O(^5S^\circ \rightarrow {}^5P)$ excitation reactions are the same – in reality, the above-threshold E-CIE cross-sections for $O(^5S^\circ \rightarrow {}^5P)$ are two orders of magnitude higher than those for $O(^3P \rightarrow {}^5S^o)$.

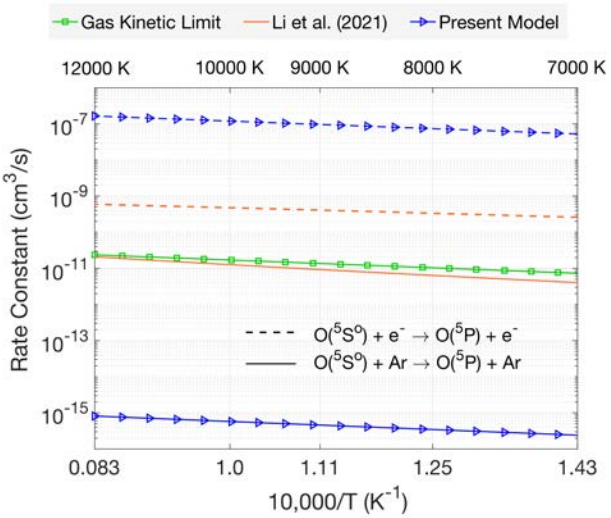

Figure 5.7: Rate constants for the excitation of O(4→6) in collisions with argon and electrons. The E-CIE rate constant from Li et al. [6] is the baseline rate constant in that study. The HP-CIE rate from Li et al. is the optimized rate constant obtained by multiplying their baseline value by 6,200.

The predicted number densities of $O(^5S^\circ)$ and $O(^5P)$ are compared with the measured data from the Li-21-2 experiment in Figure 5.8. The model successfully reproduces the observed three-stage behavior observed in the experimental data, matching quantitatively within 10-20% for $n_{O(^5S^\circ)}$ and within 30% for all but the last data point of $n_{O(^5P_J)}$. Across all of the Li-21 experiments, the agreement with $n_{O(^5S^\circ)}$ and $n_{O(^5P_J)}$ is similar to that shown in Figure 5.8, with model predictions overshooting the late-time measured number densities of $O(^5P)$ by a maximum of 65% and $O(^5S^\circ)$ number densities disagreeing with the measured data by a maximum of 33%.

All previous studies have analyzed the multistage behavior observed in Figure 5.8 using simplified collisional-radiative models involving only the ground and measured electronic states [59, 6, 60]. In those models, the multistage behavior is explained as follows. First, the population of $O(^5S^\circ)$ rises in Region I due to heavy particle impact excitation of $O(^3P)$ in collisions with argon. Note the use of Roman numerals to distinguish these time history Regions from the shock tube flow Regions. Next, the measured population decreases in Region II as the translationally cold electrons

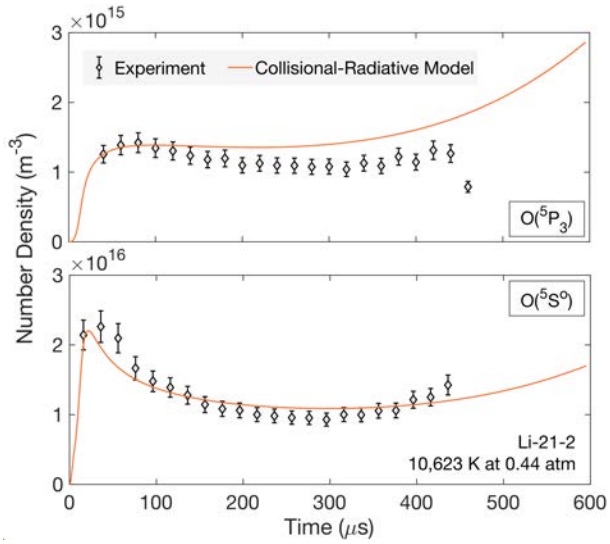

Figure 5.8: Comparison of collisional-radiative model predictions with measured data from the Li-21-2 experiment. Agreement with the experimental data is representative of other experiments in the Li-21 dataset.

scatter superelastically in collisions that de-excite O(^{5}S°) to O(^{3}P), raising the free-electron temperature in the process. Finally, in Region III, the free-electron translational temperature surpasses $T_{ex,O(1,4)}$ and the population of O(^{5}S°) begins rising again due to electron-impact excitation from O(^{3}P).

The current model also reproduces the experimentally observed three-stage behavior in the O(^{5}S°) number density time history; however, the driving mechanisms in Regions II and III are distinct from those previously proposed in [59, 6, 60]. In Region I, the previous and current models agree that the excited state number density increase is due to heavy-particle excitation processes. Predictions begin to differ in Region II, with the present model predicting T_{eex} to be almost fully relaxed, in contrast to previous models in which T_{eex} is not fully relaxed until the end of the test time. Because T_{eex} exceeds $T_{ex,O(i\leq3,4)}$ after the first 20 μs of the experiment, the de-excitation of O(^{5}S°) via electron collisions cannot occur. Rather, the present model predicts that O(^{5}S°) depopulates in Region II as a result of ladder-climbing to upper states that are subsequently ionized by the translationally hot free electrons. The high-lying electronic states, including the measured states, remain suppressed until the electron population approaches equilibrium, at which point the

state populations begin rising again (Region III) to a Boltzmann population at the equilbrium temperature.

A Boltzmann plot of the electronic states of atomic oxygen is shown in Figure 5.9 that clearly illustrates the mechanisms driving the three-stage behavior. Three key time points in the Li-21-2 experiment are shown: 20 μs, the transition point from Region I to Region II; 300 μs, the transition point from Region II to Region III; and 600 μs, the end of the simulation and well into Region III. At all three time points, the metastable ^{1}D and ^{1}S states are in equilibrium with the translational temperatures of the free electrons and heavy particles, meaning that the observed dynamics are indicative of only the upper-state kinetics. At 20 μs, the O(^{5}S) state has been driven close to equilibrium with T_{tr}, but the electron number density and temperature have just reached the critical value at which electron impact ionization begins to dominate the kinetics, and the upper electronic state populations begin falling as they are pulled toward the Saha-Boltzmann equilibrium line. At 300 μs, the highest-lying electronic states achieve Saha-Boltzmann equilibrium with the rising free-electron number density. From 300 μs to the third sampled time point at 600 μs, the upper-states remain in Saha-Boltzmann equilibrium with the rising electron number density, raising their population and leading to the observed Region III population increase.

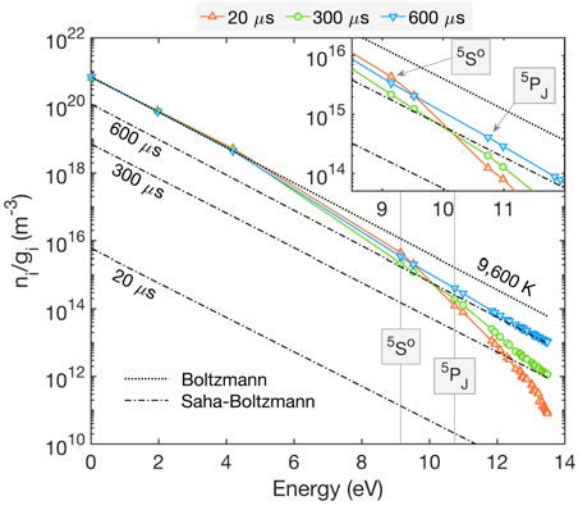

Figure 5.9: Boltzmann plot showing the electronic state distribution of oxygen atoms at three different time points in the Li-21-2 experiment.

The modeled three-stage dynamics rely on the inclusion of states both below and above the measured O(^{5}S$^\circ$) level. The metastable states drive the fast relaxation of the free electron temperature, and the upper states are required to resolve the ladder-climbing behavior of electron impact ionization [104].

Kinetics in the Li-21 experiments are primarily driven by electron-impact processes. The excellent predictions obtained across the Li-21 experiments indicate that the collisional-radiative model effectively predicts electron temperature relaxation, E-CIE, and E-CII at the studied conditions. Heavy particle kinetics can be better assessed through the analysis of experiments at lower pressure and/or temperature, as in the Li-20 dataset, or with increased time resolution, as in the Minesi dataset.

Predictions of O(^{5}S$^\circ$) are compared with experimental measurements from the Li-20-L1 and Li-20-L4 experiments in Figure 5.10. The model produces reasonable predictions for the Li-20-L1 case but underpredicts the Li-20-L4 measurements by up to 80%. The excitation of O(^{5}S$^\circ$) appears to follow a temperature dependence based on a threshold energy that is approximately 40% greater than the O(^{3}P$\rightarrow^5$S$^\circ$) excitation energy, in line with the findings of Minesi et al. [60]. Reaction thresholds do not need to exactly match the energetic difference between the two involved states; however, such a large deviation appears improbable. Radiation modeling and non-ideal pressure rise may also play a role in explaining the observed temperature dependence.

Escape factor calculations require a length scale, L_{rad}, over which the absorption takes place, and there is some ambiguity in the choice of this length scale. Two reasonable choices for the present analyses are the shock tube diameter and the characteristic length scale of flow gradients. Ambiguity in the choice of L_{rad} is introduced by the three-dimensionality of radiation transport – the shock tube diameter is the relevant length scale for absorption in the radial direction and the gradient length scale is relevant for absorption along the axial direction of the shock tube. In Figure 5.10, the choice between the two values of L_{rad} is shown to strongly influence the predicted time-histories in the low-pressure Li-20 experiments. For the Li-20-L1 experiment, the experimental data is bracketed by predictions from the two values of L_{rad}. In both cases, predictions when

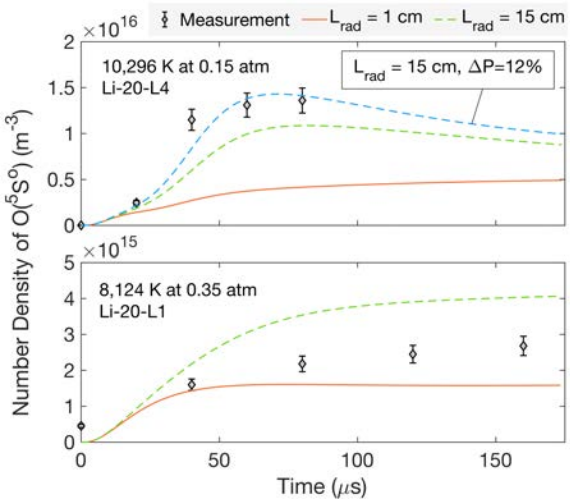

Figure 5.10: Comparison between measured data and model predictions for the number density of $O(^5S^\circ)$ in the Li-20-L1 and Li-20-L4 experiments.

$L_{rad} = D_{shock\ tube} = 15$ cm are very close to those where Λ_{51} is set to zero; i.e. when emission due to the $O(^3S^\circ \rightarrow {}^3P)$ transition is fully self-absorbed as is often assumed for vacuum ultraviolet (VUV) resonance radiation [192]. The choice of $L_{rad} = 1$ cm results in a partial escape of $O(^3S^\circ \rightarrow {}^3P)$ radiation that is consistent with the observed suppression of $O(^3S^\circ)$ populations relative to $O(^5S^\circ)$ in the Nations-16 data.

The true physics of resonance radiation transport cannot be fully accounted for within the present model because escape factors assume local absorption. If the $O(^3S^\circ \rightarrow {}^3P)$ emission partially escapes the local fluid element into the upstream and/or downstream flow directions, as the $L_{rad} = 1$ cm escape factors indicate, then the emitted light is absorbed elsewhere and influences the measured populations at those locations.

Non-ideal pressure rise may also contribute to the observed temperature dependence. The effect of a dP/dt corresponding to 12% net pressure increase is shown in Figure 5.10 for the Li-20-L4 case. The incorporation of non-ideal pressure rise results in a faster excitation of the measured state. In shock tube experiments, higher temperatures are typically accompanied by lower pressures, where non-ideal effects are more significant. Because non-ideal pressure rises are not reported in the Li-20 experiments, it is not possible to test this hypothesis. Future measurements of excited

state and electron number densities should report the measured dP/dt in each experiment.

Measurements from Minesi et al. [60] with a time resolution of 0.2 μs provide another valuable probe of excited state kinetics under the primary influence of excitation by heavy particles. Collisional-radiative model predictions are compared against two experiments from the Minesi dataset in Figure 5.11. For these experiments, the baseline model with $L_{rad} = 1$ cm obtains only order-of-magnitude agreement with the measured data, with differences exceeding a factor of 3 in some cases.

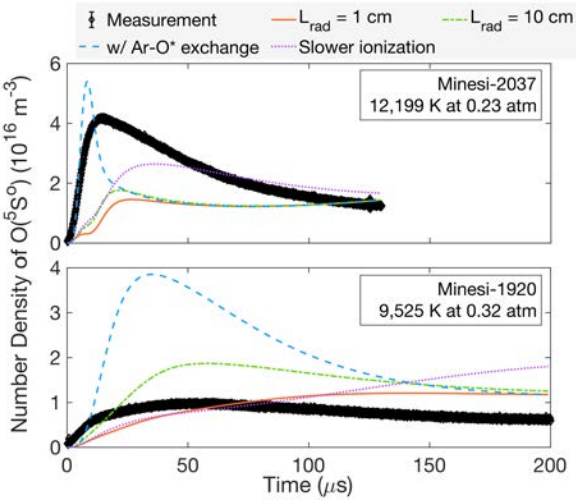

Figure 5.11: Comparison between model predictions and measured data for the number density of $O(^5S^\circ)$ in the Minesi-1920 and Minesi-2037 experiments.

There are several possibilities for the disagreements between the collisional-radiative model predictions and the Minesi data. While predictions of the Minesi-1920 experiment are sensitive to the choice of radiation length scale, those of the Minesi-2037 experiment are not strongly influenced by the choice of L_{rad}. Radiation modeling uncertainties may play a role in, but cannot completely explain, the largest discrepancies. Another important feature of the Minesi experiments is the relatively large non-ideal pressure rise compared to the other analyzed experiments. If the non-ideal pressure rise is not fully isentropic, then $dh = \nu dp$ will overpredict the enthalpy increase, potentially explaining the long-time overprediction of $O(^5S^\circ)$ populations in the Minesi-1920 experiment.

Recalling the previous explanation for the three-stage behavior in the Li-21 experiments, the

higher maximum number density of O(^{5}S$^\circ$) could be caused by slower ionization – a slower buildup of electrons would delay the onset of Region II depletion via electron impact ionization, allowing the excited state concentration to rise for longer before the onset of significant electron impact ionization. A model with slower ionization is obtained by scaling the excitation rate constants for Ar(1) + Ar $\rightarrow$ Ar(i) + Ar by a factor of 1/5, matching those of Kelly [170]. The maximum number density is increased when the slower ionization rate is adopted. Continued reduction of the ionization rate leads to progressively higher peak number densities; however, the timescale of the O(^{5}S$^\circ$) population rise remains significantly slower than the measured data suggests.

One process that produces O(^{5}S$^\circ$) on the timescale observed in the Minesi-2037 experiment is the electronic excitation exchange between the $4s$ states of argon and the $3p^3P$ state of atomic oxygen, modeled using the room temperature rate measured by Piper [140]. In general, however, including this process worsens the agreement between model predictions and measurements for most cases analyzed, the Minesi-1920 case being one such example. Measurements of metastable argon atoms, which absorb in the infrared, would clarify the potential effect of electronic exchange between excited argon and oxygen atoms.

The underprediction of O(^{5}S$^\circ$) number density measurements in the Minesi dataset is contrasted by the overprediction of early-time O(^{5}S$^\circ$) number density measurements in the high-pressure experiments performed by Li et al. [59]. An example is shown in Figure 5.12 for the Li-20-H2 case, where the peak excited state number density is overestimated by a factor of two at very early times when $L_{rad} = 1$ cm. Such a result apparently contradicts the disagreement observed in the Minesi-1920 data taken at a similar translational temperature.

5.3 Sensitivity Analysis

A major conclusion of the analysis in this chapter is that measured data for high-lying atomic electronic states behind strong shock waves must be interpreted using a more complete collisional-radiative model like the one developed in this thesis. One challenge when adopting such a model is that its predictions are the result of hundreds of different parameter choices, and it can be difficult

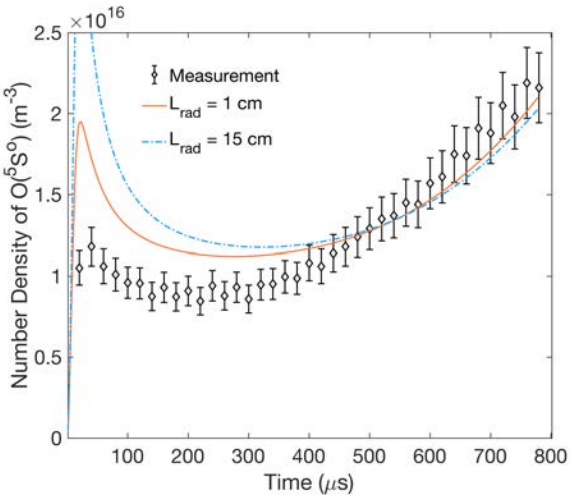

Figure 5.12: Comparison between model predictions and measured data for the number density of $O(^5S^\circ)$ in the Li-20-H2 experiment at 9,161 K and 0.95 atm in 1% O_2-Ar.

to identify which processes most sensitively influence a given model prediction.

Such ambiguity is resolved in the present Section by means of a global sensitivity analysis that quantitatively apportions the variance in model predictions to variations in individual input parameters. The quantification of variance contributions from each individual parameter is accomplished using total Sobol' indices, a popular metric used in global sensitivity analyses.

5.3.1 Parameters and Response Functions

The quantities of interest in the sensitivity analysis are the number density of the species and electronic states that are probed in each experiment. The PCE surrogate is fit to the logarithm of the number density instead of the number density itself, improving both the convergence of the Sobol' indices and the accuracy of the surrogate model. Response functions are extracted for each quantity of interest at a set of 75 logarithmically spaced time points from 0.5 μs to the end of the test time.

A total of 295 parameters are included in the sensitivity analysis. The value of each parameter is varied over a log-uniform distribution, with minimum and maximum values obtained by multiplying the parameter's value in the baseline model by 0.1 and 10, respectively. The parameters

include rate coefficients for collisionally-induced electronic transitions:

- among the lowest ten states of O in collisions with electrons and argon atoms;
- from ground-state argon to the radiatively coupled excited states in collisions with other argon atoms;
- from ground state argon to all higher levels by electron collisions;
- among the lowest five levels of argon by electron and Ar collisions;
- among the electronic states of O_2 in collisions with O_2, O, Ar, and electrons;
- and between the two excited states of Ar^+ by electron collisions.

Rate coefficients for ionization by impact with electrons and argon atoms are included for the lowest ten levels of O, all electronic levels of O_2, and the lowest 5 levels of Ar. All rate coefficients for quenching, electronic excitation exchange and energy pooling, dissociation, charge exchange, and associative ionization are also considered.

Relaxation parameters are considered as well, including the vibrational-translational relaxation times for O_2 with Ar, O, and O_2 and the energy exchange cross-sections between electrons and all six heavy species. Finally, the escape factors for radiative transitions among the lowest ten states of oxygen are included.

5.3.2 Results

Sensitivity analysis is performed for all of the experimental conditions in Table 5.1 where electronically excited oxygen atoms were measured. Results from three cases are shown in this Section that together demonstrate the full diversity of sensitivity results observed across all analyzed conditions.

Convergence metrics for the three analyzed conditions are plotted in Figure 5.13. After evaluating the collisional-radiative model 3,000 times for each condition, the maximum change to

any Sobol' index drops well below 0.01 for all three cases as shown in Figure 5.13a. The average change in Sobol' indices is considerably lower, brought down by the large number of Sobol' indices close to zero. The PCE surrogate test point error is plotted in Figure 5.13b. Test point error is reported for the number density, not its logarithm, to provide a clearer picture of the surrogate model performance. Although the maximum errors are between 300% and 1,000%, the average errors are between 6% and 30%, indicating that the maximum test point error occurs at only 1 or 2 of the 75 points in each profile. For the remaining points, the error must be closer to the average of approximately 10%, which is consistent with the averaged test point errors observed by West and Hosder [55]. Large surrogate model errors may be expected immediately after the shock passage when the excited state population is rising quickly. Higher-order effects may also be more significant in this zone, which the second-order surrogate is unable to represent. Due to the apparent locality of the maximum test point error and the excellent convergence of the total Sobol' indices, the fitted PCE surrogate is deemed acceptable.

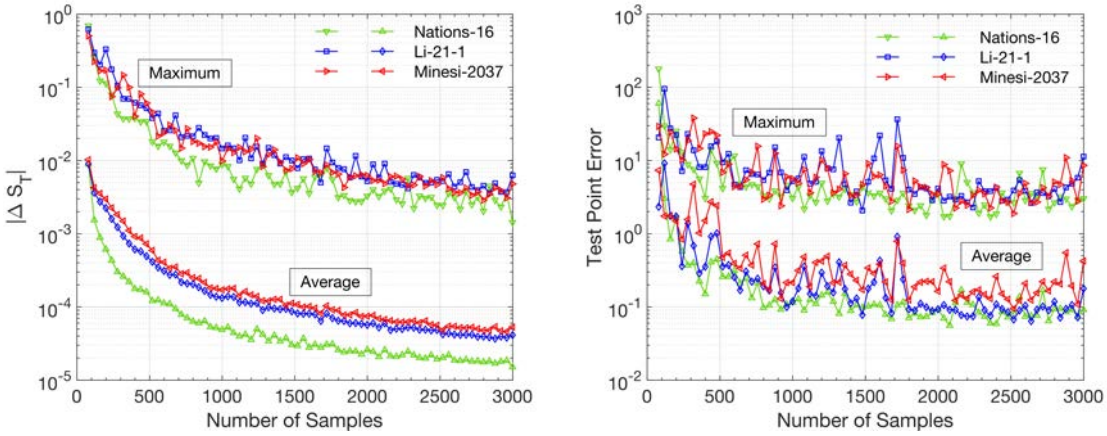

(a) Change in Sobol' indices

(b) Surrogate model test point error

Figure 5.13: Convergence metrics for the sensitivity analyses.

Sobol' indices for the number density of $O(^5S^\circ)$ and $O(^3S^\circ)$ in the Nations-16 case are plotted in Figure 5.14. The escape factor for 130 nm radiative emission from the $O(^3S^\circ \rightarrow {}^3P)$ transition, Λ_{51}, dominates the sensitivity of $O(^3S^\circ)$ and plays a leading role in the $O(^5S^\circ)$ time history as

well. In the case of $O(^3S^\circ)$, the dominance of Λ_{51} highlights the difficulty of assessing the rates of collisional excitation processes using the measured time history. The situation with $O(^5S^\circ)$ is somewhat better, with the HP-CIE of $O(^5S^\circ)$ from $O(^3P)$ showing major sensitivity, indicating that rate inferences are appropriate using this time history.

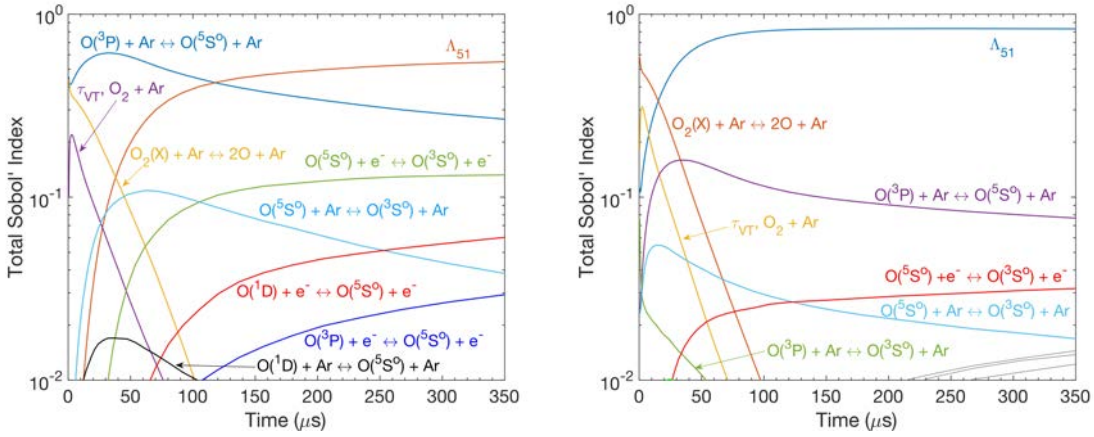

(a) $O(^5S^\circ)$ (b) $O(^3S^\circ)$

Figure 5.14: Total Sobol' indices for the number density of (a) $O(^5S^\circ)$ and (b) $O(^3S^\circ)$ in the Nations-16 experiment at 7,250 K and 0.61 atm in 1% O_2-Ar.

The sensitivity of Λ_{51} indicates that radiative loss is a major contributor to the population of $O(^3S^\circ)$ in the Nations-16 case, consistent with the suppressed $T_{ex,O(4,5)}$ calculated using the measured data. Collisional excitation between the two states is also shown to be important in Figure 5.14, likely because the two states are far from equilibrium and separated by a small energy gap. Modeling of $O(^5S^\circ)$ populations should therefore take into account the collisional excitation to and radiative loss from the $O(^3S^\circ)$ state.

The final processes worth noting from the Nations-16 sensitivities are the vibrational-translational relaxation between O_2 and Ar and the dissociation of $O_2(X)$ by Ar. Vibrational relaxation is important because it defines the time-history of T_{vib}, which in turn influences the nonequilibrium rate of dissociation. Dissociation and vibrational relaxation are only sensitive early in the test, after which the dissociation fraction of O_2 is near equilibrium. Similar short timescales for the sensitivity of these two processes are found across all conditions analyzed.

Electron number density sensitivities are plotted in Figure 5.15 for the Li-21-1 case. The most important process, by far, is the excitation of argon from its ground state to its third and fifth excited states, consistent with previous discussions on the ionization mechanism in shocked argon and the analysis in [7]. Electron impact processes rise in sensitivity over time; however, the test time ends before the electron concentration reaches a sufficient level for electron impact ionization to dominate. The excitation of $O(^1D)$ by electron and argon atom impact is also important due to the role of $O(^1D)$ in mediating energy exchange between the heavy particles and the free electrons.

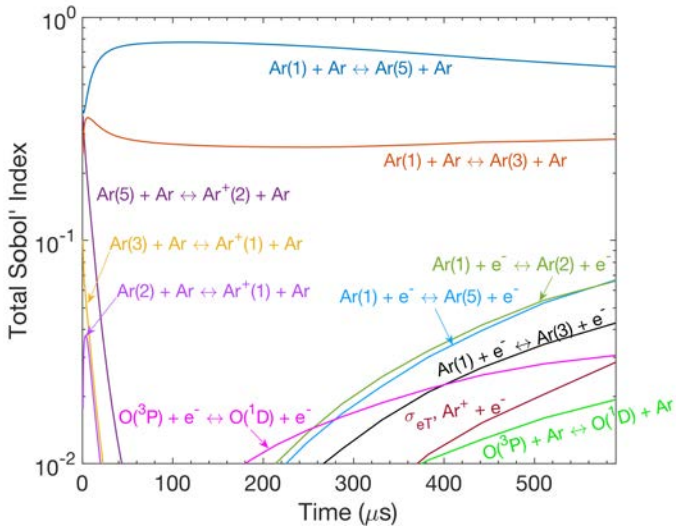

Figure 5.15: Total Sobol' indices for the prediction of electron number density in the Li-21-1 case at 10,153 K and 0.49 atm in 1% O_2-Ar.

The number of sensitive processes influencing the concentrations of $O(^5S^\circ)$ and $O(^5P)$ is far greater than the number of processes influencing the electron concentration. The total Sobol' indices for the number density of the two excited states are plotted in Figure 5.16 and are labeled by process category to highlight the overall system dynamics influencing the predicted state populations. Different processes dominate the sensitivity at different times throughout the experiment, echoing the three-stage behavior observed in the measured and predicted time histories for the Li-21 experiments. Very early in the test, before the first data point is taken, the time-histories are dominated by vibrational-translational relaxation and O_2 dissociation as in the Nations-16 ex-

periment. After approximately 30 μs, the sensitivities of both time histories become dominated by various electron impact excitation reactions involving atomic oxygen. These processes remain dominant for the majority of the test time, eventually being overtaken by the rising sensitivity of HP-CIE involving Ar + Ar collisions, which control the ionization rate of the gas and, by extension, the third stage rise of the predicted excited state populations. For the same reason, the E-CIE of argon also begins showing notable sensitivity near the end of the test time.

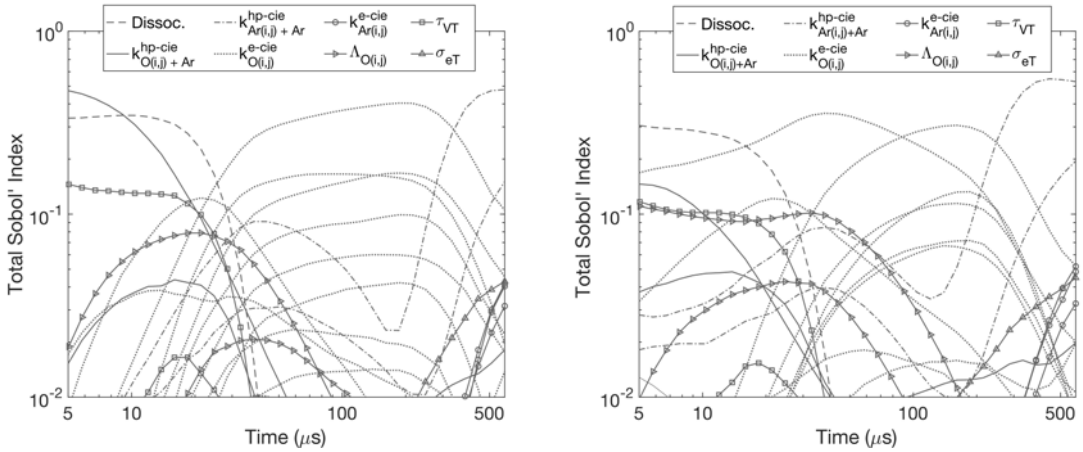

(a) O(^{5}S°) (b) O(^{5}P)

Figure 5.16: Total Sobol' indices, organized by parameter category, for the number density of (a) O(^{5}S°) and (b) O(^{5}P) in the Li-21-1 experiment at 10,153 K and 0.49 atm in 1% O_2-Ar.

A large number of sensitive processes are illustrated in Figure 5.16. To clarify the relative contributions of each process to the overall solution variance, the Sobol' indices are plotted in Figure 5.17 after being normalized so that they sum to one. The top 12 processes influencing each time history are labeled individually, with the summed contribution from the remaining 283 processes shown in gray at the top of each plot. The processes influencing each measured state are very similar, indicating that the coupling between the two states is strong.

Early in both time histories, the heavy particle impact excitation of O(^{3}P) to O(^{5}S°) dominates the sensitivity along with the dissociation of O_2(X) by argon. The escape factor for the radiative transition between the two measured states is also important, particularly for the ^{5}P number density, although the contribution is short-lived.

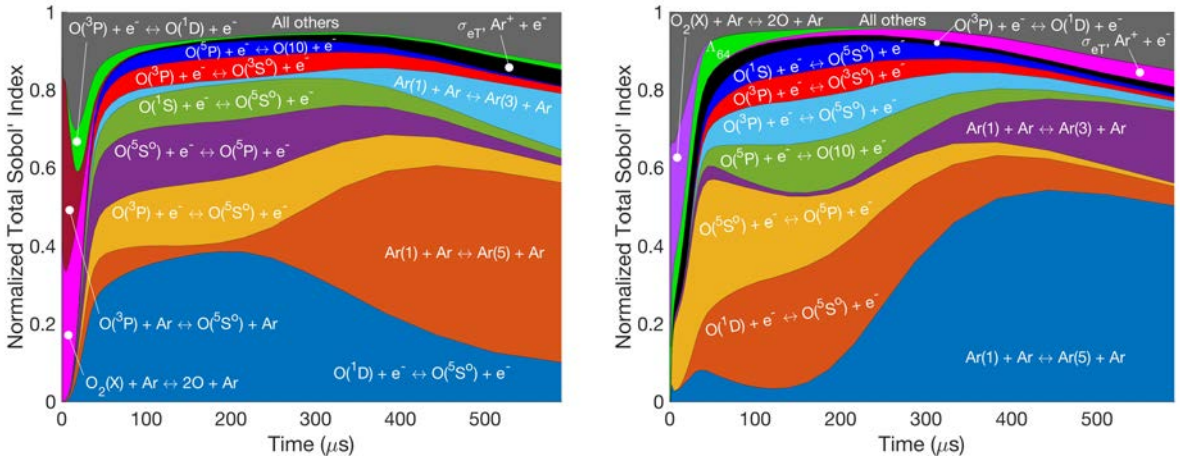

(a) $O(^5S^\circ)$ (b) $O(^5P)$

Figure 5.17: Normalized total Sobol' indices for the number density of (a) $O(^5S^\circ)$ and (b) $O(^5P)$ in the Li-21-1 experiment at 10,153 K and 0.49 atm in 1% O_2-Ar.

Similar electron impact excitation reactions play a dominant role in the sensitivity of both electronic state number densities. Excitation of $O(^5S^\circ)$ from the metastable ^1D level is significantly more sensitive than excitation from the ground, indicating that ladder-hopping to the measured state must be considered when analyzing measured time histories of $O(^5S^\circ)$ and $O(^5P)$. Excitation between the two measured states is also highly sensitive because it defines the balance of collisional and radiative coupling between the two states. The E-CIE reaction from the ^5P state to the tenth excited state of O is sensitive for the same reason. Formation of the $^3S^\circ$ state remains sensitive as in the Nations-16 case. The late-time sensitivities in Figure 5.17 are dominated by processes that influence the overall system dynamics, highlighting the ability of these high-lying states to probe the timescale of ionization in the gas.

Finally, the normalized Sobol' indices for the Minesi-2037 experiment are shown in Figure 5.18. The included processes and the timescales over which they are important are similar to the Li-21-1 experiment. In spite of the similarity in sensitive processes between both experiments, the model predictions are only consistent with the measured data from the Li-21 experiments and not from the Minesi experiments. In light of this observation, more data is needed to help identify

aspects of the flow, radiation, or kinetics modeling that may explain the discrepancies.

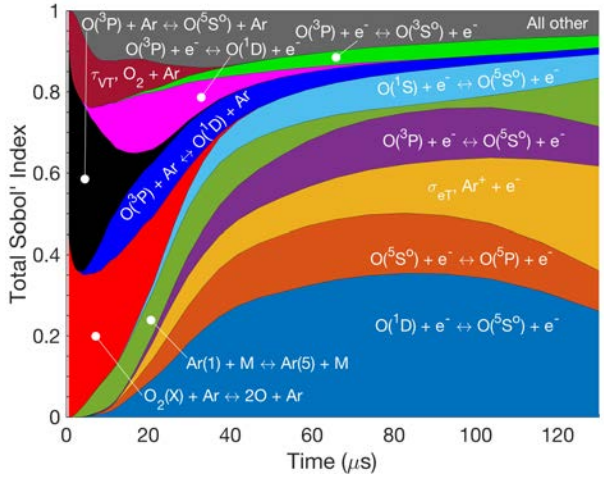

Figure 5.18: Normalized total Sobol' indices for the number density of O(^{5}S°) in the Minesi-2037 experiment at 12,199 K and 0.23 atm in 1% O_2-Ar.

There are three quantities that, if measured, could enhance the development of the present collisional-radiative model and improve the utility of the excited state measurements analyzed in this work. First, electron number density measurements would be extremely valuable, especially in the same facility where the Minesi data was measured. Next, argon electronic state population measurements would elucidate whether the ionization rate is significantly affected by impurities and whether excitation exchange between oxygen and argon is an important process. Finally, measurements of O(^{1}D), while challenging, would shed light on the proposed role of this metastable state in facilitating rapid energy exchange from the translational energy of heavy particles to the free electrons.

5.4 Summary

The dissociation, electronic excitation, and ionization occurring in shock-heated mixtures of O_2 and argon were studied in this chapter. Predictions of O_2 number density during shock-induced dissociation were within the experimental uncertainties of measured data spanning 5,000 to 10,000 K in mixtures of 2-5% O_2 in argon. Validation of the adopted dissociation model enabled the

collisional-radiative model to be confidently used to study electronic excitation in conditions where O_2 dissociation is ongoing throughout the test time.

Rate coefficients for the heavy particle impact excitation of ground state argon were determined using measurements of electron number density in experiments spanning 10,000 to 11,200 K. The inferred rate constants were larger than other published values, indicating that non-ideal pressure rises or impurities may be influencing the net ionization rate in the gas.

Measurements of electronically excited atomic oxygen in three separate states were analyzed next. Measurements at 7,000 K were used to infer a rate constant for the excitation of oxygen from its ground to its fourth excited state, the $^5S^\circ$ state, in collisions with argon. The observed depression in the population of the fifth excited state, the $^3S^\circ$ state, indicated that radiative depopulation of this state is more effective than collisional excitation. Model predictions were consistent with this experimental observation. The selected value for the escape factor self-absorption length scale was important for matching the observed population suppression.

Three-stage behavior observed in several experiments was also predicted accurately by the collisional-radiative model. The dynamics leading to the multi-stage behavior were different than those previously inferred using simpler collisional-radiative models, indicating that future measurements of excited state populations should be interpreted using more complete models like the one adopted here. The observed behavior was driven by kinetics involving states both above and below those that were measured, and a thorough description of the involved dynamics was provided.

Comparisons were made with data from two experimental facilities, one at Stanford and one at UCLA. While model predictions were generally consistent with the measured data from the Stanford facility, comparisons with the data gathered at UCLA yielded significant disagreements. Further measurements from the UCLA facility, particularly of the electron number density, could help identify whether the discrepancies are due to kinetic model inaccuracies or facility effects.

Finally, sensitivity analyses of the measured excited state populations were performed, involving nearly 300 parameters in the collisional-radiative model. The objective of the analyses was to isolate the model parameters being most effectively tested by comparisons with the measured

data. Predictions of the $O(^3S^\circ)$ population were primarily controlled by the escape factor for emission to the ground electronic state. Predictions of the fourth and sixth excited states, $O(^5S^\circ)$ and $O(^5P)$, were influenced by a large number of collisional and radiative processes. Results from the sensitivity analyses highlight the difficulty of inferring individual rate expressions from the measured data while also showing that the excited state measurements effectively test a large number of parameters in the collisional-radiative model.

Chapter 6

Electronic State-Resolved Analysis of Weakly Ionized Nitrogen Mixtures

6.1 Introduction

This chapter is devoted to the study of atomic nitrogen electronic excitation behind strong shock waves. Atomic nitrogen is of interest for several reasons. First, electronically excited nitrogen atoms are an essential precursor to the formation of free electrons in shock-heated air. The lowest threshold ionization reaction in air is the associative ionization (AI) to form NO^+, which occurs primarily through the interaction of an excited nitrogen atom with a ground-state oxygen atom [206]. In addition, all channels leading to the formation of N_2^+ require an electronically excited nitrogen atom because the $N(^4S)$ + $N(^4S)$ channel is spin-forbidden. The net rates of these key reactions are, therefore, dependent on the populations of the metastable electronic states of atomic nitrogen. However, the rate coefficients for reactions that populate these metastable states are not well characterized, particularly for excitation reactions involving heavy particle collisions.

Accurate modeling of processes involving nitrogen atoms is also essential when considering atmospheric entry flows at velocities exceeding those of Earth orbit. Electron impact ionization of N is the main source of electrons at these conditions, and electronically excited nitrogen atoms emit a significant amount of radiation in the shock layer [15, 57].

6.2 Comparison With Experiment

In this chapter, the developed collisional-radiative model is assessed using experimental measurements of $N_2(X)$ from Appleton et al. [14], and measurements of excited state atomic nitrogen

from Finch et al. [8]. The molecular nitrogen measurements enable dissociation predictions to be assessed, ensuring that the model predicts N(^{4}S) formation with sufficient accuracy to enable meaningful comparison with the measurements of excited-state nitrogen atoms.

6.2.1 Description of Experiments

All experimental data analyzed in the present work was measured behind reflected shocks in N_2-Ar mixtures. Figure 6.1 shows the Region 5 pressure and temperature in all of the experiments reported by Appleton et al. [14] and Finch et al. [8]. The measurements of N_2(X) were performed at considerably higher pressures than those of N(^{4}P), meaning that the thermochemical evolution takes place over a much shorter timescale than in the electronic excitation experiments. The N_2 concentrations are higher in the experiments from Appleton et al. as compared to those from Finch et al., who required low N_2 concentrations to maintain the high temperatures required for a detectable population of N(^{4}P) throughout the experiment. All of the experiments published by Appleton et al. [14] are analyzed in the present study, while only a representative subset of the Finch et al. experiments are analyzed in detail.

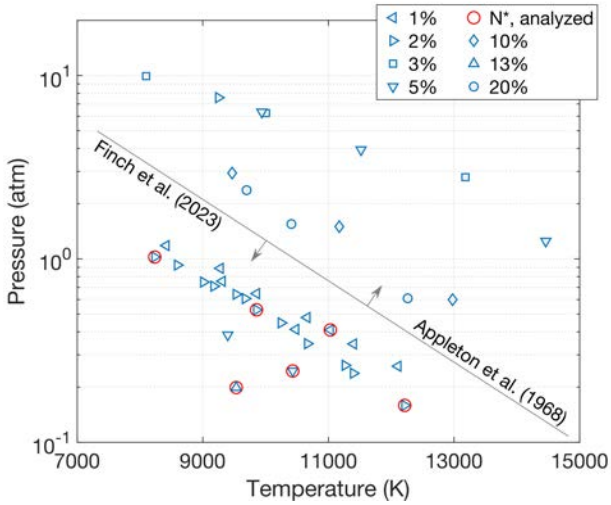

Figure 6.1: Nominal initial temperature, pressure, and N_2 mole fraction in the experiments published by Appleton et al. [14] and Finch et al. [8, 9]. All experiments from Appleton et al. [14] are analyzed, while a subset of those from Finch et al. [8, 9] are selected for detailed analysis and are marked with red circles.

6.2.2 N_2 Dissociation

Appleton et al. [14] measured $N_2(X)$ at a distance of 3 mm from the end wall using the absorption of 117.6 nm vacuum ultraviolet light. The measured number densities are not reported directly in their publication; rather, the number densities are converted to dissociation fractions of N_2 using a simple but reasonable thermodynamic model. In the present study, the experimental data are plotted in terms of atomic nitrogen mole fraction. Comparison of the model predictions with the experimental data is shown in Figure 6.2.

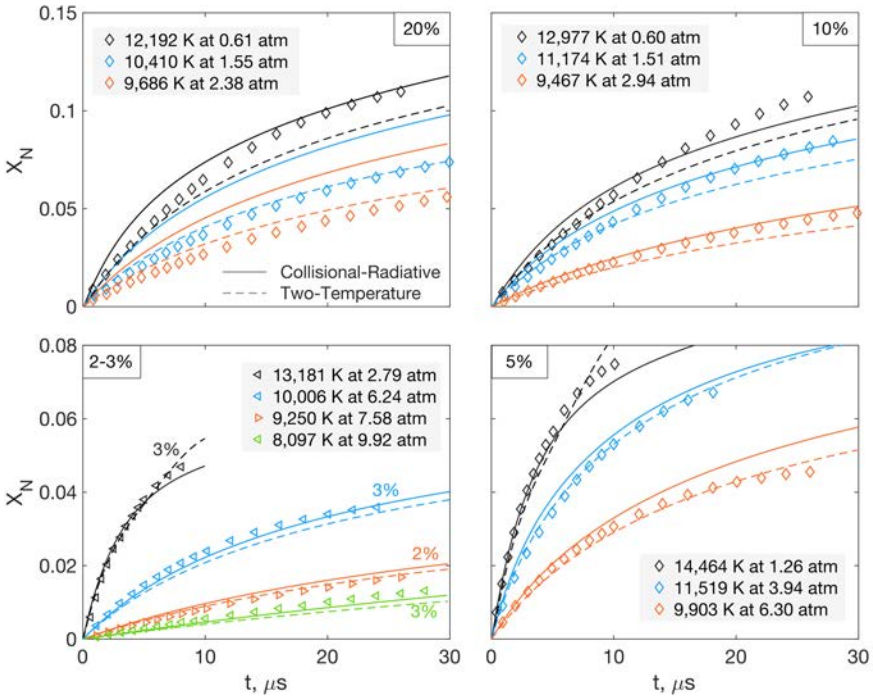

Figure 6.2: Comparison of collisional-radiative and two-temperature model predictions with the measured data from Appleton et al. [14] for the dissociation of N_2 in mixtures of 2-20% N_2 dilute in argon. Predictions from the collisional-radiative model are shown using solid lines, and, as a reference, predictions from a two-temperature model are shown using dashed lines.

In the two-temperature model, none of the individual electronic states are resolved and the electron-electronic energy is assumed to be in equilibrium with the vibrational energy at a shared vibrational-electron-electronic temperature, T_{vee}. The N_2 dissociation rate coefficients in the two-temperature model are the same as the $N_2(X)$ dissociation rate coefficients in the collisional-

radiative model, with parameters for the vibration-dissociation coupling calculated using the MMT model.

For the experiments covering 2–10% mixtures of N_2 in argon, both model formulations demonstrate good agreement with the measured data, with maximum errors rarely exceeding 10%. These results indicate that the dissociation predictions of the collisional-radiative model are sufficiently accurate to proceed with the analysis of excited state nitrogen atom kinetics in similar concentrations of N_2 dilute in argon.

For the experiments performed using a 20% N_2 test gas, the models show significant departures from the measured data, although the two-temperature model maintains a reasonable agreement with data from all but the hottest experiment in 20% N_2. Across all N_2 concentrations, the net rate of dissociation is slower in the two-temperature model than in the collisional-radiative model, with the difference between the two models increasing with the N_2 concentration. For the measurements from the 10% N_2 test gas mixtures, the higher dissociation rate of the collisional-radiative model is more consistent with the data; in contrast, the lower dissociation rate of the two-temperature model is more consistent with the data from the 20% N_2 mixtures.

In the original publication, Appleton et al. were not able to identify rate constant expressions that yielded predictions matching all of the measured data from the 10% and 20% mixtures. The present results are consistent with this finding, with the most likely explanation being that the initial condition is slightly different than that calculated using the Rankine-Hugoniot relations, the incident shock velocity, and the measured test gas fill pressure.

Source terms resulting from the dissociation of N_2 are shown in Figure 6.3 alongside the temperature profiles from the two-temperature and collisional-radiative models. The vibrational temperature is omitted because it relaxes to T_{tr} within 0.1 μs and remains in equilibrium with T_{tr} throughout the test time.

Two main reasons for the faster dissociation in the collisional-radiative model are revealed in Figure 6.3. First, the net rate of $N_2(X)$ dissociation in the CR model is faster than the rate of N_2 dissociation in the 2T model, despite the fact that both processes are modeled using the same rate

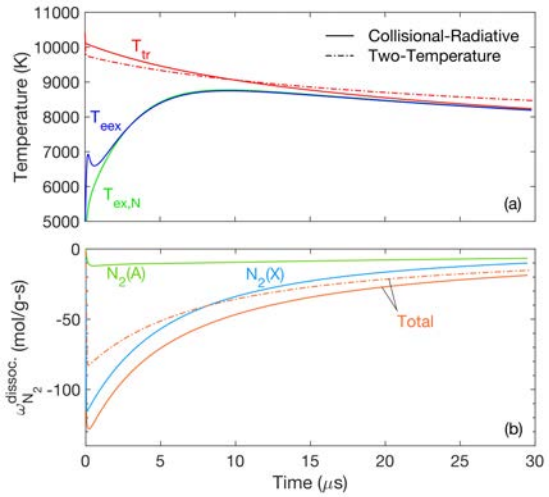

Figure 6.3: Simulated (a) temperatures and (b) N_2 dissociation source terms in the experiment from Appleton et al. [14] at 10,410 K and 1.55 atm in 20% N_2-Ar.

coefficient expressions. The reason for this difference is the lower T_{tr} in the two-temperature model, which assumes that $T_{ex,N}$ is in equilibrium with T_{vee}. Because $T_{ex,N}$ does not relax with T_{vib} in the CR model, the decrease in T_{tr} following vibrational relaxation is less than in the two-temperature model. The difference becomes more pronounced as the N_2 concentration increases and the atomic nitrogen electronic energy begins contributing significantly to e_{vee}.

Given that the CR model more rigorously simulates the relaxation of the electronic energy mode of atomic nitrogen, it should not be concluded based on the performance of the two-temperature model that the electronic temperature of $T_{ex,N}$ is truly in equilibrium with T_{vib} and T_{tr} in the Appleton experiments. Instead, the main takeaway is that a 400 K decrease in T_{tr}, like that seen here, can lead to a 35% decrease in the net rate of N_2 dissociation, indicating that uncertainties of 3-4% in the initial temperature behind the reflected shock can significantly impede model validation efforts.

The second reason that dissociation is faster in the CR model is that N_2(A) dissociation becomes appreciable as the N_2 concentration increases. The formation of N_2(A) is most efficient in the excitation reactions $N_2(X) + N \rightarrow N_2(A) + N$ and $N_2(X) + N(^2P) \rightarrow N_2(A) + N$, both of which require atomic nitrogen. Thus, as the N_2 concentration increases, the formation of N_2(A)

becomes more efficient, and the contribution of N_2(A) to the total dissociation rate goes up as well. In the last 10 μs in Figure 6.3, the rate of dissociation from N_2(A) contributes over 30% to the net dissociation rate.

Given the dispersion in the level of agreement between the CR model and the measured data in Figure 6.3, it is not possible to conclusively identify any deficiencies in the modeling of dissociation by the CR model at high N_2 concentrations. As observed in the original analysis of the experiments by Appleton et al. [14], and in the later analysis by Park [31], it is difficult to match the measurements across all experiments with one set of rate expressions. However, for the purposes of the present analysis, the predictions of dissociation are sufficiently consistent with the available data for N_2 concentrations relevant to the experiments where N(^{4}P) has been measured by Finch et al. [8].

6.2.3 Atomic Nitrogen Electronic Excitation

The nominal Region 5 initial temperatures and pressures in the six analyzed experiments from Finch et al. [8, 9] are given in Table 6.1. Measurements were performed behind reflected shocks in mixtures of 1-13% N_2 dilute in argon and spanning temperatures from 8,000-12,000 K. The laser diagnostic probed the $J = 5/2$ fine structure level of the ^{4}P term. The $J = 5/2$ level comprises half of the total degeneracy of the ^{4}P term, so the number density predictions of N(^{4}P) in the collisional-radiative model are divided by 2 when comparisons are made with the measured data.

Table 6.1: Reflected shock experiments analyzed in the present study where N(^{4}P) is measured [8, 9].

Name	X_{N_2}, %	$T_{5,0}$, K	$P_{5,0}$, atm
Finch-9	2	8,234	1.02
Finch-12	2	9,855	0.53
Finch-13	2	12,215	0.16
Finch-22	1	11,030	0.41
Finch-55	5	10,431	0.24
Finch-139	13	9,532	0.20

Pressure traces for the 1% and 2% experiments are incorporated into the simulation, while those for the 5% and 13% experiments are not available and, therefore, cannot be included. Pressure time histories from the Finch-22 and Finch-13 experiments are plotted in Figure 6.4 to illustrate two important features of the pressure traces: the overshoot of P_5 at $t = 0$ from its nominal value and the change in P_5 throughout the test time.

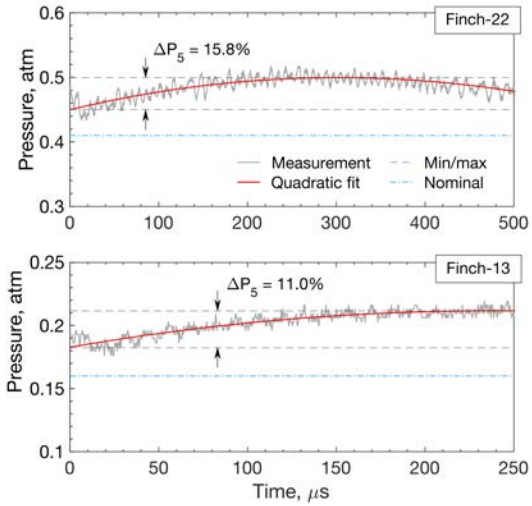

Figure 6.4: Representative pressure traces measured 5 mm from the end wall from two experiments by Finch et al. [8] with the quadratic fits used to implement the measured pressure time history into the simulations of each experiment.

The initial pressure is higher than its nominal initial value by between 6% to 16% for the experiments where P_5 time histories are available, with discrepancies increasing as the nominal value of P_5 decreases. The reason for this offset is not yet clear and warrants further study. In the current study, the measured pressure value is incorporated into the simulation by applying an isentropic compression to the Region 2 gas condition upstream of the reflected shock until the Region 5 pressure predicted by the Rankine-Hugoniot relations matches the measured value. This has the effect of increasing the temperature in Region 5 above its nominal value by as much as 3.5%. Application of the compression to Region 2 instead of Region 5 results in a smaller rise in T_5 from its nominal value and is motivated by the assumption that much of the observed overshoot in P_5 is caused by increases in the Region 2 pressure due to shock attenuation and boundary layer

growth.

The changing value of P_5 throughout the test time is fitted using a quadratic expression as shown in Figure 6.4. Time derivatives of pressure are calculated from the quadratic expression and implemented into the conservation equations using the source terms described in Section 2.3.2.

Model predictions of the N(^{4}P) number density are compared with the measured data from experiments in 1% and 2% N_2 mixtures in Figure 6.5. Predictions using two values of the reabsorption length scale, L_{rad}, are presented: L_{rad}=15.24 cm corresponds to the diameter of the shock tube, and L_{rad}=1 cm corresponds to the length scale of flow gradients in the axial direction.

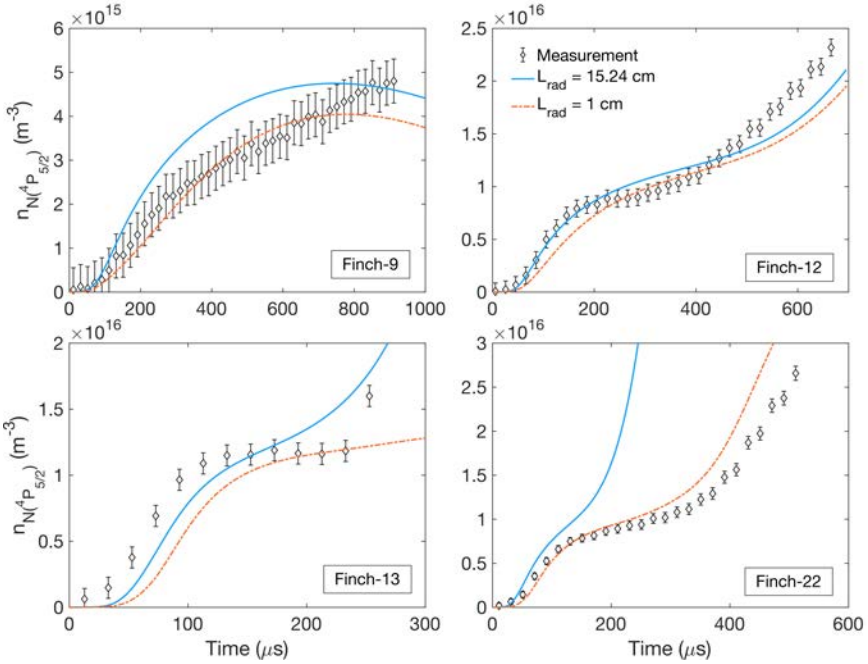

Figure 6.5: Comparison between measured data and predictions of the collisional radiative model for the experiments in Table 6.1 where the N_2 concentration is 1-2%. Model predictions are shown with two values of the self-absorption length scale, L_{rad}.

It is clear that the choice of L_{rad} can have a major impact on the predicted time histories, a result of the considerable reabsorption of vacuum ultraviolet (VUV) resonance radiation emitted at 120 nm from the $3s\ ^4\mathrm{P}\rightarrow 2p^3\ ^4\mathrm{S}$ (levels 4 to 1) transition and at 174 nm from the $3s\ ^2\mathrm{P}\rightarrow 2p^3\ ^2\mathrm{P}$ (levels 5 to 3) transition. Predictions for the Finch-22 case are most severely affected by the choice of this parameter. Because a lower value of L_{rad} implies less self-absorption, the radiative losses

from the measured state and its energetic neighbor, the $3s\ ^2$P state, compete more strongly against collisional excitation by electrons and heavy particles. As a result, the excited state population time histories predicted using $L_{rad} = 1$ cm evolve over longer timescales than those where $L_{rad} = 15.24$ cm. The mixed agreement with the measured data in Figure 6.5 shows that the choice of L_{rad} involves a tradeoff in predictive accuracy across the tested conditions.

Figure 6.5 illustrates that the collisional-radiative model is able to accurately predict many features of the excited state time histories. In all experiments, the N(^{4}P) time histories show a period of induction, lasting 50-100 μs, before the measured state begins to appreciably populate. The delay in the formation of N(^{4}P) is primarily a reflection of the time required for N_2 to dissociate. Another important factor is that the metastable N(^{2}D) and N(^{2}P) states are more efficiently excited by collisions with atomic nitrogen than with N_2 or Ar. Because the measured state is excited 10.33 eV above the ground ^{4}S state, ladder-climbing through the metastable levels is a much more efficient formation pathway than direct excitation from the ground. Because interactions between two nitrogen atoms are required to appreciably populate the metastable levels and thus facilitate ladder climbing to the ^{4}P state, the formation of N(^{4}P) is delayed until sufficient N_2 dissociation has occurred.

It's important to note that the HP-CIE rates leading to N(^{4}P) are the same for all colliders, owing to the lack of quenching or heavy particle impact excitation rate coefficients for N(^{4}P). Finch et al. [8] also found that the observed incubation time is consistent with excitation occurring primarily via N + N collisions; however, they included this effect by scaling up the rate coefficient for N + N $\rightarrow$ N(^{4}P) + N.

Previous measurements of electronically excited oxygen atoms in reflected shock experiments at similar conditions did not observe an induction time like that seen here [6, 58]. This is largely due to the faster dissociation of O_2 compared to N_2 at the studied temperatures and pressures. Additionally, the first electronically excited state of atomic oxygen is efficiently formed in collisions with argon, while the nitrogen metastable states are not.

The evolution of various system temperatures is shown in Figure 6.6. The specific time

histories are for the Finch-12 experiment; however, the behavior is similar across all of the Finch et al. [8] experimental conditions. To illustrate how the population of N(^{4}P) relates to the other mode temperatures in the gas, a two-state electronic temperature, $T_{ex,N(1,4)}$, is defined in Eq. (6.1) as the temperature characterizing the population of N(^{4}P) relative to the ground state,

$$T_{ex,N(1,4)} = \left[\frac{k_B}{\varepsilon_{ij}} \ln\left(\frac{n_1/g_1}{n_4/g_4}\right)\right] \tag{6.1}$$

where n_1, g_1, n_4, and g_4 are the number densities and electronic degeneracies of the ^{4}S and ^{4}P states, respectively. It is possible to define $T_{ex,N(1,4)}$ using the simulated time histories or the measured time histories for n_4, with the simulated ground state number density being used for n_1 in both cases.

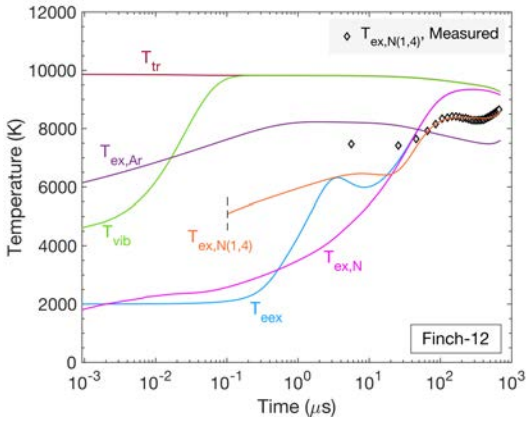

Figure 6.6: Evolution of several temperatures in the simulation of the Finch-12 experiment at 9,855 K and 0.53 atm in 2% N_2-Ar.

The simulated and measured values of $T_{ex,N(1,4)}$ are plotted alongside $T_{ex,N}$ in Figure 6.6. Because the majority of the electronic energy is contained in the metastable ^{2}D and ^{2}P levels, the value of $T_{ex,N}$ is mostly a function of those states' populations relative to the ground. The equilibrium observed in Figure 6.6 between $T_{ex,N}$ and T_{eex} thus indicates that the metastable states of atomic nitrogen are in equilibrium with the free electron temperature throughout the majority of the test time. In fact, the relaxation of T_{eex} toward T_{tr} is primarily driven by the heavy particle impact excitation of N(^{2}D) in the collision of two nitrogen atoms, followed by the superelastic

scattering of electrons to de-excite N(^{2}D) back to the ground. As a result, the dynamics of $T_{ex,N}$ and T_{eex} are highly coupled.

In three of the four experiments shown in Figure 6.5, the measured state population plateaus after approximately 100-200 μs. The plateau is also evident in Figure 6.6, occurring after the electron-electronic and translational-rotational temperatures have almost fully relaxed. Because of this, it's not possible for the plateau to be explained by the de-excitation of N(^{4}P) by electrons to the ground state as proposed by Finch et al. [8]. Instead, the plateau is caused by the onset of electron impact ionization and the strong collisional coupling between the measured state and the electronic states near the ionization limit, owing to the small energy gaps between the high-lying electronic states. Figure 6.7 shows the electronic state distributions at three time points during the simulation of the Finch-22 experiment with $L_{rad} = 1$ cm.

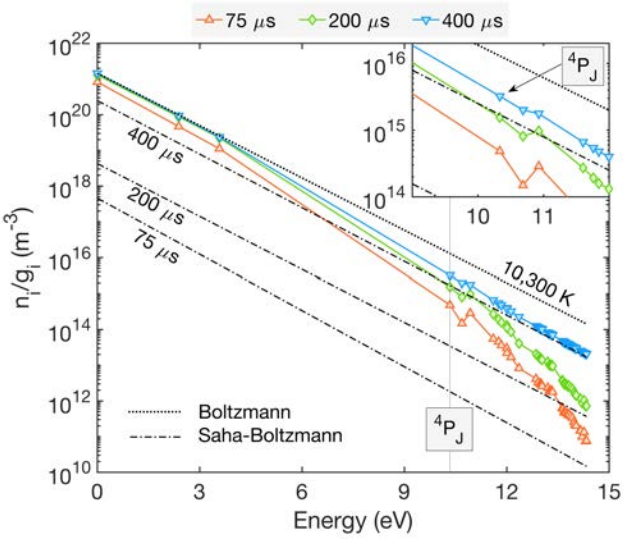

Figure 6.7: Boltzmann plot for the electronic states of atomic nitrogen at three separate times in the simulation of the Finch-22 case at 11,030 K and 0.41 atm in 1% N_2-Ar with $L_{rad} = 1$ cm .

At 75 μs, the measured state population is rising due to ladder climbing from the metastable states, which are Boltzmann populated at T_{eex}. At the next time point, 200 μs, the ^{4}P population stops rising as the highest-energy states begin rapidly ionizing due to collisions with energetic free electrons. During this time, in which the ^{4}P population briefly plateaus, the high-lying electronic

state populations are driven down toward equilibrium with the Saha-Boltzmann line shown in Figure 6.7. As more electrons are generated, three-body recombination begins to compete with electron impact ionization, and the two processes balance one another when the population of a given state reaches Saha-Boltzmann equilibrium with the continuum. The third time point plotted in Figure 6.7, at 400 μs, occurs after the plateau period as the ^{4}P population begins increasing again. In this final stage, the highest-energy electronic states are in Saha-Boltzmann equilibrium with the continuum and are rising in population as the N^+ population approaches equilibrium.

Pressure changes in Region 5 drastically alter the timescale over which the measured excited state approaches equilibrium. In Figure 6.8, model predictions obtained using a constant pressure assumption are compared with predictions obtained by taking into account the changing Region 5 pressure. Without accounting for the pressure rise, the plateau region lasts approximately twice as long as when the pressure rise is included. These results illustrate that pressure non-idealities exert a considerable influence on the measured excited state and must be included in analyses of the measured data.

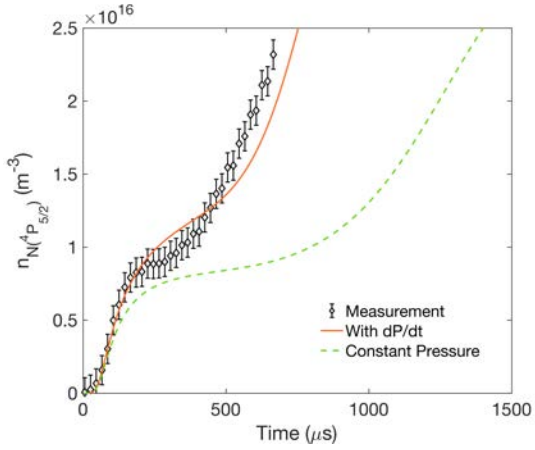

Figure 6.8: Collisional-radiative model predictions with and without the inclusion of non-ideal pressure changes for the Finch-12 experiment at 9,855 K and 0.53 atm in 2% N_2-Ar.

Note that the inclusion of non-ideal pressure rises in Figure 6.8 becomes increasingly important at late times. While the slope of the pressure rise is typically greater at early times, as seen in Figure 6.4, the total energy deposition does not become significant until several hundred microsec-

onds have passed. Total energy deposition is on the order of 2-5% of the total enthalpy, offsetting some of the temperature decrease that occurs during electron impact ionization and allowing T_{tr} and T_{eex} to remain 200-400 K hotter than in the constant-pressure case. Ionization is controlled primarily by the electronic excitation rate of argon, which occurs across an 11.5 eV energy barrier – at 9,000 K, the rate of excitation across this barrier is doubled when the temperature is increased to 9,400 K. As in the previous analysis of N_2 dissociation kinetics, small changes in the gas temperature significantly affect the highly endothermic dynamics being studied.

Three other experiments at higher N_2 concentrations were also performed by Finch [9]. Pressure data is not available for these experiments; however, the pressure rise is most important for predicting the third-stage rise in the ^{4}P population, which does not occur within the available test time. Model predictions are compared with the measured data for the Finch-55 and Finch-139 experiments in Figure 6.9. Uncertainty data are not available for the Finch-55 and Finch-139 experiments, so the error bars in Figure 6.9 are estimated using the average error from the 1% and 2% data.

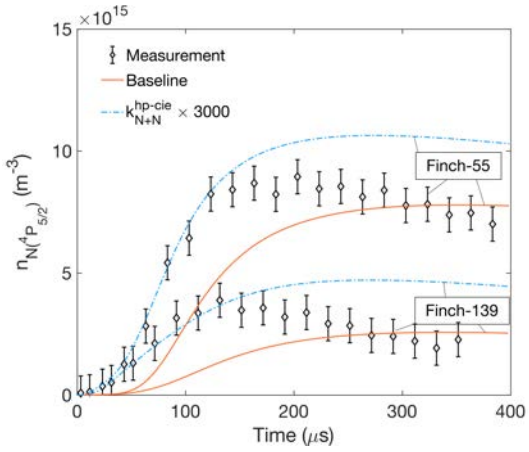

Figure 6.9: Comparison of model predictions with the Finch-55 and Finch-139 experiments performed in 5% and 13% mixtures of N_2 in argon, respectively. Baseline collisional-radiative model predictions are shown alongside predictions where the rate coefficient of HP-CIE reactions involving N + N collisions are scaled up by 3,000 whenever the rate from Lemal et al. [15] is used.

Predictions from the baseline collisional-radiative model in Figure 6.9 only match the measured data during the second half of the test time. At early times, the measured N(^{4}P) population

rises much faster than the model predicts. The difference between the measured and simulated populations increases proportional to the initial N_2 concentration, indicating that some process involving N_2 or N is likely to blame for the discrepancy. For the HP-CIE reactions involving N + N collisions where the analytical formula from Lemal et al. [15] has been used to approximate the rate coefficient, a scaling of the rate coefficient by a factor of 3000 brings the early-time N(^{4}P) population into agreement with the measurement for the 5% and 13% experiments. The same scaling also improves agreement with the early time history data in the Finch-13 experiment, where similar discrepancies are observed. Note that the scaling by 3000 brings the HP-CIE rate coefficients into closer agreement with those proposed by Park [17] and Annaloro and Bultel [121]. However, by changing these rate coefficients, the predicted time history consistently overshoots the measured values near the end of the test time when some loss mechanism for the N(^{4}P) appears to be active.

The present discrepancies between model predictions and measured data in 5% and 13% mixtures of N_2 illustrate the need for further measurements of excited state chemistry with larger concentrations of N_2 where excitation reactions involving N + N show a measurable influence. With additional data involving higher N_2 concentrations, it will be possible to better constrain the kinetics of reactions relevant to electronic excitation kinetics in air.

6.3 Sensitivity Analysis

6.3.1 Parameters and Response Functions

Collisional-radiative model predictions are the result of hundreds of different parameters that are implemented into the model. In order to quantitatively assess which of these parameters most strongly influence the predicted excited state time histories, a sensitivity analysis is performed and is described in the present Section.

Convergence of the PCE surrogate is monitored by tracking the maximum change to any given Sobol' index after solving for the basis coefficients with an increased number of samples. In the present study, Sobol' indices are evaluated after every 40 additional samples, and a total of

3,000 samples are run for each analyzed experiment. Throughout the last 1,000 sample evaluations, none of the Sobol' indices change by more than 0.01, indicating that the PCE surrogate converges with sufficient accuracy.

The quantity of interest in the sensitivity analysis is the number density of N(^{4}P) at each time after the passage of the shock. Thus, Sobol' indices are calculated for each model parameter as a function of time. Convergence of the PCE surrogate coefficients is improved significantly by fitting the surrogate to the logarithm of the excited state number density rather than to the number density directly. The Sobol' indices do not change meaningfully between surrogate models fitted to the number density or its logarithm.

6.3.2 Results

Sensitivity analysis results for three of the cases analyzed in Section 6.2.3 are presented in this Section and are representative of the sensitivities across all cases. The total Sobol' indices are shown on area plots to provide a clear and intuitive picture of the dominant sensitivities in each experiment. Because total Sobol' indices include interaction effects, which are included in the indices of both parameters involved in a given interaction, the sum of the total Sobol' indices can exceed unity. Before plotting, the total Sobol' indices are normalized so that their sum equals one.

Total Sobol' indices are presented for the Finch-9 experiment in Figure 6.10. The dissociation of N_2(X) with argon is the most sensitive parameter throughout the entire test time. This is true for all of the analyzed experiments; however, the sensitivity to N_2(X) dissociation with argon is the most pronounced in the Finch-9 experiment. Because the Finch-9 case is the lowest temperature experiment available, the observed high sensitivity to N_2 dissociation indicates that measurements at lower temperatures will rely heavily on accurate modeling of N_2 dissociation to enable accurate characterization of other processes occurring in the gas.

The next most sensitive process is the electron impact excitation of atomic nitrogen from its metastable ^{2}D level to the measured ^{4}P level, highlighting the importance of ladder-climbing to the formation of N(^{4}P). Several other electron impact excitation processes also show notable

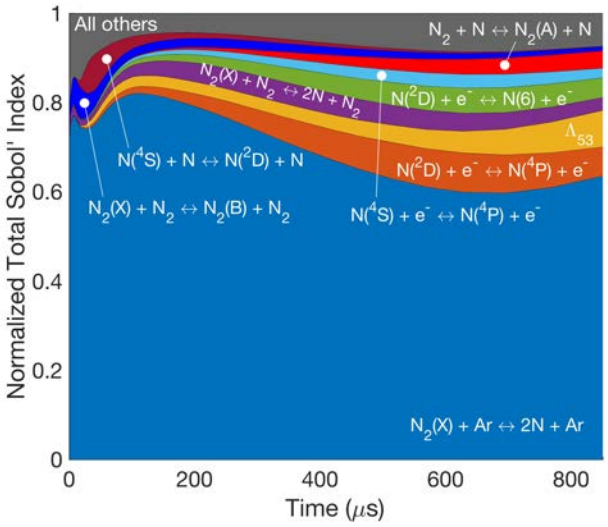

Figure 6.10: Normalized total Sobol' indices for the prediction of N(^{4}P) number density in the Finch-9 experiment with T_{tr}=8,234 K at P=1.02 atm in 2% N_2-Ar.

sensitivity, including the excitation of ^{4}P from the ground state and the collisional excitation of the sixth excited state of N, which is strongly coupled to the measured state by electron impact excitation. Processes involved in the formation of N_2(A) demonstrate sensitivity as well, likely caused by the role that N_2(A) plays in the net dissociation of N_2. The sensitivity of N_2(B) formation may be understood by considering the fact that N_2(A) and N_2(B) are strongly coupled via heavy particle impact excitation and the fast energy pooling reaction between two N_2(A) molecules that forms N_2(B). Finally, significant sensitivity is observed for the escape factor for the transition from nitrogen in its fifth excited state, $3s\ ^2$P, to its third excited state, the $2p^3\ ^2$P level. Sensitivity to the escape factor is consistent with the large effect of the self-absorption length scale, L_{rad}, discussed in Section 6.2.3.

Sobol' indices for the N(^{4}P) time history prediction in the Finch-12 case are shown in Figure 6.11. Dissociation of N_2 remains highly sensitive, as do several of the same electron impact excitation reactions that demonstrated high sensitivities at the Finch-9 experimental conditions. Because ionization begins to play a more significant role in the higher-temperature Finch-12 experiment, the excitation of argon to its fifth excited level shows increased sensitivity. Excitation of

$N(^2D)$ in the collision of two ground-state nitrogen atoms is also highly sensitive since this reaction strongly influences the relaxation time of the free electrons.

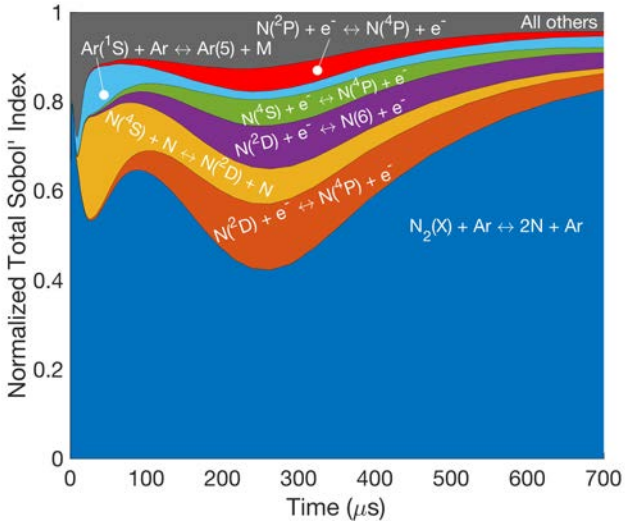

Figure 6.11: Normalized total Sobol' indices for the prediction of $N(^4P)$ number density in the Finch-12 experiment with T_{tr}=9,855 K at P=0.53 atm in 2% N_2-Ar.

The Sobol' indices in Figures 6.10 and 6.11 are representative of all 1% and 2% experiments analyzed. The observed dynamics are largely controlled by the dissociation rate of N_2 and several electron impact excitation reactions that proceed from the ground and metastable electronic states of N. The heavy particle impact excitation of $N(^4P)$ does not show significant sensitivity for any of the cases analyzed; only the excitation of metastable $N(^2D)$ showed a notable level of sensitivity. These results highlight the importance of including metastable states and ladder-hoping transitions when interpreting experimental measurements of high-lying atomic excited states.

Figure 6.12 presents the Sobol' indices for the prediction of $N(^4P)$ number densities in the Finch-139 experiment, which had the highest N_2 concentration at 13%. A notable increase in the number of sensitive parameters is observed, with a more even distribution of Sobol' index magnitudes among the top parameters than in the 1% and 2% experiments. Several of the same sensitive processes from the Finch-9 case reappear in the Finch-139 sensitivity results but with even higher Sobol' indices. The excitation exchange between $N_2(A)$ and $N(^2P)$ shows notable sensitivity

in the Finch-139 experiment but not in the Finch-9 or -12 experiments. The rate coefficient of this process is important for determining the population of $N_2(A)$, in turn affecting the net dissociation rate of N_2.

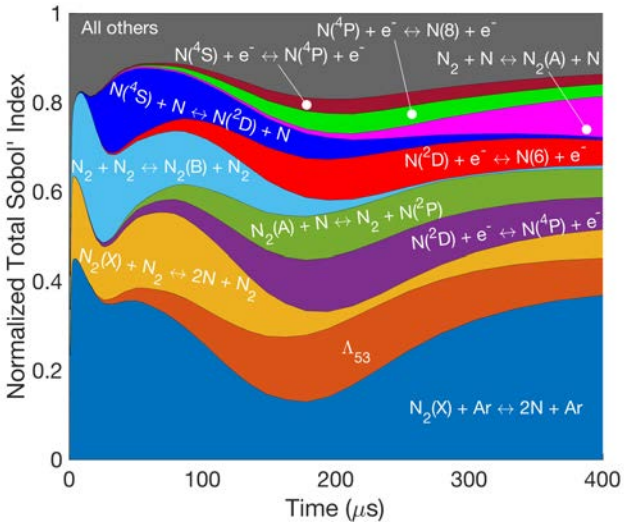

Figure 6.12: Normalized total Sobol' indices for the prediction of N(^{4}P) number density in the Finch-139 experiment with T_{tr}=9,532 K at P=0.20 atm in 13% N_2-Ar.

The more equal distribution of process sensitivity in the Finch-139 case illustrates the value of performing additional N(^{4}P) measurements in mixtures with greater amounts of N_2 present. The discrepancies between the model predictions and the measured data are a promising indication that the collisional-radiative model could be improved with further data at elevated N_2 concentrations. Sensitivity results in this Section also call attention to the importance of N_2(A), both for its exchanges with N(^{2}P) and its influence on the net dissociation rate. Measurements of N_2(A), like those in Jans et al. [207], would provide valuable constraints on the excitation kinetics predicted by the present model.

6.4 Summary

The dissociation and electronic excitation of atomic nitrogen were studied in this chapter using measured data for the concentrations of N_2(X) and atomic nitrogen in its fourth excited

state, N(^{4}P), behind reflected shock waves in mixtures of 2-20% N_2 dilute in argon. Because dissociation is ongoing during the experiments where N(^{4}P) was measured, the collisional-radiative model predictions for dissociation were assessed first. The model predictions were consistent with measurements of N_2(X) in mixtures of 2-10% N_2 from 8,000 to 14,000 K, indicating that the model is appropriate to apply for the gas mixtures in which N(^{4}P) was measured. Model predictions diverged from the measured data for some of the experiments in 20% N_2-Ar; however, previous authors have also been unable to match all of the 20% data using a single set of rate coefficients. It was shown that temperature differences on the order of 3% can be sufficient for explaining the observed discrepancies. In addition, the dissociation of N_2(A) contributed up to 30% to the net N_2 dissociation rate for the 20% mixture of N_2 in argon. Future studies should investigate the role of N_2(A) in net N_2 dissociation.

Comparison of model predictions with N(^{4}P) measurements yielded several novel insights. Predictions were consistent with the measured data for 1-2% mixtures of N_2 in argon from 8,000 to 12,000 K, with discrepancies typically being bounded between limiting values of the radiation self-absorption length scale. The choice of self-absorption length scale had a significant impact on model predictions for several of the analyzed experiments. This creates difficulty when attempting to conclusively validate rate coefficients for collisional processes using measurements of N(^{4}P). Adding to this difficulty is the large effect on model predictions that was observed when the measured non-ideal pressure rises were incorporated into the simulation. The inclusion of non-ideal pressure rise caused the measured state to relax toward equilibrium nearly twice as fast as when the pressure was assumed to be constant.

The multi-stage behavior observed in the experiments was well-matched by the developed model; however, as in the O_2-Ar experimental analysis, the reasons for the multi-stage behavior were different than those proposed by previous authors. Rather than being populated by direct excitation from the ground, the measured state was more efficiently populated by ladder-climbing through the metastable levels. These metastable levels are excited efficiently by nitrogen atoms but not by N_2 or Ar, leading to the induction time observed in the experiment.

Comparisons with measured data from 5% and 13% mixtures of N_2 in argon revealed that the collisional-radiative model may not be accurately capturing the effect of N + N collisional excitation processes. Further experiments with elevated N_2 concentrations are recommended to help better constrain the collisional-radiative model.

Sensitivity analyses of the measured excited state population were performed for a representative selection of the analyzed experiments. The N_2(X) dissociation rate constant with argon was the most sensitive parameter across all analyzed experiments, underscoring the value of assessing dissociation predictions using experimental data. As in the oxygen excited state measurements, the population of N(^{4}P) was influenced by processes involving levels of higher and lower energy. Only a detailed model like that adopted here can capture the dominant processes influencing the measured excited state population. For the experiment performed in 13% N_2 in argon, a greater diversity of air-relevant kinetic processes showed notable sensitivity than in the 1% and 2% experiments, again highlighting the value of additional experiments with higher N_2 concentrations.

Chapter 7

Modeling and Sensitivity Analysis of Electronic Excitation and Ionization in Air

*Some of the contents of this chapter have been presented at the **AIAA AVIATION Forum** in 2023 [208]. Reproduced with the permission of the American Institute of Aeronautics and Astronautics.*

7.1 Introduction

This chapter is devoted to the study of ionization in shock-heated air flows and is broken into three major sections. In Section 7.2, a sensitivity analysis of a two-temperature model is performed to identify the chemical reaction and relaxation rate parameters that most significantly influence ionization predictions. While a two-temperature model does not adopt a high-fidelity treatment of the nonequilibrium behavior leading to ionization, its computational efficiency makes it ideal for vehicle-scale hypersonic flow simulations. In studying it, the present work aims to provide recommendations for the parameters that most significantly affect the prediction of electron number density in the flowfields surrounding hypersonic vehicles.

Figure 7.1 illustrates an electron number density distribution that is typical of the flow around a slender hypersonic vehicle. Electron number densities are highest in the stagnation region due to the high temperatures and pressures induced by the normal shock. Moving downstream from the stagnation region, the electron number density decreases as the flow expands and cools. To accurately model charged species densities throughout the whole flowfield, nonequilibrium mod-

els must accurately capture both the post-shock generation of electrons and the post-expansion recombination of those electrons.

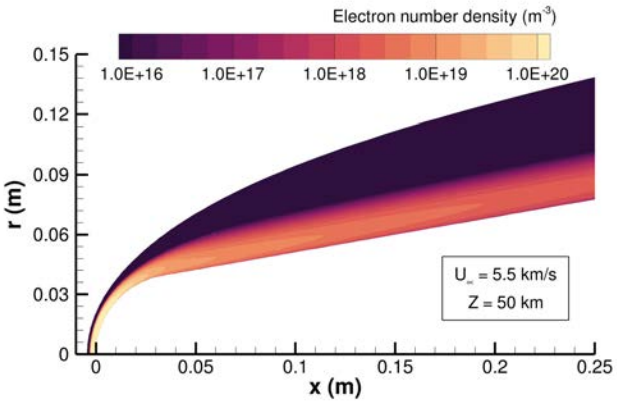

Figure 7.1: Electron number density in the flowfield around a slender hypersonic vehicle flying at 5.5 km/s with freestream conditions corresponding to 50 km altitude in the Earth's atmosphere.

Thus, both shock-heated and cooling flows are analyzed in Section 7.2 to characterize the uncertainties and sensitivities of two-temperature models in all nonequilibrium flow regions surrounding hypersonic vehicles.

The focus then changes to predictions of ionization by the collisional-radiative model in Sections 7.3 and 7.4. The effects of electronic nonequilibrium on ionization predictions behind strong shock waves are studied in detail in Section 7.3. Due to the uncertainty in HP-CIE process rate coefficients, ionization predictions are assessed using several limiting values for the HP-CIE rate coefficients. A sensitivity analysis of ionization predictions behind strong shock waves by the collisional-radiative model is then presented in Section 7.4.

7.2 Sensitivity Analysis of Ionization in a Two-Temperature Model

The shock-heated flows analyzed in this Section are modeled using the incident shock governing equations described in Section 2.3.1. The recombining flow scenarios are modeled using zero-dimensional adiabatic and isochoric chemical reactors, which obey the governing equations in Section 2.2.

7.2.1 Parameter Uncertainties

The following uncertain parameters are considered in the sensitivity analysis of the two-temperature model:

- Arrhenius pre-exponential factors for each of the 47 reactions in the 11-species [1] model of air;
- scale factors on the vibrational-translational relaxation times for N_2 and O_2 with partners N_2, O_2, N, and O;
- scale factors on the energy exchange cross-section for electron-translational relaxation in collisions with N and O.

All uncertain parameters are sampled in logarithmic space from a uniform distribution defined by upper and lower uncertainty bounds. The baseline rate coefficients and uncertainty intervals for the 47 reactions in the two-temperature model are taken from [102], who determined uncertainty intervals following an extensive review of available data. No such reference exists for uncertainty intervals on VT relaxation times, so a literature review is performed to obtain the relaxation times and uncertainty intervals given in Table 7.1.

Table 7.1: Baseline formulations for VT relaxation times and relative uncertainty intervals for each.

Target	Collider	Baseline $P\tau_{vt}$	U_i	Uncertainty Ref.
N_2	N_2	[78]	[0.3, 1.5]	[78]
N_2	N	[78]	[0.5, 2.0]	[78]
N_2	O_2	[1, 2]	[0.1, 10.0]	[209]
N_2	O	[1, 2]	[0.1, 10.0]	[209]
O_2	O_2	[5]	[0.5, 2.0]	[5]
O_2	O	[77]	[0.5, 4.0]	[209, 77]
O_2	N_2	[1, 2]	[0.1, 5.0]	[209]
O_2	N	[1, 2]	[0.3, 2.0]	[209]

Intervals, U_i, correspond to the multiplicative factors applied to the baseline rate to obtain upper and lower uncertainty bounds. Relaxation times are scaled up and down by an order of

magnitude whenever there is no experimental data to inform uncertainties at high temperatures. Following [57], the eT energy exchange cross-sections for N and O are scaled up and down by an order of magnitude from the baseline formulations given by Gnoffo [76].

7.2.2 Sampling

For the 58 uncertain input parameters considered in the current study, a total of 1,770 deterministic model evaluations are required to fully determine the point collocation solution – an achievable number of samples with reasonable computational cost. Following recommendations from Hosder et al. [210], a total of 3,540 samples are run for each analysis to achieve an oversampling ratio (OSR) equal to two.

7.2.3 Results

The quantities of interest in the current study are the number density and mole fraction of free electrons. Sobol' indices are calculated for these quantities at a set of 50 logarithmically spaced x and t values for the 1D and 0D simulations, respectively. The electron mole fraction is considered in order to distinguish between sensitive processes that influence the electron number density, n_e, via ionization and those that influence electron number density primarily through bulk density variation. Electron mole fraction sensitivities are found to be similar to the electron number density sensitivities, indicating that the processes influencing n_e are sensitive because of the ionization kinetics and not bulk density variation; therefore, only the n_e sensitivities are shown.

Confidence intervals for the electron number density are an important component of the present study. To most accurately represent these intervals and the variances used to calculate them, the PCE surrogate is fit to the logarithm n_e instead of to n_e directly. The Sobol' indices do not change significantly when $\log(n_e)$ is used as the QoI instead of n_e; however, the 95% confidence intervals become much more reasonable with the logarithmic QoI and do not encompass negative values as is the case when n_e is the QoI. The logarithm of the electron number density is therefore chosen as the QoI based on these favorable properties of the PCE surrogate.

7.2.3.1 Shock-heated flows

Table 7.2 outlines the shock-heated flow conditions analyzed in this Section. Sensitivity analyses are run for shock velocities at 1 km/s intervals from 5-9 km/s and the results at 5, 7, and 9 km/s are found to be sufficient for describing the variation of sensitive parameters throughout velocity space. Freestream conditions corresponding to 30 and 60 km altitudes are tested; however, only the 60 km results are shown. Results at 30 km are found to be qualitatively similar, highlighting the same sensitive processes that influence n_e at 60 km.

Table 7.2: Post shock flow conditions, all have a freestream T_{tr} = 247.0 K and P=2.20 Pa corresponding to 60 km altitude.

	Normal Shock Velocity		
	5 km/s	7 km/s	9 km/s
P (Pa)	6,422	12590	20,820
T_{tr} (K)	12,280	23,850	39,270
T_{vee} (K)	247.0	247.0	247.0
X_{O_2}	0.21	0.21	0.21
X_{N_2}	0.79	0.79	0.79

Total Sobol' indices are shown alongside the electron number density profile behind a 5 km/s shock in Figure 7.2. The x-axis is scaled logarithmically to illustrate the processes that influence the electron number density over a range of length scales. During the most active region of ionization, where n_e is changing the fastest, the associative ionization to form NO^+ dominates the uncertainty. This is the expected result, considering that NO^+ is the dominant ion at the 5 km/s condition. Before n_e begins rising appreciably, the dissociation of O_2 with partner N_2 and the AI to form O_2^+ are most sensitive. Sensitivity to O_2 dissociation is expected since oxygen atoms are required before AI to form O_2^+ or NO^+ can begin.

Downstream of 1 cm behind the shock, the dominant sensitive reactions all involve NO. In particular, the sensitivity is dominated by the second Zel'dovich reaction, $O_2 + N \leftrightharpoons NO + O$, as well as NO dissociation with partners N and O. The importance of these reactions to the formation of free electrons is clarified through an analysis of the source term for NO^+ plotted in Figure 7.3.

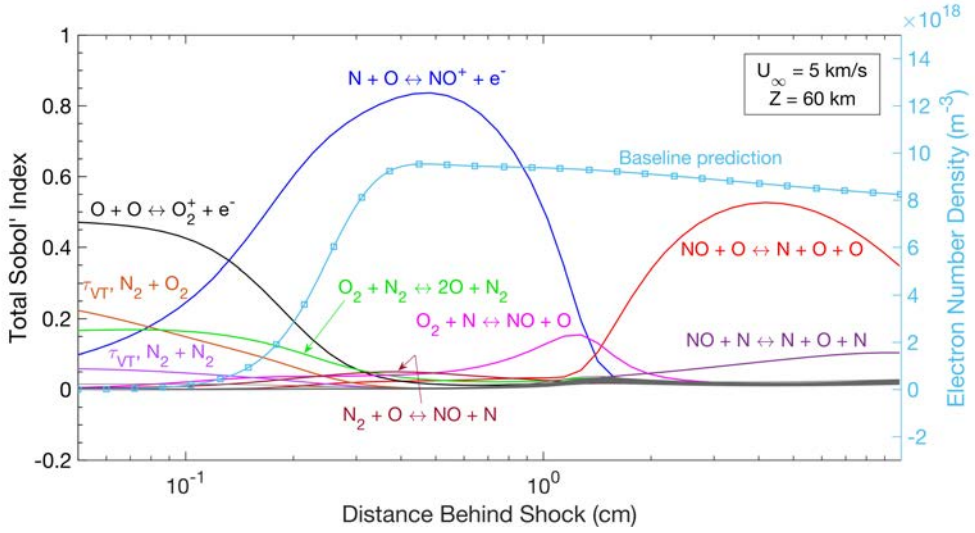

Figure 7.2: Total Sobol' indices for the electron number density profile behind a 5 km/s normal shock with freestream conditions corresponding to 60 km altitude.

The NO^+ source term begins in a net ionizing (forward) direction before transitioning to a net recombining (backward) direction at x = 0.46 cm, indicating that NO^+ ions are dissociatively recombining with electrons to form N and O.

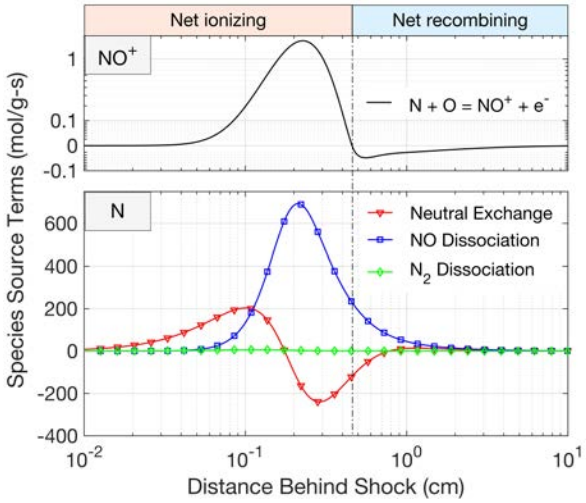

Figure 7.3: Dominant source terms for N (bottom) and NO^+ (top) in the 5km/s normal shock condition.

Dissociative recombination occurs in post-shock flows when the electron number density overshoots its equilibrium value, a result of n_e increasing toward equilibrium with the translational

temperature that is simultaneously decreasing due to vibrational relaxation and dissociation. At 5 km/s, the overshoot caused by this effect is mild because associative ionization is not proceeding rapidly. The overshoot is more pronounced at the higher shock velocities of 7 and 9 km/s, where associative ionization occurs more rapidly, forming an overabundance of electrons that then recombine as the temperature drops due to vibrational relaxation and dissociation.

Nitric oxide chemistry is important during the recombination period because NO is the dominant species involved in the production of nitrogen atoms, which are important to the net rate of dissociative recombination. Figure 7.3 also illustrates the dominant source terms for atomic nitrogen; NO dissociation and neutral exchange (Zel'dovich) reactions dominate, while direct N_2 dissociation is negligible. The sensitivity of these nitrogen-generating reactions implies that uncertainty in the population of nitrogen atoms is the dominant contributor to the predictive uncertainty of electron number density during the net recombining phase behind the 5 km/s shock.

The mean and 95% confidence intervals for the electron number density in the 5 km/s normal shock case are given in Figure 7.4. The variance is significant near the peak value of n_e, implying that the existing uncertainty in the rate of associative ionization to form NO^+ is associated with major predictive uncertainties in ionization at suborbital velocities. Downstream of 1 cm behind the normal shock, the uncertainty in the predicted electron number density decreases significantly. Referring to Figure 7.2, the dominant sensitive processes within the first 1 cm behind the shock are the associative ionization reactions to form O_2^+ and NO^+. Based on the small uncertainty intervals downstream of 1 cm in Figure 7.4, neutral chemical processes do not contribute meaningfully to the absolute uncertainty in the n_e prediction in the 5 km/s condition.

Mole fractions of ionized species are plotted in Figure 7.5 for the 7 km/s normal shock condition. Associative ionization to form O_2^+ dominates the early production of electrons, but charge exchange to form NO^+ and N^+ quickly depletes the O_2^+ population before the peak electron concentration is achieved. In contrast to the 5 km/s condition, where NO^+ is the only ionic species present in appreciable quantities, the atomic ions O^+ and N^+ begin significantly contributing to the net equilibrium electron concentration at 7 km/s.

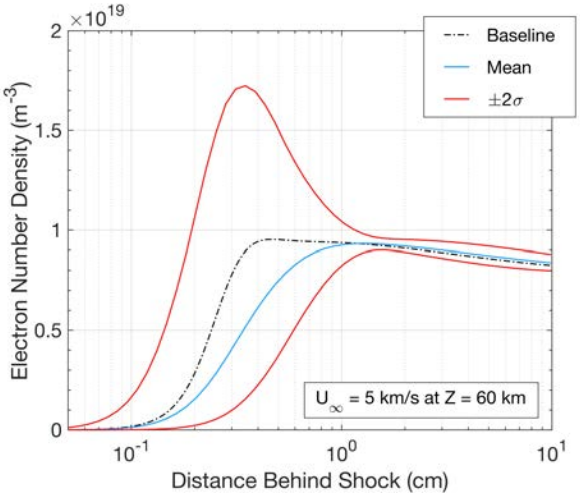

Figure 7.4: Absolute uncertainty of the electron number density predictions for the 5 km/s normal shock condition.

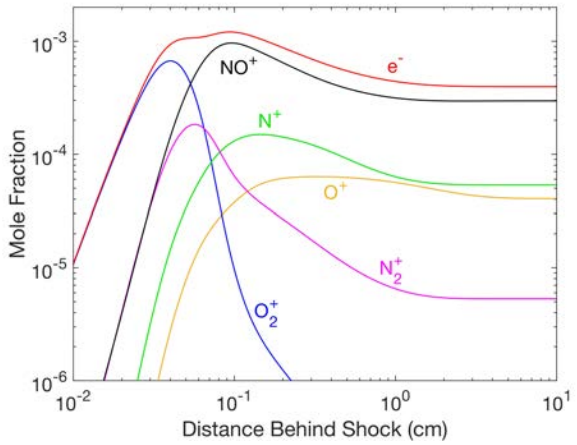

Figure 7.5: Mole fractions of charged species in the 7 km/s normal shock case.

Mole fractions in Figure 7.5 provide essential context for interpreting the Sobol' indices in Figure 7.6 for the electron number density profile behind the 7 km/s normal shock. A greater diversity of processes influences the predicted n_e profile at 7 km/s than is observed for the 5 km/s condition. This complexity arises in part because of the greater diversity of ionic species. Additionally, the increased equilibrium dissociation fraction of N_2 means that the first Zel'dovich reaction, which breaks down N_2 with a lower energetic barrier than direct N_2 dissociation, also demonstrates increased importance at 7 km/s.

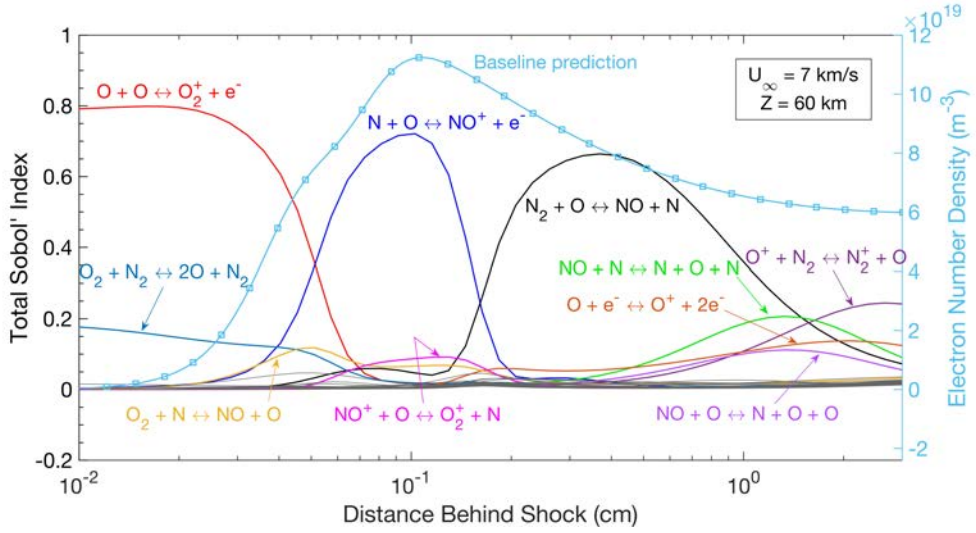

Figure 7.6: Total Sobol' indices for the electron number density profile behind a 7 km/s normal shock with freestream conditions corresponding to 60 km altitude.

It is again useful to consider the total Sobol' indices with respect to the predictive uncertainty at each point behind the shock. To clarify the relation between Sobol' indices and total variance, the 95% confidence intervals in Figure 7.7 are shown alongside an area plot that is generated by multiplying the total Sobol' indices at each point by the width of the 95% confidence intervals for n_e at that point. The area plot provides a simple visual representation of the relative contribution made by each process to the changing absolute uncertainty level. The gray strip at the top of the area plot is the summed uncertainty contribution from the 52 unlabeled processes on the plot. Note that the Sobol' index profiles in Figure 7.6 provide a more complete picture of the process sensitivities, while the area plot in Figure 7.7 highlights only the top sensitive reactions at the post-shock locations with greatest predictive uncertainty.

Results in Figure 7.7 show that associative ionization to form NO^+ is still dominant near the peak value of n_e, signifying that AI to form NO^+ is the most sensitive determinant of the maximum electron number density under these conditions. Immediately downstream of the location where n_e peaks, the most sensitive reaction switches to the first Zel'dovich reaction, $N_2 + O \leftrightharpoons NO + N$, which is the dominant contributor to the approximately $\pm 20\%$ uncertainty in n_e at 0.3 cm behind the shock. Downstream of 1 cm behind the shock, NO dissociation with N and O becomes the

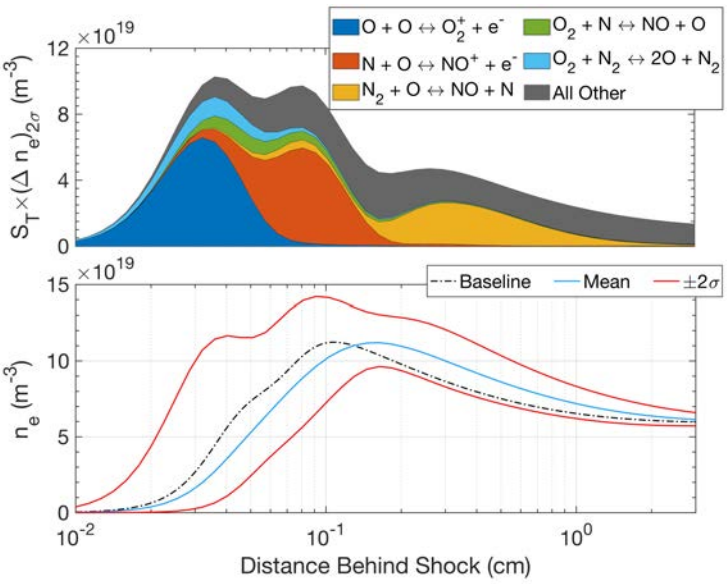

Figure 7.7: 95% confidence bounds for n_e predictions behind the 7 km/s normal shock (bottom) and visualization of the absolute uncertainty contribution from each parameter (top).

dominant source of predictive uncertainty.

While the specifics of the Sobol' indices differ between 5 and 7 km/s, the general trend is similar: associative ionization to form O_2^+ and NO^+ dominates the electron number density uncertainty near the shock, while NO kinetics dominate the region downstream of peak n_e where the electron population is falling. The main difference between the 5 and 7 km/s normal shock conditions is that the absolute uncertainty is increased for the 7 km/s case during the fall-off from peak electron number density.

Similarities in the sensitivities at 5 and 7 km/s may have been expected based on the dominance of molecular ions at equilibrium for both enthalpies. In contrast, the dominant ions in the 9 km/s normal shock condition are atoms. The mole fractions of ionic species are plotted in Figure 7.8 for the 9 km/s normal shock condition. As in the 5 and 7 km/s conditions, the formation of O_2^+ occurs first, but its mole fraction then falls quickly due to charge exchange with the ions that will come to dominate at equilibrium. The N_2^+ ion is briefly dominant but is quickly superseded by the N^+ population being driven upwards first by charge exchange with O_2^+, NO^+, and N_2^+, and later by electron impact ionization.

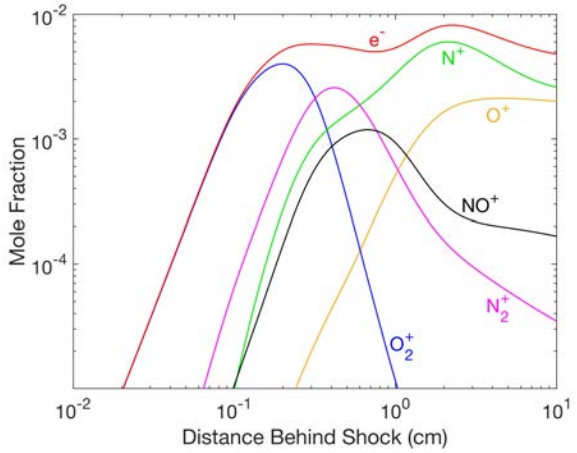

Figure 7.8: Mole fractions of charged species in the 9 km/s normal shock case.

Sobol' indices for the electron number density prediction behind the 9 km/s shock are presented in Figure 7.9. The number of highly sensitive parameters is greatly increased compared to the 5 and 7 km/s conditions. The increased complexity of the sensitivity results reflects the increased complexity of the chemical pathway leading to atomic ion formation, as opposed to that leading to molecular ion formation, the latter of which is found in this study to overwhelmingly depend on just the rate of associative ionization. Atomic ions, in contrast, are most efficiently formed via charge exchange and reassociation reactions, as well as by electron impact ionization.

Charge exchange reactions, which begin to show increased sensitivity at 7 km/s, become dominant contributors to the electron number density uncertainty at the 9 km/s condition. These reactions are important because, while associative ionization is still the dominant path to form electrons near the shock front, the dominant ion at equilibrium is actually N^+, as seen in Figure 7.8. Charge exchange reactions serve to move charge from the rapidly-produced O_2^+ ions, which dominate the early rise in n_e, to the O^+ and N^+ ions. By moving charge over to the atoms, more molecular ions can be generated and ionization can continue to proceed at the rapid, AI-controlled rate. The Sobol' indices in Figs. 7.6 and 7.9 indicate that this process is rate-limited by the reassociation reaction $NO^+ + O \leftrightharpoons O_2^+ + N$, and via direct charge exchange between O_2^+ and N^+.

In addition to the Zel'dovich exchange reactions, the direct dissociation of N_2 becomes a

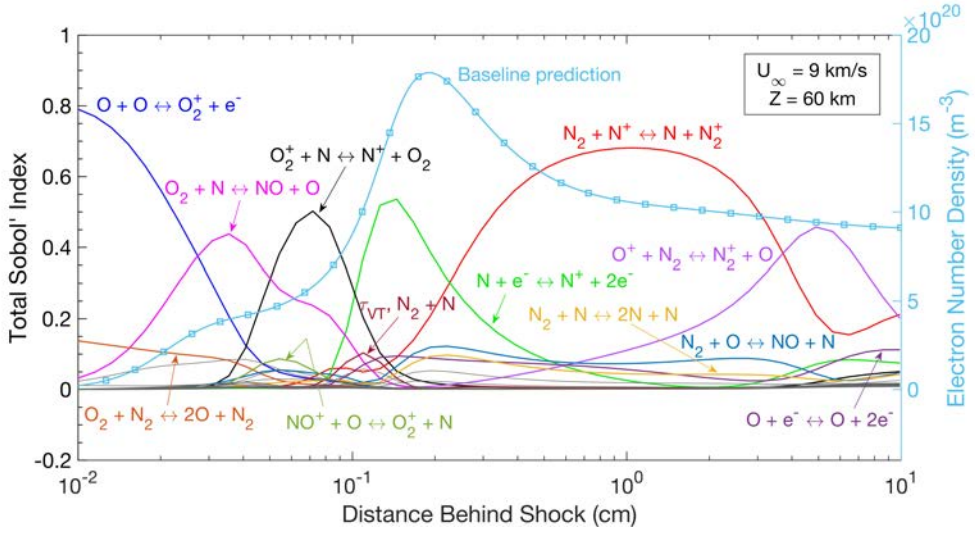

Figure 7.9: Total Sobol' indices for the electron number density profile behind a 9 km/s normal shock with freestream conditions corresponding to 60 km altitude.

major contributor to the production of nitrogen atoms at 9 km/s. This fact is reflected in the appearance of N_2 dissociation with N_2 as a sensitive rate in Figure 7.9. The AI to form NO^+ is notably absent from the list of dominant reactions because O_2^+ is the dominant molecular ion early in the time history. Reactions generating atomic nitrogen are also sensitive during this early time period near the shock front, likely due to their role in forming N_2^+.

The electron number density profile exhibits a sharp change in slope at approximately 1 mm behind the shock, brought on by the onset of electron impact ionization. Both the electron source terms and the Sobol' indices reflect the dominance of electron impact ionization to form N^+ during this time. Downstream of the peak, the charge exchange from N^+ to N_2 becomes the dominant contributor to the overall uncertainty.

Uncertainties in the n_e profile for the 9 km/s post-shock condition are presented in Figure 7.10 alongside the parameter-specific contributions to the overall uncertainty. Similar to the previous two velocities analyzed, the greatest uncertainty is found at the peak electron number density value. The peak value varies across nearly an order of magnitude within the 95% uncertainty bounds at 0.2 cm behind the shock. The majority of the uncertainty at the location where n_e peaks is driven by electron impact ionization to form N^+ and O^+, as well as N_2 dissociation with N and the

first Zel'dovich reaction. Once the electron concentration begins to fall from its peak value, the dominant contributor to the uncertainty becomes the charge exchange between N_2^+ and N.

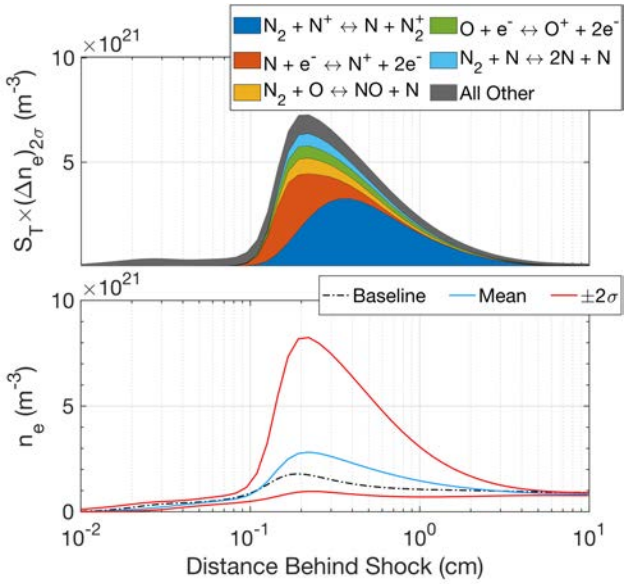

Figure 7.10: 95% confidence bounds for n_e predictions behind the 9 km/s normal shock (bottom) and visualization of the absolute uncertainty contribution from each parameter (top).

Comparison of the Sobol' indices in Figure 7.9 and the uncertainty intervals in Figure 7.10 illustrates the value of presenting Sobol' indices within the context of total variance. Without consideration of the regions where n_e is most uncertain, the Sobol' index results in Figure 7.9 seem to motivate the increased study of a multitude of reactions. However, when considered in context with the regions where the n_e variance is greatest, as in Figure 7.10, the number of reactions meriting further study is greatly decreased. A similar effect is also observed for the sensitivity results at 5 and 7 km/s.

7.2.3.2 Recombining flows

The post-shock flows analyzed in the previous Section are illustrative of the vehicle stagnation point, where the electron number density is highest. Outside of this small region, the electron number density is influenced by nonequilibrium thermochemistry within both net ionizing and net recombining flowfield regions. This Section presents an analysis of ionization chemistry within net

recombining flows.

Recombination is studied using zero-dimensional adiabatic isochoric reactors that are initialized to the equilibrium chemical composition behind the 5, 7, and 9 km/s normal shocks studied in the previous section. To instigate the recombination of the flow, the translational-rotational temperature and pressure are set to their freestream values at 60 km altitude, mimicking the condition of flow that was in equilibrium at the post-shock condition but which has just passed through a strong flow expansion. The initial mole fractions, temperatures, and pressures for the three studied recombination cases are given in Table 7.3.

Table 7.3: Initial conditions for the analyzed recombining flow scenarios.

	Case Name		
	Rec-5kms	Rec-7kms	Rec-9kms
P (Pa)	2.20	2.20	2.20
T_{tr} (K)	247.0	247.0	247.0
T_{vee} (K)	5132	6302	7939
X_O	3.225×10^{-1}	2.626×10^{-1}	2.121×10^{-1}
X_{O_2}	1.281×10^{-4}	1.705×10^{-5}	1.706×10^{-6}
X_N	1.177×10^{-1}	4.763×10^{-1}	7.592×10^{-1}
X_{N_2}	5.548×10^{-1}	2.587×10^{-1}	1.962×10^{-2}
X_{NO}	4.683×10^{-3}	1.735×10^{-3}	2.316×10^{-4}
X_{O^+}	8.375×10^{-7}	4.265×10^{-5}	7.583×10^{-4}
$X_{O_2^+}$	2.179×10^{-8}	9.564×10^{-8}	1.449×10^{-7}
X_{N^+}	2.150×10^{-8}	9.416×10^{-6}	3.484×10^{-3}
$X_{N_2^+}$	8.524×10^{-8}	5.687×10^{-6}	1.796×10^{-5}
X_{NO^+}	8.517×10^{-5}	3.151×10^{-4}	1.571×10^{-4}
X_{e^-}	8.614×10^{-5}	3.729×10^{-4}	4.418×10^{-3}

The evolution of translational-rotational as well as vibrational-electron-electronic temperatures in the three studied conditions is plotted in Figure 7.11. All three cases show similar behavior, with the translational-rotational temperature slowly relaxing upward through relaxation with the vibrational-electron-electronic temperature, as well as through the energy released by endothermic chemical reactions. Once T_{tr} and T_{vee} relax, the two temperatures rise together due to the continued energy release by endothermic chemical processes.

Because of these dynamics, all three cases demonstrate a prolonged period of electron recom-

bination that is followed by a recovery of the electron number density to a new equilibrium value that is lower than at $t = 0$. Sensitivities throughout both phases will be presented; however, the main interest of the current Section is the sensitivities during the recombination phase. As will be seen, the sensitivities during the ionization phase are similar to those found in the post-shock flows.

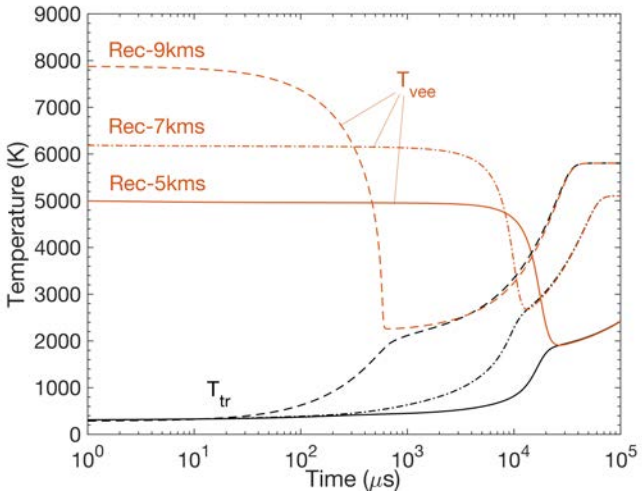

Figure 7.11: Temperatures in the recombining flow scenarios.

The baseline prediction of electron number density for the Rec-5kms case is shown alongside total Sobol' indices for n_e in Figure 7.12 as a function of time in the 0D adiabatic reactor. Electron number density falls steadily throughout the first 20 milliseconds as the electrons and ions, predominantly NO^+, dissociatively recombine. After 20 milliseconds, the translational temperature has increased sufficiently to reinitiate ionization processes as the gas seeks equilibrium at the rising temperature value. During a brief period near $t = 20$ ms, the most sensitive reaction changes from DR of NO^+ to the reassociation reaction that moves charge from NO^+ to O^+. The VT relaxation time in N_2 + O collisions also shows sensitivity for a brief period that corresponds to the rapid relaxation of T_{tr} and T_{vee} observed in Figure 7.11.

As with the shocked flow cases, it's worthwhile to consider Sobol' indices within the context of the variance at each time point. It's important to note that the variance of the n_e profile has a different relevance in the recombining flow cases than in the shocked flow cases. Because the

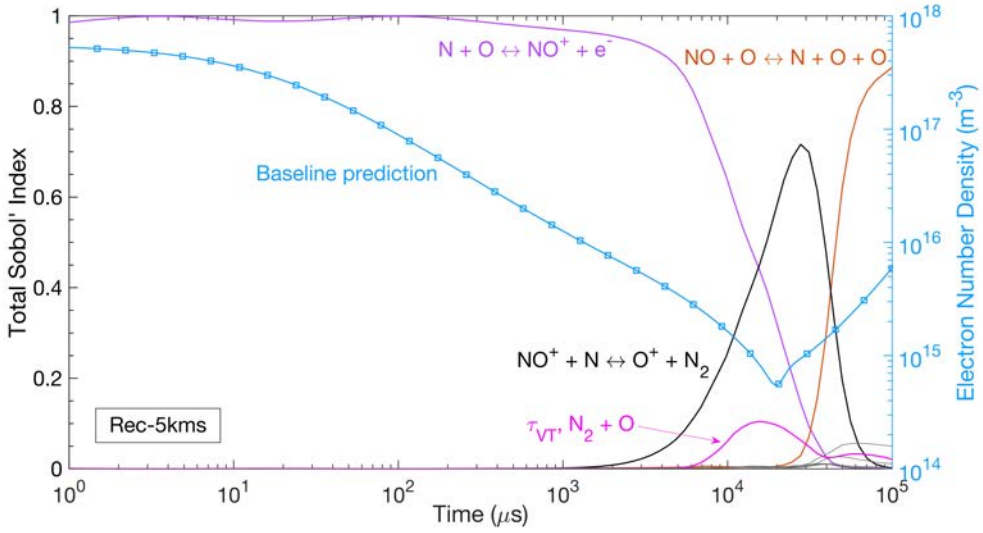

Figure 7.12: Total Sobol' indices for the electron number density as a function of time in a 0D isochoric reactor initialized to the 5 kms/s equilibrium condition.

shocked flow cases are representative of relatively localized regions of flow that have been processed by a strong normal shock, such as the stagnation region, the region of peak n_e variance is of greatest interest. As seen in the previous section, this region of peak variance corresponds to the region of peak electron concentration. In contrast, the recombining flow conditions are representative of flow that has been expanded and is moving with high velocity through the flowfield. Therefore, each point in the time-history is of interest, regardless of the magnitude of the electron number density at that point, since each point in the time-history roughly corresponds to a unique location in the flowfield where n_e predictions may be needed. It is the relative uncertainty in electron number density that matters more in the recombining cases, as opposed to the absolute uncertainty magnitude in the shocked flow cases.

Figure 7.13 illustrates the mean and 95% confidence intervals for the electron number density in the Rec-5kms case, plotted on a logarithmic y-axis to illustrate the relative uncertainties across the full range of n_e magnitudes. For the majority of the 100 millisecond simulation time, the n_e predictions span approximately one order of magnitude within the 95% confidence intervals. All of the sensitive processes in Figure 7.12 are, therefore, of approximately equal importance in the

Rec-5kms case.

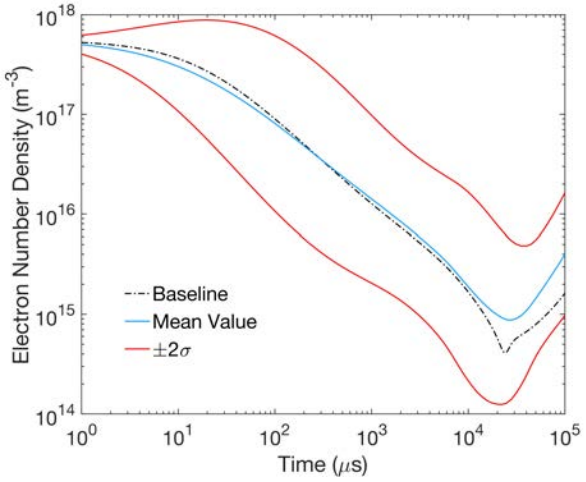

Figure 7.13: 95% confidence bounds for electron number density predictions in the Rec-5kms case.

Total Sobol' indices for the Rec-7kms case are plotted in Figure 7.14 alongside the baseline prediction for n_e. As in the Rec-5kms case, the DR of NO^+ is most sensitive during the period when recombination is the fastest, with the $NO^+ + N \leftrightharpoons O^+ + N_2$ reassociation reaction dominating the sensitivity throughout the remainder of the recombination phase. Dissociation reactions involving NO then take over as the most sensitive reactions when ionization levels begin to increase again.

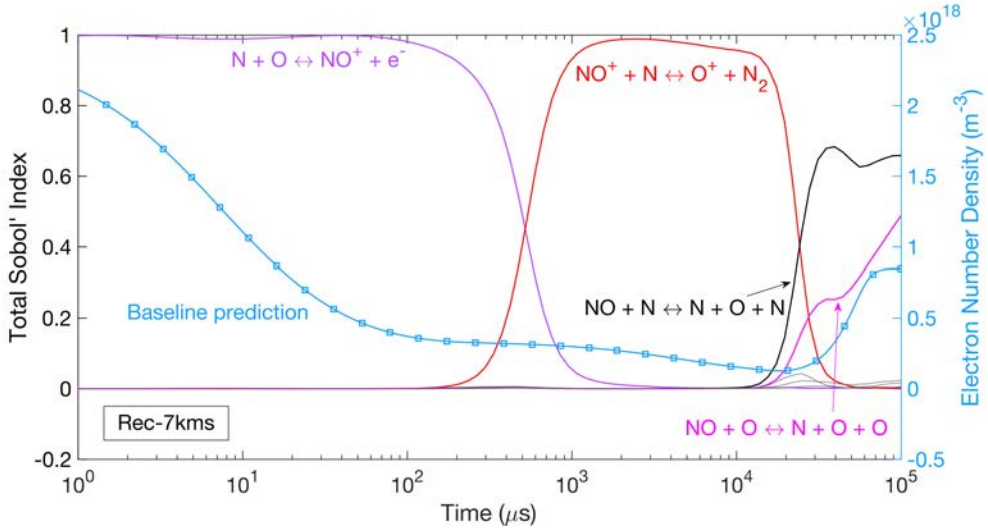

Figure 7.14: Total Sobol' indices for the electron number density as a function of time in a 0D isochoric reactor initialized to the 7 kms/s equilibrium condition.

The role of the reassociation reaction $NO^+ + N \leftrightharpoons O^+ + N_2$ may be understood through an analysis of the ionized species mole fractions in Figure 7.15. At early times, the dominant ion is NO^+, and its dissociative recombination is the primary driver of recombination. After approximately 50 μs, the dominant ion changes from NO^+ to O^+. As seen in Figure 7.15, the removal of O^+ is much less efficient than the removal of NO^+, slowing the recombination process significantly. Looking at the sensitivity indices, it's clear that the rate-limiting process during this period is the reassociation reaction $NO^+ + N \leftrightharpoons O^+ + N_2$ that moves charge from O^+ to the quickly-recombining NO^+. Three-body recombination of O^+ with electrons is not efficient in the Rec-7kms condition due to the low pressure and electron number density, and the other two reactions that destroy O^+ are endothermic – charge exchange with N_2^+ and reassociation with NO to form N^+ and O_2 – and so do not remove O^+ in the recombining scenario.

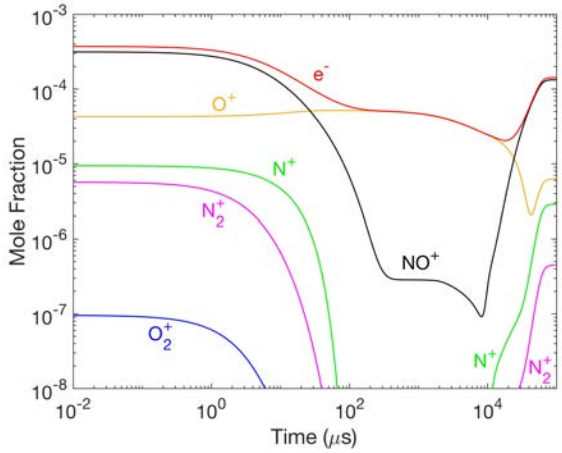

Figure 7.15: Mole fractions of charged species in the Rec-7kms case.

The baseline, mean, and 95% confidence intervals for the Rec-7kms condition are plotted in Figure 7.16. The 95% confidence intervals span a maximum of one order of magnitude in the region where NO^+ dissociative recombination is the dominant sensitive reaction. The confidence intervals are separated by over two orders of magnitude in the region where reassociation between O^+ and NO^+ is the dominant contributor to the overall uncertainty.

Finally, the sensitivity indices for the Rec-9kms case are presented in Figure 7.17. At the

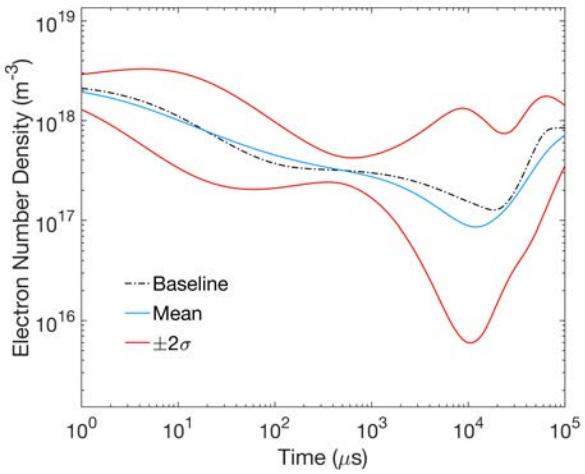

Figure 7.16: 95% confidence bounds for electron number density predictions in the Rec-7kms case.

electron number densities found in this case, the three-body recombination of N^+ and O^+ is efficient and dominates the main region of net recombination. The energy exchange cross-section between nitrogen atoms and electrons is a major contributor to the uncertainty, indicating that uncertainty in the relaxation between T_{tr} and T_{vee} is primarily driven by uncertainty in this cross-section for the Rec-9kms condition. Otherwise, the sensitive processes influencing recombination are generally similar in the Rec-9kms case as in the flow behind the 9 km/s normal shock.

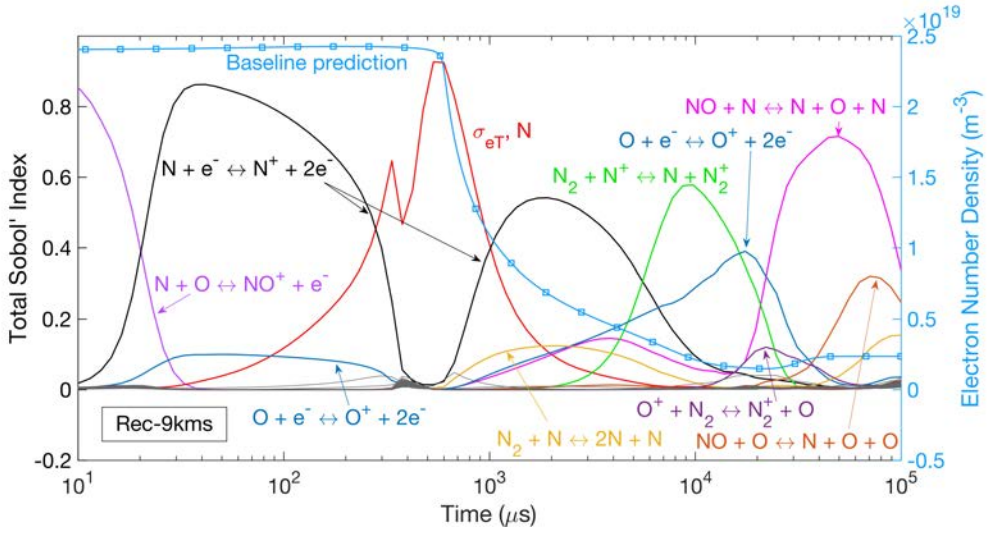

Figure 7.17: Total Sobol' indices for the electron number density as a function of time in a 0D isochoric reactor initialized to the 9 kms/s equilibrium condition.

7.2.4 Discussion

The uncertainty quantification results presented in this Section provide an informative picture of the predictive accuracy of existing two-temperature ionization models. In addition, the sensitivity analysis results help to isolate the model parameters that should be targeted in efforts to improve the prediction of plasma formation in hypersonic flows.

Given a basic knowledge of the kinetics at play, the demonstrated sensitivity of several parameters is expected. For example, the associative ionization to form NO^+ and the electron impact ionization to form N^+ are the dominant drivers of ionization at the low and high ends, respectively, of the analyzed shock velocities. Several rate coefficients, however, demonstrate large sensitivities that are not intuitively obvious.

In the shocked flow cases, particularly at 5 and 7 km/s, the chemical reactions involving NO demonstrate a major influence on the net rate of dissociative recombination taking place downstream of the peak electron number density. Results from the present study indicate that improved predictions of NO dissociation with N and O, as well as the second Zel'dovich reaction ($N_2 + O \leftrightharpoons NO + N$), can provide major improvements to the predictive accuracy of nonequilibrium plasma formation models under some conditions.

Charge exchange between N_2^+ and N dominates the uncertainty of plasma formation predictions in the 9 km/s normal shock condition. This finding is in line with the study by Cruden and Brandis, in which the same reaction is found to strongly influence electron number density behind 10 km/s normal shocks in pure nitrogen [41]. The current study adds to this by isolating $N_2^+ +$ N charge exchange as a highly sensitive reaction influencing ionization in air, in which many other charge exchange and reassociation reactions are active. Experimental studies targeting ionization in pure N_2, with its considerably simpler chemical mechanism compared to air, may, therefore, have great potential to inform improvements to models of air plasma formation at superorbital velocities.

It's worth noting that across all of the shocked flow cases, the associative ionization to form

O_2^+ is found to be the main sensitive process influencing electron number density near the shock front. Uncertainties in this region are significant across all three shocked-flow scenarios. However, outside of this thin layer near the shock front, O_2^+ is not a dominant species, and its generation is not a sensitive contributor to the uncertainty in peak electron number density.

Uncertainty in the electron number density during recombination is driven by a similar collection of processes to those influencing ionization behind strong shocks. As in the shocked flow analyses, the rate coefficients for electron impact ionization to form N^+ and associative ionization to form NO^+ dominate the uncertainty in regions where n_e is changing most rapidly.

A distinguishing feature of the recombining cases, as compared to the shocked cases, is the large sensitivity to the reassociation reaction $NO^+ + N \leftrightharpoons O^+ + N_2$. This reaction controls the rate of depopulation of O^+, the slowest ion to recombine, and contributes significant predictive uncertainty to the Rec-5kms and Rec-7kms conditions. A more accurate characterization of this reaction rate is likely to improve the predictions of ionization in strongly expanded flowfield regions, such as vehicle wake flows.

7.3 Ionization in the Collisional-Radiative Model

7.3.1 Validation

Before proceeding with investigations of ionization kinetics, it is important to validate the developed collisional-radiative model. However, as discussed in Chapter 1, experimental measurements of electron number density at suborbital speeds are scarce. For velocities in excess of 10 km/s, suitable measurements of n_e for model validation have been published by Lemal et al. [15] using data from the Electric Arc Shock Tube (EAST) at NASA Ames [211]. Figure 7.18 shows a comparison between measured and predicted electron number density for a 10.54 km/s normal shock. The model predictions and experimental data are considered to be in good agreement, given the ± 0.2 cm uncertainty in the alignment of the optical system [15]. Predictions from the two-temperature model due to Park do not match the experimental measurements, likely due to the fast rates of

electron impact ionization for N and O. A similar overprediction of the electron number density by the 2T model was demonstrated in [20]. The good performance of the collisional-radiative model in predicting the EAST measurements is a result of the high-quality electron impact excitation and ionization rates employed in the model, particularly for atomic nitrogen.

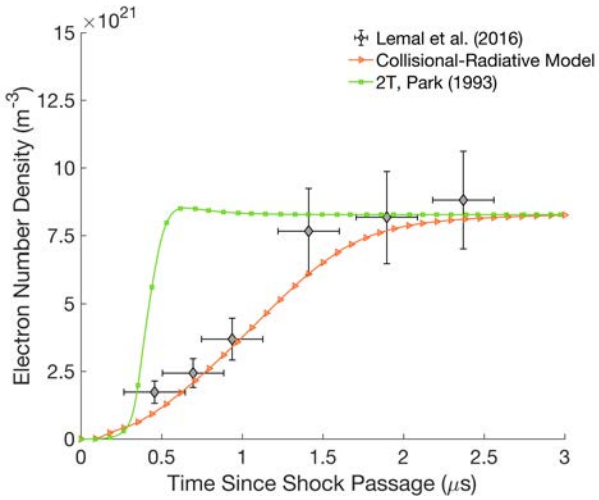

Figure 7.18: Comparison of the baseline collisional-radiative model with electron number density measurements behind a 10.54 km/s shock in air with P_0=0.1 torr.

In recent attempts to infer the electron number density behind 8-9 km/s normal shocks, the electron number density in the equilibrium post-shock region is observed to exceed its equilibrium value by up to a factor of two [212, 213]. These overshoots may be due to non-ideal effects such as boundary layer growth [64], shock deceleration [214], or impurity species, none of which are included in the present modeling approach. As a result, those data are not used in the validation effort.

Comparison with electron number density measurements by Lin, Neal, and Fyfe [16] for normal shock velocities ranging from 5 to 7 km/s is shown in Figure 7.19. Two-temperature model predictions are shown alongside the collisional-radiative model predictions. In general, none of the models accurately predict the peak electron number density. Such a discrepancy may be due to non-idealities like shock deceleration or boundary layer growth. Alternatively, the discrepancies could be caused by errors in the ionization rates, which have not been conclusively validated at

the conditions explored in Figure 7.19. When comparing predictions across the three models, note that the collisional-radiative model predictions are within the scatter of two-temperature model predictions. Thus, while the collisional-radiative model cannot be conclusively validated using these experimental measurements, the comparison with 2T models illustrates that the CR model produces reasonable predictions of ionization at suborbital shock velocities.

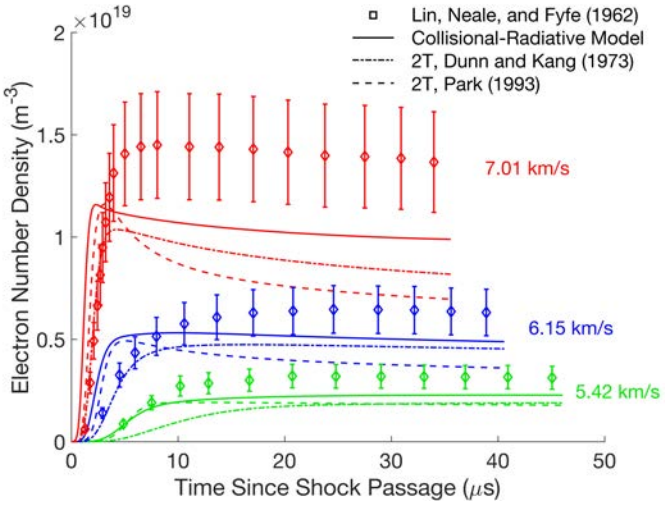

Figure 7.19: Comparison between experimental electron number density measurements from Lin, Neale, and Fyfe [16] and predictions from several models. The freestream pressure is 0.02 torr for all of the experiments shown.

7.3.2 Associative Ionization

A principal aim of the present work is to assess the importance of electronic nonequilibrium to the ionization of shock-heated air. One way to assess the impact of electronic nonequilibrium is to calculate the flow evolution using two variations of the CR model: the first model considers AI as proceeding via the multiple channels in Table 3.13, and the second model uses the equilibrium AI rate constants from Table 3.13 to approximate the net rate of AI using a single channel that proceeds through the interaction of ground state atoms. For the single-channel approach, the forward rate controlling temperature is set to $\sqrt{T_{tr}T_{vib}}$ to approximate the effect of atomic electronic relaxation on the net rate coefficient. Owing to the uncertainty in the extrapolation process used to leverage

room-temperature atomic quenching rates, the single-channel and multi-channel models are also run using two models of HP-CIE. The first model is the baseline CR model described in Chapter 3, which makes use of extrapolated room-temperature quenching and electronic excitation exchange rates. The second model does not make use of these rate coefficients, modeling all HP-CIE rate coefficients using the cross-section suggested by Lemal et al. [15] and neglecting electronic excitation exchange entirely. This second model is important because many modern CR models do not make use of room-temperature data for heavy-particle processes involving excited atoms [20, 15, 161].

Figure 7.20 shows the profiles of electron number density predicted behind shocks at 5 km/s and 9 km/s using the four model formulations. Freestream conditions correspond to an altitude of 60 km, chosen as a realistic altitude for the velocities investigated. Within the baseline model, the modeling of associative ionization via separate channels does not have a significant effect on the electron number density profile at any of the velocities tested from 5-9 km/s.

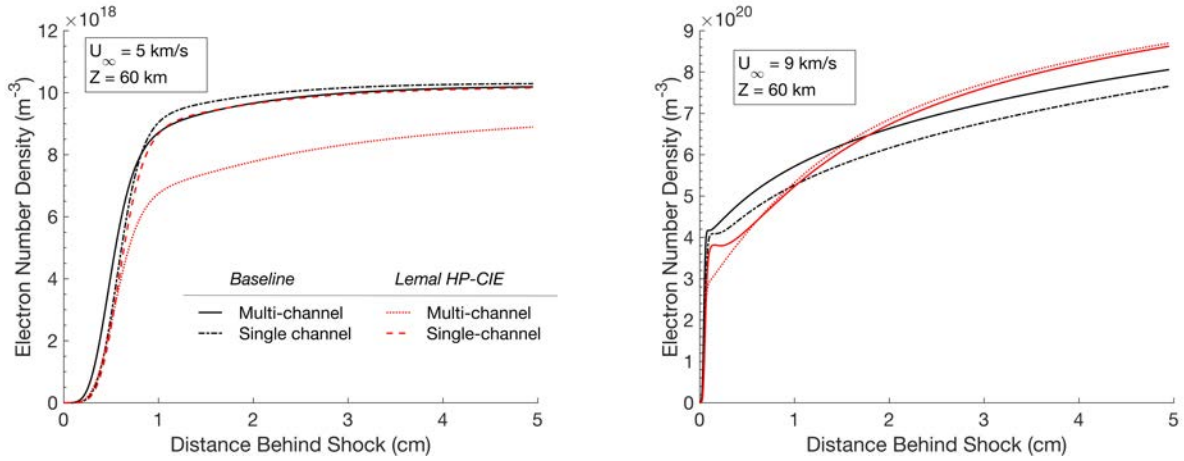

(a) 5 km/s (b) 9 km/s

Figure 7.20: Electron number densities predicted by single and multi-channel models of associative ionization. The baseline model with atomic quenching and electronic excitation exchange is compared against a model using Eq. (3.12) for HP-CIE of atoms and which makes no use of extrapolated room-temperature atomic quenching or excitation exchange rates.

Many of the room-temperature atom-atom quenching rates for metastable N and O yield HP-CIE rates that are much faster than those predicted by Eq. (3.12) with σ_0 from Lemal et al. When the excitation of the metastable atomic states is relatively fast, like in the baseline CR model,

the net rate of AI can be effectively modeled using a single-channel approximation. Within the model that does not use extrapolated room-temperature rates for reactions with excited atoms, the electron number density profile is significantly affected by the explicit modeling of separate reactive channels for AI. The difference is most pronounced at 5 km/s, where the ionization is driven entirely by AI processes. This difference can be explained by the comparatively longer period of atomic electronic non-equilibrium in the model that does not make use of the room-temperature quenching data.

At this point, it is worthwhile to note that the HP-CIE cross-section scale factor determined by Lemal et al. [15] was based on model comparisons with radiative intensity in the vacuum ultraviolet (VUV) and near-infrared (NIR) behind 10-11 km/s normal shocks. All of the N and O lines that dominate the VUV and NIR spectra originate from levels significantly above the metastable states that participate in AI. The impressive predictive accuracy of the derived scale factor, therefore, may not imply accurate metastable state populations.

To further illustrate the difference in predictions between the models with and without the extrapolated room-temperature rate coefficients, representative time-histories of state variables behind a 7 km/s normal shock are shown in Figures 7.21a and 7.21b. Electronic temperatures shown in Figure 7.21a are calculated based on the Boltzmann population of electronic states that would yield the same energy as the true non-Boltzmann state distribution. As mentioned in previous chapters, the majority of the electronic energy of N and O is stored in the metastable states, so the electronic temperature of these species can be used to understand the population of the metastable states relative to the various nonequilibrium modes in the gas.

Within the baseline model, the electronic temperature of atomic oxygen is tightly coupled to the translational temperature. Fast excitation of $O(^1D)$ in the baseline model is driven by the $O(^3P) + O(^3P) \rightarrow O(^1D) + O(^1D)$ reaction with energy-dependent cross section calculated in [167]. The excitation temperature of atomic nitrogen is also more tightly coupled to T_{tr} in the baseline model; however, the effect is less dramatic. In Figure 7.21b, the metastable state populations from all four model formulations can be seen to converge with one another within 1 cm of the shock

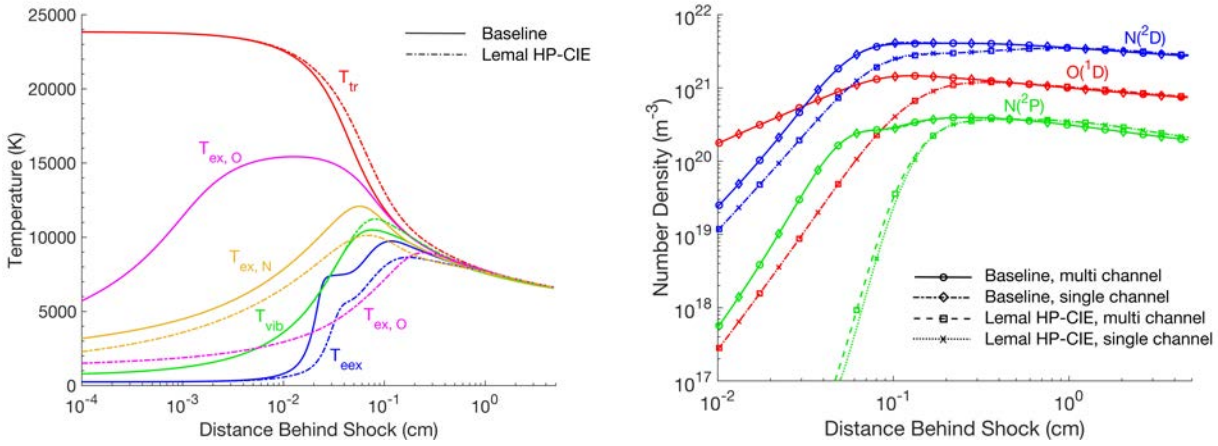

(a) Nonequilibrium temperatures (b) Atomic metastable state number densities

Figure 7.21: Evolution of (a) mode temperatures and (b) number densities of the atomic metastable states involved in associative ionization downstream of a 7 km/s normal shock with freestream conditions corresponding to 60 km altitude.

front. Relaxation within 1 cm is consistent with the length scale of thermal nonequilibrium in Figure 7.21a.

It is important to emphasize that the number densities of the atomic excited states do not differ based on whether a single or multi-channel model of associative ionization is used. This observation underscores a key finding: there is no indication of atomic electronic nonequilibrium being influenced by the selective depletion of metastable states due to associative ionization. If such a coupling existed, the atomic metastable state populations predicted by the multi-channel models should be lower than those predicted by single-channel models. Even the model that relies solely on Lemal's cross section for HP-CIE, which lies at the lower end of accepted rate constants [20], does not suggest that AI can meaningfully deplete the metastable states under the investigated conditions.

In Figure 7.22, the atomic excited state distributions predicted by the baseline model are plotted at two distances behind a 7 km/s shock. For both atoms, the first excited state above the ground reaches equilibrium with the translational temperature within 1 mm of the shock front. Note that these states are not in equilibrium with the free electron temperature as the two-temperature

model would predict. The ^{2}P state of N, which participates in AI to form N_2^+ stays populated below equilibrium by 20-30% during the full 5 cm post-shock distance that is simulated. At the suborbital velocities analyzed in the current study, the atomic excited state relaxation is driven primarily by the heavy particle translational temperature rather than the free-electron translational temperature. Tibre-Inglesse and Cruden have recently shown such heavy-particle-driven electronic relaxation to be consistent with radiation measurements in pure nitrogen behind ~7 km/s incident shocks [215].

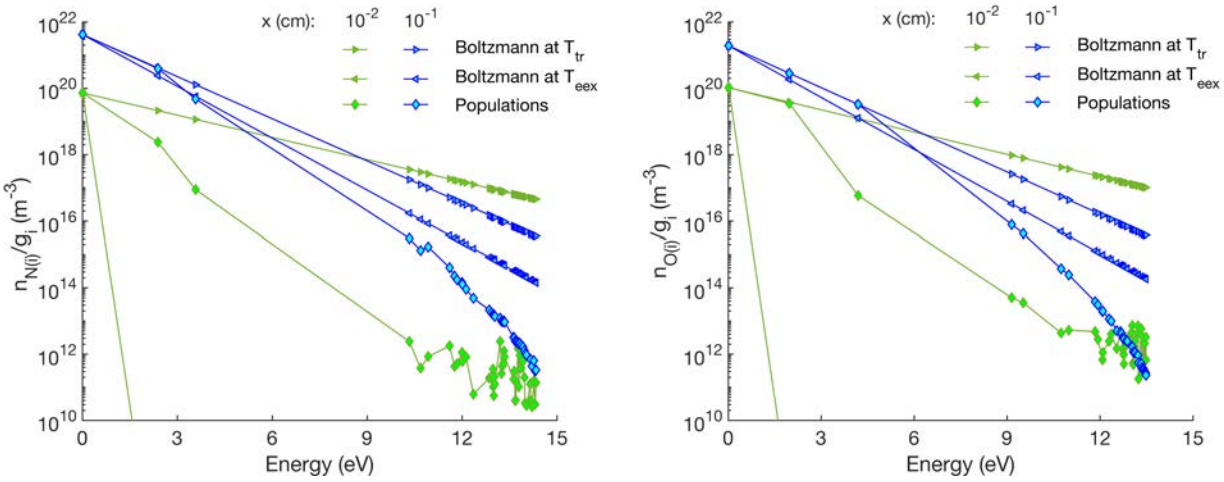

(a) N (b) O

Figure 7.22: Electronic state distributions of atomic nitrogen and oxygen behind a 7 km/s normal shock with freestream conditions corresponding to 60 km altitude.

Figure 7.23 shows the prediction of ion number densities for 7 and 9 km/s normal shocks at 60 km altitude. Predictions are shown for the baseline model with a multi-channel treatment of AI and with single-channel treatments where the controlling temperature is $\sqrt{T_{tr}T_{vib}}$ or T_{tr}, the latter of which is more commonly used [1]. Multi-channel model predictions lie closer to the curve predicted by the model using T_{tr} as the rate controlling temperature. This result is consistent with the fast relaxation of the metastable states to T_{tr} illustrated in Figs. 7.22 and 7.21a. The number densities of the most dominant ions, NO^+ and N^+, are changed only slightly between the three modeling approaches. Predictions of N_2^+ and O_2^+ are more significantly affected by the

explicit modeling of AI through excited state channels. For these two ions, the multi-channel model overshoots the predictions from the single-channel approximations. Faster AI in the multi-channel model is enabled by the fast excitation of metastable atoms that ionize via the fast, low-threshold AI channels.

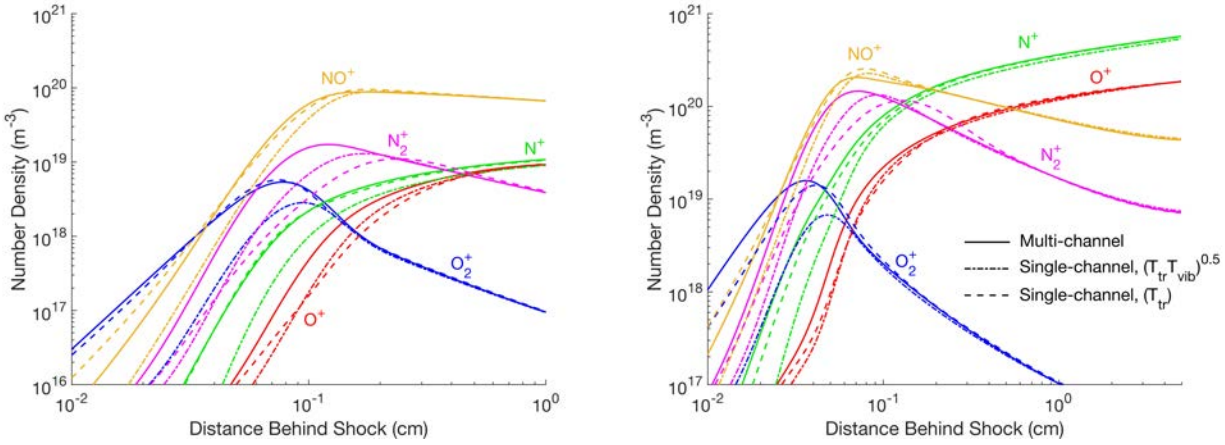

(a) 7 km/s (b) 9 km/s

Figure 7.23: Post-shock evolution of ion number densities predicted by several alternate AI modeling approaches with freestream conditions corresponding to 60 km altitude.

7.4 Sensitivity Analysis of the Collisional-Radiative Model

A sensitivity analysis of the collisional-radiative model is presented in this Section to better highlight the critical processes influencing net ionization predictions in the electronic state-specific approach. This Section follows the same pattern as Section 7.2, beginning with a description of the analysis setup and then moving to a discussion of convergence and Sobol index results.

7.4.1 Uncertain Parameters and Quantities of Interest

Over 20,000 collisional processes are included in the collisional-radiative model for air described in Chapters 2 and 3. The vast majority of these processes are bound-bound transitions between atomic electronic states, many of which are not expected to sensitively control the electron number density. A drastic reduction in the number of bound-bound transition rate parameters can

be achieved by 1) only considering atomic electronic transitions involving the lowest ten levels of N and O and 2) treating all heavy particle colliders with the same rate coefficient when an analytical cross-section is used for all. If the rate coefficient of HP-CIE of a specific transition with a specific collider has been determined using quenching data, then the rate coefficients with each other collider are treated as separate parameters. If there is no data to distinguish between colliding particles, all are modeled using the same rate parameters. For the molecules, rate coefficients for the HP-CIE transitions involving neutral colliders are considered separately. Uncertainty intervals of ± 1 order of magnitude are applied for all HP-CIE reactions. Larger intervals, such as ± 2 orders of magnitude, may be justified in a future analysis by the large scatter in predictions from the various analytical closures for HP-CIE.

Electron impact excitation rate coefficients for the atoms and molecules are varied over an interval of $U_i = [0.1, 10]$ following Johnston and Kleb [216], who found a ± 1 order of magnitude variation covered the range of atomic and molecular E-CIE rates proposed in the literature. A total of 188 chemical reactions are considered, including 27 electronic excitation exchange reactions. Thirty-one quenching reactions, mostly involving low-lying atomic states, are considered as well. Due to the absence of experimental measurements for electronic-specific reactions at high temperatures, all chemical reaction and quenching rates are varied up and down by an order of magnitude.

Electron and heavy particle impact ionization rate coefficients involving the lowest 10 states of the atoms, and all electronic states of the molecules are considered as well. As with the atomic bound-bound transitions, the heavy-particle rates are modeled using one rate coefficient for each atomic and molecular bound-free transition. All electronic bound-free transition rates are varied over an interval $U_i = [0.1, 10]$. Finally, the VT relaxation times and uncertainty intervals in Table 7.1 are included, as are the same variations on Gnoffo's eT relaxation cross-sections.

The quantities of interest in the collisional-radiative and two-temperature sensitivity analyses are the same. As in the two-temperature case, the electron number density and mole fraction sensitivities are similar, so only the n_e sensitivities are shown.

7.4.2 Sobol Indices

There are 625 uncertain parameters considered in the sensitivity analysis of the collisional-radiative model for air. In Figure 7.24, the maximum change in any given total Sobol index for the electron number density is seen to drop below 3% within approximately 2,000 model evaluations for the three velocities tested.

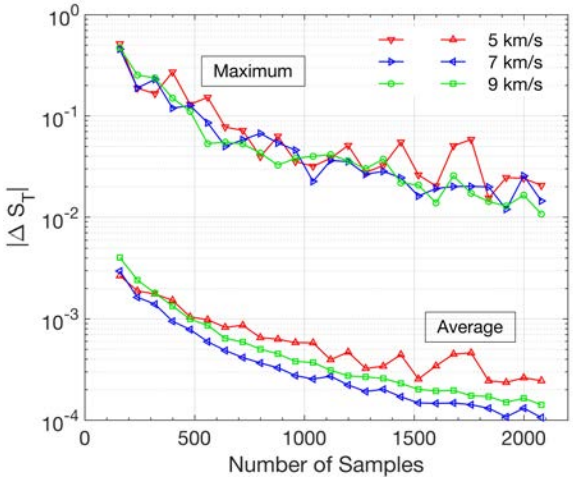

Figure 7.24: Convergence of the Sobol indices for the three velocities simulated using the collisional-radiative model.

Total Sobol indices are shown in Figure 7.25 for electron number density behind a 5 km/s normal shock. Explicit electronic state identifications are applied for all species that receive an electronic state-resolved treatment. Electronic states are not labeled for non-reacting collider species – these are all in their ground electronic state. Many of the same processes show high sensitivity in the two-temperature and collisional-radiative models, particularly the dissociation of O_2 and the associative ionization to form NO^+. Among the production channels for NO^+, the $N(^2D) + O(^3P)$ channel is the dominant contributor to n_e sensitivity in the post-shock region where ionization is most active.

Channel-specific source terms for the generation of NO^+ at 5 km/s are shown in Figure 7.26 alongside the number density profile of NO^+. The dominance of the $N(^2D) + O(^3P)$ channel in the source terms is consistent with the high sensitivity of the rate coefficient for this interaction

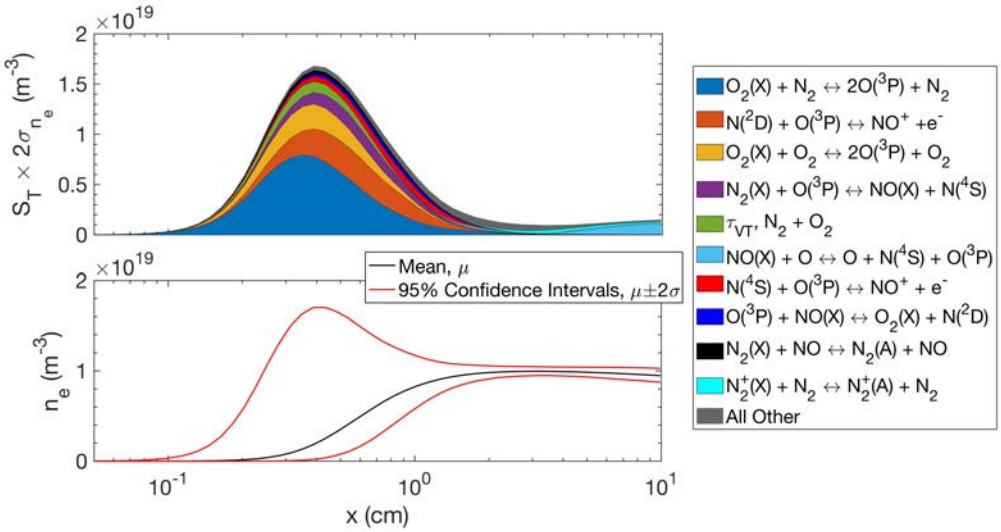

Figure 7.25: Total Sobol indices for the electron number density profile behind a 5 km/s normal shock with freestream conditions corresponding to 60 km altitude.

in Figure 7.25. The only reaction involving the production of N(^{2}D) with notable sensitivity is the formation of N(^{2}D) in O(^{3}P) + NO(X) collisions, which was studied using three-dimensional quantum scattering by Lu et al. [180]. The lack of sensitivity to N(^{2}D)-forming reactions is consistent with the observation that electronic nonequilibrium does not significantly affect the net rate of plasma production at 5 km/s. At the furthest distances from the shock, the dissociation of NO(X) with partner O is the most sensitive reaction rate coefficient, as is the case in the two-temperature analysis as well.

Sensitivity results for the 7 km/s condition are shown in Figure 7.27 and are similar in several ways to the 5 km/s results. As in the two-temperature analyses, the Zel'dovich reactions become more sensitive at the 7 km/s condition as compared to the 5 km/s shock. Several more reactions involving N(^{2}D) show notable sensitivity. This is again aligned with previous results from Section 7.3.2, which showed an increasing role of electronic nonequilibrium in the net rate of ionization as shock velocity increases. Unlike in the two-temperature analysis, the associative ionization of O_2^+ and charge exchange reactions from O_2^+ do not show notable sensitivity - likely due to the lower rate of O_2^+ formation adopted in the CR model.

Figure 7.28 illustrates the evolution of total Sobol indices and electron number density be-

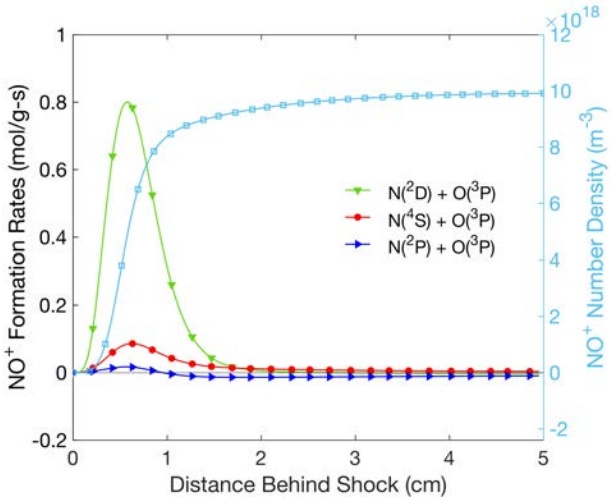

Figure 7.26: Channel-specific rates for the production of NO^+ via associative ionization. Conditions correspond to a 5 km/s normal shock at 60 km altitude.

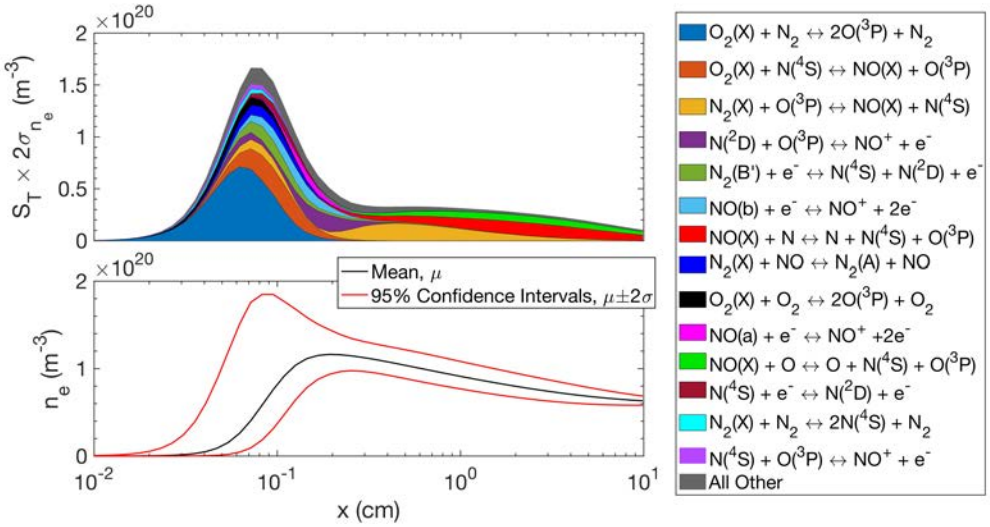

Figure 7.27: Total Sobol indices for the electron number density profile behind a 7 km/s normal shock at 60 km altitude.

hind a 9 km/s normal shock. Many more interactions involving electronically excited states show sensitivity in the 9 km/s case, as compared to the 5 and 7 km/s cases. Several reactions leading to $N(^2D)$ show major sensitivity, particularly the excitation of $N(^4S \rightarrow ^2D)$ by electrons and by nitrogen atoms. Because the electron impact ionization of N is the main ionization interaction downstream of 1 mm behind the shock, a number of E-CIE interactions for N also show significant sensitivity.

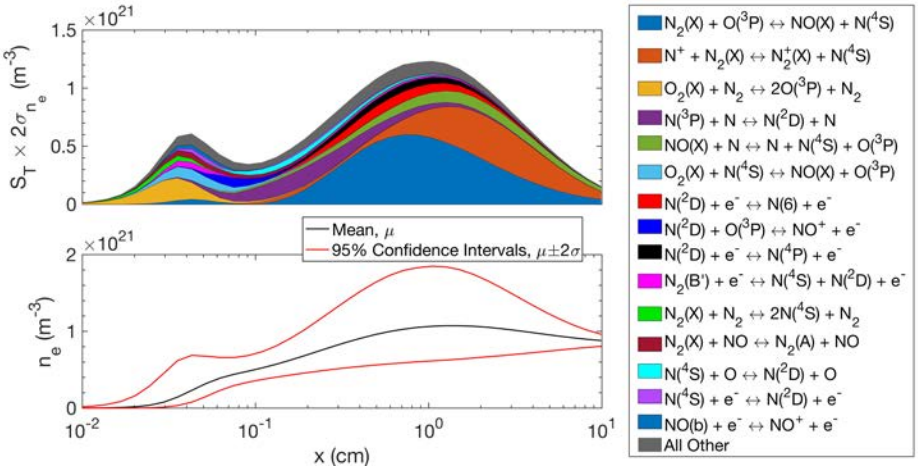

Figure 7.28: Total Sobol indices for the electron number density profile behind a 9 km/s normal shock with freestream conditions corresponding to 60 km altitude.

Unlike the two-temperature result, the greatest variance at 9 km/s is caused by the $N_2(X)$ + $O(^3P)$ Zel'dovich exchange reaction instead of the N^+ + $N_2(X)$ charge exchange reaction. This is likely caused by the different uncertainty intervals used for these reactions in the two-temperature and collisional-radiative sensitivity analyses – note that the current analysis uses ± 1 order of magnitude variation on every parameter, with the exception of the relaxation times. While such a strategy is effective for identifying major trends, the sensitivity analysis can be improved by implementing literature-informed uncertainty intervals on all parameters. This is a difficult task for the collisional-radiative model, for which many rate coefficients are extrapolated from room temperature or estimated using analytical expressions; however, it is possible in principle and can help cultivate a clearer picture of the collisional-radiative model parameters that warrant further study. The present work illustrates that Sobol' indices can successfully be calculated for the 600+ uncertain parameters relevant to a collisional-radiative model prediction; future work should improve on this result by determining uncertainty intervals for those parameters that more accurately reflect their true uncertainty.

7.5 Summary

Nonequilibrium charged particle kinetics in shock-heated air were studied using two-temperature and collisional-radiative models in this chapter. In the first section, uncertainty quantification and sensitivity analysis were performed to study the ionization and recombination predicted by two-temperature models. Enthaplies in the post-shock and recombining flow analyses corresponded to freestream velocities of 5-9 km/s at 60 km standard altitude. For the 5 and 7 km/s normal shock conditions, the associative ionization (AI) to form NO^+ was the most significant contributor to uncertainty in the electron number density. While the sensitivity at 5 km/s was dominated by AI to form NO^+, several other reactions, including Zel'dovich exchange and NO dissociation, showed notable importance behind the 7 km/s incident shock. In the 9 km/s post-shock condition, the charge exchange between N_2 and N^+ contributed most sensitively to the electron number density uncertainty, with the electron impact ionization to form N^+ also considerably affecting predictions.

Similar processes showed sensitivity in the recombining scenarios as in the post-shock flows. One reassociation reaction, $O^+ + N_2 \leftrightharpoons NO^+ + N$, was highly sensitive in the recombining flows, even though it did not show major sensitivity in the post-shock flows. Apportionment of predictive uncertainty to the uncertainty in individual rate parameters can help to inform the allocation of resources toward the future improvement of ionization models for hypersonic flows.

In the remainder of the chapter, ionization was studied using a collisional-radiative model. First, the potential importance of atomic electronic nonequilibrium on net rates of associative ionization was assessed. The explicit modeling of associative ionization involving excited atoms was not found to significantly impact predictions of net ionization; however, if the rates of heavy particle impact excitation were much slower, as some authors suggest, then explicitly accounting for separate associative ionization pathways involving excited atoms may influence the electron number density by up to 20%. Improved characterization of the heavy particle impact excitation rates of metastable N and O atoms would help to further assess the influence of atomic electronic nonequilibrium on associative ionization.

Finally, a sensitivity analysis of ionization predictions by the collisional-radiative model was performed for 5-9 km/s normal shocks at a standard altitude of 60 km. Associative ionization showed a similar importance as in the two-temperature sensitivity analysis, with the channels involving excited atoms being the most sensitive. Several excitation reactions for the metastable atomic electronic states also showed marked sensitivity. Future work on the collisional-radiative model should focus on identifying more representative uncertainty intervals for the 600+ parameters that were considered in the sensitivity analysis.

Chapter 8

Conclusion

In this chapter, the key results and conclusions from the dissertation are summarized. Conclusions from each chapter are provided in Section 8.1, followed by an overview of the main research contributions in this thesis in Section 8.2. Finally, recommendations for future work are discussed in Section 8.3.

8.1 Summary of Completed Work

8.1.1 Model and Code Development

Two major numerical tools were developed to perform the research presented in this thesis. First, a general-purpose nonequilibrium chemical kinetics solver was developed. The solver is capable of simulating zero-dimensional adiabatic reactors or one-dimensional shock tube flows. Electronic and vibrational states can be tracked individually or can be assumed to be Boltzmann populated at characteristic temperatures. It is also possible to solve separate conservation equations for the rotational, vibrational, and electron-electronic energies. The mathematical formulation of the electronic state-resolved model was described in detail. Several benchmarking cases were presented as well.

The second major numerical tool was a sensitivity analysis wrapper that is tightly coupled to the chemical kinetics solver. Global sensitivity analyses involving over 500 uncertain parameters are possible using the developed tool, which leverages L_1 regularization to fit a polynomial chaos expansion surrogate model with reasonable computational cost. The mathematical background and

implementation of the sensitivity analysis wrapper were discussed in detail. A discussion was then given on the scaling limits of the code and the efforts taken to enable the large analyses presented in later chapters.

8.1.2 Collisional-Radiative Model

All of the collisional and radiative rate parameters required for an electronic state-resolved model of an N_2-O_2-Ar plasma were presented in this chapter. The selected rate constants for each process were selected following a comprehensive literature review of the available data. Rate coefficients for electronic excitation and ionization by electron impact were modeled using a combination of several high-quality cross-section databases. In addition, particular efforts were taken to accurately model heavy particle impact excitation and electronic excitation exchange processes, which are particularly important to the electronic excitation kinetics when free electrons are scarce. Dissociation and associative ionization also received considerable attention.

8.1.3 Two-Temperature Modeling of Coupled Vibrational Relaxation and Dissociation in Oxygen

A parametric assessment of two-temperature (2T) modeling approaches for the vibrational relaxation and dissociation of oxygen was performed using low uncertainty measured data from pure O_2 reflected shock experiments. The low uncertainties in the measured data enabled a clear distinction between the performance of various approaches and model parameters. The legacy 2T modeling approach – Millikan & White relaxation times, Park's reaction rate constants, and nonequilibrium dissociation modeling – produced predictions in poor agreement with the measured data. In contrast, the modified Marrone and Treanor (MMT) model generated much more accurate predictions of vibrational relaxation and dissociation. The use of the MMT correction factors for non-Boltzmann vibrational state distributions produced improved predictions at high temperatures; however, the measured data for the lower temperature experiments were matched more closely when the non-Boltzmann correction was omitted. Therefore, it is recommended that the accuracy

of these non-Boltzmann correction factors be assessed using vibrational state-resolved simulations of the analyzed experiments.

8.1.4 Electronic State-Resolved Analysis of Weakly Ionized Oxygen Mixtures

In this chapter, the electronic excitation and ionization kinetics occurring in oxygen-argon reflected shock experiments were analyzed using the developed three-temperature collisional-radiative model. Model predictions were compared with experimental measurements for the number density of molecular oxygen, electrons, and three electronic states of atomic oxygen.

Predictions for the dissociation of O_2 were consistent with the available data, ensuring that dissociation was predicted with sufficient accuracy to study the measurements of excited atoms in conditions where dissociation was ongoing. Rate coefficients for the heavy particle impact excitation of argon, which determine the net ionization rate in the analyzed experiments, were inferred using comparison with electron number density measurements at 10,000 to 11,200 K. The inferred rate constant was higher than other published values, potentially due to impurities or pressure non-idealities behind the reflected shock.

Next, the excited state number density measurements were analyzed using the collisional-radiative model. Excited state measurements at 7,000 K were used to infer a rate constant for the excitation of $O(^3P)$ to $O(^5S^\circ)$ in collisions with argon. Multi-stage behavior, observed in several experiments, was also predicted by the collisional-radiative model, and a detailed explanation for it was given. The reason for the multi-stage behavior was different from previously proposed mechanisms, underscoring the value of analyzing the measured data using a more complete model.

Non-ideal pressure rises were incorporated into the governing equations when data was available, and their effect on the excited state population predictions was significant in several cases. It was recommended that non-ideal pressure rise be reported alongside measured data for electron and excited atomic state populations in future reflected shock experiments. Parameters describing the reabsorption of resonance radiation were also found to play a major role in the excited state predictions, presenting a challenge for the model assessment due to the uncertainties inherent in

the use of escape factors to model self-absorption.

The atomic excited state data came from shock tubes at Stanford and at UCLA. Model predictions were generally consistent with the Stanford data across a wide range of temperatures and pressures, with discrepancies typically being bounded by reasonable limits on the non-ideal pressure rise and escape factor self-absorption length scale. When comparing with the data measured at UCLA, which has considerably finer time resolution than the Stanford data, major discrepancies between the model and experiment were observed. Several potential explanations were provided for the disagreement, but more data from the UCLA shock tube is necessary to identify whether facility effects or kinetic modeling inaccuracies are to blame; electron number density measurements would be particularly revealing.

Finally, a sensitivity analysis was performed to determine the rate coefficients and relaxation parameters that most influenced the electron and atomic excited state number densities. Predictions of the $O(^3S^\circ)$ population were primarily dependent on the escape factor for radiative de-excitation from $O(^3S^\circ)$ to $O(^3P)$. Rate coefficients coupling the three measured states were sensitive across all experimental conditions. In general, each excited state number density was influenced by collisionally induced excitation involving multiple lower and upper states, highlighting the value of adopting a detailed modeling approach to analyze the measured data, as well as the difficulty of inferring individual rate coefficients from the measurements.

8.1.5 Electronic State-Resolved Analysis of Weakly Ionized Nitrogen Mixtures

Understanding the detailed excitation kinetics of atomic nitrogen is essential for constructing accurate models of ionization in hypersonic flows and the radiative heating of high-speed reentry vehicles. To this end, the collisional-radiative model was used to analyze recent experimental measurements of electronically excited nitrogen atoms in a shock tube. Predictions from the model were compared with measured data from reflected shock tube experiments for the concentrations of $N_2(X)$ and electronically excited atomic nitrogen.

The model predictions of dissociation in mixtures of 2-10% N_2 in argon were consistent with

all experimental measurements [14] in the temperature range of 8,000-14,000 K. For the analysis of experiments performed in 20% mixtures of N_2 in argon, dissociation was predicted to proceeded faster than was observed in the experiment. Difficulties in matching the measured data across all N_2 concentrations were reported by previous authors, including in the original experimental study by Appleton et al. [14], and in a later analysis by Park [31]. The discordance may be the result of deviations from the ideal initial condition in the test gas, with temperature changes on the order of 3% being shown to significantly influence the model predictions at the studied temperatures.

Next, a comparison was made between model predictions and measured data [8, 9] for the concentration of atomic nitrogen in its fourth electronic state, the $3s\ ^4P$ level. For the test gas mixtures with 1% and 2% N_2 concentrations, the model accurately predicted the three-stage behavior observed in the measured time histories and captured the induction behavior observed near time zero. The initial rise in the N(^{4}P) population was caused by heavy particle impact excitation via ladder-climbing through the metastable levels, reaching a plateau as electron impact ionization began to deplete the high-lying electronic levels of N. The plateau period ended when three-body recombination became significant, slowing the removal rate of high-lying electronic states by electron impact ionization and allowing the measured population to rise toward its equilibrium value.

Model predictions were strongly influenced by the choice of the self-absorption length scale used in the escape factor calculation for atomic resonance lines. Additionally, the incorporation of enthalpy increases caused by the non-ideal pressure rise was essential for predicting the timescale of excited state evolution observed in the experiment. The duration of the plateau stage was particularly affected by the inclusion of non-ideal pressure effects. Measured pressure traces should, therefore, be incorporated into the interpretation of future atomic excited state measurements in reflected shock experiments.

Further measurements of N(^{4}P) behind reflected shocks in mixtures of 5% and 13% N_2 dilute in argon were also analyzed. Two notable discrepancies were observed between the measurements and predictions: first, the measured induction time was shorter than the model predicted, and second, the measured time history exhibited a steady decrease from its peak value that the model

also did not predict. Similar, but smaller, induction time discrepancies were observed in the lowest-pressure experiment with the 2% N_2 test gas, with the data at 5% and 13% establishing the trend that these discrepancies increase proportionally to the N_2 concentration. Results indicated that heavy particle impact excitation involving N + N collisions may explain the decreased induction times observed at elevated N_2 concentrations. However, it was not possible to infer appropriate modifications to the kinetic model due to the unavailability of pressure data for the 5% and 13% experiments.

Model disagreements with data taken at 5% and 13% N_2 concentrations highlight the value of further $N(^4P)$ measurements at elevated N_2 concentrations. The experimental data show a clear effect from the increased presence of N_2, indicating that excitation kinetics relevant to high-temperature air can be probed by applying the experimental techniques of Finch et al. [9] to test gas mixtures with more N_2.

Finally, a global sensitivity analysis of the $N(^4P)$ predictions was performed using the techniques presented in West and Hosder [55]. Total Sobol' indices were presented for several representative experimental conditions in 2% and 13% N_2 test gas mixtures. The dissociation rate coefficient of $N_2(X)$ with argon was the most sensitive parameter in all experiments, highlighting the value of comparing model predictions with $N_2(X)$ dissociation measurements taken by Appleton et al .[14]. Processes involved in the production of $N_2(A)$ were also sensitive, owing to the influence that $N_2(A)$ may have on the net dissociation rate. Experimental measurements of $N_2(A)$ could help to further constrain the adopted collisional-radiative model and provide valuable information on the potential role of $N_2(A)$ in the net dissociation of N_2.

A large number of electron impact excitation reactions also showed marked sensitivity, particularly those involving the excitation of $N(^4P)$ from the metastable levels. Excitation of the sixth and eighth levels of N was also important since these states are strongly coupled to the measured level by electron impact excitation and, in the case of the eighth level, radiative transition. The sensitivity results illustrated the diversity of formation and removal mechanisms for the measured electronic level, underscoring the importance of adopting a high-fidelity representation of the elec-

tronic states and their transitions when interpreting the experimental measurements.

8.1.6 Modeling and Sensitivity Analysis of Electronic Excitation and Ionization in Air

In this chapter, the uncertainties and input sensitivities of ionization predictions were analyzed in the context of a two-temperature model, the most common model of nonequilibrium thermochemistry used in vehicle-scale hypersonic flow simulations. To capture the range of flow conditions around a hypersonic vehicle, both post-shock and recombining flows were studied, with enthalpies corresponding to freestream velocities of 5-9 km/s at a standard altitude of 60 km. A total of 58 uncertain input parameters were considered, including relaxation times, reaction rate coefficients, and electron-heavy particle energy exchange cross-sections. Uncertainty intervals for each input parameter were selected based on the scatter in available values across the literature.

Behind normal shocks at 5 km/s and 7 km/s, associative ionization to form NO^+ was the main contributor to electron number density predictive uncertainty. The vast majority of uncertainty in the electron number density at 5 km/s was due to associative ionization processes, with a negligible influence from chemical reactions involving only neutral species. However, rate coefficients for several reactions involving NO showed a notable impact on the electron number density uncertainties in the higher velocity 7 and 9 km/s normal shock cases. Charge exchange reactions also began to show sensitivity for the 7 km/s normal shock condition and contributed to significant uncertainties for the 9 km/s condition. At 9 km/s, charge exchange involving N_2^+ and N was the greatest contributor to the overall uncertainty alongside the electron impact ionization of atomic nitrogen. Note that these two dominant contributors to the uncertainty in ionization behind the 9 km/s shock may be studied using experiments in pure N_2, which are considerably simpler to analyze than experiments performed in air.

Relative uncertainties were larger in the recombining flow scenarios than in the ionizing post-shock flows, indicating that electron number density predictions downstream of strong expansions are more uncertain than predictions behind strong shocks. The electron recombination rate demon-

strated high sensitivity to the dissociative recombination rate of NO^+, similar to the shocked flow cases, but also depended heavily on the rate coefficient of $O^+ + N_2 \leftrightharpoons NO^+ + N$.

Parameter-specific contributions to the uncertainty in electron number density provided valuable insight into the areas of greatest weakness in existing nonequilibrium ionization models. Several of the identified reactions were already known to be important for ionization predictions; however, many were not, highlighting the value of the global sensitivity analysis and uncertainty quantification presented in this chapter. The identified rate coefficient parameters should be the first targets of any effort to improve the predictive accuracy of two-temperature models for ionization in hypersonic air flows.

Next, an electronic state-resolved approach to modeling the ionization of air behind strong shock waves was applied to the study of ionization behind normal shocks at velocities of 5-9 km/s. A large number of elementary processes were included in the model, with special attention given to the excitation of metastable N and O atoms and to the associative ionization (AI) leading to NO^+, N_2^+, and O_2^+. The effect of explicitly including AI reactions involving metastable N and O atoms was investigated using several forms of the collisional-radiative model. Within the baseline model, the explicit modeling of AI from metastable reactant atoms was not found to significantly influence the overall electron number density at the conditions tested. If heavy particle impact excitation is much slower, as predicted by some authors, then the electron number density can be affected by up to 20% for a 5 km/s normal shock.

Finally, a sensitivity analysis of the collisional-radiative model was performed, considering 578 uncertain parameters, for electron number density predictions behind normal shocks in the velocity range of 5-9 km/s. Electron number density predictions in the collisional-radiative model showed similar sensitivities as in the two-temperature sensitivity analysis, with some differences as well. In regions where AI is highly active, the reactions involving metastable atoms dominated the sensitivity. Zel'dovich reactions also exhibited considerable sensitivity in the analysis of the collisional-radiative model, as did several of the charge exchange reactions that were important in the 2T model. The results of these sensitivity analyses provide quantitative information on the

electronic state-specific processes that are most relevant to the accurate modeling of ionization behind strong shock waves in air.

8.2 Contributions

- **Development of a general-purpose nonequilibrium chemical kinetics solver.** The work in this dissertation was enabled by the generalization and significant enhancement of the electronic state-resolved code originally developed by Jae Gang Kim for simulating pure nitrogen shock tube flows [82]. The code was extended to handle a general ionized flow consisting of atomic, diatomic, and polyatomic species, with the ability to solve separate conservation equations for vibrational, rotational, and electron-electronic energy. State-resolved treatments can be applied to the electronic states of all species and to the vibrational states of diatomic species. User-selected source terms can also be printed for later analysis.

- **Development of a sensitivity analysis wrapper for the chemical kinetics solver.** A brand new code was developed to enable all of the sensitivity analyses presented throughout this thesis. This code enables large-scale global sensitivity analyses to be performed using the chemical kinetics solver. The new tool provides a third window into the complex dynamics being studied, highlighting behavior that neither the state variables nor the source terms can show.

- **Formulated and benchmarked an approach for modeling reflected shock experiments in gases undergoing significant density change.** An approach for modeling reflected shock experiments was formulated. The new formulation was benchmarked using unsteady one-dimensional computational fluid dynamics. It was shown that the new approach accurately computes the reflected shock deceleration in experiments probing highly endothermic relaxation processes. The evolution of the test gas at the measurement location was predicted accurately, even in the presence of unsteady shock motion.

- **Comprehensive assessment of coupled vibrational relaxation and dissociation models for shock-heated oxygen.** Several leading modeling approaches for O_2 vibrational relaxation and dissociation were assessed using low-uncertainty experimental measurements of T_{vib} and n_{O_2} in several pure O_2 shock tube experiments. Of the tested models, the predictions using the Modified Marrone and Treanor (MMT) model were most consistent with the measured data.

- **Formulated a three-temperature electronic state-resolved model of an O_2-N_2-Ar plasma.** Performed a comprehensive literature review to identify the best available formulations of the necessary rate and relaxation parameters to include in the model. Particular attention was paid to the modeling of dissociation, heavy particle electronic excitation, and associative ionization. The latest data for electron impact excitation and ionization were also included.

- **Revised previous interpretations of atomic oxygen and nitrogen excited state measurements behind reflected shocks.** Previous analysis of the atomic excited state measurements was done using simplified collisional-radiative kinetic models. Several interpretations of the observed behavior were put forward using those simplified models. By simulating the experiments using the detailed collisional-radiative model developed here, several aspects of the previous interpretations were shown to be incomplete or incorrect. The detailed model was able to accurately predict many experimental observations while also providing a more comprehensive and accurate explanation of the system dynamics driving the observed behavior.

- **Identified sensitive parameters influencing atomic excited state measurements.** Global sensitivity analyses considering nearly 300 model parameters were performed to assess the sensitivity of the measured excited state population to the parameters used in the collisional-radiative model. This analysis provided information on the model parameters that data from each experiment could usefully inform. The dominant formation and de-

struction pathways of the measured states were clearly identified, providing useful guidance for the interpretation of future atomic excited state measurements.

- **Performed sensitivity analysis and uncertainty quantification for the evolution of plasma density in net-ionizing and net-recombining flow scenarios in air using a two-temperature model.** Carried out a novel assessment of the uncertainty in electron number density predictions behind strong shock waves in air. Investigated recombining flow scenarios as well, which are representative of strongly expanded flow. Sensitivity information was combined with uncertainty magnitudes to provide a picture of the reactions that contribute the most in regions where the plasma density is highly uncertain.

- **Analyzed the role of atomic metastable electronic excitation in associative ionization behind strong shock waves.** Investigated how the separation of ground and excited-state channels for associative ionization can affect the net rate of ionization behind strong shocks. The conditions under which the atomic electronic excitation can significantly impact ionization predictions were identified. A detailed discussion was given on the reasons behind the observed behavior.

- **Performed sensitivity analysis for the prediction of plasma formation behind strong shock waves in air using the collisional-radiative model.** Identified several reactions in the electronic state-resolved air model that warrant further study. Provided an electronic state-resolved picture of the processes leading to plasma formation behind strong shock waves, helping to more precisely identify the processes that contribute to predictive uncertainty in current models of ionization in air.

8.3 Recommendations for Future Work

8.3.1 Facility Modeling for Reflected Shock Experiments

In all of the reflected shock experiments analyzed throughout this thesis, the measured pressure in the test gas was higher than what is predicted using the Rankine-Hugoniot relations. The cause of this pressure offset is probably some combination of boundary layer growth, shock attenuation, and end-wall heat transfer. The best way to test this hypothesis is by performing a facility simulation that includes some or all of these effects. Moving beyond the approach adopted in this thesis, the logical next step in model complexity is to solve the unsteady one-dimensional Navier-Stokes equations. Grogan and Ihme solved the Navier-Stokes equations in several one-dimensional simulations of reflected shock flows for combustion applications and found that the inclusion of simple boundary layer source terms was sufficient for reproducing the measured pressure traces [217]. The stronger shocks required for investigations of high-temperature air chemistry are more challenging to simulate; however, previous studies have successfully simulated high Mach number moving shock waves [218].

In Chapter 4, none of the two-temperature models were able to predict the measured O_2 number density for the highest temperature pure O_2 experiment. If a one-dimensional CFD calculation that includes boundary layer terms can accurately predict the pressure in reflected shock experiments, then the O_2 number density data could be used with much more confidence. If pressure traces could be accurately predicted, then it would also be possible to assess any connection between the reflected shock velocity and the non-ideal pressure rise in Region 5, a point that is mentioned in Section 2.3.2. It would also be possible to quantify the accuracy of assuming the dP/dt causes adiabatic compression. Results shown in Chapters 5 and 6 demonstrate that this compression can have a significant effect on the quantities of interest and, therefore, kinetic model validation efforts.

A challenge in attempting to simulate non-ideal effects is the difficulty of capturing shot-to-shot variation. Satchell et al. [219, 220] avoid this problem by directly implementing the measured

shock velocity profile into their simulations of incident shock experiments. Such an approach is not readily applicable to reflected shock experiments, which require an Eulerian solver, as opposed to the Lagrangian solver developed by Satchell et al. While the exact form of input data is unclear, it is likely that a successful prediction of non-ideal effects in reflected shock experiments will require some kind of input of measured data from the shock tube to specify the shot-dependent non-ideal conditions.

8.3.2 Further Validation of Collisional-Radiative Model in Air Flows

The collisional-radiative model has been primarily validated using experiments performed in O_2 or N_2 dilute in argon, with limited validation for air mixtures. Further development of the collisional-radiative model should focus on comparisons to spectra measured behind shocks in air [211] and nitrogen [221, 215] shock tube experiments. These data provide a valuable test for the developed model in mixtures that contain only species relevant to plasma formation in air. Note that validation of the model at the sub-orbital shock velocities will require shock tube data at lower shock speeds than is currently available.

8.3.3 Effects of Molecular Electronic Excitation on Dissociation

Accurate dissociation predictions by the collisional-radiative model are important for ensuring useful predictions of ionization in air flows. Thus, further validation of the adopted dissociation rate constants should be performed in tandem with future studies of ionization in air. Electronically excited molecular nitrogen, $N_2(A)$ contributed significantly to the net dissociation rate of N_2 in the results of Chapters 6 and 7. Measurements of $N_2(A)$ will be an important pre-requisite for future studies of how electronic excitation may affect net N_2 dissociation.

The dissociation of O_2 is also known to be impacted by the dissociation of electronically excited states [5]. The dissociation of O_2 from electronically excited states may be readily studied using the measurements by Streicher et al. [5]; however, increased accuracy in the predictions of test gas pressure is necessary for such an analysis, which would rely primarily on n_{O_2} measurements

instead of T_{vib} measurements.

Effects of the dissociation from electronically excited states should be studied more generally as the collisional-radiative model matures and is extended to include more species. For example, electronic excitation has also been proposed as a reason for the experimentally observed induction time for the dissociation of CO by Mick et al. [222]. The electronic state-resolved model developed in this thesis is an ideal tool for further analyzing the unresolved questions surrounding the influence of dissociation from electronically excited molecules.

Bibliography

[1] Chul Park. Review of Chemical-Kinetic Problems of Future NASA Missions, I: Earth Entries. Journal of Thermophysics and Heat Transfer, 7(3):385–398, September 1993.

[2] Roger C. Millikan and Donald R. White. Systematics of Vibrational Relaxation. The Journal of Chemical Physics, 39(12):3209–3213, December 1963.

[3] H. Harvey Michels. Electronic Structure of Excited States of Selected Atmospheric Systems. In J. Wm. McGowan, editor, Advances in Chemical Physics, pages 225–340. John Wiley & Sons, Inc., Hoboken, NJ, USA, 1981.

[4] Chul Park. Rate Parameters for Electronic Excitation of Diatomic Molecules 1. Electron-Impact Processes. In 46th AIAA Aerospace Sciences Meeting and Exhibit, Reno, Nevada, January 2008. American Institute of Aeronautics and Astronautics.

[5] Jesse W. Streicher, Ajay Krish, and Ronald K. Hanson. Coupled vibration-dissociation time-histories and rate measurements in shock-heated, nondilute O_2 and O_2-Ar mixtures from 6,000 to 14,000 K. Physics of Fluids, 33(5):056107, May 2021.

[6] Yang Li, Yu Wang, David F. Davidson, and Ronald K. Hanson. Collisional excitation kinetics for $O(3s^5S^o)$ and $O(3p^5P_3)$ states using laser absorption spectroscopy in shock-heated weakly ionized O_2-Ar mixture. Physical Review E, 103(6):063211, June 2021.

[7] M. G. Kapper and J.-L. Cambier. Ionizing shocks in argon. Part I: Collisional-radiative model and steady-state structure. Journal of Applied Physics, 109(11):113308, June 2011.

[8] Peter M. Finch, Zev N. Granowitz, Jesse W. Streicher, Ajay Krish, Christopher L. Strand, and Ronald K. Hanson. Shock-Tube Measurements of Atomic Nitrogen Collisional Excitation in 8000-12000 K Partially Ionized Nitrogen-Argon Mixtures. The Journal of Physical Chemistry A, 127(6):acs.jpca.2c07839, February 2023.

[9] Peter M. Finch. Applications of Laser Absorption Spectroscopy to the Study of Hypersonic Flows in Ground Test Facilities. PhD thesis, Stanford University, 2023.

[10] R Dalbey, S Eldred, Kathryn A Maupin, Jason A Monschke, D Thomas Seidl, Laura P Swiler, and Anh Tran. Dakota, A Multilevel Parallel Object-Oriented Framework for Design Optimization, Parameter Estimation, Uncertainty Quantication, and Sensitivity Analysis: Version 6.15 Theory Manual. Technical Report SAND2021-14254, Sandia National Laboratories, November 2021.

[11] Michael G. Dunn and Sang-Wook Kang. Theoretical and Experimental Studies of Reentry Plasmas. NASA Contractor Report CR-2232, NASA, April 1973.

[12] Ross S. Chaudhry, Iain D. Boyd, Erik Torres, Thomas E. Schwartzentruber, and Graham V. Candler. Implementation of a Chemical Kinetics Model for Hypersonic Flows in Air for High-Performance CFD. In AIAA Scitech 2020 Forum, Orlando, FL, January 2020. American Institute of Aeronautics and Astronautics.

[13] Jesse W. Streicher, Ajay Krish, Ronald K. Hanson, Kyle M. Hanquist, Ross S. Chaudhry, and Iain D. Boyd. Shock-tube measurements of coupled vibration-dissociation time-histories and rate parameters in oxygen and argon mixtures from 5,000 K to 10,000 K. Physics of Fluids, 32(7):076103, July 2020.

[14] J. P. Appleton, M. Steinberg, and D. J. Liquornik. ShockTube Study of Nitrogen Dissociation using VacuumUltraviolet Light Absorption. The Journal of Chemical Physics, 48(2):599–608, January 1968.

[15] A. Lemal, C. M. Jacobs, M.-Y. Perrin, C. O. Laux, P. Tran, and E. Raynaud. Prediction of Nonequilibrium Air Plasma Radiation Behind a Shock Wave. Journal of Thermophysics and Heat Transfer, 30(1):197–210, January 2016.

[16] Shao-Chi Lin, Richard A. Neal, and Walter I. Fyfe. Rate of Ionization behind Shock Waves in Air. I. Experimental Results. Physics of Fluids, 5(12):1633, 1962.

[17] Chul Park. Nonequilibrium Hypersonic Aerothermodynamics. John Wiley & Sons, 1990.

[18] P. Hammerling, J. D. Teare, and B. Kivel. Theory of Radiation from Luminous Shock Waves in Nitrogen. Physics of Fluids, 2(4):422, 1959.

[19] Arnaud Bultel, Bruno G. Chéron, Anne Bourdon, Ousmanou Motapon, and Ioan F. Schneider. Collisional-radiative model in air for earth re-entry problems. Physics of Plasmas, 13(4):043502, April 2006.

[20] Sung Min Jo, Oh Joon Kwon, and Jae Gang Kim. Electronic-state-resolved analysis of high-enthalpy air plasma flows. Physical Review E, 100(3):033203, September 2019.

[21] Ross S Chaudhry and Iain D Boyd. Vehicle-Scale Simulations of Hypersonic Flows using the MMT Chemical Kinetics Model. In AIAA Aviation 2020 Forum, page 26, Virtual Event, 2020. American Institute of Aeronautics and Astronautics.

[22] Pawel Sawicki, Ross S. Chaudhry, and Iain D. Boyd. Influence of Chemical Kinetics Models on Plasma Generation in Hypersonic Flight. In AIAA Scitech 2021 Forum, VIRTUAL EVENT, January 2021. American Institute of Aeronautics and Astronautics.

[23] Qinglin Niu, Zhichao Yuan, Biao Chen, and Shikui Dong. Infrared radiation characteristics of a hypersonic vehicle under time-varying angles of attack. Chinese Journal of Aeronautics, 32(4):861–874, April 2019.

[24] Leonardo Scalabrin and Iain Boyd. Numerical Simulation of Weakly Ionized Hypersonic Flow for Reentry Configurations. In 9th AIAA/ASME Joint Thermophysics and Heat Transfer Conference, San Francisco, California, June 2006. American Institute of Aeronautics and Astronautics.

[25] Graham V. Candler, Heath B. Johnson, Ioannis Nompelis, Vladimyr M. Gidzak, Pramod K. Subbareddy, and Michael Barnhardt. Development of the US3D Code for Advanced Compressible and Reacting Flow Simulations. In 53rd AIAA Aerospace Sciences Meeting, Kissimmee, Florida, January 2015. American Institute of Aeronautics and Astronautics.

[26] Vincent Casseau, Rodrigo Palharini, Thomas Scanlon, and Richard Brown. A Two-Temperature Open-Source CFD Model for Hypersonic Reacting Flows, Part One: Zero-Dimensional Analysis. Aerospace, 3(4):34, October 2016.

[27] Ross S. Chaudhry and Graham V. Candler. Statistical Analyses of Quasiclassical Trajectory Data for Air Dissociation. In AIAA Scitech 2019 Forum, San Diego, California, January 2019. American Institute of Aeronautics and Astronautics.

[28] Robyn Lindsay Macdonald. Reduced-order model framework for thermochemical non-equilibrium hypersonic flows. Doctoral, University of Illinois, 2019.

[29] Maitreyee P. Sharma, Yen Liu, and Marco Panesi. Coarse-grained modeling of thermochemical nonequilibrium using the multigroup maximum entropy quadratic formulation. Physical Review E, 101(1):013307, January 2020.

[30] Amal Sahai. Reduced-order modeling of non-Boltzmann thermochemistry and radiation for hypersonic flows. Doctoral, University of Illinois, Urbana, Illinois, 2019.

[31] Chul Park. Two-temperature interpretation of dissociation rate data for N_2 and O_2. In 26th Aerospace Sciences Meeting, Reno,NV,U.S.A., January 1988. American Institute of Aeronautics and Astronautics.

[32] Chul Park. The Limits of Two-Temperature Kinetic Model in Air. In 48th AIAA Aerospace Sciences Meeting Including the New Horizons Forum and Aerospace Exposition, Orlando, Florida, January 2010. American Institute of Aeronautics and Astronautics.

[33] Ross S. Chaudhry and Iain D. Boyd. Parametric Comparison of the Park and MMT Chemical Kinetics Models for Hypersonic Blunt Cones. In AIAA AVIATION 2022 Forum, Chicago, IL & Virtual, June 2022. American Institute of Aeronautics and Astronautics.

[34] Ross S. Chaudhry and Iain D. Boyd. Parametric Comparison of the Park and MMT Chemical Kinetics Models with Multiple Freestream Speeds. In AIAA AVIATION 2023 Forum, San Diego, CA and Online, June 2023. American Institute of Aeronautics and Astronautics.

[35] Varishth T. Baluckram and Daniil Andrienko. Comparison of O_2-O vibrational relaxation and dissociation rate coefficients computed on potential energy surfaces of different fidelity. In AIAA Scitech 2020 Forum, Orlando, FL, January 2020. American Institute of Aeronautics and Astronautics.

[36] Varishth T. Baluckram and Daniil Andrienko. First-principle simulation of vibrational activation and dissociation in oxygen shock flows. In AIAA Scitech 2021 Forum, VIRTUAL EVENT, January 2021. American Institute of Aeronautics and Astronautics.

[37] Kyle M. Hanquist, Ross S. Chaudhry, Iain D. Boyd, Jesse Streicher, Ajay Krish, and Ronald Hanson. Detailed Thermochemical Modeling of O_2-Ar Mixtures in Reflected Shock Tube Flows. In AIAA AVIATION 2020 FORUM, VIRTUAL EVENT, June 2020. American Institute of Aeronautics and Astronautics.

[38] Varishth T Baluckram, Alexander J Fangman, and Daniil A Andrienko. Simulation of Oxygen Chemical Kinetics Behind Incident and Reflected Shocks via Master Equation. Journal of Thermophysics and Heat Transfer, page 15, 2022.

[39] A. Lemal, C. M. Jacobs, M.-Y. Perrin, C. O. Laux, P. Tran, and E. Raynaud. Air Collisional-Radiative Modeling with Heavy-Particle Impact Excitation Processes. Journal of Thermophysics and Heat Transfer, 30(1):226–239, January 2016.

[40] Iain D. Boyd and Eswar Josyula. Analysis of Associative Ionization Rates for Hypersonic Flows. Journal of Thermophysics and Heat Transfer, pages 1–10, May 2021.

[41] Brett A. Cruden and Aaron M. Brandis. Analysis of Shockwave Radiation Data in Nitrogen. In AIAA Aviation 2019 Forum, Dallas, Texas, June 2019. American Institute of Aeronautics and Astronautics.

[42] Christopher J. Ciccarino and Daniel W. Savin. Electron-Impact Ionization of Atomic Nitrogen. Journal of Thermophysics and Heat Transfer, 33(1):154–162, January 2019.

[43] Yang Wang, Oleg Zatsarinny, and Klaus Bartschat. B-spline R-matrix-with-pseudostates calculations for electron-impact excitation and ionization of nitrogen. Physical Review A, 89(6):062714, June 2014.

[44] Winifred M. Huo, Yen Liu, Marco Panesi, Alan Wray, and Duane F. Carbon. Electron-Impact Excitation Cross Sections for Modeling Non-Equilibrium Gas. In 53rd AIAA Aerospace Sciences Meeting, Kissimmee, Florida, January 2015. American Institute of Aeronautics and Astronautics.

[45] P. S. Barklem, A. K. Belyaev, M. Guitou, N. Feautrier, F. X. Gadéa, and A. Spielfiedel. On inelastic hydrogen atom collisions in stellar atmospheres. Astronomy & Astrophysics, 530:A94, June 2011.

[46] B. R. L. Galvão, A. J. C. Varandas, J. P. Braga, and J. C. Belchior. Electronic Quenching of $N(^2D)$ by N_2: Theoretical Predictions, Comparison with Experimental Rate Constants, and Impact on Atmospheric Modeling. The Journal of Physical Chemistry Letters, 4(14):2292–2297, July 2013.

[47] Dandan Lu, Breno R. L. Galvo, Antonio J. C. Varandas, and Hua Guo. Quantum and semiclassical studies of nonadiabatic electronic transitions between $N(^4S)$ and $N(^2D)$ by collisions with N_2. Physical Chemistry Chemical Physics, 25(23):15656–15665, 2023.

[48] Yan Sun and A. Dalgarno. Collisional excitation of metastable $O(^1D)$ atoms. The Journal of Chemical Physics, 96(7):5017–5019, April 1992.

[49] H.W. Drawin and F. Emard. Atom-atom excitation and ionization in shock waves of the noble gases. Physics Letters A, 43(4):333–335, March 1973.

[50] Sergey T. Surzhikov. Radiative-Collisional Models in Non-Equilibrium Aerothermodynamics of Entry Probes. Journal of Heat Transfer, 134(3):031002, March 2012.

[51] J Vlcek. A collisional-radiative model applicable to argon discharges over a wide range of conditions. I. Formulation and basic data. Journal of Physics D: Applied Physics, 22(5):623–631, May 1989.

[52] A. Frohn and P.C.T. de Boer. Measurement of Ionization Relaxation Times in Shock Tubes. Physics of Fluids, 12(5):I–54, 1969.

[53] Bryan Niblett and Vernon H. Blackman. An approximate measurement of the ionization time behind shock waves in air. Journal of Fluid Mechanics, 4(02):191, June 1958.

[54] Andrea Saltelli, Ksenia Aleksankina, William Becker, Pamela Fennell, Federico Ferretti, Niels Holst, Sushan Li, and Qiongli Wu. Why so many published sensitivity analyses are false: A systematic review of sensitivity analysis practices. Environmental Modelling & Software, 114:29–39, April 2019.

[55] Thomas K. West and Serhat Hosder. Uncertainty Quantification of Hypersonic Reentry Flows with Sparse Sampling and Stochastic Expansions. Journal of Spacecraft and Rockets, 52(1):120–133, January 2015.

[56] Thomas K. West, Andrew J. Brune, Serhat Hosder, and Christopher O. Johnston. Uncertainty Analysis of Radiative Heating Predictions for Titan Entry. Journal of Thermophysics and Heat Transfer, 30(2):438–451, April 2016.

[57] Thomas K. West, Christopher O. Johnston, and Serhat Hosder. Uncertainty and Sensitivity Analysis of Afterbody Radiative Heating Predictions for Earth Entry. Journal of Thermophysics and Heat Transfer, 31(2):294–306, April 2017.

[58] Marcel Nations, Shengkai Wang, Christopher S. Goldenstein, David F. Davidson, and Ronald K. Hanson. Kinetics of Excited Oxygen Formation in Shock-Heated O_2-Ar Mixtures. The Journal of Physical Chemistry A, 120(42):8234–8243, October 2016.

[59] Yang Li, Shengkai Wang, Christopher L Strand, and Ronald K Hanson. Two-temperature Collisional-radiative Modeling of Partially Ionized O_2-Ar Mixtures over 8,000-10,000 K Behind Reflected Shock Waves. J. Phys. Chem. A, page 11, 2020.

[60] Nicolas Q. Minesi, Anil P. Nair, Miles O. Richmond, Nicholas M. Kuenning, Christopher C. Jelloian, and R. Mitchell Spearrin. Excited oxygen kinetics at electronvolt temperatures via 5-MHz RF-diplexed laser absorption spectroscopy. Applied Optics, 62(3):782, January 2023.

[61] Timothy T. Aiken and Iain D. Boyd. Assessment of Detailed Thermochemistry and Excitation Models for Shock-Heated Oxygen Mixtures. In AIAA AVIATION 2022 Forum, Chicago, IL & Virtual, June 2022. American Institute of Aeronautics and Astronautics.

[62] J P Appleton. ShockTube Study of the Vibrational Relaxation of Nitrogen Using VacuumUltraviolet Light Absorption. J. Chem. Phys., 47(9):3231–3240, 1967.

[63] L.L Presley and R.K. Hanson. Exact Solutions of Reflected Normal Shock-Wave Flow Fields with Nonequilibrium Chemical Reactions. In AIAA Fluid and Plasma Dynamics Conference, Los Angeles, CA, 1968. AIAA.

[64] Maitreyee Sharma, Alessandro Munafò, Aaron M. Brandis, Brett A. Cruden, and Marco Panesi. One-dimensional modeling methodology for shock tubes: Application to the EAST facility. In 2018 Joint Thermophysics and Heat Transfer Conference, Atlanta, Georgia, June 2018. American Institute of Aeronautics and Astronautics.

[65] G. B. Whitham. On the propagation of shock waves through regions of non-uniform area or flow. Journal of Fluid Mechanics, 4(04):337, August 1958.

[66] Harold Mirels. Test Time in Low-Pressure Shock Tubes. Physics of Fluids, 6(9):1201, 1963.

[67] National Institute of Standards and Technology. Atomic spectra database, 2021.

[68] Jae Gang Kim and Iain D. Boyd. State-resolved master equation analysis of thermochemical nonequilibrium of nitrogen. Chemical Physics, 415:237–246, March 2013.

[69] Daniil A. Andrienko and Iain D. Boyd. Rovibrational energy transfer and dissociation in O_2-O collisions. The Journal of Chemical Physics, 144(10):104301, March 2016.

[70] Klaus P. Huber, Gerhard H. Herzberg (data prepared by Jean W. Gallagher, and III) Russell D. Johnson. NIST Chemistry WebBook, NIST Standard Reference Database Number 69, Eds. P.J. Linstrom and W.G. Mallard. National Institute of Standards and Technology, Gaithersburg MD.

[71] P. S. Barklem and R. Collet. Partition functions and equilibrium constants for diatomic molecules and atoms of astrophysical interest. Astronomy & Astrophysics, 588:A96, April 2016.

[72] H.A. Bethe and E. Teller. Deviations from thermal equilibrium in shock waves. Technical Report X-117, Aberdeen Proving Ground, MD, 1941.

[73] V. Laporta, K.L. Heritier, and M. Panesi. Electron-vibration relaxation in oxygen plasmas. Chemical Physics, 472:44–49, June 2016.

[74] V Laporta and D Bruno. Electron-vibration energy exchange models in nitrogen-containing plasma flows. J. Chem. Phys., 138(104319):10, 2013.

[75] Minkwan Kim, Ali Gülhan, and Iain D. Boyd. Modeling of Electron Energy Phenomena in Hypersonic Flows. Journal of Thermophysics and Heat Transfer, 26(2):244–257, April 2012.

[76] A Gnoffo, N Gupta, and L Shinn. Conservation Equations and Physical Models for Hypersonic Air Flows in Thermal and Chemical Nonequilibrium. NASA Technical Paper 2867, National Aeronautics and Space Administration, February 1989.

[77] Maninder S. Grover, Thomas E. Schwartzentruber, Zoltan Varga, and Donald G. Truhlar. Vibrational Energy Transfer and Collision-Induced Dissociation in $O+O_2$ Collisions. Journal of Thermophysics and Heat Transfer, 33(3):797–807, July 2019.

[78] Alexander J. Fangman and Daniil A. Andrienko. Vibrational-Specific Model of Simultaneous N_2-N and N_2-N_2 Relaxation Under Postshock Conditions. Journal of Thermophysics and Heat Transfer, 36(3):568–583, July 2022.

[79] Jesse W. Streicher, Ajay Krish, and Ronald K. Hanson. High-temperature vibrational relaxation and decomposition of shock-heated nitric oxide. I. Argon dilution from 2,200 to 8,700 K. Physics of Fluids, 34(11):116122, November 2022.

[80] Jesse W. Streicher, Ajay Krish, and Ronald K. Hanson. High-temperature vibrational relaxation and decomposition of shock-heated nitric oxide: II. Nitrogen dilution from 1,900 to 8,200 K. Physics of Fluids, 34(11):116123, November 2022.

[81] Kyle M. Hanquist and Iain D. Boyd. Modeling of Electronically Excited Oxygen in O_2-Ar Shock Tube Studies. In AIAA Aviation 2019 Forum, Dallas, Texas, June 2019. American Institute of Aeronautics and Astronautics.

[82] Jae Gang Kim and Iain D. Boyd. Master Equation Analysis of Post Normal Shock Waves of Nitrogen. Journal of Thermophysics and Heat Transfer, 29(2):241–252, April 2015.

[83] Saruñas S. Lazdinis. Free electron and vibrational temperature nonequilibrium in high temperature nitrogen. Physics of Fluids, 17(8):1539, 1974.

[84] Michio Nishida and Masashi Matsumotob. Thermochemical Nonequilibrium in Rapidly Expanding Flows of High-Temperature Air. Zeitschrift fr Naturforschung A, 52(4):358–368, April 1997.

[85] Oleg Zatsarinny, Yang Wang, and Klaus Bartschat. Electron-impact excitation of argon at intermediate energies. Physical Review A, 89(2):022706, February 2014.

[86] S. S. Tayal and Oleg Zatsarinny. B-spline R-matrix-with-pseudostates approach for excitation and ionization of atomic oxygen by electron collisions. Physical Review A, 94(4):042707, October 2016.

[87] I.P. Shkarofsky, M.P. Bachynski, and T.W. Johnston. Collision frequency associated with high temperature air and scattering cross-sections of the constituents. Planetary and Space Science, 6:24–46, June 1961.

[88] J. P. Appleton and K. N. C. Bray. The conservation equations for a non-equilibrium plasma. Journal of Fluid Mechanics, 20(4):659–672, December 1964.

[89] C. Goldbach, G. Nollez, S. Popović, and M. Popović. Electrical Conductivity of High Pressure Ionized Argon. Zeitschrift für Naturforschung A, 33(1):11–17, January 1978.

[90] Erin Farbar, Iain D. Boyd, and Alexandre Martin. Numerical Prediction of Hypersonic Flowfields Including Effects of Electron Translational Nonequilibrium. Journal of Thermophysics and Heat Transfer, 27(4):593–606, October 2013.

[91] Arnaud Bultel, Bruno van Ootegem, Anne Bourdon, and Pierre Vervisch. Influence of Ar_2^+ in an argon collisional-radiative model. Physical Review E, 65(4):046406, March 2002.

[92] Jae Gang Kim. Expansion of the equilibrium constants for the temperature range of 300 K to 20,000 K. International Journal of Aeronautical and Space Sciences, 17(4):455–466, December 2016.

[93] H Lomax. Stable implicit and explicit numerical methods for integrating quasi-linear differential equations with parasitic-stiff and parasitic-saddle eigenvalues. NASA Technical Note D-4703, National Aeronautics and Space Administration, Washington, D.C., 1968.

[94] Alexandre Martin, Leonardo C Scalabrin, and Iain D Boyd. High performance modeling of atmospheric re-entry vehicles. Journal of Physics: Conference Series, 341:012002, February 2012.

[95] Alessandro Munafò and Marco Panesi. Plato: a high-fidelity tool for multi-component plasmas. In AIAA AVIATION 2023 Forum, San Diego, CA and Online, June 2023. American Institute of Aeronautics and Astronautics.

[96] G. Deman, K. Konakli, B. Sudret, J. Kerrou, P. Perrochet, and H. Benabderrahmane. Using sparse polynomial chaos expansions for the global sensitivity analysis of groundwater lifetime expectancy in a multi-layered hydrogeological model. Reliability Engineering & System Safety, 147:156–169, March 2016.

[97] Nora Lüthen, Stefano Marelli, and Bruno Sudret. Sparse Polynomial Chaos Expansions: Literature Survey and Benchmark. SIAM/ASA Journal on Uncertainty Quantification, 9(2):593–649, January 2021.

[98] Ole Tange. Gnu parallel 20230222 ('gaziantep'), February 2023.

[99] Ewout Van Den Berg and Michael P. Friedlander. Probing the Pareto Frontier for Basis Pursuit Solutions. SIAM Journal on Scientific Computing, 31(2):890–912, January 2009.

[100] Ewout Van Den Berg and Michael P. Friedlander. Sparse Optimization with Least-Squares Constraints. SIAM Journal on Optimization, 21(4):1201–1229, October 2011.

[101] Jonathan Feinberg and Hans Petter Langtangen. Chaospy: An open source tool for designing methods of uncertainty quantification. Journal of Computational Science, 11:46–57, November 2015.

[102] Thomas K. West and Christopher O. Johnston. Efficient Parametric Uncertainty Analysis of an Earth Entry Vehicle Concept using Least Angle Regression. In AIAA SCITECH 2023 Forum, National Harbor, MD & Online, January 2023. American Institute of Aeronautics and Astronautics.

[103] Julien Annaloro, Philippe Teulet, Arnaud Bultel, Yann Cressault, and Alain Gleizes. Non-uniqueness of the multi-temperature law of mass action. Application to 2T plasma composition calculation by means of a collisional-radiative model. The European Physical Journal D, 71(12):342, December 2017.

[104] A. Bourdon, Y. Térésiak, and P. Vervisch. Ionization and recombination rates of atomic oxygen in high-temperature air plasma flows. Physical Review E, 57(4):4684–4692, April 1998.

[105] Marco Panesi, Thierry Magin, Anne Bourdon, Arnaud Bultel, and O. Chazot. Fire II Flight Experiment Analysis by Means of a Collisional-Radiative Model. Journal of Thermophysics and Heat Transfer, 23(2):236–248, April 2009.

[106] R. E. Kennerly. Absolute total electron scattering cross sections for N_2 between 0.5 and 50 eV. Physical Review A, 21(6):1876–1883, June 1980.

[107] P. C. Cosby. Electron-impact dissociation of nitrogen. The Journal of Chemical Physics, 98(12):9544–9553, June 1993.

[108] Paul V. Marrone and Charles E. Treanor. Chemical Relaxation with Preferential Dissociation from Excited Vibrational Levels. Physics of Fluids, 6(9):1215–1221, 1963.

[109] Timothy T. Aiken and Iain D. Boyd. Two-Temperature Modeling of Nonequilibrium Relaxation and Dissociation in Shock-Heated Oxygen. Journal of Thermophysics and Heat Transfer, pages 1–10, May 2023.

[110] Jae Gang Kim and Iain D. Boyd. Thermochemical nonequilibrium analysis of O_2+Ar based on state-resolved kinetics. Chemical Physics, 446:76–85, January 2015.

[111] Sergey O. Macheret and Igor V. Adamovich. Semiclassical modeling of state-specific dissociation rates in diatomic gases. The Journal of Chemical Physics, 113(17):7351–7361, November 2000.

[112] Ven H. Shui, John P. Appleton, and James C. Keck. ThreeBody Recombination and Dissociation of Nitrogen: A Comparison between Theory and Experiment. The Journal of Chemical Physics, 53(7):2547–2558, October 1970.

[113] Deborah A. Levin, Matthew Braunstein, Graham V. Candler, Robert J. Collins, and Gregory P. Smith. Examination of theory for bow shock ultraviolet rocket experiments. II. Journal of Thermophysics and Heat Transfer, 8(3):453–459, July 1994.

[114] Chul Park. Rate Parameters for Electronic Excitation of Diatomic Molecules II. Heavy Particle-Impact Processes. In 46th AIAA Aerospace Sciences Meeting and Exhibit, Reno, Nevada, January 2008. American Institute of Aeronautics and Astronautics.

[115] R. L. Macdonald, A. Munafò, C. O. Johnston, and M. Panesi. Nonequilibrium radiation and dissociation of CO molecules in shock-heated flows. Physical Review Fluids, 1(4):043401, August 2016.

[116] A. Aliat, Elena V. Kustova, and A. Chikhaoui. State-to-state dissociation rate coefficients in electronically excited diatomic gases. Chemical Physics Letters, 390(4-6):370–375, June 2004.

[117] Erik Torres, Thomas Gross, and Thomas E. Schwartzentruber. Implementation of new multitemperature nonequilibrium air chemistry model for CFD based on first-principles calculations. In AIAA AVIATION 2023 Forum, San Diego, CA and Online, June 2023. American Institute of Aeronautics and Astronautics.

[118] Michael C. Drake and John W. Ratcliffe. High temperature quenching cross sections for nitric oxide laserinduced fluorescence measurements. The Journal of Chemical Physics, 98(5):3850–3865, March 1993.

[119] Ven H Shui, John P Appleton, and James C Keck. The Three-Body Recombination and Dissociation of Diatomic Molecules: A Comparison Between Theory and Experiment. In International Symposium on Combustion, volume 13, Massachusetts Institute of Technology, 1971.

[120] P Teulet, J P Sarrette, and A M Gomes. Calculation of electron impact inelastic cross sections and rate coefficients for diatomic molecules. Application to air molecules. Journal of Quantitative Spectroscopy and Radiative Transfer, 62:549–569, 1999.

[121] Julien Annaloro and Arnaud Bultel. Vibrational and electronic collisional-radiative model in air for Earth entry problems. Physics of Plasmas, 21(12):123512, December 2014.

[122] D.-H. Kwon and Y.-S. Cho. Electron-impact excitation cross sections for Ar and Ar^+ by unitarized distorted-wave approximation. Atomic Data and Nuclear Data Tables, 137:101385, January 2021.

[123] A. Bourdon and P. Vervisch. Three-body recombination rate of atomic nitrogen in low-pressure plasma flows. Physical Review E, 54(2):1888–1898, August 1996.

[124] P V Johnson, J W McConkey, S S Tayal, and I Kanik. Collisions of electrons with atomic oxygen: current status. Canadian Journal of Physics, 83:28, 2005.

[125] H.W. Drawin. Atomic cross sections for inelastic electronic collisions. Association Euratom-CEA EUR-CEA-FC 236, 1963.

[126] H. Deutsch, K. Becker, S. Matt, and T.D. Märk. Theoretical determination of absolute electron-impact ionization cross sections of molecules. International Journal of Mass Spectrometry, 197(1-3):37–69, February 2000.

[127] H. Deutsch, K. Becker, A.N. Grum-Grzhimailo, K. Bartschat, H. Summers, M. Probst, S. Matt-Leubner, and T.D. Märk. Calculated cross sections for the electron-impact ionization of excited argon atoms using the DM formalism. International Journal of Mass Spectrometry, 233(1-3):39–43, April 2004.

[128] Adrien Lemal. Prediction of air nonequilibrium radiation with a collisional-radiative model: Application to shock-tube conditions relevant to Earth reentry. PhD thesis, Ecole Centrale Paris, July 2013.

[129] M.J. Jamieson, M. Finch, R.S. Friedman, and A. Dalgarno. Collisional excitation of metastable oxygen $O(^1D)$ atoms through the $B^3\Sigma_u^-$ channel of O_2. Planetary and Space Science, 40(12):1719–1721, 1992.

[130] Mark A. Blitz, Terry J. Dillon, Dwayne E. Heard, Michael J. Pilling, and Ian D. Trought. Laser induced fluorescence studies of the reactions of $O(^1D_2)$ with N_2, O_2, N_2O, CH_4, H_2, CO_2, Ar, Kr and n-C_4H_{10}. Physical Chemistry Chemical Physics, 6(9):2162, 2004.

[131] Mario Capitelli, Carlos M. Ferreira, Boris F. Gordiets, and Alexey I. Osipov. Plasma Kinetics in Atmospheric Gases, volume 31 of Springer Series on Atomic, Optical, and Plasma Physics. Springer Berlin Heidelberg, Berlin, Heidelberg, 2000.

[132] R. Atkinson, D. L. Baulch, R. A. Cox, J. N. Crowley, R. F. Hampson, R. G. Hynes, M. E. Jenkin, M. J. Rossi, and J. Troe. Evaluated kinetic and photochemical data for atmospheric chemistry: Part 1 - gas phase reactions of O_x, HO_x, NO and SO species. Technical report, December 2003.

[133] N A Popov. Pulsed nanosecond discharge in air at high specific deposited energy: fast gas heating and active particle production. Plasma Sources Science and Technology, 25(4):044003, August 2016.

[134] David R. Bates. Theoretical considerations regarding some inelastic atomic collision processes of interest in aeronomy : Deactivation and charge transfer. Planetary and Space Science, 37(3):363–368, March 1989.

[135] W. Felder and R. A. Young. Quenching of $O(^1S)$ by $O(^3P)$. The Journal of Chemical Physics, 56(12):6028–6030, June 1972.

[136] Keith Schofield. Rate Constants for the Gaseous Interactions of $O(^1D)$ and $O(^1S)$ - A Critical Evaluation. Journal of Photochemistry, 9:55–68, 1978.

[137] I A Kossyi, A Yu Kostinsky, A A Matveyev, and V P Silakov. Kinetic scheme of the non-equilibrium discharge in nitrogen-oxygen mixtures. Plasma Sources Science and Technology, 1(3):207–220, August 1992.

[138] S. V. Filseth, F. Stuhl, and K. H. Welge. Erratum: Collisional Deactivation of O(^{1}S). The Journal of Chemical Physics, 57(9):4064–4064, November 1972.

[139] H U Kiefl and J Fricke. De-excitation of O(^{5}S) metastables in inelastic collisions with noble gases. Journal of Physics B: Atomic and Molecular Physics, 13(6):1185–1193, March 1980.

[140] Lawrence G. Piper. Electronic Energy Transfer Between Metastable Argon Atoms and Ground-State Oxygen Atoms. Chemical Physics Letters, 28(2), 1974.

[141] Paul J Dagdigian, Brad E Forch, and Andrzej W Miziolek. Collisional transfer between and quenching of the $3p^3$p and ^{5}p states of the oxygen atom. Chemical Physics Letters, 148(4):10, 1988.

[142] J.T. Herron. Evaluated Chemical Kinetics Data for Reactions of N(^{2}D), N(^{2}P), and $N_2(A^3\Sigma_u^+)$ in the Gas Phase. Journal of Physical and Chemical Reference Data, 28(5):1453–1483, 1999.

[143] J. Henriques, E. Tatarova, and C. M. Ferreira. Microwave N_2-Ar plasma torch. I. Modeling. Journal of Applied Physics, 109(2):023301, January 2011.

[144] A Salmon, N A Popov, G D Stancu, and C O Laux. Quenching rate of N(^{2}P) atoms in a nitrogen afterglow at atmospheric pressure. Journal of Physics D: Applied Physics, 51(31):314001, August 2018.

[145] K. A. Vereshchagin, V. V. Smirnov, and V. A. Shakhatov. CARS study of the vibrational kinetics of nitrogen molecules in the burning and afterglow stages of a pulsed discharge. Technical Physics, 42(5):487–494, May 1997.

[146] Lawrence G. Piper. The reactions of N(^{2}P) with O_2 and O. The Journal of Chemical Physics, 98(11):8560–8564, June 1993.

[147] Hironobu Umemoto, Naoki Terada, Kunikazu Tanaka, and Shigeki Oguro. Deactivation processes of highly excited atomic nitrogen, N($2p^2 3p$ ^{2}S). Physical Chemistry Chemical Physics, 2(15):3425–3428, 2000.

[148] N. Sadeghi, D. W. Setser, A. Francis, U. Czarnetzki, and H. F. Döbele. Quenching rate constants for reactions of Ar(4p[1/2]^0, 4p[1/2]^0, 4p[3/2]^2, and 4p[5/2]^2) atoms with 22 reagent gases. The Journal of Chemical Physics, 115(7):3144–3154, August 2001.

[149] A V Volynets, D V Lopaev, T V Rakhimova, O V Proshina, A A Chukalovsky, and J P Booth. Fast quenching of metastable $O_2(a^1\Delta_g)$ and $O_2(b^1\Sigma_g^+)$ molecules by O(^{3}P) atoms at high temperature. Plasma Sources Science and Technology, 29(11):115020, November 2020.

[150] Andrew P. Billington and Peter Borrell. The low-temperature Quenching of Singlet Molecular Oxygen $O_2(a^1\Delta_g)$. J. Chem. Soc., Faraday Trans. 2, 82:963–970, 1986.

[151] C. Yamabe and A. V. Phelps. Excitation of the $O_2(a^1\Delta_g)$ state by low energy electrons in O_2-N_2 mixtures. The Journal of Chemical Physics, 78(6):2984–2989, March 1983.

[152] M. V. Zagidullin, N. A. Khvatov, I. A. Medvedkov, G. I. Tolstov, A. M. Mebel, M. C. Heaven, and V. N. Azyazov. $O_2(b^1\Sigma_g^+)$ Quenching by O_2, CO_2, H_2O, and N_2 at Temperatures of 300-800 K. The Journal of Physical Chemistry A, 121(39):7343–7348, October 2017.

[153] Patricia M. Borrell, Peter Borrell, Kevin R. Grant, and Michael D. Pedley. Rate constants for the energy-pooling and quenching reactions of singlet molecular oxygen at high temperatures. The Journal of Physical Chemistry, 86(5):700–703, March 1982.

[154] Peter Borrell, Patricia M. Borrell, M. D. Pedley, and K. R. Grant. High temperature studies of singlet excited oxygen, $O_2(^1\Sigma_g^+)$ and $O_2(^1\Delta_g)$, with a combined discharge flow/shock tube method. Proceedings of the Royal Society of London. A. Mathematical and Physical Sciences, 367:395–410, 1979.

[155] Jichun Shi and John R. Barker. Kinetic Studies of the Deactivation of $O_2(^1\Sigma_g^+)$ and $O(^1D)$. International Journal of Chemical Kinetics, 22:1283–1301, 1990.

[156] N.A. Khvatov, M.V. Zagidullin, G.I. Tolstov, I.A. Medvedkov, A.M. Mebel, M.C. Heaven, and V.N. Azyazov. Product channels of the reactions of $O_2(b^1\Sigma_g^+)$. Chemical Physics, 521:85–91, May 2019.

[157] R. D. Kenner and E. A. Ogryzlo. Deactivation of $O_2(A^3\Sigma_u^+)$ by O_2, O, and Ar. International Journal of Chemical Kinetics, 12(7):501–508, July 1980.

[158] Richard C. Flagan and John P. Appleton. Excitation Mechanisms of the Nitrogen FristPositive and FirstNegative Radiation at High Temperature. The Journal of Chemical Physics, 56(3):1163–1173, February 1972.

[159] A M Starik, N S Titova, and I V Arsentiev. Comprehensive analysis of the effect of atomic and molecular metastable state excitation on air plasma composition behind strong shock waves. Plasma Sources Science and Technology, 19(1):015007, 2010.

[160] J.M. Thomas and Frederick Kaufman. An Upper Limit on the Formation of $NO(X^2\Pi_r)$ in the Reactions $N_2(A^3\Sigma_u^+) + O(^3P)$ and $N_2(A^3\Sigma_u^+) + O_2(X^3\Sigma_g^-)$ at 298 K. J. Phys. Chem, 100:8901–8906, March 1996.

[161] Brett A Cruden and Aaron M Brandis. Measurement and Prediction of Radiative Nonequilibrium for Air Shocks Between 7-9 km/s. In 47th AIAA Thermophysics Conference, page 36, Denver, Colorado, 2017. AIAA.

[162] C Foissac, J Krištof, A Annušová, V Martišovitš, P Veis, and P Supiot. Vacuum UV and UV spectroscopy of a N_2-Ar mixture discharge created by an RF helical coupling device. Plasma Sources Science and Technology, 19(5):055006, October 2010.

[163] Feng An and Shanyu Han. First-principles Dynamics of Collisional Intersystem Crossing: Resonance Enhanced Quenching of $C(^1D)$ by N_2. Physical Chemistry Chemical Physics, 18(1):21–46, 2019.

[164] Kevin M. Hickson, Jean-Christophe Loison, François Lique, and Jacek Kłos. An Experimental and Theoretical Investigation of the $C(^1D) + N_2 \rightarrow C(^3P) + N_2$ Quenching Reaction at Low Temperature. The Journal of Physical Chemistry A, 120(16):2504–2513, April 2016.

[165] Paul J. Dagdigian, Millard H. Alexander, and Jacek Kłos. Theoretical investigation of the dynamics of $O(^1D \rightarrow {}^3P)$ electronic quenching by collision with Xe. The Journal of Chemical Physics, 143(5):054306, August 2015.

[166] Tien V. Pham and M.C. Lin. Ab initio quantum-chemical and kinetic studies of the $O(^1D)$ + $N_2(X^1\Sigma_g^+)$ spin-forbidden quenching process. Chemical Physics Letters, 780:138955, October 2021.

[167] Y. Sun and A. Dalgarno. Excitation of two $O(^1D)$ atoms in the collision of ground state oxygen atoms. Journal of Geophysical Research: Space Physics, 98(A8):13715–13716, August 1993.

[168] H. U. Kiefl, W. L. Borst, and J. Fricke. Excitation of $O(^3S)$ resonance radiation in inelastic collisions between $O(^5S)$ metastables and O_2 and N_2 gases. Physical Review A, 21(2):518–524, February 1980.

[169] I. I. Glass and W. S. Liu. Effects of hydrogen impurities on shock structure and stability in ionizing monatomic gases. Part 1. Argon. Journal of Fluid Mechanics, 84(01):55, January 1978.

[170] Arnold J Kelly. AtomAtom Ionization Cross Sections of the Noble GasesArgon, Krypton, and Xenon. The Journal of Chemical Physics, 45(1723):11, 1966.

[171] Kenneth E. Harwell and Robert G. Jahn. Initial Ionization Rates in Shock-Heated Argon, Krypton, and Xenon. Physics of Fluids, 7(2):214, 1964.

[172] T. I. McLaren and R.M. Hobson. Initial Ionization Rates and Collision Cross Sections in Shock-Heated Argon. Physics of Fluids, 11(10):2162, 1968.

[173] Edward J. Morgan and Robert D. Morrison. Ionization Rates behind Shock Waves in Argon. The Physics of Fluids, 8(9):1608–1615, September 1965.

[174] Paul O. Haugsjaa and Robert C. Amme. Ionization and Metastable Excitation in LowEnergy Collisions of GroundState Argon Atoms. The Journal of Chemical Physics, 52(9):4874–4877, May 1970.

[175] J. R. Peterson, A. Le Padellec, H. Danared, G. H. Dunn, M. Larsson, A. Larson, R. Peverall, C. Strömholm, S. Rosén, M. af Ugglas, and W. J. van der Zande. Dissociative recombination and excitation of N_2^+: Cross sections and product branching ratios. The Journal of Chemical Physics, 108(5):1978–1988, February 1998.

[176] L. Vejby-Christensen, D. Kella, H. B. Pedersen, and L. H. Andersen. Dissociative recombination of NO^+. Physical Review A, 57(5):3627–3634, May 1998.

[177] A. Le Padellec. Partial Near Threshold Cross Sections for the Associative Ionization to Form CO^+, NO^+, and $O_2{}^+$. Physica Scripta, 71(6):621–626, January 2005.

[178] Robert Peverall, Stefan Rosén, James R. Peterson, Mats Larsson, Ahmed Al-Khalili, Ljiljana Vikor, Jacek Semaniak, Rolf Bobbenkamp, Arnaud Le Padellec, A. N. Maurellis, and Wim J. van der Zande. Dissociative recombination and excitation of O_2^+: Cross sections, product yields and implications for studies of ionospheric airglows. The Journal of Chemical Physics, 114(15):6679–6689, April 2001.

[179] Clint H. Sheehan. Dissociative recombination of N_2^+, O_2^+, and NO^+ : Rate coefficients for ground state and vibrationally excited ions. Journal of Geophysical Research, 109(A3):A03302, 2004.

[180] Dandan Lu, Miguel González, and Hua Guo. Formation of N(^{2}D) from Hyperthermal Collisions between O(^{3}P) and NO(X$^2\Pi$). The Journal of Physical Chemistry A, page acs.jpca.3c05680, October 2023.

[181] Miguel González, Irene Miquel, and R. Sayós. VTST kinetics study of the N(^{2}D) + O_2(X) = NO(X) O(^{3}P; ^{1}D) reactions based on CASSCF and CASPT2 ab initio calculations including excited potential energy surfaces. Chemical Physics Letters, 335:339–347, 2001.

[182] Jing Li, Pedro J. S. B. Caridade, and António J. C. Varandas. Quasiclassical Trajectory Study of the Atmospheric Reaction N(^{2}D) + NO(X$^2\Pi$) → O(^{1}D) + N_2(X$^1\Sigma_g^+$). The Journal of Physical Chemistry A, 118(8):1277–1286, February 2014.

[183] Deepak Bose and Graham V. Candler. Thermal rate constants of the N_2+O→NO+N reaction using ab initio 3A" and 3A' potential energy surfaces. The Journal of Chemical Physics, 104(8):2825–2833, February 1996.

[184] Deepak Bose and Graham V. Candler. Thermal rate constants of the O_2+N→NO+O reaction based on the A2' and A4' potential-energy surfaces. The Journal of Chemical Physics, 107(16):6136–6145, October 1997.

[185] Alexey V. Pelevkin, Boris I. Loukhovitski, and Alexander S. Sharipov. Reaction of the N Atom with Electronically Excited O_2 Revisited: A Theoretical Study. The Journal of Physical Chemistry A, 125(37):8294–8312, September 2021.

[186] L Isola, M López, and B J Gómez. Study of the excitation mechanisms of the second positive system in the negative glow of a N_2-Ar discharge. Journal of Physics D: Applied Physics, 44(37):375204, September 2011.

[187] Irmak T. Karpuzcu, Matthew P. Jouffray, and Deborah A. Levin. Collisional Radiative Modeling of Electronically Excited States in a Hypersonic Flow. Journal of Thermophysics and Heat Transfer, pages 1–21, April 2022.

[188] Ronald Olson. Calculation of the Quenching Rate of O(^{1}S) by O(^{3}P). Chemical Physics Letters, March 1973.

[189] A.V. Phelps. Cross Sections and Swarm Coefficients for Nitrogen Ions and Neutrals in N_2 and Argon Ions and Neutrals in Ar for Energies from 0.1 eV to 10 keV. J. Phys. Chem. Ref. Data, 20(3), 1991.

[190] W. Freysinger, F. A. Khan, P. B. Armentrout, P. Tosi, O. Dmitriev, and D. Bassi. Chargetransfer reaction of $^{14,15}N^+(^3P_j)$+$N_2(^1\Sigma^+{}_g)$ from thermal to 100 eV. Crossed-beam and scattering-cell guided-ion beam experiments. The Journal of Chemical Physics, 101(5):3688–3695, September 1994.

[191] Christophe Laux. Optical diagnostics and radiative emission of air plasmas. PhD thesis, Stanford University, 1993.

[192] M. Panesi, T. E. Magin, A. Bourdon, A. Bultel, and O. Chazot. Electronic Excitation of Atoms and Molecules for the FIRE II Flight Experiment. Journal of Thermophysics and Heat Transfer, 25(3):361–374, July 2011.

[193] T. Holstein. Imprisonment of Resonance Radiation in Gases. Physical Review, 72(12):1212–1233, December 1947.

[194] T. Holstein. Imprisonment of Resonance Radiation in Gases. II. Physical Review, 83(6):1159–1168, September 1951.

[195] Aaron M Brandis and Brett A Cruden. NEQAIR v15.0 Release Notes Nonequilibrium and Equilibrium Radiative Transport and Spectra Program. Technical Report ARC-E-DAA-TN72963, 2019.

[196] H Nussbaumer and P.J. Storey. Dielectronic recombination at low temperatures. Astronomy and Astrophysics, 126:75–79, April 1983.

[197] Michael E. Holloway and Iain D. Boyd. Sensitivity Analysis of Thermochemical Kinetics Modeling for Hypersonic Air Flows. Journal of Thermophysics and Heat Transfer, 36(3):584–593, July 2022.

[198] Ajay Krish, Jesse W. Streicher, and Ronald K. Hanson. Ultraviolet absorption cross-section measurements of shock-heated o_2 from 2,000-8,400 K using a tunable laser. Journal of Quantitative Spectroscopy and Radiative Transfer, 247:106959, May 2020.

[199] Ajay Krish, Jesse W. Streicher, and Ronald K. Hanson. Spectrally-resolved absorption cross-section measurements of shock-heated o_2 for the development of a vibrational temperature diagnostic. Journal of Quantitative Spectroscopy and Radiative Transfer, 270:107704, August 2021.

[200] Leonardo C Scalabrin. Numerical Simulation of Weakly Ionized Hypersonic Flow over Reentry Capsules. PhD thesis, University of Michigan, 2007.

[201] Maninder S. Grover, Erik Torres, and Thomas E. Schwartzentruber. Direct molecular simulation of internal energy relaxation and dissociation in oxygen. Physics of Fluids, 31(7):076107, July 2019.

[202] John H. Kiefer and Robert W. Lutz. The effect of oxygen atoms on the vibrational relaxation of oxygen. Symposium (International) on Combustion, 11(1):67–76, January 1967.

[203] Ross S Chaudhry. Modeling and Analysis of Chemical Kinetics for Hypersonic Flows in Air. PhD thesis, University of Minnesota, November 2018.

[204] Yang Li, Shengkai Wang, Christopher L Strand, and Ronald K Hanson. Development of a Stark shift measurement technique using excited-state oxygen atoms to determine electron number density in shock heated O_2-Ar above 10,000 K. Plasma Sources Science and Technology, 30(2):025007, February 2021.

[205] H. Wong and D. Bershader. Thermal equilibration behind an ionizing shock. Journal of Fluid Mechanics, 26(3):459–479, November 1966.

[206] Geoffrey Ringer and W. Ronald Gentry. A merged molecular beam study of the endoergic associative ionization reaction $N(^2D)+O(^3P) \rightarrow NO^+ + e^-$. The Journal of Chemical Physics, 71(4):1902–1909, August 1979.

[207] Elijah R. Jans, Ilya Gulko, Dirk C. M. van den Bekerom, Terry A. Miller, and Igor V. Adamovich. Measurements of Metastable $N_2(A^3\Sigma_u^+,v)$ Molecules in Nonequilibrium Supersonic Flows. Journal of Thermophysics and Heat Transfer, 36(1):196–206, January 2022.

[208] Timothy T Aiken and Iain D Boyd. Analysis of Critical Rate Processes for Ionization in Shock-Heated Air. In AIAA AVIATION 2023 Forum, San Diego, CA and Online, June 2023. AIAA.

[209] Erik Torres, Eric C. Geistfeld, and Thomas E. Schwartzentruber. Direct molecular simulation of rovibrational relaxation and chemical reactions in air mixtures. In AIAA SCITECH 2022 Forum, San Diego, CA & Virtual, January 2022. American Institute of Aeronautics and Astronautics.

[210] Serhat Hosder, Robert Walters, and Michael Balch. Efficient Sampling for Non-Intrusive Polynomial Chaos Applications with Multiple Uncertain Input Variables. In 48th AIAA/ASME/ASCE/AHS/ASC Structures, Structural Dynamics, and Materials Conference, Honolulu, Hawaii, April 2007. American Institute of Aeronautics and Astronautics.

[211] Aaron M. Brandis and Brett A. Cruden. Benchmark Shock Tube Experiments of Radiative Heating Relevant to Earth Re-entry. In 55th AIAA Aerospace Sciences Meeting, Grapevine, Texas, January 2017. American Institute of Aeronautics and Astronautics.

[212] Brett A. Cruden. Electron Density Measurement in Reentry Shocks for Lunar Return. Journal of Thermophysics and Heat Transfer, 26(2):222–230, April 2012.

[213] J. Wilson. Ionization Rate of Air behind High-Speed Shock Waves. Physics of Fluids, 9(10):1913, 1966.

[214] Matthew Satchell, Justin Clarke, Peter L. Collen, Matthew McGilvray, and Luca di Mare. Advancements in the Modeling and Simulation of Shock Tube Flows. In AIAA SCITECH 2022 Forum, San Diego, CA & Virtual, January 2022. American Institute of Aeronautics and Astronautics.

[215] Augustin Tibère-Inglesse and Brett A. Cruden. Analysis of nonequilibrium atomic and molecular nitrogen radiation in pure N_2 shockwaves. Journal of Quantitative Spectroscopy and Radiative Transfer, 290:108302, November 2022.

[216] Christopher O. Johnston and Bil Kleb. Uncertainty Analysis of Air Radiation for Lunar-Return Shock Layers. Journal of Spacecraft and Rockets, 49(3):425–434, May 2012.

[217] K. Grogan and M. Ihme. StanShock: a gas-dynamic model for shock tube simulations with non-ideal effects and chemical kinetics. Shock Waves, 30(4):425–438, June 2020.

[218] Michael G. Kapper. A High Order Transport Scheme for Collisional-Radiative and Nonequilibrium Plasma. PhD thesis, The Ohio State University, 2009.

[219] Matthew Satchell, Matthew McGilvray, and Luca Di Mare. Analytical Method of Evaluating Nonuniformities in Shock Tube Flows: Theory and Development. AIAA Journal, 60(2):654–668, February 2022.

[220] Matthew Satchell, Alex Glenn, Peter Collen, Rowland Penty-Geraets, Matthew McGilvray, and Luca Di Mare. Analytical Method of Evaluating Nonuniformities in Shock Tube Flows: Application. AIAA Journal, 60(2):669–676, February 2022.

[221] Aaron M. Brandis and Brett A. Cruden. Shock Tube Radiation Measurements in Nitrogen. In 2018 Joint Thermophysics and Heat Transfer Conference, Atlanta, Georgia, June 2018. American Institute of Aeronautics and Astronautics.

[222] Hans-Jurgen Mick, Michael Burmeister, and Paul Roth. Atomic resonance absorption spectroscopy measurements on high-temperature CO dissociation kinetics. AIAA Journal, 31(4):671–676, April 1993.

Appendix A

Electronic State Data

Table A.1: Electronic state energies and degeneracies for neutral atomic species.

	N		O		Ar	
i	ε_i (cm^{-1})	g_i	ε_i (cm^{-1})	g_i	ε_i (cm^{-1})	g_i
1	0.0	4	78.0	9	0.0	1
2	19227.9	10	15867.9	5	93143.8	5
3	28839.2	6	33792.6	1	93750.6	3
4	83335.6	12	73768.2	5	94553.7	1
5	86192.8	6	76795.0	3	95399.8	3
6	88132.4	12	86629.1	15	104102.1	3
7	93581.6	2	88631.0	9	105462.8	7
8	94837.8	20	95476.7	5	105617.3	5
9	95509.9	12	96225.0	3	106087.3	3
10	96750.8	4	97420.7	25	106237.6	5
11	96833.5	10	97488.5	15	107054.3	1
12	97794.0	6	99094.1	15	107131.7	3
13	99663.6	10	99681.1	9	107289.7	5
14	103693.9	12	101143.4	15	107496.4	3
15	104196.0	6	102116.7	5	108722.6	1
16	104628.3	6	102412.0	3	111667.8	1
17	104719.6	28	102662.0	5	111818.0	3
18	104849.0	26	102865.6	25	112138.9	5
19	105007.3	20	102908.4	15	112750.2	9
20	105134.2	10	102968.3	56	113020.4	7
21	106477.8	2	103626.3	15	113426.0	5
22	106823.3	20	103870.0	9	113468.5	5
23	107014.0	12	105019.3	5	113643.3	3
24	107225.0	10	105165.2	3	113716.6	7
25	107445.6	4	105394.2	40	114147.7	3
26	107615.0	6	105441.7	56	114641.0	5
27	109884.2	12	105788.7	15	114805.1	5
28	110081.1	6	105912.0	9	114821.9	7
29	110310.0	90	106545.4	5	114861.6	1
30	110453.5	126	106627.9	3	114975.0	3
31	110639.1	24	106779.6	168	115366.9	3
32	111060.9	2	107446.0	5		
33	111241.0	38	107497.2	3		
34	111501.4	4	107587.6	96		
35	111884.6	10	108034.4	8		
36	112311.2	6	108109.0	40		
37	112666.1	18	108421.1	8		
38	112843.9	96	108472.7	40		
39	113189.3	126	108705.5	3		
40	114167.9	32	108733.2	40		
41	114189.6	18				
42	114241.4	90				
43	114577.7	126				
44	115051.7	20				
45	115393.4	108				
46	115624.1	20				

Table A.2: Electronic state energies and degeneracies for ionized atomic species.

	N^+		O^+		Ar^+	
i	ε_i (cm^{-1})	g_i	ε_i (cm^{-1})	g_i	ε_i (cm^{-1})	g_i
1	88.89	9	0.0	4	0.0	4
2	15316.2	5	26819.0	10	1431.6	2
3	32688.6	1	40468.0	6		
4	46784.6	5	119932.6	12		
5	92243.9	15	165991.7	10		

Table A.3: Electronic state information and diatomic spectroscopic constants for considered molecules. All constants are given in units of cm^{-1}.

s	i	State	ε_i	g_i	$D_{0,s(i)}$	ω_e	$\omega_e x_e$	$\omega_e y_e$	$\omega_e z_e$	B_e	α_e	β_e
O_2	1	$X^3\Sigma_g^-$	0.0	3	41260	1580.19	11.981	4.747E-2	-1.27E-3	1.4456	0.0159	0.0
	2	$a^1\Delta_g$	7918.1	2	33410	1509.76	13.065	1.100E-2	0.0	1.4264	0.0172	0.0
	3	$b^1\Sigma_g^+$	13195.1	1	28160	1432.77	14.00	0.0	0.0	1.4004	0.0182	3.2E-8
	4	$c^1\Sigma_u^-$	33057.0	1	8620	794.20	12.73	-2.44E-1	0.0	0.9150	0.0139	0.0
	5	$A'^3\Delta_u$	34690.0	6	6960	850.00	20.00	0.0	0.0	0.9600	0.0262	0.0
	6	$A^3\Sigma_u^+$	35397.8	3	6270	799.07	12.16	-5.50E-1	0.0	0.9106	0.0141	5.0E-7
	7	$B^3\Sigma_u^-$	49793.3	3	7790	709.31	10.65	-1.39E-1	-2.40E-2	0.8190	0.0120	2.2E-7
N_2	1	$X^1\Sigma_g^+$	0.0	1	78741	2358.57	14.324	-2.26E-3	0.0	1.9982	0.0173	0.0
	2	$A^3\Sigma_u^+$	50203.6	3	28537	1460.64	13.872	1.030E-2	0.0	1.4546	0.0180	0.0
	3	$B^3\Pi_g$	59619.3	6	38350	1733.39	14.122	-5.69E-2	0.0	1.6374	0.0179	0.0
	4	$W^3\Delta_u$	59808.0	6	38160	1501.4	11.6	0.0	0.0	1.5	0.0	0.0
	5	$B'^3\Sigma_u^-$	66272.4	8	31696	1516.88	12.181	4.186E-2	0.0	1.4733	0.0167	0.0
	6	$C^3\Pi_u$	89136.9	6	8960	2047.18	28.445	0.0	0.0	1.8247	0.0187	0.0
NO	1	$X^2\Pi$	119.82	4	52275	1904.20	14.100	0.0	0.0	1.7202	0.0171	0.0
	2	$a^4\Pi$	38440.0	8	13895	1017.0	11.0	0.0	0.0	1.8	0.0	0.0
	3	$A^2\Sigma^+$	43965.7	2	8369	2374.31	10.106	-4.65E-2	0.0	1.9965	0.0192	0.0
	4	$B^2\Pi$	45942.6	4	25631	1037.2	7.70	1.0E-1	0.0	1.092	0.012	0.0
	5	$b^4\Sigma^-$	48680.0	4	19523	1206.0	15.0	0.0	0.0	1.0	0.0	0.0
O_2^+	1	$X^2\Pi_g$	0.0	4	54689	1904.77	16.259	0.0	0.0	1.6913	0.0198	0.0
	2	$a^4\Pi_u$	32964.0	8	21725	1035.69	10.39	0.0	0.0	1.1046	0.0158	0.0
	3	$A^2\Pi_u$	40669.0	4	14020	898.20	13.573	0.0	0.0	1.0617	0.0194	0.0
	4	$b'^4\Pi_g$	48000.0	8	6689	1000.00	15.0	0.0	0.0	1.0	0.01	0.0
	5	$b^4\Sigma_g^-$	49552.0	4	5137	1196.77	17.09	0.0	0.0	1.2872	0.0221	0.0
N_2^+	1	$X^2\Sigma_g^+$	0.0	2	70301	2207.00	16.10	-4.0E-2	0.0	1.9318	0.0188	0.0
	2	$A^2\Pi_u$	9167.0	4	61133	1903.70	15.02	0.0	0.0	1.7444	0.0188	0.0
	3	$B^2\Sigma_u^+$	25461.5	2	44839	2419.84	23.19	-5.38E-1	0.0	2.0746	0.024	0.0
	4	$D^2\Pi_g$	52318.2	4	18637	907.71	11.91	1.6E-2	0.0	1.113	0.020	0.0
NO^+	1	$X^1\Sigma^+$	0.0	1	87516	2376.42	16.262	0.0	0.0	1.9973	0.0190	0.0

Appendix B

Radiative Transition Data

Table B.1: Included Einstein A coefficients for atomic nitrogen.

j	i	A (s^{-1})	j	i	A (s^{-1})	j	i	A (s^{-1})	j	i	A (s^{-1})	j	i	A (s^{-1})
2	1	1.27e-05	9	4	3.08e+07	19	9	2.56e+07	36	13	3.14e+07	30	24	9.87e+04
3	1	5.20e-03	10	4	3.71e+07	20	9	9.45e+04	22	14	3.06e+06	38	24	1.53e+05
4	1	4.04e+08	11	4	2.08e+04	27	9	2.53e+06	23	14	3.94e+06	39	24	2.14e+04
5	1	4.20e+04	12	4	1.56e+03	29	9	2.34e+05	25	14	4.14e+06	27	25	2.87e+05
6	1	1.47e+08	13	4	1.99e-03	30	9	5.10e+05	33	14	9.98e+04	29	25	3.39e+05
13	1	5.78e+02	25	4	1.90e+06	39	9	1.64e+05	34	14	4.84e+05	37	25	8.90e+04
14	1	5.78e+07	7	5	8.82e+06	14	10	1.13e+06	21	15	7.53e+05	38	25	6.06e+04
15	1	3.06e+05	9	5	3.37e+03	15	10	4.05e+03	24	15	2.52e+06	40	25	2.88e+04
16	1	3.74e+05	10	5	2.97e+04	16	10	4.92e+04	26	15	4.37e+06	42	25	2.26e+04
17	1	7.42e+04	11	5	2.51e+07	17	10	5.81e+03	31	15	3.96e+04	43	25	7.41e+02
18	1	8.43e+07	12	5	3.16e+07	18	10	6.00e+06	32	15	1.91e+05	44	25	2.43e+04
19	1	7.02e+06	13	5	1.03e-03	19	10	6.41e+05	33	15	1.42e+04	45	25	3.58e+03
20	1	5.66e+05	21	5	2.57e+06	20	10	2.99e+04	35	15	1.02e+06	28	26	2.34e+06
27	1	2.92e+07	26	5	9.73e+05	27	10	6.94e+05	36	15	3.46e+05	29	26	2.60e+04
29	1	1.33e+07	31	5	1.67e+06	29	10	1.74e+05	21	16	1.01e+06	30	26	2.49e+05
37	1	1.01e+07	32	5	1.72e+06	37	10	2.48e+05	24	16	2.46e+05	39	26	3.94e+04
38	1	6.83e+06	35	5	2.50e+06	38	10	3.40e+04	26	16	2.36e+04	33	27	6.83e+05
40	1	3.30e+06	36	5	5.57e+06	40	10	8.22e+04	31	16	1.72e+04	34	27	8.64e+05
42	1	4.33e+06	8	6	1.00e+06	42	10	1.13e+04	33	16	7.85e+03	31	28	5.67e+03
43	1	8.79e+04	9	6	6.98e+05	43	10	2.16e+03	35	16	9.70e+04	32	28	9.32e+04
44	1	2.78e+06	10	6	4.39e+06	44	10	6.91e+04	36	16	6.07e+04	33	28	7.35e+04
45	1	4.15e+05	11	6	3.36e+03	45	10	1.04e+04	22	17	7.26e+05	35	28	6.47e+05
3	2	8.82e-02	12	6	2.46e+03	13	11	7.96e+03	33	17	6.09e+04	36	28	3.55e+05
5	2	3.44e+08	22	6	2.03e+05	14	11	5.27e+03	22	18	4.43e+04	31	29	1.43e+03
13	2	3.45e+08	23	6	1.22e+05	15	11	7.33e+06	23	18	1.19e+05	32	29	4.21e+05
14	2	1.24e+05	14	7	5.85e+03	16	11	3.46e+06	24	18	9.04e+05	33	29	1.93e+05
15	2	9.77e+07	15	7	1.29e+05	18	11	1.11e+07	25	18	1.85e+06	34	29	7.78e+05
16	2	1.05e+07	16	7	3.21e+07	19	11	1.95e+05	33	18	1.90e+04	35	29	5.66e+05
17	2	1.54e+06	17	7	5.26e+04	20	11	6.20e+06	34	18	3.60e+05	36	29	3.78e+03
18	2	5.93e+07	18	7	2.08e+04	28	11	2.30e+06	35	18	4.14e+05	33	30	1.02e+05
19	2	7.80e+05	19	7	1.74e+04	29	11	3.13e+05	22	19	9.28e+04	35	30	6.45e+04
20	2	3.21e+07	20	7	6.52e+04	30	11	4.74e+04	23	19	5.95e+05	36	30	1.20e+05
28	2	4.00e+07	29	7	2.40e+05	38	11	4.01e+04	33	19	3.01e+04	38	31	1.97e+05
29	2	9.87e+06	38	7	1.14e+05	39	11	1.03e+04	24	20	1.30e+05	39	31	2.31e+04
38	2	5.03e+06	14	8	1.50e+07	13	12	2.67e+03	26	20	9.43e+05	38	32	6.59e+04
5	3	1.25e+08	15	8	1.90e+04	14	12	2.62e+03	31	20	2.88e+04	38	33	4.85e+05
13	3	5.39e+07	16	8	3.36e+05	15	12	7.53e+06	33	20	1.71e+04	39	33	3.25e+05
14	3	3.06e+04	17	8	3.84e+07	16	12	2.34e+06	29	21	2.71e+05	37	34	5.95e+04
15	3	9.75e+06	18	8	1.86e+06	17	12	6.80e+03	38	21	7.86e+04	38	34	8.26e+04
16	3	7.26e+07	19	8	1.01e+07	18	12	4.07e+04	27	22	2.71e+06	40	34	1.52e+04
17	3	1.46e+05	20	8	9.08e+04	19	12	1.47e+04	29	22	1.86e+06	42	34	2.37e+04
18	3	3.64e+05	27	8	4.36e+06	20	12	1.34e+07	30	22	2.13e+05	43	34	3.62e+02
19	3	1.09e+05	29	8	1.56e+06	28	12	1.40e+06	38	22	4.17e+05	44	34	1.24e+04
20	3	7.73e+07	30	8	2.23e+05	30	12	6.52e+04	39	22	6.42e+04	45	34	1.78e+03
29	3	2.70e+06	38	8	4.05e+05	38	12	1.25e+04	27	23	2.19e+06	38	35	7.03e+04
30	3	3.50e+06	39	8	7.82e+04	39	12	8.38e+03	29	23	3.13e+05	39	35	1.05e+04
38	3	1.34e+06	14	9	1.00e+07	24	13	4.51e+05	30	23	6.02e+05	38	36	7.27e+01
39	3	1.91e+06	15	9	3.09e+04	26	13	1.81e+05	38	23	4.27e+04	39	36	5.44e+03
6	4	4.97e-03	16	9	9.95e+04	31	13	2.72e+07	39	23	1.62e+05			
7	4	1.22e+04	17	9	7.89e+04	33	13	9.56e+05	28	24	1.90e+06			
8	4	2.53e+07	18	9	5.96e+06	35	13	1.40e+07	29	24	7.94e+05			

Table B.2: Included Einstein A coefficients for atomic oxygen.

j	i	A (s^{-1})	j	i	A (s^{-1})	j	i	A (s^{-1})	j	i	A (s^{-1})	j	i	A (s^{-1})
2	1	7.48e-03	6	4	3.69e+07	16	7	6.72e+06	20	11	5.52e+06	34	13	3.66e+04
3	1	7.56e-02	7	4	8.70e+02	19	7	3.53e+06	22	11	1.83e+05	36	13	5.10e+04
4	1	5.56e+03	12	4	4.89e+05	24	7	3.15e+06	26	11	1.81e+06	20	14	5.86e+03
5	1	6.12e+08	6	5	1.60e+02	25	7	3.40e+05	28	11	8.52e+04	22	14	2.58e+04
9	1	1.70e+08	7	5	3.22e+07	30	7	1.75e+06	31	11	2.85e+05	26	14	1.63e+04
11	1	7.63e+07	13	5	7.58e+05	31	7	3.20e+04	34	11	2.81e+05	31	14	3.13e+03
14	1	2.26e+08	22	5	9.30e+04	33	7	1.07e+06	15	12	5.51e+06	34	14	3.38e+03
16	1	6.93e+07	8	6	2.67e+07	34	7	2.75e+04	18	12	6.45e+06	20	18	1.50e+02
17	1	1.32e+05	10	6	4.45e+07	36	7	3.74e+04	19	12	4.26e+02	21	18	2.02e+05
19	1	5.84e+07	11	6	7.75e+02	12	8	4.29e+06	23	12	1.99e+06	26	18	1.68e+06
24	1	3.48e+07	15	6	8.25e+06	21	8	2.35e+05	25	12	1.21e+06	27	18	1.35e+04
25	1	1.05e+07	18	6	7.62e+06	27	8	4.54e+04	29	12	1.04e+06	31	18	2.85e+05
30	1	1.99e+07	19	6	4.49e+02	12	9	3.01e+01	31	12	1.29e+05	34	18	2.87e+05
31	1	1.48e+06	23	6	3.86e+06	13	9	4.10e+06	32	12	6.19e+05	20	19	1.75e+01
33	1	1.24e+07	25	6	1.69e+06	22	9	2.86e+05	34	12	1.22e+05	22	19	3.62e+05
34	1	1.66e+06	29	6	2.14e+06	12	10	4.97e+05	36	12	1.79e+05	26	19	1.02e+06
36	1	2.70e+06	31	6	1.89e+05	20	10	9.23e+06	16	13	4.82e+06	28	19	6.75e+04
3	2	1.26e+00	32	6	1.31e+06	21	10	4.04e+04	18	13	2.24e+02	31	19	1.67e+05
4	2	5.32e-03	34	6	1.82e+05	26	10	3.10e+06	19	13	5.04e+06	34	19	1.66e+05
5	2	1.83e+03	36	6	2.69e+05	27	10	2.09e+04	24	13	1.70e+06	25	20	4.02e+04
14	2	1.38e+04	9	7	2.14e+07	31	10	4.95e+05	25	13	4.43e+05	31	20	4.18e+03
17	2	5.28e+08	10	7	3.31e+02	34	10	4.89e+05	30	13	8.88e+05	34	20	3.91e+03
5	3	4.61e+00	11	7	3.09e+07	12	11	5.70e+00	31	13	4.15e+04	36	20	5.64e+03
14	3	1.81e+03	14	7	5.61e+04	13	11	9.86e+05	33	13	5.31e+05			

Table B.3: Included Einstein A coefficients for argon.

j	i	A (s^{-1})	j	i	A (s^{-1})	j	i	A (s^{-1})	j	i	A (s^{-1})	j	i	A (s^{-1})
3	1	1.32e+08	14	3	1.83e+06	21	7	1.20e+05	18	10	2.50e+06	22	13	1.20e+05
5	1	5.32e+08	15	3	2.36e+05	22	7	1.10e+07	20	10	8.80e+04	23	13	2.90e+04
23	1	7.70e+07	6	4	9.80e+05	24	7	3.10e+06	22	10	3.30e+06	24	13	9.80e+03
25	1	2.70e+08	9	4	2.43e+06	17	8	3.90e+04	23	10	2.70e+06	26	13	2.20e+06
30	1	3.50e+07	12	4	1.86e+07	18	8	1.20e+05	27	10	3.76e+06	28	13	1.50e+07
31	1	3.13e+08	14	4	1.17e+07	20	8	1.10e+07	30	10	1.39e+06	30	13	8.90e+06
6	2	1.89e+07	6	5	1.90e+05	21	8	5.70e+06	31	10	3.96e+05	16	14	3.60e+05
7	2	3.30e+07	8	5	1.47e+06	22	8	1.10e+06	23	11	1.30e+06	17	14	1.70e+05
8	2	9.30e+06	9	5	1.06e+06	23	8	8.90e+06	25	11	4.30e+06	18	14	1.10e+05
9	2	5.20e+06	10	5	5.00e+06	24	8	2.00e+06	30	11	3.80e+05	22	14	3.10e+05
10	2	2.45e+07	12	5	1.39e+07	25	8	9.52e+05	31	11	4.20e+05	23	14	3.00e+04
12	2	6.30e+05	13	5	2.23e+07	26	8	8.30e+05	16	12	1.20e+05	27	14	6.20e+06
13	2	3.80e+06	14	5	1.53e+07	30	8	2.10e+05	17	12	3.20e+04	29	14	5.10e+06
14	2	6.40e+06	15	5	4.50e+07	18	9	2.60e+05	22	12	5.90e+04	30	14	3.40e+06
6	3	5.40e+06	16	6	8.10e+06	21	9	7.30e+06	23	12	4.50e+05	31	14	7.10e+06
8	3	2.15e+07	17	6	7.40e+06	22	9	4.60e+05	26	12	1.30e+07	23	15	1.60e+05
9	3	2.50e+07	18	6	4.90e+06	23	9	4.60e+06	29	12	1.00e+07	30	15	1.90e+06
10	3	4.90e+06	22	6	4.90e+06	25	9	1.10e+07	30	12	2.00e+06	31	15	5.20e+06
11	3	4.00e+07	23	6	2.44e+06	27	9	3.69e+05	31	12	4.50e+06			
12	3	2.20e+04	29	6	3.26e+06	29	9	2.22e+06	17	13	1.40e+05			
13	3	8.50e+06	30	6	1.76e+06	30	9	2.80e+05	18	13	3.90e+05			